Western Graduate&PostdoctoralStudies

Western University
Scholarship@Western

Electronic Thesis and Dissertation Repository

8-27-2013 12:00 AM

Vascular Segmentation Algorithms for Generating 3D Atherosclerotic Measurements

Eranga Ukwatta
The University of Western Ontario

Supervisor
Dr. Aaron Fenster
The University of Western Ontario

Graduate Program in Biomedical Engineering
A thesis submitted in partial fulfillment of the requirements for the degree in Doctor of Philosophy
© Eranga Ukwatta 2013

Follow this and additional works at: https://ir.lib.uwo.ca/etd

Part of the Bioimaging and Biomedical Optics Commons

Recommended Citation

Ukwatta, Eranga, "Vascular Segmentation Algorithms for Generating 3D Atherosclerotic Measurements" (2013). *Electronic Thesis and Dissertation Repository*. 1568.
https://ir.lib.uwo.ca/etd/1568

This Dissertation/Thesis is brought to you for free and open access by Scholarship@Western. It has been accepted for inclusion in Electronic Thesis and Dissertation Repository by an authorized administrator of Scholarship@Western. For more information, please contact wlswadmin@uwo.ca.

Vascular Segmentation Algorithms for Generating 3D Atherosclerotic Measurements

(Thesis format: Integrated-Article)

by
Eranga Ukwatta

Graduate Program
in
Biomedical Engineering

A thesis submitted in partial fulfillment
of the requirements for the degree of
Doctor of Philosophy

School of Graduate and Postdoctoral Studies
The University of Western Ontario
London, Ontario, Canada

© Eranga Ukwatta 2013

Abstract

Atherosclerosis manifests as plaques within large arteries of the body and remains as a leading cause of mortality and morbidity in the world. Major cardiovascular events may occur in patients without known preexisting symptoms, thus it is important to monitor progression and regression of the plaque burden in the arteries for evaluating patient's response to therapy. In this dissertation, our main focus is quantification of plaque burden from the carotid and femoral arteries, which are major sites for plaque formation, and are straight forward to image noninvasively due to their superficial location. Recently, 3D measurements of plaque burden have shown to be more sensitive to the changes of plaque burden than one-/two-dimensional measurements. However, despite the advancements of 3D noninvasive imaging technology with rapid acquisition capabilities, and the high sensitivity of the 3D plaque measurements of plaque burden, they are still not widely used due to the inordinate amount of time and effort required to delineate artery walls plus plaque boundaries to obtain 3D measurements from the images. Therefore, the objective of this dissertation is developing novel semi-automated segmentation methods to alleviate measurement burden from the observer for segmentation of the outer wall and lumen boundaries from: (1) 3D carotid ultrasound (US) images, (2) 3D carotid black-blood magnetic resonance (MR) images, and (3) 3D femoral black-blood MR images.

Segmentation of the carotid lumen and outer wall from 3DUS images is a challenging task due to low image contrast, for which no method has been previously reported. Initially, we developed a 2D slice-wise segmentation algorithm based on the level set method, which was then extended to 3D. The 3D algorithm required fewer user interactions than manual delineation and the 2D method. The algorithm reduced user time by ≈ 79% (1.72 vs. 8.3 min) compared to manual segmentation for generating 3D-based measurements with high accuracy (Dice similarity coefficient (DSC) $>$ 90%). Secondly, we developed a novel 3D multi-region segmentation algorithm, which simultaneously delineates both the carotid lumen and outer wall surfaces from MR images by evolving two coupled surfaces using a convex max-flow-based technique. The algorithm required user interaction only on a single transverse slice of the 3D image for generating 3D surfaces of the lumen and outer wall. The algorithm was parallelized using graphics processing units (GPU) to increase computational speed, thus reducing user time by $\approx 93\%$ (0.78 vs. 12 min) compared to manual segmentation. Moreover, the algorithm yielded high accuracy (DSC $> 90\%$) and high precision (intra-observer CV $< 5.6\%$ and inter-observer CV $< 6.6\%$). Finally, we developed and validated an algorithm based on convex max-flow formulation to segment the femoral arteries that enforces a tubular shape prior and an inter-surface consistency of the outer wall and lumen to maintain a minimum separation distance between the two surfaces. The algorithm required the observer to choose only about 11 points on its medial axis of the artery to yield the 3D surfaces of the lumen and outer wall, which reduced the operator time by 97% (1.8 vs. 70–80 min) compared to manual segmentation. Furthermore, the proposed algorithm reported DSC greater than 85% and small intra-observer variability (CV $\approx 6.69\%$). In conclusion, the development of robust semi-automated algorithms for generating 3D measurements of plaque burden may accelerate translation of 3D measurements to clinical trials and subsequently to clinical care.

Keywords:
Image segmentation, carotid atherosclerosis, peripheral artery disease, 3D carotid ultrasound, carotid MRI, contour evolution, convex optimization, level sets.

Co-Authorship

This dissertation includes materials from manuscripts that have been published in, and submitted to peer-reviewed journals. Permissions to reproduce these manuscripts appear in appendix B.

Chapter 2 presents materials from the publication in *Medical Physics*, entitled "Three-dimensional ultrasound of carotid atherosclerosis: Semiautomated segmentation using a level set-based method", by E. Ukwatta, J. Awad, A. D. Ward, D. Buchanan, J. Samarabandu, G. Parraga, and A. Fenster. I developed and implemented the algorithms, performed experiments, analyzed the results, and wrote the manuscript. J. Awad provided ideas on level set energies. A. Fenster and A. D. Ward provided ideas for segmentation evaluation. D. Buchanan performed manual segmentations. All the authors helped in revising the manuscript.

Chapter 3 presents materials from the publication in *Medical Physics*, entitled "Three-dimensional segmentation of three-dimensional ultrasound carotid atherosclerosis using sparse field level sets", by E. Ukwatta, J. Yuan, D. Buchanan, B. Chiu, J. Awad, G. Parraga, and A. Fenster. I designed and implemented the algorithms, experiments, analyzed the results, and wrote the manuscript. All the authors aided in revising the manuscript.

Chapter 4 presents materials from the publication in *IEEE Transactions on Medical Imaging*, entitled "3D carotid mutli-region MRI segmentation by globally optimal evolution of coupled surfaces", by E. Ukwatta, J. Yuan, M. Rajchl, W. Qiu, D. Tessier and A. Fenster. I implemented the algorithm for testing, performed experiments, analyzed the results, and wrote the manuscript. J. Yuan derived the continuous max-flow formulation, developed the optimizer code for multi-region segmentation, and aided in writing the method section of the manuscript. All the authors helped in revising the manuscript.

Chapter 5 presents materials from the publication that has been submitted to *IEEE Transactions on Medical Imaging*, entitled "Joint segmentation of lumen and outer wall from 3D femoral artery MR images: Towards volumetric phenotypes of peripheral arterial disease", by E. Ukwatta, J. Yuan, M. Rajchl, W. Qiu, B. Chiu, and A. Fenster. I implemented the algorithm for testing, performed experiments, analyzed the results, and wrote the manuscript. J. Yuan derived the continuous max-flow formulation, developed the optimizer code for multi-region segmentation, and aided in writing the method section of the manuscript. All the authors helped in revising the manuscript.

Acknowledgements

The completion of this dissertation was possible due to the generous support from numerous individuals whom I feel indebted to. Firstly, I would like to sincerely thank my supervisor, Dr. Aaron Fenster, for his leadership and immeasurable guidance. His mentorship was instrumental throughout my doctoral studies in both my research and personal development. His influence encouraged me to participate in a broader research community and his continual support was evident by the prompt responses and reviews he provided, even on holidays.

I would also like to thank my advisory committee members, Drs. Terry Peters, Grace Parraga, Jagath Samarabandu, and Aaron Ward for their invaluable direction which helped me achieve key milestones. Dr. Terry Peters was involved with steering my research interests and this assisted me in achieving key goals. Dr. Grace Parraga equipped me with key research technicalities and further extended her support by providing invaluable reviews on numerous occasions despite tight deadlines and this is very much appreciated. Dr. Jagath Samarabandu provided me with a strong foundation in academia and was influential in my personal development which I feel indebted to. The numerous intellectual and personal discussions with Dr. Aaron Ward and his invaluable advice on my academic goals will always be appreciated.

I am especially grateful to Dr. Jing Yuan for his support during my doctoral studies. The wealth of intellectual and personal advice he extended is very much appreciated. His convex max-flow solvers were the foundation for segmentation methodologies described in Chapter 4 and 5 in my dissertation. I also very much appreciate the technical support provided by Dr. Joseph Awad to initially get accustomed to level set methods. I would also like to thank the co-authors of my articles, Dr. Wu Qiu, Mr. Martin Rajchl, and Dr. Bernard Chiu for their contributions and productive collaborations, which were interesting highlights in my research and Mr. Dan Buchanan and Tamas Lindenmaier for performing time-consuming expert delineations of 3D ultrasound images for algorithm evaluation. Mr. Igor Gyacskov integrated my nonoptimized Matlab codes to 3DQuantify, which greatly assisted me in performing algorithm segmentations. Dr. David Tessier helped me obtain several imaging scans.

In addition, I would like to thank members of the Fenster lab (i.e., Eli Gibson, Hamid Neshat, Tharindu De Silva, Jeremy Cepek, Chandima Edirisinghe, Lori Gardi, Brandon Miles, Joy Sun, Maysam Shahedi, Manale Saikaly, *et al.*) for the many interesting discussions we have shared on research and unrelated topics.

I acknowledge the funding support received from numerous sources including Natural Science and Engineering Research Council of Canada Graduate Scholarship (NSERC CGS), Ontario Graduate Scholarship (OGS), and Ontario Graduate Scholarships in Science and Technology (OGSST), which were all crucial for me to gain productivity and focus on research.

I appreciate the continuous encouragement offered by my parents and extended family during these years. I would also like to thank my wife, Oshani, for her incredible encouragement and support in focusing on the research front.

Table of Contents

Abstract ii

Co-Authorship iv

Acknowledgements vi

List of tables xiv

List of figures xvi

List of Abbreviations xxii

1 Introduction 1
- 1.1 Atherosclerosis 1
- 1.2 Carotid atherosclerosis 2
  - 1.2.1 Ischemic stroke 4
- 1.3 Monitoring of carotid arthrosclerosis 4
- 1.4 Imaging of carotid atherosclerosis 5
  - 1.4.1 Computed tomography angiography (CTA) 5
  - 1.4.2 2D B-mode ultrasound 6
  - 1.4.3 Intra-vascular ultrasound (IVUS) 6
  - 1.4.4 Doppler ultrasound 7
  - 1.4.5 3D ultrasound (3DUS) 7
    - 1.4.5.1 3DUS image acquisition 8
  - 1.4.6 Magnetic resonance imaging (MRI) 9
- 1.5 Imaging phenotypes 12
  - 1.5.1 Carotid artery stenosis (CAS) 12
  - 1.5.2 Intima-media thickness (IMT) 13
  - 1.5.3 Total plaque area (TPA) 14
  - 1.5.4 Total plaque volume (TPV) 14
  - 1.5.5 3DUS and MRI vessel wall volume (VWV) 16
  - 1.5.6 Vessel wall thickness/change (VWT) maps and flattened VWT maps 17
- 1.6 Peripheral arterial disease (PAD) 17
- 1.7 Imaging phenotypes for PAD 18
  - 1.7.1 Ankle-brachial index (ABI) 18
  - 1.7.2 Stenosis 19

1.7.3 Vessel wall area and vessel wall volume measurements 19
1.8 Motivation and objectives 20
1.8.1 Motivation for developing segmentation algorithms 20
1.8.2 Carotid artery lumen and outer wall segmentation from 3DUS images 22
1.8.3 Carotid artery lumen and outer wall segmentation from MR images 23
1.8.4 Femoral artery lumen and outer wall segmentation 23
1.9 Image segmentation 24
1.9.1 Segmentation algorithms 24
1.9.1.1 Heuristic methods 25
1.9.1.2 Clustering methods 25
1.9.1.3 Functional optimization methods 25
1.9.2 Level set methods 28
1.9.2.1 Sparse field level set (SFLS) method 29
1.9.3 Convex optimization using continuous max-flow methods . . . 29
1.9.4 Level sets and convex max-flow: a brief comparison 32
1.10 Segmentation evaluation 32
1.10.1 Accuracy 34
1.10.2 Precision 36
1.11 Overview of dissertation 36
References 40

2 3DUS of carotid atherosclerosis: Semi-automated segmentation using a level set-based method 53
2.1 Introduction 53
2.1.1 Previous work 53
2.1.2 Contributions 55
2.2 Materials and methods 56
2.2.1 Study subjects and imaging 56
2.2.2 Overview and summary of approach 57
2.2.3 User interaction 57
2.2.4 Preprocessing 58
2.2.5 Segmentation using level sets 59
2.2.6 MAB segmentation 60
2.2.7 LIB segmentation 63
2.2.8 Parameters of the segmentation 65
2.3 Validation 66
2.3.1 Experiment design 66
2.3.2 Evaluation metrics 67
2.3.3 Mean boundary computation 69
2.4 Results 70

2.4.1 Accuracy 72
2.4.2 Intra-observer variability 73
2.4.3 Number of initialized points 73
2.4.4 Execution time 76
2.5 Discussion 76
2.5.1 Discussion 76
References 81

3 3D segmentation of 3DUS carotid atherosclerosis using sparse field level sets 86
3.1 Introduction 86
3.1.1 Previous studies 86
3.1.2 Contributions 89
3.2 Materials and methods 89
3.2.1 Algorithm initialization 89
3.2.2 3D image preprocessing 92
3.2.3 Sparse field level set (SFLS) method 93
3.2.4 MAB segmentation 93
3.2.5 LIB segmentation 96
3.3 Validation 98
3.3.1 Evaluation metrics 99
3.4 Results 100
3.4.1 Computational time and user interaction 100
3.4.2 Accuracy 101
3.4.3 Reproducibility 110
3.5 Discussion 110
3.5.1 Methodology 110
3.5.2 Computational time 111
3.5.3 Accuracy 112
3.5.4 Reproducibility 114
3.5.5 Comparison to previous methods 115
3.5.6 Selection of proper ISD 116
References 117

4 3D carotid multi-Region MRI segmentation by globally optimal evolution of coupled surfaces . . . 122
- 4.1 Introduction . . . 122
  - 4.1.1 Previous studies . . . 122
  - 4.1.2 Contributions . . . 124
- 4.2 Method . . . 125
  - 4.2.1 Optimization model with geometrical constraint . . . 127
  - 4.2.2 Global optimization-based coupled contour evolution . . . 129
    - 4.2.2.1 Single contour evolution by convex optimization . . . 130
    - 4.2.2.2 Global optimization-based evolution of coupled contours 132
  - 4.2.3 Convex relaxation and continuous max-flow approach . . . 134
    - 4.2.3.1 Continuous max-flow model . . . 134
    - 4.2.3.2 Continuous max-flow based algorithm . . . 135
- 4.3 Experiment design and implementations . . . 137
  - 4.3.1 Study subjects and image acquisition . . . 137
  - 4.3.2 Segmentation pipeline . . . 137
    - 4.3.2.1 Interpolation . . . 137
    - 4.3.2.2 User interaction . . . 138
    - 4.3.2.3 2D AB-LIB segmentation and generation of intensity PDF models . . . 139
    - 4.3.2.4 Generation of initial surfaces for 3D segmentation . . . 142
    - 4.3.2.5 3D AB-LIB segmentation . . . 142
  - 4.3.3 Validation . . . 144
- 4.4 Experiment results . . . 145
  - 4.4.1 Computational time . . . 145
  - 4.4.2 Accuracy . . . 147
  - 4.4.3 Vessel wall volume (VWV) computation . . . 151
  - 4.4.4 Precision . . . 152
- 4.5 Discussion . . . 153
  - 4.5.1 Computational time . . . 155
  - 4.5.2 Accuracy . . . 155
  - 4.5.3 Precision . . . 157
  - 4.5.4 Other potential applications . . . 157
  - 4.5.5 Comparison to previous studies . . . 158
- References . . . 159

5 Joint segmentation of 3D femoral artery lumen and outer wall from 3D black-blood MR images 165
5.1 Introduction 165
  5.1.1 Previous studies 166
  5.1.2 Contributions 168
5.2 Methods 169
  5.2.1 Muti-region segmentation formulation 169
  5.2.2 Spatial consistency prior between adjacent slices 171
  5.2.3 Optimization formulation 172
  5.2.4 Convex relaxation and coupled continuous max-flow model . . 172
  5.2.5 Coupled continuous max-flow (CCMF) model 173
  5.2.6 Global and exact optimization of (5.7) 175
  5.2.7 Coupled continuous max-flow (CCMF) algorithm 175
5.3 Implementation and data 176
  5.3.1 User initialization 177
  5.3.2 Medial axis computation 177
  5.3.3 3D CCMF segmentation 177
  5.3.4 Data and acquisition 178
  5.3.5 Validation 179
5.4 Results 180
  5.4.1 Computational time 182
  5.4.2 Accuracy 182
  5.4.3 Precision 185
5.5 Discussion 186
  5.5.1 Accuracy 186
  5.5.2 Precision 187
  5.5.3 Comparison to previous methods 188
References 188

6 Summary and future directions 192
6.1 Summary 192
6.2 2D slice-wise segmentation of carotid 3DUS images (Chapter 2) . . . 193
6.3 3D segmentation of carotid 3DUS images (Chapter 3) 193
6.4 3D segmentation of carotid MR images (Chapter 4) 194
6.5 3D segmentation of femoral MR images (Chapter 5) 195
6.6 Limitations 195
6.7 Future directions 197
6.7.1 Towards automated segmentation 197
6.7.2 Adaptive parameters and parameter optimization 198
6.7.3 3DUS carotid ICA segmentation 198
6.7.4 Plaque composition and inflammation 199
6.7.5 Morphological analysis 200
6.7.6 Multi-region segmentation of the carotid lumen, outer wall, and plaque 200
References 201

A Continuous max-flow based algorithm 205
References 206

B Copyright reprint permissions 207

Curriculum Vitae 212

List of Tables

1.1 Comparison of level sets and convex max-flow methods 33

2.1 Parameters and their optimized values for the preprocessing. 59
2.2 Parameters and their optimized values for MAB and LIB segmentations. 66
2.3 Overall performance results of the algorithm for 231 2D slices extracted from the 21 3DUS images. 72

3.1 Previous papers describing carotid LIB and/or MAB segmentations from 3DUS/B-mode images. 87
3.2 Parameters and their optimized values for the preprocessing 98
3.3 Parameters and their optimized values for MAB and LIB segmentations. 98
3.4 Results for the MAB and LIB segmentation using region-based and distance-based metrics for the 21 3DUS images using the average boundaries. The results of the 3D algorithm are given for ISD of 1, 2, 3, 4, and 10 mm. 108
3.5 Results for the VWV, MAB, and LIB using volume-based metrics for the 21 3DUS images. The results of the 3D algorithm are given for ISD of 1, 2, 3, 4, and 10 mm. 108
3.6 Comparison of algorithm- and manually-generated VWV for 21 3DUS images using statistical testing and Pearson r. The results of the 3D algorithm are given for ISD of 1, 2, 3, 4, and 10 mm. 109
3.7 Standard deviation (SD), coefficient-of-variation (CV), and minimum detectable difference (MDD) of volume measurements for 21 3DUS images computed using the repeated measurements of algorithm and manual segmentations. The results of the 3D algorithm are given for ISD of 1, 2, 3, 4, and 10 mm. 109

4.1 Previous studies describing carotid LIB and/or AB segmentation methods for black-blood MR imaging. 123
4.2 Magnetic Resonance Imaging Parameters for T1-weighted Double Inversion Recovery scans at 1.5T and 3.0T. 138
4.3 Algorithm parameters values for the experiments. 143
4.4 Confidence intervals (CI) and Pearson correlation coefficients for computing VWV. 148
4.5 Accuracy results for 12 T1-weighted 3T MR images using the proposed algorithm. 151

4.6 Accuracy results for 26 T1-weighted 1.5T MR images using the proposed algorithm. 151
4.7 Results of inter- and intra-observer variability of the algorithm for 8 T1-weighted 3T MR images using the proposed algorithm. 152
4.8 Results of inter- and intra-observer variability of the algorithm for 8 T1w 1.5T MR images using the proposed algorithm. 152

5.1 Performance results of the proposed algorithm for 355 2D slices extracted from the 10 femoral 3D MR images. The voxel size of the MR images is $\approx 1.0 \times 1.0 \times 1.0$ mm^3. 183
5.2 Intra-observer variability of the algorithm using five repetitions of the same observer for 176 2D slices extracted from six femoral 3D MR images, which were chosen randomly from the entire data set. 183
5.3 Comparison of the algorithm to Chiu *et al.* [14] using 176 2D slices extracted from six femoral 3D MR images used in their study. 185

List of Figures

1.1 (a) The anatomy of the carotid artery. The image is courtesy from 20^{th} U. S. edition of Gray's Anatomy page #549 (Also available at `https://en.wikipedia.org/wiki/Common_carotid_artery`); (b) schematic sagittal cross-section of a carotid artery showing the bifurcation point (BF), common carotid artery (CCA), internal carotid artery (ICA), and external carotid artery (ECA); and (c) transverse cross-section of a carotid artery showing the adventitia (A), media (M), intima (I), and lumen (L), as well as the IMT measurement. 3

1.2 (a) Mechanically assisted 3DUS transducer probe; and (b) acquiring a 3DUS image by translating the transducer along the patient's neck at least up to a distance of 4 cm encompassing portions of the CCA, ICA, and ECA. 8

1.3 Multi-planer views of the 3DUS images. (a) Transverse view of a 3DUS image of carotid artery for a subject with moderate stenosis; (b) longitudinal view of a 3DUS image of carotid artery for the subject with moderate stenosis; (c) transverse view of a 3DUS image of carotid artery for a subject with ulceration; and (d) longitudinal view of a 3DUS image of carotid artery for the subject with ulceration. 10

1.4 Transverse view of the left and right CCA of an T1w black-blood MR image of a patient with mild stenosis. 11

1.5 (a) Manual delineation of the IMT measurement of the CCA from a longitudinal 2D US image; and (b) manual delineation of the plaque boundary for TPA measurement from a longitudinal 2D US image. . 13

1.6 (a) Manual segmentation of the plaque boundaries of the 3D US image used for TPV measurement; and (b) reconstructed plaque surfaces from the manual segmentations. 15

1.7 (a) An example 3DUS image of a patient's carotid artery; (b) and (c) manual segmentation of the CCA, ICA, and ECA lumen and outer wall boundaries from 3DUS images; and (d) reconstructed surfaces for the lumen and outer wall boundaries from the manual segmentations. The outer wall surface of the CCA, ICA, and ECA is rendered in yellow. The lumen surfaces of the CCA, ICA, and ECA are rendered in red, blue, and green, respectively. 15

1.8 (a) Vessel-wall-plus-plaque thickness (VWT) map for a patient with moderate stenosis. Manual segmentations of the lumen and outer wall boundaries were used to generate the VWT maps. The thickness is indicated in millimeters; and (b) corresponding flattened VWT map for better visualization. 18
1.9 The anatomy of the femoral artery. The image is courtesy from 20^{th} U. S. edition of Gray's Anatomy page #550 (Also available at `https://en.wikipedia.org/wiki/Femoral_artery`). 19
1.10 (a) Transverse and sagittal views of a 3DUS image; (b) same image with overlaid manual segmentation of lumen-intima boundary (LIB) and media-adventitia boundary (MAB); and (c) image intensity histogram of the lumen, outer wall and background. 21
1.11 (a) A 3D view of a T1-weighted 3T carotid MR image showing the transverse and sagittal cross sections of the CCA, ICA, and ECA. The CCA divides into the ICA and ECA at the bifurcation (BF); (b) the same 3D carotid MR image with the overlaid manual segmentations of the adventitia (AB) and lumen-intima (LIB) of the CCA, ICA, and ECA. The manual segmentations are performed on each transverse slice; and (c) image intensity histogram of the lumen, outer wall, and background. 22
1.12 (a) An example 3D femoral MR image with manual delineations; and (b) a transverse slice of a 3D femoral MR image with manual delineations of the femoral lumen and outer wall. 23
1.13 The current contour $\mathcal{C}^t$ evolves to the contour $\mathcal{C}^{t+1}$ at next time frame $t+1$. A voxel pays cost e^- for a pixel transitioning from object region to the background region and a voxel pays cost e^+ for a pixel transitioning from background region to the object region during the current iteration. Costs e^+ and e^- are region-based costs that are usually computed by matching the current segmentation with a prior model that is characteristic of the object region. 30

2.1 (a) Sagittal cross-section of the common carotid artery (CCA) in a 3DUS image. The contours overlaid on the image represent the manual delineations done by an expert with an ISD of 1 mm; and (b) transverse view of a 3DUS image of the CCA showing expert-drawn contours delineating the MAB and LIB. 54
2.2 Block diagram of the workflow of the algorithm. Our contributions are shown in bold italic letters. 56

2.3 (a) Algorithm-generated boundaries for the MAB, (b) manually outlined boundaries for the MAB, (c) algorithm-generated boundaries for the LIB, and (d) manually outlined boundaries for the LIB. Legend: dotted contours - five segmented boundaries, dashed contour - corresponding mean boundary. 69
2.4 Sample results of the MAB and LIB segmentations for three patients using four anchor points chosen from the initial eight anchor points. (Dashed outer contour - manual MAB, dashed inner contour - manual LIB, dotted outer contour - algorithm-generated MAB, dotted inner contour - algorithm-generated LIB) 1, 5, 7, and 10 mm indicate the distance to the BF from each slice. 71
2.5 Bland-Altman plot of the VWVs generated using four anchor points chosen from the initial eight anchor points. The plot graphs the difference between the algorithm-generated and manual VWVs as a function of their mean. 74
2.6 Correlation plot of VWV measurements for the algorithm and manual method. The VWVs were generated using four anchor points chosen from the initial eight anchor points for the algorithm. 74
2.7 (a) Graph of DSC against distance to BF; (b) graph of MAD against distance to BF; and (c) graph of MAXD against distance to BF for the 231 images. The error bars represent one standard deviation. 75
2.8 (a) Graph of $\delta V_{VWV}, \delta V_{MAB}$ and δV_{LIB} with varying number of initialized points; (b) graph of $|\delta V_{VWV}|, |\delta V_{MAB}|$ and $|\delta V_{LIB}|$ with varying number of initialized points; (c) graph of DSC for MAB and LIB with varying number of initialized points; and (d) graph of CV in computing VWV, MAB volume, and LIB volume with increasing number of initialized points. 77

3.1 Two example transverse views of the CCA with overlaid manual segmentations of the MAB and LIB from 3DUS images of two subjects with carotid stenosis of more than 60%. Note that although the MAB has a relatively low order convex shape, the LIB may have a nonconvex shape. 87
3.2 Block diagram of the workflow of the 3D algorithm. 90
3.3 The process of creating a 3D mask from anchor points as the initial surface for the algorithm with an ISD of 2 mm. 91
3.4 3D image preprocessing steps of the algorithm. The results here are shown for a single slice of the 3DUS image. 92

3.5 2D slice-by-slice comparisons of algorithm segmentations to manual segmentations for a subject with a mild stenosis. Results for ISD from 1–4, and 10 mm are shown. The contours are as follows: Continuous yellow contour mean manual MAB and LIB, dashed purple contour mean algorithm MAB and LIB, and cyan dashed contour one round of algorithm MAB and LIB. Each row corresponds to the distance from the BF and each column corresponds to the ISD used for initialization. 102

3.6 2D slice-by-slice comparisons of algorithm segmentations to manual segmentations for a subject with a moderate stenosis (stenosis is between 30% and 70%). Results for ISD from 1–4 mm, and 10 mm are shown. The accuracy dropped at 4 and 10 mm. The contours are as follows: Continuous yellow contour mean manual MAB and LIB, dashed purple contour mean algorithm MAB and LIB, and cyan dashed contour one round of algorithm MAB and LIB. Each row corresponds to the distance from the BF and each column corresponds to the ISD used for initialization. 103

3.7 Comparison of the MAB and LIB algorithm segmentations to manual segmentations for an ISD of 3 mm for two example 3DUS images that were used for Fig. 6 and 7. The algorithm-generated surfaces are shown in purple and the manually-generated surfaces are shown in yellow. (a) LIB surface comparison with manual segmentation for a subject with a mild stenosis; (b) MAB surface comparison with manual segmentation of the same subject; (c) LIB surface comparison with manual segmentation for a subject with a moderate stenosis; and (d) MAB surface comparison with manual segmentation of the same subject. 105

3.8 Algorithm and manually-generated flattened VWT maps of the surfaces shown in Fig. 8 for the same two example 3DUS images. The first row corresponds to algorithm-generated flattened VWT maps, whereas second row corresponds to manually-generated flattened VWT maps. (a) Subject with a mild stenosis; and (b) Subject with a moderate stenosis. 106

3.9 Bland-Altman plot for comparing algorithm- and manually-generated 3DUS VWV, where ISD of 3 mm is used for the algorithm initialization. The red continuous line indicates the bias, the blue dotted lines indicate the level of agreement, and the red dashed lines indicate the 95% CI. 107

3.10 Correlation plot for algorithm- and manually-generated 3DUS VWV, where ISD of 3 mm is used for the algorithm initialization. The dashed lines indicate the 95% CI of the best fit line. 107

4.1 A 3D view of a T1-weighted 3T carotid MR image showing the transverse and sagittal cross sections of the CCA with overlaid manual segmentations. The manual segmentations are performed on each transverse slice. 126
4.2 (a) Pictorial representation of image domain Ω and its sub-domains: Lumen region (R_l), wall region (R_w), and background (R_b); (b) region differences by the evolution of the two surfaces $\mathcal{C}_{AB}$ and $\mathcal{C}_{LIB}$; and (c) the spatially continuous flow configurations used in the continuous max-flow formulation. 127
4.3 Block diagram of our segmentation pipeline. The proposed continuous max-flow algorithm with ordered geometric constraints is used in two occasions: It is used initially for a 2D segmentation on a single transverse slice to for the purpose of generating intensity PDFs of the three regions to aid in the 3D segmentation. It is then used to segment the carotid arteries in 3D. The only user interaction required is to mark seed points on the lumen, wall, and background regions prior to 2D coupled evolution. 136
4.4 Example user initializations and the 2D AB-LIB segmentations using the proposed continuous max-flow algorithm. The only user interaction in the pipeline is choosing the sampled voxels on a single transverse slice. The voxels marked by green, red, and blue correspond to the lumen, wall and background regions respectively. (a) and (b): Initializations for two 3T MR images, (c) and (d): Initializations for two 1.5T MR images. (e) and (f): 2D Segmentations for two 3T MR images, (g) and (h): 2D segmentations for two 1.5T MR images. 139
4.5 Normalized intensity probability density functions (PDF) used in 3D AB-LIB segmentation for Bhattacharyya distance matching for a single 3D image. Gaussian kernel width of seven is used to generated the PDFs. 140
4.6 Example segmentations of a T1-weighted 3T image: (a) Initial surface for LIB obtained using region growing, (b) algorithm generated AB and LIB surfaces. Example segmentations of a T1-weighted 1.5T image: (c) Initial surface for LIB obtaining using region growing, (d) algorithm generated AB and LIB segmented surfaces. 146
4.7 Visual surface comparisons of some example algorithm-generated AB and LIB surfaces to manually generated surfaces. The manually segmented surface is shown in blue color whereas the algorithm generated surface is shown in purple color. (a) AB surface segmented from a T1-weighted 3T MR image, (b) LIB surface segmented from the same T1-weighted 3T MR image, (c) AB surface segmented from a T1-weighted 1.5T MR image, and (d) LIB surface segmented from the same T1-weighted 1.5T MR image. 147

4.8 2D slice-by-slice comparisons of algorithm-generated surface to manual segmentations for two example images. The algorithm generated surface is sliced on the same planes as the 2D manual segmentations. Algorithm segmentations are shown as a green continuous line whereas the manual segmentations are shown in red dashed lines. 149
4.9 Bland-Altman plots [49] of the vessel wall volume (VWV) measurements. Confidence interval (CI) of mean of differences between the VWVs are also indicated by the green dotted line. **1st Column:** Graph for 12 3T images, **2nd Column:** Graph for 26 1.5T images. . 150
4.10 The evaluation of intra- and inter-observer variability of DSC of the proposed method. The error bars indicate the standard deviation. . . 154

5.1 (a) An example femoral MR image of a patient; (b) same image with overlaid manual annotations of the femoral artery lumen and outer wall; (c) reorientation of the femoral MR image using the medial axis of the artery. The reorientation procedure is described in Section 5.3.2; and (d) Long axis view of reoriented 3D MR image. 167
5.2 (a) A transverse slice of a 3D femoral MR image with manual delineations; and (b) schematic diagram denoting the notation used for lumen and outer wall contours C_i^L, C_i^W and lumen, outer wall, and backgound regions $\mathcal{R}_i^L, \mathcal{R}_i^W, \mathcal{R}_i^B$. 168
5.3 Flow configurations of the proposed *coupled continuous max-flow model.* 172
5.4 The block diagram of the segmentation pipeline. User interaction is performed only in the first step. 176
5.5 The impact of the proposed spatial consistency prior is illustrated here: **Column 1:** Algorithm results without the spatial consistency prior. **Column 2:** Algorithm results with the spatial consistency prior. The algorithm generated-contours are shown as cyan continuous lines whereas the manual contours are shown as dashed yellow lines. . . . 180
5.6 Surfaces. (a) Manual segmented boundaries of the lumen; (b) manual segmented boundaries of the wall; (c) algorithm-generated lumen surface; (d) algorithm-generated wall surface; (e) reoriented algorithm-generated lumen surface; and (f) reoriented algorithm-generated wall surface. 181
5.7 Slice-wise comparison of the computation results (cyan) to the manual segmentation (yellow) for the femoral wall and lumen boundaries for three 3D MR images. Each column corresponds to images for a different patient. The slices are separated by 30 mm from each other. 184

List of Abbreviations

2D	Two-Dimensional
3D	Three-Dimensional
AB	Adventitia Boundary
ABI	Ankle-brachial Index
AD	Area Difference
AHA	American Heart Association
AO	Area Overlap
BF	Bifurcation
CAS	Carotid Artery Stenosis
CCA	Common Carotid Artery
CCMF	Coupled continuous max-flow
CFL	Courant-Friedrichs-Lewy condition
CNR	Contrast-to-Noise Ratio
CT	Computed Tomography
CV	Coefficient of Variation
DSC	Dice Similarity Coefficient
ECA	External Carotid Artery
GPU	Graphics Processing Unit
ICA	Internal Carotid Artery
ICC	Intra-class Correlation Coefficient
IMT	Intima-Media Thickness
ISD	Inter-slice Distance
IVUS	Intravascular Ultrasound
LIB	Lumen-intima Boundary
MAB	Media-Adventitia Boundary
MAD	Mean Absolute Distance
MDD	Minimum Detectable Difference
MAXD	Maximum Absolute Distance

MR	Magnetic Resonance
MRA	Magnetic Resonance Angiography
PAD	Peripheral Arterial Disease
PDE	Partial Differential Equations
PDF	Probability Density Function
RF	Radio Frequency
RMSE	Root Mean Square Error
ROI	Region of Interest
SD	Standard Deviation
SEM	Standard Error of Measurement
SFA	Superficial Femoral Artery
SFLS	Sparse Field Level Set
SNR	Signal-to-Noise Ratio
T1w	T1-weighted
TIA	Transient Ischemic Attack
TPA	Total Plaque Area
TPV	Total Plaque Volume
US	Ultrasound
VWA	Vessel Wall Area
VWV	Vessel Wall Volume
VWT	Vessel-wall-plus-plaque thickness maps

Chapter 1
Introduction

1.1 Atherosclerosis

Atherosclerosis is an inflammatory disease, in which the inner layer of the arteries progressively accumulates low density lipoproteins and macrophages over a period of several decades forming plaque [1]. Disease progression commences at adolescence with the dysfunction of the endothelial layer of the artery and continues to build up plaque, which may be accelerated by risk factors including hypercholesterolemia, smoking, hypertension, diabetes mellitus, physical inactivity, rheumatoid arthritis, overweight, and obesity to name a few [2, 3]. Atherosclerosis is the disease of interest for this dissertation, and substantial portion of it is devoted to describing algorithms for generating vascular atherosclerotic measurements.

The American heart association (AHA) has classified the atherosclerotic process into six main stages [4, 5], which can be broadly divided into three main categories: fatty streak, intermediate lesions, and advanced lesions. The initial stage known as the fatty streak stage could occur in childhood, and is a pure inflammatory lesion [6]. It appears as a yellow streak running along the major arteries, which consists of smooth muscle cells filled with cholesterol and macrophages. Over time, the fatty streak may progress into an intermediate lesion (also known as preatheroma), which consists of microscopically visible extracellular lipid droplets [4]. The plaque forms in the inner layer of the artery and, as it continues to grow, may narrow the lumen of the artery or may change arterial cross-sectional area, which is also known as ‘arterial remodeling’ [7]. As intermediate lesions progress to advanced lesions, they tend to form a fibrous cap that covers the lesion from the lumen. The fibrous cap covers a mixture of leukocytes, lipid, and debris, which might form a necrotic core [6].

Despite efforts to lower cholesterol levels and lifestyle changes to include more exercises, cardiovascular disease continues to be the principle cause of death in the world [6, 8]. Atherosclerotic lesions occur mostly in large- and medium-sized muscular arteries and can lead to ischemia of the brain, heart or extremities, resulting in infarction [6]. The coronary, carotid, renal, and femoral arteries are major sites for developing atherosclerosis in patients. As a result, different disease conditions may develop based on which arteries are affected. For example, atherosclerosis in the coronary arteries causes ischemic heart attack, the leading cause of death in the world [2, 9]. Atherosclerosis occurring in the carotid arteries (see Fig. 1.1) may lead to ischemic stroke whereas atherosclerosis occurring in the superficial femoral arteries (see Fig. 1.6) may lead to critical limb ischemia. Imaging of coronary arteries is challenging due to the heart and respiratory motion, and their interior location within the body compared to carotid and superficial femoral arteries. The main focus of this dissertation is on imaging and quantification of atherosclerosis in the carotid and femoral arteries using noninvasive techniques. Carotid atherosclerosis and its imaging techniques are described in Section 1.2 and peripheral arterial disease of femoral arteries and its imaging are described in Section 1.6.

1.2 Carotid atherosclerosis

Carotid arteries are paired structures located in both the left and right sides of the neck. The left common carotid artery (CCA) originates at the aortic arch, whereas the right CCA originates at brachiocephalic artery. The CCA bifurcates into the internal carotid artery (ICA) and external carotid artery (ECA) as shown in Fig. 1.1(a). Schematic sagittal cross-section of a carotid artery showing the bifurcation point (BF) and the CCA, ICA, and ECA are shown in Fig. 1.1(b). The ICA supplies oxygenated blood to the brain and the ECA supplies oxygenated blood to the face, scalp, and skull. Figure 1.1(c) shows the layers of an artery: the intima, media, and adventitia. The intima layer is the inner layer of the artery, which comprises of elastic membrane lining and a smooth endothelium. The middle layer is the media, which is comprised of smooth muscle cells and elastic fibers. The outermost layer is the adventitia, which contains connective tissue, collagen, and elastic fibers.

In particular, plaque formation at the carotid bifurcation is a major cause for the generation of thrombosis and subsequent cerebral emboli [10]. An unstable plaque may suddenly rupture forming a thrombus causing an embolism, which may ultimately lead to an ischemic stroke by blocking the oxygenated blood supply to parts

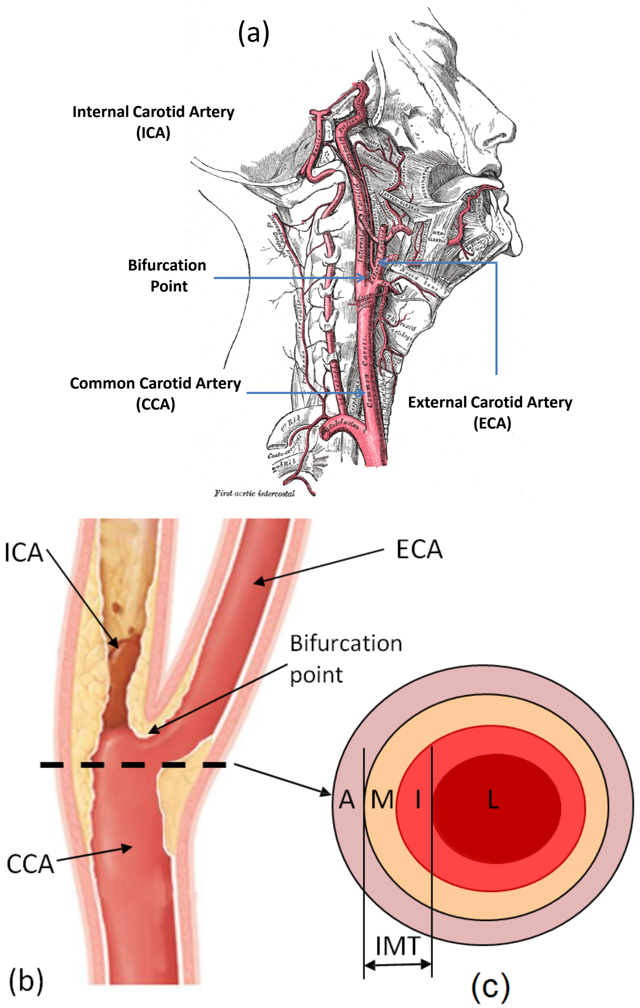
(a)
Internal Carotid Artery
(ICA)
Bifurcation
Point
Common Carotid Artery
(CCA)
External Carotid Artery
(ECA)
First aortic intercostal
ICA
ECA
Bifurcation
point
CCA
(b)
A
M
I
L
IMT
(c)

Figure 1.1: (a) The anatomy of the carotid artery. The image is courtesy from 20^{th} U. S. edition of Gray's Anatomy page #549 (Also available at `https://en.wikipedia.org/wiki/Common_carotid_artery`); (b) schematic sagittal cross-section of a carotid artery showing the bifurcation point (BF), common carotid artery (CCA), internal carotid artery (ICA), and external carotid artery (ECA); and (c) transverse cross-section of a carotid artery showing the adventitia (A), media (M), intima (I), and lumen (L), as well as the IMT measurement.

المنـــارة للاستشارات

of the brain [10, 11]. Plaque formation in the arteries often has no symptoms and is unknown to the patient and doctor until it disrupts blood flow to the brain [11].

1.2.1 Ischemic stroke

Stroke remains the third leading cause of mortality and morbidity worldwide in the developed world, and is expected to take a growing toll in the developing world [2, 9]. It is the most common, serious neurological problem globally and the third leading cause of death among North American adults [8]. Approximately 87% of all stroke cases are ischemic, mostly due to a blockage of a cerebral artery by a thrombotic embolus [12]. Therefore, improved methods to identify patients at increased risk for stroke, and better techniques to treat and monitor them will have an enormous impact in the management of patients who are at risk of stroke.

1.3 Monitoring of carotid arthrosclerosis

Framingham risk factors such as age, sex, obesity, smoking, diabetes, lipid levels, and hypertension are still used to stratify stroke risk and monitor treatment effect [13]. In addition to Framingham risk factors, biochemical biomarkers of lipid metabolism and inflammation [14] have been investigated and shown to be stronger predictor of cardiovascular events. However, these risk factors are indirect measurements of the disease and do not consider current status of the plaque burden in the arteries. Thus, they are limited in assessing the actual risk of stroke.

Treatment of severe carotid artery stenosis includes carotid endarterectomy, carotid angioplasty, and stenting [15]. However, not all the plaques are high risk to the patient, thus it is important to evaluate vulnerability of the plaque to rupture to determine patient's eligibility for invasive procedures [16, 17].

Some treatment strategies of carotid atherosclerosis focuses on the prevention of progression [11]. Patients who are at risk of stroke due to atherosclerosis may either undergo changes in their diet and overall lifestyle habits, or be treated with medical interventions for atherosclerosis to prevent stroke [18]. Therefore, monitoring the carotid plaque progression and regression in patients over a period of time is very important for proper risk management of the patients [19, 20]. There have been new therapies developed to regress plaque and inflammation, but they lack intermediate end points to use as efficacious targets. To study such treatments, it is necessary to directly measure changes in plaque burden, morphology and/or composition.

Medical imaging is widely used for diagnosis of carotid atherosclerosis and can be used to assess severity of the disease [21]. Unlike the blood-based biomarkers, the imaging biomarkers provide direct measurements of plaque burden. Even though diagnosis of the disease is possible with Doppler ultrasound (see Section 1.4.4), the challenge and impact lie in quantitative monitoring of the carotid plaque progression and regression in patients for evaluating efficacy of treatments and for assessing vulnerability of the plaque to rupture. In this chapter, we describe carotid imaging techniques in Section 1.4 and the corresponding carotid phenotypes in Section 1.5.

1.4 Imaging of carotid atherosclerosis

Noninvasive and sensitive imaging systems capable of detecting and monitoring carotid atherosclerosis in populations may be the next leap in patient management. Recently, there has been an increased interest in area and volumetric measurements of carotid plaque burden [22, 23]. The hypothesis is that the area and volumetric measurements are more reflective of the plaque burden, thus they are more sensitive and may provide complementary information to one/two dimensional measurements. As such, new sensitive and specific measurements may provide critically needed and more specific risk management tools and more sensitive ways to assess new patient treatments. One main advantage is shorter clinical trials with imaging end-points as opposed to long clinical trials with hard endpoints. Here we briefly describe some of the imaging modalities that have been recently investigated for carotid imaging.

1.4.1 Computed tomography angiography (CTA)

The advent of high-speed multi-detector computed tomography angiography (CTA) allows for direct evaluation and measurement of lumen diameter and stenosis in 3D [24]. CTA is an accurate modality for the detection of severe carotid artery disease, especially for detection of occlusions [25]. Although, CTA provides information about lumen stenosis, aneurysms, and calcifications, it does not provide high image contrast of the outer wall boundary and vessel wall composition except calcifications [26, 27]. Moreover, CTA exposes patients to radiation as well as requires injection of iodinated contrast agents. Therefore, CTA is not practical for longitudinal monitoring of asymptomatic patients.

1.4.2 2D B-mode ultrasound

2D B-mode ultrasound (US) is widely used in clinical studies for imaging of carotid atherosclerosis due to its noninvasiveness, cost-effectiveness, and short acquisition times [28]. Since the carotid arteries are superficial structures, it is relatively easy to acquire high quality B-mode ultrasound images of the carotid arteries for the purpose of quantitative analysis. Carotid B-mode US of the long axis view of the artery allows evaluation of lumen diameter, intima-media thickness (IMT), and presence and extent of plaques [29]. The IMT measurement, a one dimensional measurement of the arterial thickness, has been widely used as an surrogate end point for cardiovascular disease [29, 30, 31].

Since plaque growth occurs in 3D, measurements based on 2D are not very sensitive to changes in plaque burden. The 2D US image represents a thin plane at some arbitrary angle in the body. Therefore, it is difficult to localize the image plane and reproduce it at a later time for follow-up studies [32]. In addition, with extensive plaque burden, particularly if calcified, acoustic shadowing may hamper insonation of the area distal to the calcification.

1.4.3 Intra-vascular ultrasound (IVUS)

Intravascular ultrasound (IVUS) uses a miniaturized US probe attached to a catheter and the images are acquired while the catheter is guided through the vessel [33]. Unlike angiographic techniques, IVUS provides high-resolution images of the vessel wall and is widely used during coronary artery interventions [34]. Moreover, virtual histology IVUS [15] is a new development of the IVUS technology allowing analysis of both the intensity and frequency of the reflected US signals. This capability has been used to identify individual plaque components in the carotid arteries. Although, IVUS is used during interventional procedures including carotid artery stenting [35] for patients with severe CAS, IVUS is too expensive and invasive to be used for longitudinal monitoring of plaque burden.

1.4.4 Doppler ultrasound

Doppler US measures the direction and speed of blood cells flowing through the arteries and shows blood flow as a colour-coded dynamic image. It is noninvasive and cost-effective, and has been widely used as a diagnostic and screening tool of carotid stenosis [11, 36, 37]. A measurement of the velocity of flow in the longitudinal view of the artery is usually performed and is used as an indirect estimate of the degree of luminal narrowing [38]. In particular, colour Doppler images are primarily used in diagnosis and grading of ICA stenosis [39].

For Doppler US, angle of insonation should remain unchanged for obtaining velocity measurements, since subtle changes in angle may affect absolute velocity measurements [38]. Although, Doppler US is a very useful in its utility to detect CAS, it does not provide good contrast of the vessel wall for further analysis of the plaque burden.

1.4.5 3D ultrasound (3DUS)

3D ultrasound (3DUS) has shown promise in quantifying carotid atherosclerosis for monitoring carotid disease progression and regression in clinical trials. As such, 3DUS has been increasingly investigated over the last decade due to its ability to obtain volumetric and morphological measurements rapidly, non-invasively, and cost-effectively [23, 37, 40, 41, 42]. Thus, 3DUS imaging capability is now widely available in commercial systems and in ones developed in research laboratories. Advances in computing capabilities and visualization technology have made 3DUS imaging a viable technology for carotid imaging applications [32]. 3DUS imaging overcomes several limitations of the conventional US techniques. For instance, 3DUS imaging avoids the inherent variability of the conventional 2D US exam due to need to mentally integrate multiple 2D images to produce a 3D impression of the anatomy [32]. Because plaque burden changes occur in three-dimensions, 3DUS imaging provides sensitive and reproducible measurements of carotid atherosclerosis [19, 37]. Due to availability of the out-of-plane information, the outer wall and lumen boundaries may also be robustly located in 3DUS images. However, similar to the conventional US technique, 3DUS is low contrast and is also affected by numerous US artifacts [43].

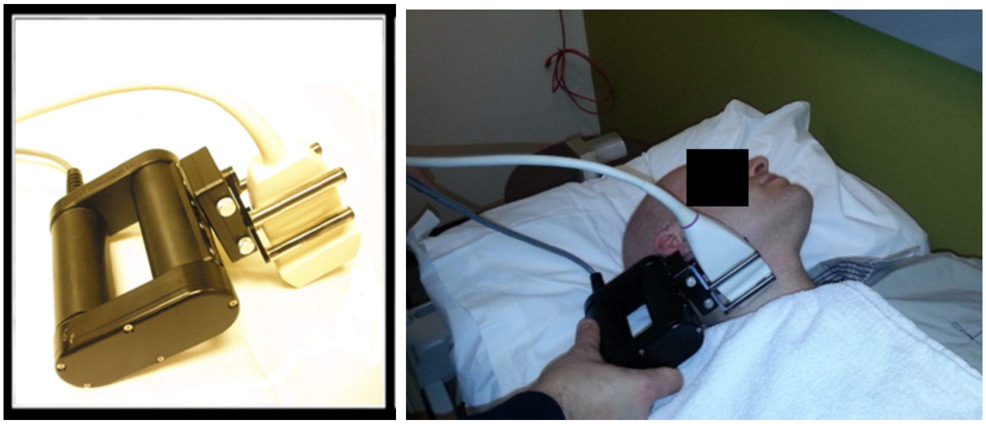
[redacted]

(a) (b)

Figure 1.2: (a) Mechanically assisted 3DUS transducer probe; and (b) acquiring a 3DUS image by translating the transducer along the patient's neck at least up to a distance of 4 cm encompassing portions of the CCA, ICA, and ECA.

Chapter 2 and 3 of this dissertation is based on algorithm developments for 3D carotid US images. Therefore, the 3DUS image acquisition process is briefly described in the following subsections.

1.4.5.1 3DUS image acquisition

Although, 2D transducer arrays are available for real-time 3D imaging [44], such transducer arrays are expensive and the transducer apertures are too small for imaging the carotid arteries at least up to a length of 4 cm [32, 45]. Therefore, most of the 3DUS systems use a conventional US linear transducer, which is translated either by free-hand or mechanically to obtain 3DUS images [32]. Irrespective of the method used for translating the US probe along the patient's neck, the position and orientation of the transducer are required to be tracked to reconstruct 3DUS images. The two translation mechanisms are concisely described below.

Free-hand scanning One of the main advantages of the free-hand scanner is that it does not require a bulky mechanical moving system and scanning is done only using a regular probe. The most commonly used tracking method is based on magnetic field sensing technology. A sensor is mounted on to the US probe, which comprises of three orthogonal coils to track in six degrees-of-freedom. The sensor measures a time-varying 3D magnetic field, which is transmitted using a device close to the sensor [32]. The signals induced in each orthogonal coil of the sensor can be used to track the position and the orientation of the probe. The main disadvantage of free-hand scanning is the need for the probe to be moved at a suitable consistent speed to maintain proper spatial sampling and to avoid any gaps in the reconstructed image.

Mechanical scanner A linear US transducer is translated using a motorized mechanism along the patient's neck over the carotid arteries as shown in Fig 1.2(b). To ensure that each acquired 2D image is spaced equally and all images are parallel to each other, a motor is used to move the transducer linearly at a constant velocity. In our experiments, 2D US images are acquired every 0.2 mm. When the 2D US images are acquired at a frame rate of 30 per second, a 4 cm length of the artery can be acquired in 6.7 s without cardiac gating. The in-plane resolution of the 3DUS image is isotropic. However, the resolution in the scanning direction depends on the elevation resolution of the transducer and is coarser than in-plane resolution.

System used in our experiments The 3DUS images were acquired using a ATL HDI 5000 US machine (Philips, Bothell, WA, USA) by translating a L12-5 linear US transducer (Philips, Bothell, WA, USA) with a central frequency of 8.5 MHz along the patient's neck at a uniform speed of 3 mm/s for about 4 cm, without cardiac gating [41, 46]. The transducer was attached to a motorized linear mover (see Fig. 1.2(a)) driven by 3DUS acquisition system consisting of a computer workstation with a video capture device digitizing 2D frames at 30 Hz. 3D images were constructed in real time as the images are acquired and displayed using multi-planar reformatting [32]. Figure 1.3 shows transverse and longitudinal views of two example 3DUS images for a subject with moderate stenosis and a subject with ulceration.

1.4.6 Magnetic resonance imaging (MRI)

Excellent soft tissue contrast and noninvasiveness of MR imaging make it ideally suited for carotid *in vivo* imaging. Multi-parametric MR imaging techniques including black-blood MR, bright-blood MR, diffusion-weighted (DW) MR, and 3D time-of-flight (TOF) MR angiography have allowed high contrast imaging of the arterial wall and plaque [47, 48]. Figure 1.4 shows a transverse view of the left and right CCA

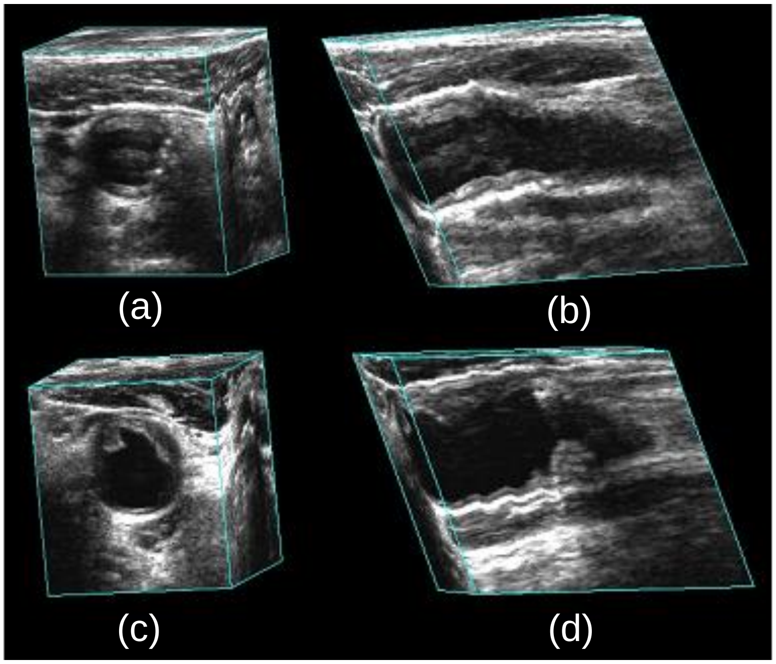

Figure 1.3: Multi-planer views of the 3DUS images. (a) Transverse view of a 3DUS image of carotid artery for a subject with moderate stenosis; (b) longitudinal view of a 3DUS image of carotid artery for the subject with moderate stenosis; (c) transverse view of a 3DUS image of carotid artery for a subject with ulceration; and (d) longitudinal view of a 3DUS image of carotid artery for the subject with ulceration.

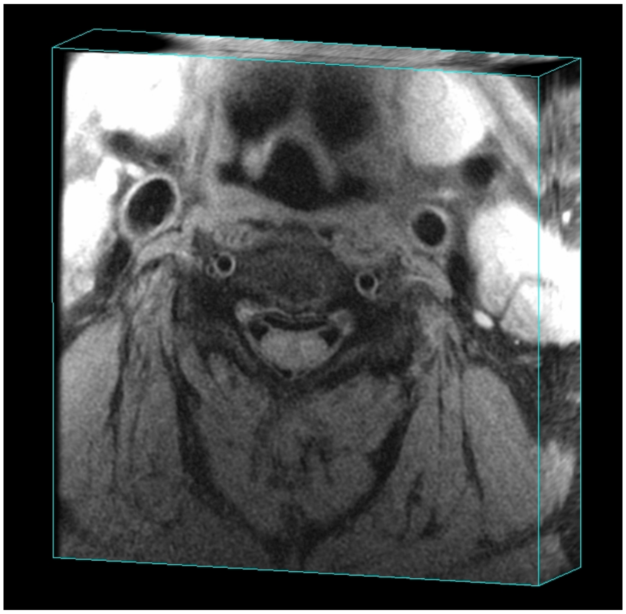

Figure 1.4: Transverse view of the left and right CCA of an T1w black-blood MR image of a patient with mild stenosis.

of a patient with mild stenosis. Note that, the carotid vessel wall boundaries are better defined in MR images than 3DUS images shown in Fig. 1.3. In addition, there have been recent developments in dedicated pulse sequences, gradient technology, and specially designed radio frequency (RF) coils to improve the overall quality of imaging.

MR has shown promise in providing accurate and reproducible measurements of not only volumetric and morphological measurements of carotid plaque burden [47, 49], but also plaque composition [48, 50] and inflammation [51, 52], which are important indicators of vulnerability of plaque and, in turn, risk of stroke. Chapter 4 of this dissertation is based on segmentation algorithms developed for generating volumetric measurements of plaque burden from carotid MR images.

Although capabilities of carotid MR imaging are substantial, its main limitations for monitoring of large numbers of asymptomatic patients are limited availability and high cost.

1.5 Imaging phenotypes

Some carotid imaging modalities were described in the previous section. In this section, I describe imaging phenotypes that are derived from medical images for quantifing carotid plaque burden. As described in Section 1.4, carotid imaging techniques are increasingly becoming popular as tools to quantify surrogate end-points of carotid atherosclerosis due to their capability of direct measurement of plaque as opposed to indirect measurements (i.e, blood serum levels [53]). Such carotid imaging phenotypes allow assessment of atherosclerotic disease progression, and reduce the need for studying the effect of interventions on hard clinical end-points including stroke or myocardial infraction (MI) [54]. The ideal phenotypes should correlate with the extent of atherosclerotic disease and ideally be obtained from noninvasive, reliable, safe, inexpensive, and reproducible techniques [55].

Numerous phenotypes of carotid atherosclerosis have been used in the past, which have been investigated as surrogate end points of vascular outcomes for monitoring the progression and regression of atherosclerotic plaque burden in patients during medical interventions. The focus of this dissertation is on noninvasive phenotypes derived from US and MR images, and more specifically on volumetric phenotypes. Some of the most relevant US and MR imaging phenotypes, which have been used recently, such as carotid artery stenosis (CAS) [56], intima media thickness (IMT) [30], total plaque area (TPA) [57], total plaque volume (TPV) [58], vessel wall volume (VWV) [59], and vessel-wall-plus-plaque thickness (VWT) maps [60, 61], are described below.

1.5.1 Carotid artery stenosis (CAS)

Carotid artery stenosis (CAS) is a one dimensional measurement of lumen narrowing, which is often measured using duplex US. CAS is a noninvasive measurement and is the current clinical imaging standard for diagnosing carotid plaque burden and is a deciding factor for patient's eligibility of carotid endarterectomy [62]. For example, the North American symptomatic carotid endarterectomy trial (NASCET) trial [63] showed that a CAS of $\geq 70\%$ identifies a group of subjects who will benefit from carotid endarterectomy. However, the presence of stenosis alone is not a good indicator of risk of stroke, since the early stages of the disease progress outwards without actually obstructing the lumen. The results from NASCET showed that 74% of the subjects with severe stenosis (>70%) did not experience stroke within two

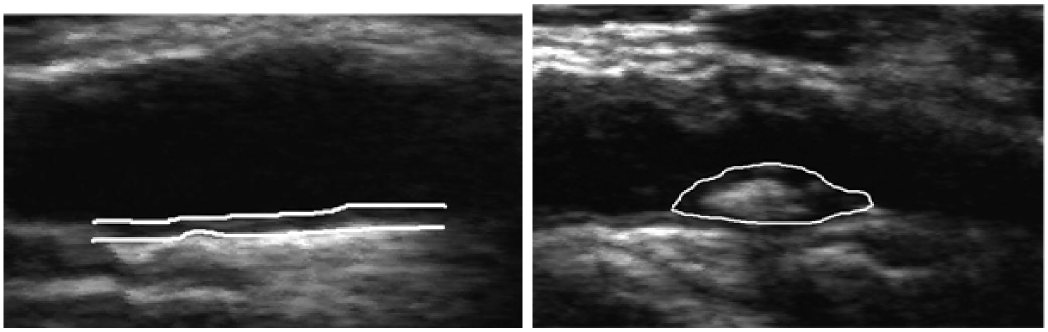

(a) (b)

Figure 1.5: (a) Manual delineation of the IMT measurement of the CCA from a longitudinal 2D US image; and (b) manual delineation of the plaque boundary for TPA measurement from a longitudinal 2D US image.

years [64]. The results from European carotid surgery trial (ECST) showed that 10% of symptomatic subjects with low-grade stenosis (17-50% by NASCET) experienced ipsilateral stroke within 4 years [65]. Moreover, recent studies suggest that CAS is less sensitive than lesion size expressed by vessel wall volume, which is also used as a measurement of therapeutic effects [47, 49, 50].

1.5.2 Intima-media thickness (IMT)

Intima-media thickness (IMT) is a one dimensional measurement of combined thickness of the intima and media layers of the artery, which is measured using longitudinal 2D US images. When the measurement is obtained over a specified vessel length, as shown in Fig. 1.5(a), the mean thickness is considered as IMT. During the last two decades 2D US IMT measurement has been widely investigated as a surrogate end-point of vascular outcomes for monitoring carotid atherosclerosis in subjects during medical interventions [28, 66].

Even though CCA IMT is a reproducible measurement that correlates with the risk factors of stroke in large clinical trials [66, 67], it is not sensitive to the changes in plaque burden, which is a stronger predictor of cardiovascular events [68, 69, 70, 71]. Moreover, changes in IMT occur at a rate of a fraction of a millimeter per year [72], resulting in long follow-up times. In addition, it is challenging to design algorithms with required high precision to detect subtle changes in IMT.

1.5.3 Total plaque area (TPA)

Total plaque area (TPA) is a 2D measurement of the carotid plaque burden (see Fig. 1.5b), which is the sum of the maximum longitudinal cross-sectional areas of all the plaques within a specified length of the carotid artery [66]. TPA has been widely used in clinical studies in the past [55, 73, 74, 75, 76], and has been shown to be more sensitive than IMT. For example, the results from the six-year follow up of the Tromso study [77] involving more than 6000 subjects showed that in the general population, carotid TPA was a stronger predictor of myocardial infarction than IMT. With a 10-year follow-up, the study also reported that the TPA is a strong predictor of first-ever ischemic stroke than IMT [78]. In addition, unlike IMT, the quantities being measured are larger in value relative to the resolution of the US image.

1.5.4 Total plaque volume (TPV)

Total plaque volume (TPV) is a direct volumetric measurement of plaque burden in the left and right carotid arteries [19, 79]. TPV measurements encompass more complex plaque morphologies and geometries than TPA measurements that are performed only in 2D longitudinal view with maximum area. TPV has shown to be more sensitive to change than CAS, IMT, and TPA [80]. Both TPA and TPV reflect more advanced stages of the disease than IMT [66]. Currently, TPV measurements are obtained by manual segmentation of the plaque [45, 58, 79]. Initially, the observer defines the medial axis of the artery in a longitudinal view. After familiarizing with the orientation and geometry of the plaque, the observer outlines the plaque boundary on transverse slices with inter-slice distance (ISD) of 1 mm. Figure 1.6 shows the manual segmentations of plaque overlaid on a 3DUS image and the reconstructed surface of plaque for the computation of TPV.

TPV has been used in several clinical studies [41, 42, 80]. For instance, Ainsworth *et al.* [41] has conducted a small randomized control trial to evaluate the effect of atorvastatin using 3DUS TPV. The control group had a progression of 16.81 ± 74.10 mm^3 whereas the atorvastatin group had a regression of 90.25 ± 85.12 mm^3. A significant difference has been reported between the two groups.

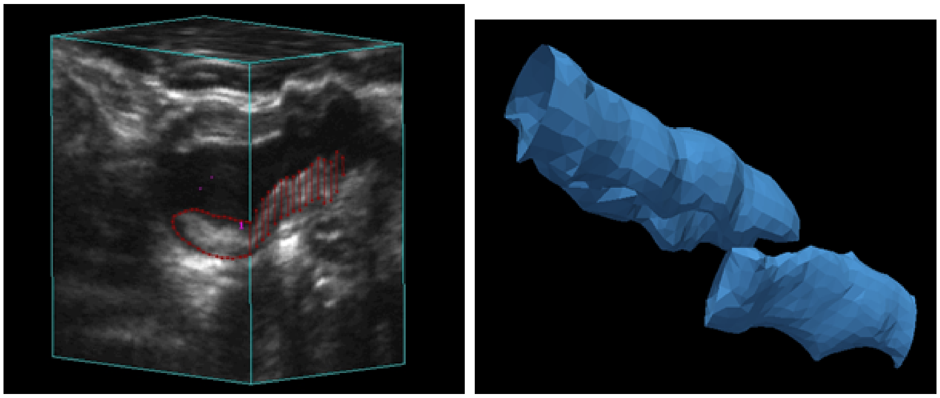
(a) (b)

Figure 1.6: (a) Manual segmentation of the plaque boundaries of the 3D US image used for TPV measurement; and (b) reconstructed plaque surfaces from the manual segmentations.

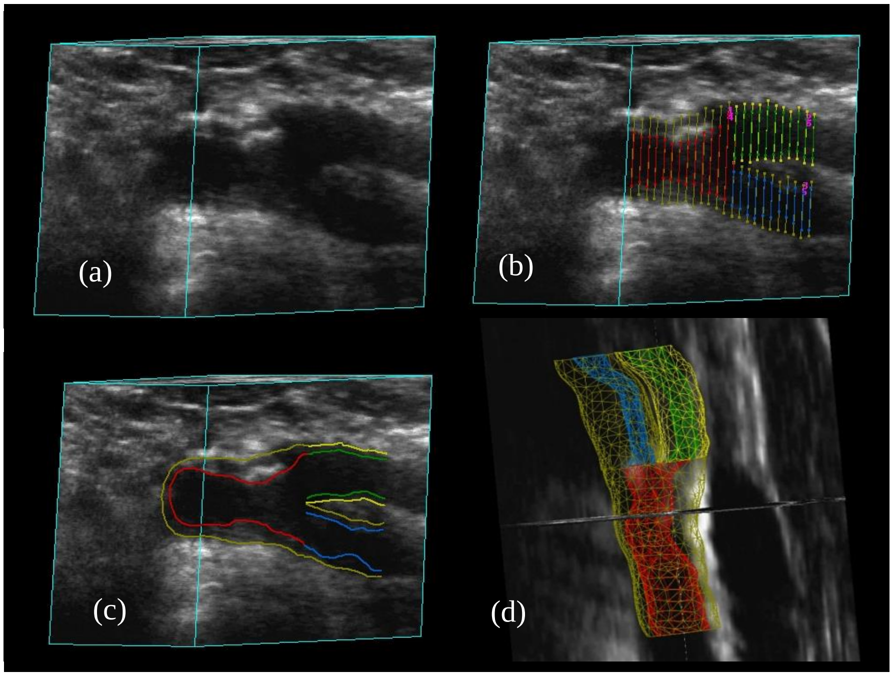

Figure 1.7: (a) An example 3DUS image of a patient's carotid artery; (b) and (c) manual segmentation of the CCA, ICA, and ECA lumen and outer wall boundaries from 3DUS images; and (d) reconstructed surfaces for the lumen and outer wall boundaries from the manual segmentations. The outer wall surface of the CCA, ICA, and ECA is rendered in yellow. The lumen surfaces of the CCA, ICA, and ECA are rendered in red, blue, and green, respectively.

1.5.5 3DUS and MRI vessel wall volume (VWV)

Vessel wall volume (VWV) is the volume enclosed between the outer wall and the lumen boundaries for the CCA, ICA, and less commonly for ECA [49, 59]. VWV is a combined measurement of both the plaque and wall thickness. The primary measurement of interest of this dissertation is VWV. Chapter 2, 3, 4, and 5 of this dissertation describe segmentation algorithms developed for the purpose of generating VWV.

The measurement of VWV requires an observer to manually outline the lumen-intima/plaque and media-adventitia boundaries. Both 3DUS and MR images [49] can be used to generate VWV. 3DUS VWV is generated by outlining the lumen-intima boundary (LIB) and media-adventitia boundary (MAB), whereas MRI VWV is generated by outlining the LIB and adventitia boundary (AB).

Figure 1.7 shows manual segmentations of the outer wall and lumen boundaries overlaid on a 3DUS image and the surfaces of the outer wall and lumen for computing VWV. Manual segmentation of the boundaries is performed on transverse slices with an inter-slice distance of 1 mm. The VWV measurements have higher reproducibility than TPV measurements [37], because lumen-intima/plaque and media-adventitia boundaries are more straightforward to interpret than plaque-lumen and wall boundaries in 3DUS images. In addition, VWV boundaries are more regular and circular, which may simplify the development of semi-automated segmentation technique to delineate the outer wall and lumen boundaries. VWV measurements have a higher reproducibility than TPV measurements due to the fact that the outer wall and lumen boundaries are easier to delineate than plaque boundaries [37]. Egger *et al.* [37] compared the coefficient-of-variation (CV) and intra-class correlation coefficients (ICC) of VWV and TPV measurements for 10 subjects. CV (4.6% vs. 22.7%) and ICC (0.95 vs. 0.85) measurements indicated a higher intra-observer variability and inter-scan variability in TPV measurements.

3DUS VWV imaging is increasingly being used as a surrogate for monitoring carotid plaque burden in patients in clinical trials during medical interventions. Shai *et al.* [23] used 3DUS VWV measurements to assess the effect of dietary interventions for reducing the carotid plaque burden. The study [23] found that diet-mediated weight loss over a 2-year period induced significant regression of 3DUS carotid VWV, even though the effect is similar in low-fat, Mediterranean, or low-carbohydrate diets.

Krasinski *et al.* [59] used 3DUS VWV measurement to assess the effect of atorvastatin in reducing the carotid plaque burden. The randomized control trial of three months [59] had 35 subjects with carotid stenosis $> 60\%$, where subjects were assigned to either the statin drug or placebo. The results have showed an increase of 70 ± 140 mm^3 in 3DUS VWV in the placebo group and a reduction of 30 ± 130 mm^3 in the atorvastatin group.

1.5.6 Vessel wall thickness/change (VWT) maps and flattened VWT maps

The measurements discussed so far are global measurements of plaque progression and/or wall thickening, which provide a single value of measurement, such as an area or volume. While such phenotypes provide valuable quantitative information about global plaque burden, they do not identify the locations with substantial changes in the vessel. Identification of the locations of change in plaque burden will enable more precise evaluation of changes in plaque burden and will provide insights to the disease progression during medical interventions. Chiu *et al.* [81] proposed 3DUS vessel-wall-plus-plaque thickness (VWT) maps, which visualize the thickness of the vessel wall plus plaque at each location as a colour map as shown in Fig. 1.8(a). 3DUS VWT change maps [61] quantify and allow visualization of local changes in plaque morphology on a point-by-point basis between a baseline and follow-up measurements. To facilitate the visualization and interpretation of these maps for clinicians, Chiu *et al.* [61] proposed a technique to flatten the 3D VWT maps and VWT change maps to 2D. Similar to the VWV, VWT maps require segmented surfaces of the lumen and outer wall of the carotid arteries.

1.6 Peripheral arterial disease (PAD)

Peripheral arterial disease (PAD) is a common circulatory disease, which occludes the arteries in the lower extremities including the superficial femoral artery (SFA) with long term accumulation of plaque due to atherosclerosis. PAD affects 12%−14% of the general population and its prevalence increases with age affecting up to 20% of patients over the age of 75 [82]. PAD has long been underestimated, and may

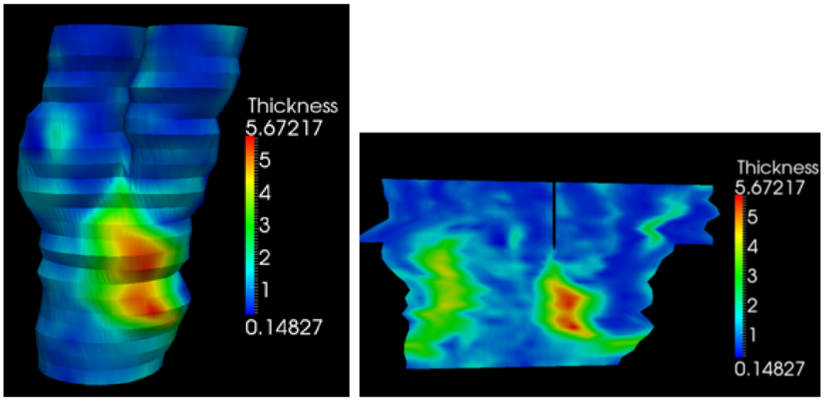

(a) (b)

Figure 1.8: (a) Vessel-wall-plus-plaque thickness (VWT) map for a patient with moderate stenosis. Manual segmentations of the lumen and outer wall boundaries were used to generate the VWT maps. The thickness is indicated in millimeters; and (b) corresponding flattened VWT map for better visualization.

have been overshadowed by cardio- and cerebro-vascular disease. In addition, asymptomatic and symptomatic PAD are consistent and powerful independent predictors of coronary artery disease (CAD) and cerebrovascular disease (CBVD) [83]. The symptoms due to PAD may range from intermittent claudication to critical limb ischemia, which may lead to gangrene and in serious cases limb amputation [84].

1.7 Imaging phenotypes for PAD

So far, imaging phenotypes pertaining to carotid atherosclerosis have been described. Compared to carotid atherosclerosis, fewer imaging phenotypes have been investigated for quantifying PAD plaque burden, which are described below.

1.7.1 Ankle-brachial index (ABI)

Ankle-brachial index (ABI) is an approximate estimate of the relative blood flow in the ankle compared to the brachial artery. In particular, ABI is the ratio of the systolic blood pressure of the lower legs and arms, which is measured using a Doppler US blood flow detector [85]. Currently, ABI is used for diagnosis and assessment of the severity of PAD [86]. Typically, normal range for ABI is $1.10 - 1.29$ and ABI < 0.9 is an indication of stenosed femoral arteries [85]. Although ABI has been

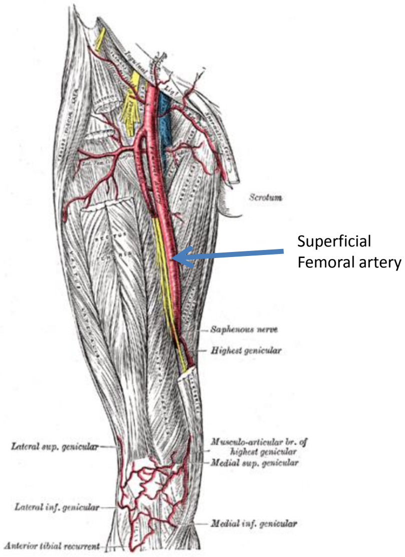
Scrotum
Superficial
Femoral artery
Saphenous nerve
Highest genicular
Lateral sup. genicular
Musculo-articular br. of
highest genicular
Medial sup. genicular
Lateral inf. genicular
Medial inf. genicular
Anterior tibial recurrent

Figure 1.9: The anatomy of the femoral artery. The image is courtesy from 20^{th} U. S. edition of Gray's Anatomy page #550 (Also available at `https://en.wikipedia.org/wiki/Femoral_artery`).

significantly correlated with carotid IMT and Framingham risk score [85, 86], ABI is an indirect measurement of plaque burden for assessing the progression of the disease and prediction of clinical events.

1.7.2 Stenosis

Patients with ABIs less than 0.9 may be followed up with CTA [87]. However, similar to carotid lumenographic techniques, the femoral vessel wall is imaged with low contrast. Therefore, CTA has limited capabilities for assessing the progression of the disease and prediction of clinical events [88]. Similar to carotid atherosclerosis, stenosis measurements are more suitable for latter stages of the disease.

1.7.3 Vessel wall area and vessel wall volume measurements

Although, 2D US/3DUS imaging has not been widely investigated for the assessment of femoral artery plaque burden, MR imaging has been investigated for assessment of PAD [88] plaque burden, because it facilitates thickness and volumetric measurements, which may be more sensitive to clinical outcomes than ABI and stenosis.

Assessment of PAD using MR imaging has continued to be developed [89], due to its noninvasiveness and its ability to image the femoral artery vessel wall with high image contrast. In this dissertation, we use 3D black-blood MRI images acquired using the 3D motion-sensitized driven equilibrium (MSDE) prepared rapid gradient echo sequence (3D MERGE) [90, 91], which enables evaluation of the femoral artery vessel wall up to a length of 50 cm. Due to the high vessel wall image contrast, MR imaging facilitates morphological and volumetric measurements of plaque burden, which may be more sensitive to clinical outcomes [84, 88, 89, 92]. Chapter 5 of this dissertation is based on the development of segmentation algorithms to quantify VWA and VWV measurements from femoral black-blood MR images.

1.8 Motivation and objectives

In this section, the motivation and specific objectives of this dissertation are described.

1.8.1 Motivation for developing segmentation algorithms

Major cardiovascular events, such as stroke and myocardial infraction may occur in patients without known preexisting symptoms [86]. With the advancements of medical imaging hardware towards high resolution 3D imaging and clinical advancements of therapeutics and personalized medicine, there is a great requirement for more sensitive measurements of vascular atherosclerotic measurements. As discussed in Section 1.5, 3D measurements of carotid plaque burden, such as VWV and TPV, are more sensitive than 1D and 2D measurements, and there is an increased interest to use them in clinical trials. Although 3D measurements provide many advantages compared to measurements of arterial wall thickening or TPA alone, they are still not widely used in research or clinical practice because of the inordinate amount of time required to train observers and to generate 3D measurements using manual segmentation. Even though, manual segmentation is still widely used for segmentation tasks, semi-automated or automated segmentation algorithms are preferred over manual techniques since manual techniques are tedious, time-consuming, and require more expertise.

In this dissertation, the main objective is to develop accurate and robust semi-automated algorithms for the following three segmentation problems of interest:

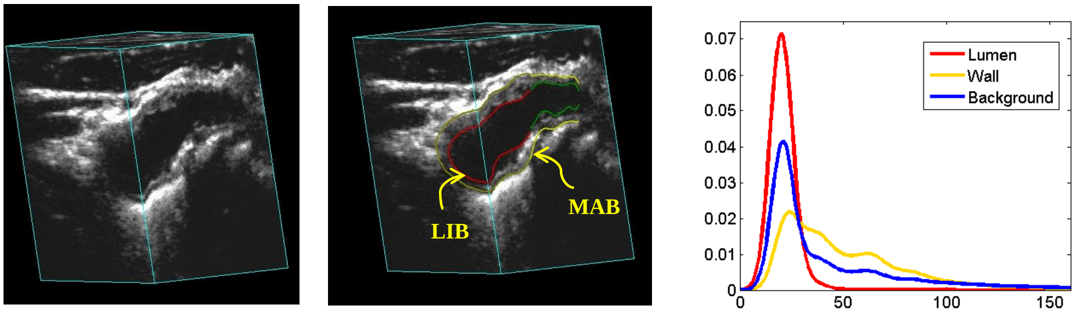

(a) (b) (c)

Figure 1.10: (a) Transverse and sagittal views of a 3DUS image; (b) same image with overlaid manual segmentation of lumen-intima boundary (LIB) and media-adventitia boundary (MAB); and (c) image intensity histogram of the lumen, outer wall and background.

- Carotid artery lumen and outer wall segmentation from 3DUS images
- Carotid artery lumen and outer wall segmentation from MR images
- Femoral artery lumen and outer wall segmentation from MR images

for the purpose of generating measurements of VWV. We anticipate that the semi-automated algorithms will alleviate measurement burden from the observer for generating volumetric measurements (i.e., VWV) of plaque burden. The algorithm development for each of the problem is motivated by: (1) increased interest in 3DUS imaging for noninvasive monitoring of plaque burden, but lack of available segmentation methods; (2) a segmentation algorithm for carotid MR imaging would not only be useful for volumetric imaging, but also for plaque component analysis for assessment of vulnerability of the plaque; and (3) femoral vessel wall is yet to be explored using femoral MR vessel wall images and robust algorithms for segmentation may accelerate their use in clinical trials.

In the following subsections, each segmentation problem is briefly described by providing a concise description of image segmentation algorithms and motivation for the choices of the segmentation algorithm.

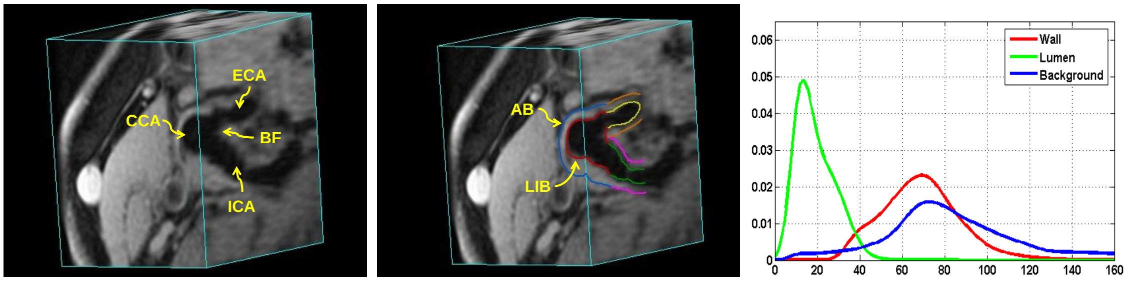

(a) (b) (c)

Figure 1.11: (a) A 3D view of a T1-weighted 3T carotid MR image showing the transverse and sagittal cross sections of the CCA, ICA, and ECA. The CCA divides into the ICA and ECA at the bifurcation (BF); (b) the same 3D carotid MR image with the overlaid manual segmentations of the adventitia (AB) and lumen-intima (LIB) of the CCA, ICA, and ECA. The manual segmentations are performed on each transverse slice; and (c) image intensity histogram of the lumen, outer wall, and background.

1.8.2 Carotid artery lumen and outer wall segmentation from 3DUS images

Figure 1.10(a) and (b) show an example 3DUS image with overlaid manual segmentations of the lumen and outer wall boundary (also referred to as lumen-intima boundary (LIB) and media-adventitia boundary (MAB)). Out of the three research goals, segmentation of the carotid outer wall and lumen from 3DUS images is the most challenging task, mostly due to the lack of image contrast at the lumen and outer wall boundaries and overlapping intensity probability density functions (PDF) (also known as "intensity histograms") Moreover, 3DUS images suffer from artifacts, such as poor definition of the vessel boundaries, image speckle, and acoustic shadowing. These artifacts decrease differentiation between the object of interest and background with respect to image features and pose a challenge for segmentation algorithms. Due to such challenges posed to image-based segmentation algorithms by plaque and US imaging artifacts, high-level user interaction and domain knowledge are required for the segmentation. Figure 1.10(c) shows the intensity histograms of the lumen, outer wall, and background regions. Segmentations algorithms can be easily automated when the histograms are separable, whereas more manual interactions are needed when the histograms overlap.

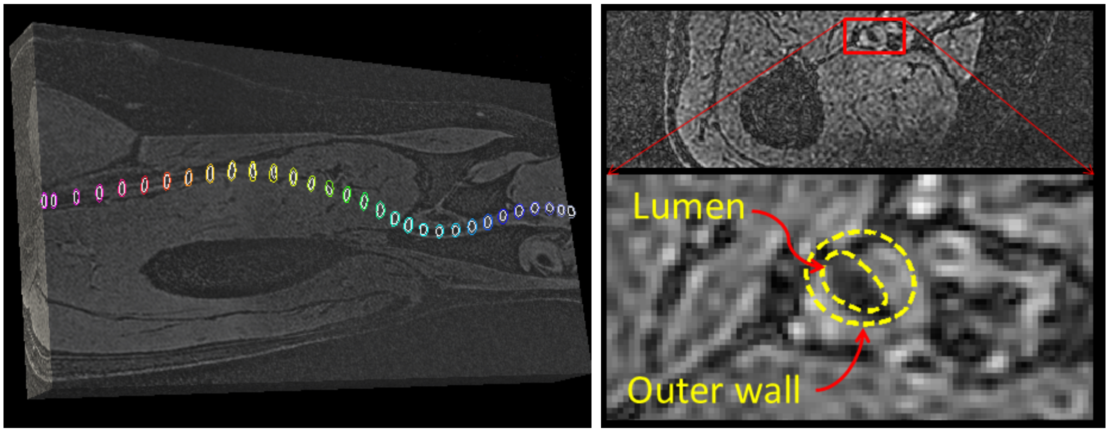

(a) (b)

Figure 1.12: (a) An example 3D femoral MR image with manual delineations; and (b) a transverse slice of a 3D femoral MR image with manual delineations of the femoral lumen and outer wall.

1.8.3 Carotid artery lumen and outer wall segmentation from MR images

For MRI VWV, the carotid lumen and outer wall boundaries are also referred to as the lumen-intima boundary (LIB) and adventitia (AB) boundary. Compared to 3DUS images, the lumen boundary of MR images has high image contrast, the outer wall boundary is relatively more distinguishable as shown in Fig. 1.11(c), and the intensity PDFs are more distinguishable from each other than for 3DUS. As such, segmentation of the carotid wall and lumen from MR images is less challenging than 3DUS segmentation. Therefore, due to distinguishing image features and with the incorporation of some anatomical prior knowledge, the algorithm can be automated to a higher extent requiring fewer user interactions to drive the segmentation.

1.8.4 Femoral artery lumen and outer wall segmentation

With the advent of rapid and noninvasive 3D black-blood MRI sequences, such as the 3D motion-sensitized driven equilibrium (MSDE) prepared rapid gradient echo sequence (3D MERGE), femoral artery vessel wall can be assessed up to a length of 50 cm for monitoring PAD plaque burden. Therefore, precise segmentation of the femoral artery outer wall and lumen is important for generating volumetric and morphological measurements of plaque burden for longitudinal monitoring of PAD. An MR image of a patient's leg is shown in Fig. 1.12 along with the manual delineations of the femoral artery lumen and outer wall. The major challenges for a segmentation algorithm of the femoral lumen and outer wall are thin and elongated shape appearance of the femoral artery (see Fig. 1.12(a)) as well as the lack of distinctive image boundary at the outer wall boundary, and strong similarity in image intensity (i.e. intensity PDFs of outer wall and background overlap with each other) between the outer wall and its surrounding region.

1.9 Image segmentation

Image segmentation is a way of partitioning an image $I(x), x \in \Omega$ into two or more meaningful regions or objects-of-interest. In computer vision research, image segmentation is one of the oldest and most widely investigated problems [93]. Image segmentation algorithms have been developed to segment images of scenes, videos, and 2D/3D/4D/nD medical images. Specifically, the focus of this dissertation is on medical image segmentation. Image segmentation algorithms are required in clinical applications to assist the observer in generating quantitative measurements and aid in medical interventions. For example, in this dissertation, the carotid and femoral lumen and wall boundaries are required to be segmented for generating VWV measurements.

The main objective of this section is to provide a brief description of the state-of-the-art segmentation algorithms and their evaluation methods, before describing our proposed algorithms in Chapters 2-5.

1.9.1 Segmentation algorithms

While it is possible to classify segmentation algorithms based on many criteria, such as mathematical principle (variational methods vs. graph partitioning methods), degree of automation, global- or local-optimality, here we broadly categorize image segmentation into three based on the way the segmentation problem is formulated:

- Heuristic methods e.g., thresholding, region growing, region split-and-merge, etc.

- Clustering methods e.g., K-means clustering, mean shift algorithm, etc.

- Functional optimization methods e.g., active contours, level sets, live wire, graph cuts, convex relaxation techniques, etc.

1.9.1.1 Heuristic methods

Heuristic methods rely entirely on the image features in order to perform segmentation and are mostly based on a heuristic criterion to obtain the segmentation. Some examples of heuristic methods are thresholding, region-growing [94], and region split and merge [95] to name a few. These methods rely on heuristically defined criteria for segmentation and make decisions based on local pixel information and ignore spatial information. Thus, heuristic methods are effective when the intensity levels of the objects fall squarely outside the range of intensities of the background. Although, heuristic methods are fast and simple, they are often not suitable for US and MR segmentation tasks due to numerous variations, image artifacts, and poor image quality.

1.9.1.2 Clustering methods

An intuitive way of segmentation is to determine which voxels of a data set belong together based on some similarity [96]. Such similarity is determined based on a distance measure. Clustering algorithms form clusters from images based on voxel intensity, colour, texture, location, or some combination of these. Numerous clustering algorithms have been developed with different induction principle. Readers are referred to Rokach *et al.* [96] for more information.

K-means [97] and mean shift algorithms [98] are some example clustering algorithms that have been used for image segmentation. For clustering algorithms the starting locations of the partitions are important for achieving optimal solution since they are susceptible to termination when achieving a local maximum. A main challenge for clustering algorithms in medical image segmentation applications is the difficulty to incorporate anatomical and spatial information into segmentation.

1.9.1.3 Functional optimization methods

Unlike the heuristic and clustering methods, functional optimization methods allow for the incorporation of high-level knowledge of the desired segmentation result, such as boundary smoothness, shape, and appearance [99, 100]. In contrast to the heuristic methods, funtional optimization methods first formalize a mathematical criterion for the "goodness" of a given segmentation. This allows formulation of the segmentation problem as an optimization problem under certain geometric constraints. For $I(x), x \in \Omega$, there are many possible decision boundaries (contours) C partitioning the domain Ω into subdomains. The main idea is to start with some initial boundary shape represented in the form of spline curves, and iteratively modify it by applying various shrinking/expansion operations according to some energy function. An objective function $E(C)$ is then minimized to find the best boundary as follows

$$C^* = \arg\min_{c} E(C). \tag{1.1}$$

The objective function contains two types of energy terms: external energy and internal energy. External energies are derived from the (preprocessed) image data to guide the segmentation. Internal energy terms are derived from high-level knowledge of the expected shape of the boundaries as well as from user-specified anchor points. The most widely used internal energy term is a regularization term, which minimizes the length of the boundary. Various approaches are available for solving this optimization problem and defining the curve C. A variety of constraints can be incorporated into an energy functional $E(C)$ in a form of internal or external energies, in which case E(C) becomes a weighted sum of a number of subcomponents:

$$E(C) = \sum_{i} w_i E_i(C), \quad i = 1 \ldots N\,, \tag{1.2}$$

where w_i are balancing weights and N is the number of energy terms. Most widely used segmentation based tasks are performed using optimization approaches. Active contours, level sets, graph cuts, and convex relaxation methods are some examples of funtional optimization methods. Here is a brief description of each of the methods. In this dissertation, I used the level set technique and convex max-flow based techniques for segmentations. The motivations for using such techniques are discussed in the corresponding chapters.

Snakes\Active contours Proposed by Kass [101], active contours use a parametric representation of a contour by explicitly defining it using a set of points. The points on the boundary are evolved iteratively by minimizing an objective function towards image features such as strong edges. Snakes depend on local optimization schemes, so the initialization needs to be close to the desired boundary to obtain an accurate segmentation. It is challenging for these techniques to change topology of the initially defined contour and to perform multi-region based segmentations.

Level set methods Level set methods proposed by Osher and Sethian [102] provide an implicit representation of a contour/surface by defining it using a level set function, which is of one dimension greater than object dimension. Cassels [103] and Malladi *et al.* [104] introduced level sets for image segmentation. Unlike deformable snakes, level set methods can implicitly change their topology and incorporate region-based statistics into the segmentation. Level set methods also rely on local optimization by explicitly solving the associated convection partial differential equations (PDE) for which the Courant-Friedrichs-Lewy (CFL) condition restricts the discrete propagation time step-size [105]. In addition, level set methods are also extendable to multi-region segmentations. One of the main disadvantages of the level set method is that it is computationally expensive.

Graph Cuts In graph-based segmentation methods the pixels are represented as vertices and their boundaries as edges in a graph. For the binary case, any pixel is attached to two terminals: source s and sink t. s/t cut of a graph partitions a graph into two disjoint subsets and the cost of the cut is the sum of all costs of the edges and the *minimum cut* offers a globally optimal object extraction method for n-dimensional images [106]. This minimum s/t cut problem can be solved by finding a maximum flow from the source s to the sink t. There are numerous polynomial time algorithms to solve min-cut/max-flow problems [107].

Graph cuts-based methods use implicit representation of object boundaries, which makes them a discrete counterpart of level sets. Metrication artifacts are a limitation of graph-based approaches [105, 108]. Although, reducing metrication artifacts is possible with increasing the number of neighbouring graph nodes, it substantially increases computation and memory load [109, 110].

Continuous max-flow methods We use convex optimization methods for the carotid MR and femoral MR segmentations in Chapter 4 and 5. Continuous max-flow-based approaches have advantages of both the level sets and graph cuts, and have recently been widely investigated for image segmentation problems. Comparison of discrete and continuous optimization techniques have shown that, in the case of 3D or higher-dimensional grids, continuous max-flow-based approaches outperformed graph cuts in speed and accuracy [111]. Moreover, the implementation of convex relaxation approaches can be parallelized to reduce computational time [112].

Convex optimization methods have been successfully used in recent studies for solving the classical piece-wise constant binary segmentation model [110, 113] and multi-region segmentation problems [112]. Moreover, a new global optimization-based approach to the contour evolution has been proposed by Yuan *et al.* [105] using continuous max-flow techniques, which provides the basic mathematical foundation for the methods described in Chapter 4 and 5 of this dissertation. More precisely, their method formulates evolving a contour/surface at each discrete time frame by achieving the minimum cost of region changes, which can be identically modeled as a spatially continuous min-cut problem. To this end, a continuous max-flow model is proposed, which provides an elegant dual formulation to the convex relaxed continuous min-cut formulation and proves the global optimality of the computed continuous min-cut solution by means of convex relaxation.

Compared to the discrete contour evolution methods [114], the contour evolution is solved in the spatially continuous setting by the continuous max-flow based approach [105]. The method also avoids metrication artifacts [115, 116], and obtains a sub-pixel accuracy of the contour position.

1.9.2 Level set methods

In Chapter 2 and 3, a level set method is used for 3DUS lumen and wall segmentation. In level set, the segmentation boundary is represented as the zero level of an implicit function. The segmentation boundary is iteratively evolved by optimizing an objective function to find the boundary of an object.

Let the bounded open subset $\Omega \subset \mathcal{R}^3$ represent the image domain. Each image is defined as $I : \Omega \to \mathcal{R}$, and $x \in \Omega$ is a spatial variable representing a single point within the image domain Ω. The level set is an implicit representation of a boundary defined by the function $\phi(x) : \Omega \to \mathcal{R}$. The boundary is specified as the zero level of the level set function, i.e., the set of spatial locations x for which $\phi(x) = 0$. During the segmentation process, the function $\phi(x)$ is evolved, rather than explicitly evolving the boundary itself as when using a parametric boundary representation. The level set evolution equation is given by

$$\frac{\partial \phi(x)}{\partial t} + F|\nabla \phi(x)| = 0, \tag{1.3}$$

where F is the speed function. Equation (1.3) is often derived by minimizing an energy E following the standard Euler-Lagrange descent equations [117], with t an artificial algorithmic time parameterizing the descent direction. The mean curvature motion given by $F = \operatorname{div}(\nabla \phi(x)/|\nabla \phi(x)|)$ is widely used to evolve the level set as follows:

$$\frac{\partial \phi(x)}{\partial t} = |\nabla \phi(x)| \operatorname{div}\left(\frac{\nabla \phi(x)}{|\nabla \phi(x)|}\right). \tag{1.4}$$

1.9.2.1 Sparse field level set (SFLS) method

One of the main drawbacks of classical level set methods is that they are computationally expensive, because many computations are required to maintain $\phi(x)$ during the contour evolution. In this dissertation, we use a narrowband level set implementation (known as sparse field level set (SFLS)) proposed by Whitaker [118]. Narrowband methods update only the level set evolution around the neighbourhood of the zero level set rather than computing $\phi(x)$ for the entire image domain.

The SFLS method uses lists of points that represent the zero level set as well as points adjacent to the zero level set. An efficient representation of $\phi(x)$ can be maintained, by carefully moving points to and from the appropriate list [119].

1.9.3 Convex optimization using continuous max-flow methods

The conventional contour evolution methods, e.g., [99, 101, 120, 121] etc., gradually propagate a contour/surface subject to the minimization of a certain energy function, while the associated time-explicit convection equations are often solved by local-optimization methods. In practice, the computational result and efficiency of such approaches are limited since the contour may be trapped in a locally optimal position during each time frame. The final result depends heavily on the initial position of the segmentation. The discrete time-step has an upper bound to achieve numerical

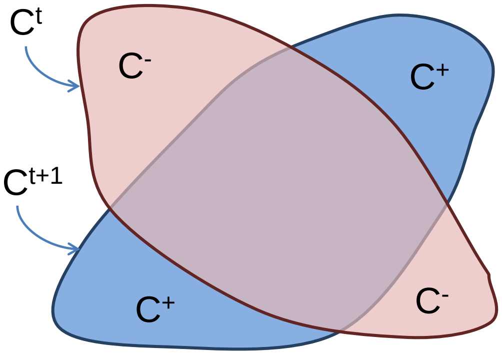

Figure 1.13: The current contour $\mathcal{C}^t$ evolves to the contour $\mathcal{C}^{t+1}$ at next time frame $t+1$. A voxel pays cost e^- for a pixel transitioning from object region to the background region and a voxel pays cost e^+ for a pixel transitioning from background region to the object region during the current iteration. Costs e^+ and e^- are region-based costs that are usually computed by matching the current segmentation with a prior model that is characteristic of the object region.

stability, such as the Courant–Friedrichs–Lewy (CFL) condition for explicitly solving the convection partial differential equations (PDE) [122]. The nonlinear high-order derivatives, such as curvature, are also highly affected by image noise.

In contrast, global optimization-based contour evolution approaches [114, 123] overcome such challenges and generate simple, efficient, and robust algorithms for computation. For example, the convex relaxation-based approach proposed by Yuan *et al.* [105] propagates a contour to its globally optimal position at each discrete time frame by solving a sequence of convex optimization problems, for which an efficient continuous max-flow algorithm [124] is available. In addition, the new contour position at each evolution step is computed in a fully time-implicit manner, which allows a large time-step and substantially speeds up contour propagation [105, 125].

As shown in Fig. 1.13, for the given contour $\mathcal{C}^t$ at the current time t, its new position $\mathcal{C}^{t+1}$ at the next discrete time $t+1$ can be achieved by solving the following optimization problem [105]:

$$\min_{\mathcal{C}} \int_{\mathcal{C}^+} e^+(x)\, dx + \int_{\mathcal{C}^-} e^-(x)\, dx + \int_{\partial\mathcal{C}} g(s)\, ds\,, \tag{1.5}$$

where $\mathcal{C}^+$ and $\mathcal{C}^-$ are the expansion and shrinkage regions with respect to the current contour $\mathcal{C}^t$, and the functions $e^+(x)$ and $e^-(x)$ define the cost corresponding to the pixel x in $\mathcal{C}^+$ and $\mathcal{C}^-$.

1. $\mathcal{C}^+$ indicates the region expansion w.r.t. $\mathcal{C}^t$: for $\forall x \in \mathcal{C}^+$, it is initially outside $\mathcal{C}_t$ at time t, and 'jumps' to be inside $\mathcal{C}^{t+1}$ at $t+1$; for such a 'jump', it pays the cost $e^+(x)$.

2. $\mathcal{C}^-$ indicates the region shrinkage w.r.t. $\mathcal{C}^t$: for $\forall x \in \mathcal{C}^-$, it is initially inside $\mathcal{C}^t$ at t, and 'jumps' to be outside $\mathcal{C}^{t+1}$ at $t+1$; for such a 'jump', it pays the cost $e^-(x)$.

In (1.5), the functions $g(s)$ is the weighted length smoothness term. In this dissertation, $g(s)$ is considered as

$$g(|\nabla I(x)|) = \lambda_1 + \lambda_2 \exp(-\lambda_3 \, |\nabla I(x)|) \, , \tag{1.6}$$

where $I(x) \in \mathcal{Z}$ is the given image and $\lambda_{1,2,3} > 0$.

When the cost functions $e^+(x)$ and $e^-(x)$ are given by the distance between x and the boundary of $\mathcal{C}^t$, the contour evolution given by (1.5), is equivalent to the well-known mean-curvature driven contour motion [105]. Moreover, the other typical contour evolutions applied in image processing can also be well described by (1.5) with different configurations of $e^+(x)$ and $e^-(x)$.

In particular, the optimization problem (1.5) can be equivalently formulated as a spatially continuous min-cut problem:

$$\min_{u(x) \in \{0,1\}} \; \left\langle 1 - u, D^1 \right\rangle + \left\langle u, D^2 \right\rangle + \int_\Omega g(x) \, |\nabla u| \; dx \, , \tag{1.7}$$

where $u(x) \in \{0,1\}$ is the indicator function of the contour $\mathcal{C}$, and the two label assignment functions $D^1(x)$ and $D^2(x)$ are given by

$$D^1(x) \; := \begin{cases} e^-(x) \, , & \text{where } x \in \mathcal{C}^t \\ 0 \, , & \text{otherwise} \end{cases} \tag{1.8}$$

$$D^2(x) \; := \begin{cases} e^+(x) \, , & \text{where } x \notin \mathcal{C}^t \\ 0 \, , & \text{otherwise} \end{cases} \, . \tag{1.9}$$

It is challenging to solve the combinatorial optimization problem (1.7), because it is non-linear and non-convex. However, it has be proven that using continuous max-flow theory [105], the combinatorial optimization problem (1.7) can be solved globally and exactly via convex relaxation such that

$$\min_{u(x)\in[0,1]} \left\langle 1-u, D^1 \right\rangle + \left\langle u, D^2 \right\rangle + \int_\Omega g(x)\,|\nabla u|\,dx\,, \tag{1.10}$$

where $u(x) \in \{0,1\}$ is now relaxed to $u(x) \in [0,1]$. According to the convex max-flow theory, thresholding the result of the convex relaxation of (1.10) provides the exact and global optimum of (1.5) [126].

An efficient continuous max-flow algorithm [124] can be employed to solve the continuous min-cut (1.7) globally and exactly, which implies that the new contour $\mathcal{C}^{t+1}$ at the next time step $t+1$ is globally optimal. In addition, the solution of (1.5) provides exactly a fully time-implicit scheme of the contour evolution, for which a large time evolution step-size is allowed to substantially speed up the evolution process [105]. The readers are referred to Yuan *et al.* [105] for more information on continuous max-flow algorithm.

1.9.4 Level sets and convex max-flow: a brief comparison

A brief qualitative comparison is provided for the level sets and convex max-flow-based methods in Table 1.1. Both level sets and convex max-flow methods are useful for image segmentation tasks. However, convex max-flow methods can usually yield higher computational speed than the level set methods, due to allowable large step-size and ability to fully parallelize the algorithm. In addition, the convex max-flow methods are easily extendable to multi-region segmentations than level sets-based methods. Therefore, with the advent of novel convex max-flow techniques [105] in our lab in 2011, convex max-flow based approaches were used for Chapter 4 and 5.

1.10 Segmentation evaluation

So far, we discussed our segmentation objectives and numerous segmentation methods available to be adapted to our segmentation problems. When a segmentation algorithm is developed, it needs to be properly validated. The performance of the proposed algorithms are evaluated in terms of accuracy, intra- and inter-observer vari-

Table 1.1: Comparison of level sets and convex max-flow methods

Level set methods
1. Have flexibility in integrating numerous energy functionals
2. Defined in a continuous setting, thus provides sub-voxel accuracy
3. Use a local optimization method
4. Widely used for medical image segmentation
5. Can be partially parallelized in a GPU
6. Explicit evolution of contours using PDEs, thus speed is limited by the time-step size
7. Require large number of iterations for convergence
8. Implementations of multi-region segmentations are challenging
Convex max-flow-based methods
1. Have flexibility in integrating numerous energy functionals
2. Defined in a continuous setting, thus provides sub-voxel accuracy
3. Use a global optimization method at each iteration, but cannot guarantee global optimum across iterations
4. Recently introduced to medical image segmentation
5. Can be fully parallelized in a GPU
6. Implicit evolution of contours. Thus large time-step size is allowed
7. Usually require fewer number of iterations for convergence
8. Easily extendable to multi-region segmentations

للاستشارات المنارة

abilities, and computational time. Interactions and expertise required from the user are other aspects of the algorithm.

Since the actual boundaries cannot be determined in patients, expert manual delineations of the medical images are often used as a surrogate for ground truth. Therefore, the validations of the proposed algorithms were carried out by evaluating the accuracy of the algorithm-generated contours in comparison to the expert-drawn contours.

1.10.1 Accuracy

We used volume\area-based, region-based, and boundary distance-based metrics to evaluate the accuracy of the algorithm. Volume-based metrics capture the aspect of the segmentation that is of greatest clinical interest: the VWV. Region- and boundary distance-based metrics evaluate the spatial fidelity of the segmentations to those generated manually by the user. Most of the metrics used in the following chapters are described below.

Let V_A^i be algorithm generated volume and V_M^i be the manual volume for either outer wall or lumen of a single 3D image i. We used volume error $\delta V_j^i = V_A^i - V_M^i$ and percentage volume error as

$$\delta V_j^i = \frac{(V_A^i - V_M^i)}{V_M^i} \times 100\% \quad j = VWV, LIB, MAB \tag{1.11}$$

for volume-based metrics. In addition, we also computed absolute volume error $|\delta V_j| = |V_A - V_M|$ and absolute volume error

$$|\delta V_j^i| = \frac{|V_A^i - V_M^i|}{V_M} \times 100\% \quad j = VWV, LIB, MAB \tag{1.12}$$

as a percentage. The mean volume error δV_j is

$$\delta V_j = \frac{\sum_{i=1}^{N_I} \delta V_j^i}{N_I} \quad j = VWV, LIB, MAB \tag{1.13}$$

where N_I is the number of images. The mean absolute volume difference $|\delta V_j|$ is the geometric mean of the absolute volume error for each image. Similar to volume-based metrics, area-based metrics can be computed for the date set.

We used the Dice similarity coefficient (DSC) [127], area overlap (AO), and area difference (AD) as region-based metrics. DSC is given by

$$DSC = \frac{2(R_M \cap R_A)}{R_M + R_A} \times 100\%, \tag{1.14}$$

where R_M and R_A denote the regions enclosed by the manual and algorithm-generated surfaces.

The AO and AD measures are given by

$$AO = \frac{(R_M \cap R_A)}{R_M \cup R_A} \times 100\%, \tag{1.15}$$

and

$$AD = \frac{|R_M - R_A|}{R_M} \times 100\%. \tag{1.16}$$

The mean absolute distance (MAD) error, root-mean squared error (RMSE), maximum absolute distance (MAXD) error are used as distance-based metrics. We denote the manual contour M as a set of vertices $\{m_i : i = 1, ..., K\}$, the algorithm-generated contour A as the vertice set $\{a_i : i = 1, ..., N\}$, and $d(m_i, A)$ as the distance between the vertex m_i of the contour M and its closest vertex on the contour A.

The MAD error, RMSE of distance, and MAXD error are given by

$$MAD = \frac{1}{K}\sum_{i=1}^{K} d(m_i, A), \tag{1.17}$$

$$RMSE = \sqrt{\frac{1}{K}\sum_{i=1}^{K} d(m_i, A)^2}, \tag{1.18}$$

and

$$MAXD = \max_{i\in[1,K]} \{d(m_i, A)\}, \tag{1.19}$$

respectively. Averages of DSC, RMSE, and MAXD were computed for the entire data set to obtain overall estimates of each metric.

1.10.2 Precision

We used the coefficient-of-variation (CV)

$$CV = \frac{SD}{V_{mean}} \times 100\% \tag{1.20}$$

to evaluate the intra- and/or inter-observer variability of the algorithm in computing the clinically relevant VWV and/or VWA. The intra-observer CVs were computed to evaluate the variability (relative to the mean) among repeated measurements of each of the user, whereas inter-observer CV was computed to evaluate the variability among users. The intra-class correlation coefficient (ICC) [128] was also used to evaluate the algorithms. ICC measures the reliability by computing the proportion of variance between observations. A single measure of absolute agreement using a two-way mixed study was used to compute ICC.

The minimum detectable difference (MDD) [129] provides an indication of the change in volume between two successive measurements that can be detected at a given confidence level [129]. We computed the MDD

$$MDD = Z_a\sqrt{2} \times SEM \tag{1.21}$$

for the algorithm segmentation in generating VWV, where Z_a is the standard normal deviate exceeded in either direction with probability α (i.e for $\alpha = 0.05$, $Z_a = 1.96$) and SEM is the standard error of the measurement.

1.11 Overview of dissertation

This dissertation consists of the papers that have been published in, or submitted to, peer-reviewed international journals. Chapters 2–5 of the dissertation explain the details of implementation, and validation of the various aspects of the research of developing segmentation algorithms for 3D images of arteries. The dissertation ends with chapter 6 containing a summary and discussion of the research work presented and future directions. The following is a description of each chapter.

Chapter 2: 2D segmentation of the carotid lumen and outer wall from 3DUS images using a modified SFLS method

The main purpose of this chapter was to develop and evaluate a semi-automated segmentation algorithm for delineating the MAB and LIB of the CCA from 3DUS images. At the beginning of my doctoral studies, I first attempted a 2D slice-by-slice segmentation algorithm for this problem. To segment the MAB and LIB, we used a SFLS method and combined several low-level image cues with high-level domain knowledge and limited user interaction. First, the operator initialized the algorithm by choosing anchor points on the boundaries, identified in the images. The MAB was segmented using local region- and edge-based energies and an energy that encourages the boundary to pass through the anchor points from the preprocessed images. For the LIB segmentation, we used local and global region-based energies, anchor point-based energy, as well as a constraint promoting a boundary separation between the MAB and LIB. The data set consisted of 231 2D images (11 2D images per each of 21 subjects) extracted from 3DUS images. The image slices were segmented five times each by an observer using the algorithm and manual method. Volume-based, region-based, and boundary distance-based metrics were used to evaluate accuracy and repeated measures analysis was used to evaluate precision. The algorithm yielded an absolute VWV difference of $5.0 \pm 4.3\%$ with a segmentation bias of $-0.9 \pm 6.6\%$. For the MAB and LIB segmentations, respectively, the method gave absolute volume differences of $2.5 \pm 1.8\%$ and $5.6 \pm 3.0\%$. DSCs (1.14) of $95.4 \pm 1.6\%$ and $93.1 \pm 3.1\%$, MAD errors of 0.1 ± 0.1 and 0.2 ± 0.1 mm, MAXD errors of 0.6 ± 0.3 and 0.7 ± 0.6 mm, respectively. The CVs of the algorithm (5.1%) and manual methods (3.9%) were not significantly different but the average time saved using the algorithm (2.8 vs. 8.3 min) was substantial.

Chapter 3: 3D segmentation of the carotid lumen and outer wall from 3DUS images using a modified SFLS method

One of the main limitations of the method presented in Chapter 3 is the need for user initializations on every slice. In this work, we describe a 3D algorithm based on a modified sparse field level set (SFLS) method for segmenting the MAB and LIB of the CCA from 3DUS images. To our knowledge, the proposed algorithm is the first direct 3D segmentation method, which has been validated for segmenting both the carotid

MAB and LIB from 3DUS images for the purpose of computing VWV. Initialization of the algorithm requires the observer to choose anchor points on each boundary on a set of transverse slices with a user-specified inter-slice distance (ISD), in which larger ISD requires fewer user interactions than smaller ISD. The main contribution of this work is the extension of the 2D segmentation algorithm into 3D. To address the challenges of the MAB and LIB segmentations from 3DUS images, we integrated regional- and boundary-based image statistics, expert initializations, and anatomically motivated boundary separation into the segmentation. The MAB is segmented by incorporating local region-based image information, image gradients, and the anchor points provided by the observer. Moreover, a local smoothness term is utilized to maintain the smooth surface of the MAB. The LIB is segmented by constraining its evolution using the already segmented surface of the MAB, in addition to the global region-based information and the anchor points. The algorithm-generated surfaces were sliced and evaluated with respect to manual segmentations on a slice-by-slice basis using 21 3DUS images. We used ISD of 1, 2, 3, 4, and 10 mm for algorithm initialization to generate segmentation results. The algorithm-generated accuracy and intra-observer variability results are comparable to the previous methods, but with fewer user interactions. For example, for the ISD of 3 mm, the algorithm yielded an average DSC of $94.4 \pm 2.2\%$ and $90.6 \pm 5.0\%$ for the MAB and LIB and the CV of 6.8% for computing the VWV of the CCA, while requiring only 1.72 min (vs. 8.3 min for manual segmentation) for a 3DUS image.

Chapter 4: 3D carotid multi-region MRI segmentation using globally optimal evolution of coupled surfaces

In this chapter, we describe a novel global optimization based 3D multi-region segmentation algorithm for T1-weighted black-blood carotid MR images. The proposed algorithm partitions a 3D carotid MR image into 3 regions: wall, lumen, and background. The algorithm performs such partitioning by simultaneously evolving two coupled 3D surfaces of carotid artery adventitia boundary (AB) and lumen-intima boundary (LIB) while preserving their anatomical inter-surface consistency such that the LIB is always located within the AB. In particular, we show that the proposed algorithm results in a fully time implicit scheme that propagates the two linearly ordered surfaces of the AB and LIB to their globally optimal positions during each discrete time frame by convex relaxation. In this regard, we introduce the continuous max-flow model and prove its duality/equivalence to the convex relaxed optimization problem with respect to each evolution step. We then propose a fully parallelized continuous max-flow-based algorithm, which can be readily implemented on a GPU to achieve high computational efficiency. Extensive experiments, with four users using 12 3T MR and 26 1.5T MR images, demonstrate that the proposed algorithm yields high accuracy (DSC $> 90\%$ for the carotid CCA and ICA) and small observer variability ((intra-observer CV $< 5.6\%$ and inter-observer CV $< 6.6\%$)) in computing VWV. In addition, we show the algorithm outperforms previous methods in terms of high computational efficiency and robustness with fewer user interactions.

Chapter 5: Joint segmentation of lumen and outer wall from 3D femoral artery MR images

In this chapter, we propose a novel algorithm to jointly segment the femoral artery lumen and outer wall surfaces from 3D black-blood MR images. Initially, the femoral artery lumen and outer wall are straightened by reorienting the femoral MR transverse slices using the medial axis of the femoral artery. The proposed segmentation algorithm enforces a spatial consistency prior between adjacent slices of the reoriented MR slices in a global optimization manner. We demonstrate that the reduced challenging combinatorial optimization problem can be solved globally and exactly by means of convex relaxation. For this task, we introduce a novel *coupled continuous max-flow (CCMF) model* based on an Ishikawa-type flow configuration and show its duality to the studied convex relaxed optimization problem. Using the proposed *CCMF model*, the exactness and globalness of its dual convex relaxation problem is proven. Moreover, the *CCMF model* is implemented in a GPU to achieve high computational speed. Experiments were conducted using 355 2D slices extracted from 10 3D black-blood MR images of seven subjects. The proposed method yielded high accuracy (i.e., DSC greater than 85%) for both the lumen and outer wall and high reproducibility (ICC of 0.95) for generating vessel wall area. The proposed method also outperformed the previous method in terms of reproducibility and computation time by a factor of ~ 20.

Chapter 6: Conclusions and future directions

This chapter summarizes the results and conclusions from the research presented in the proceeding chapters. It also provides directions for future work.

References

[1] A. J. Lusis, “Atherosclerosis,” *Nature*, vol. 407, no. 6801, pp. 233–241, 2000. 1

[2] V. Roger, A. Go, D. Lloyd-Jones, R. Adams, J. Berry, T. Brown, M. Carnethon, S. Dai, G. de Simone, E. Ford *et al.*, “Heart disease and stroke statistics 2011 update1,” *Circulation*, vol. 123, no. 4, pp. e18–209, 2011. 1, 2, 4

[3] A. Semb, T. Kvien, A. Aastveit, I. Jungner, T. Pedersen, G. Walldius, and I. Holme, “Lipids, myocardial infarction and ischaemic stroke in patients with rheumatoid arthritis in the apolipoprotein-related mortality RISk (AMORIS) study,” *Annals of the rheumatic diseases*, vol. 69, no. 11, pp. 1996–2001, 2010. 1

[4] H. C. Stary, A. B. Chandler, S. Glagov, J. R. Guyton, W. Insull, M. E. Rosenfeld, S. A. Schaffer, C. J. Schwartz, W. D. Wagner, and R. W. Wissler, “A definition of initial, fatty streak, and intermediate lesions of atherosclerosis. a report from the committee on vascular lesions of the council on arteriosclerosis, american heart association.” *Arteriosclerosis, Thrombosis, and Vascular Biology*, vol. 14, no. 5, pp. 840–856, 1994. 1

[5] H. Stary, A. Chandler, R. Dinsmore, V. Fuster, S. Glagov, W. Insull, M. Rosenfeld, C. Schwartz, W. Wagner, and R. Wissler, “A definition of advanced types of atherosclerotic lesions and a histological classification of atherosclerosis a report from the committee on vascular lesions of the council on arteriosclerosis, american heart association,” *Arteriosclerosis, thrombosis, and vascular biology*, vol. 15, no. 9, pp. 1512–1531, 1995. 1

[6] F. Epstein and R. Ross, “Atherosclerosisan inflammatory disease,” *New England journal of medicine*, vol. 340, no. 2, pp. 115–126, 1999. 1, 2

[7] M. R. Ward, G. Pasterkamp, A. C. Yeung, and C. Borst, “Arterial remodeling: mechanisms and clinical implications,” *Circulation*, vol. 102, no. 10, pp. 1186–1191, 2000. 1

[8] V. Roger, A. Go, D. Lloyd-Jones, E. Benjamin, J. Berry, W. Borden, D. Bravata, S. Dai, E. Ford, C. Fox *et al.*, “Heart disease and stroke statistics2012

update a report from the american heart association," *Circulation*, vol. 125, no. 1, pp. e2–e220, 2012. 1, 4

[9] A. D. Lopez, C. D. Mathers, M. Ezzati, D. T. Jamison, and C. J. Murray, "Global and regional burden of disease and risk factors, 2001: systematic analysis of population health data," *The Lancet*, vol. 367, no. 9524, pp. 1747–1757, May 2006. 2, 4

[10] J. Golledge, R. Greenhalgh, and A. Davies, "The symptomatic carotid plaque," *Stroke*, vol. 31, no. 3, pp. 774–781, 2000. 2, 4

[11] P. Sobieszczyk and J. Beckman, "Carotid artery disease," *Circulation*, vol. 114, no. 7, pp. e244–e247, 2006. 4, 7

[12] D. Lloyd-Jones, R. Adams, T. Brown, M. Carnethon, S. Dai, G. De Simone, T. Ferguson, E. Ford, K. Furie, C. Gillespie *et al.*, "Executive summary: heart disease and stroke statistics–2010 update: a report from the american heart association." *Circulation*, vol. 121, no. 7, p. 948, 2010. 4

[13] R. B. DAgostino, R. S. Vasan, M. J. Pencina, P. A. Wolf, M. Cobain, J. M. Massaro, and W. B. Kannel, "General cardiovascular risk profile for use in primary care the framingham heart study," *Circulation*, vol. 117, no. 6, pp. 743–753, 2008. 4

[14] P. M. Ridker, N. Rifai, L. Rose, J. E. Buring, and N. R. Cook, "Comparison of c-reactive protein and low-density lipoprotein cholesterol levels in the prediction of first cardiovascular events," *New England Journal of Medicine*, vol. 347, no. 20, pp. 1557–1565, 2002. 4

[15] E. B. Diethrich, M. P. Margolis, D. B. Reid, A. Burke, V. Ramaiah, J. A. Rodriguez-Lopez, G. Wheatley, D. Olsen, and R. Virmani, "Virtual histology intravascular ultrasound assessment of carotid artery disease: the carotid artery plaque virtual histology evaluation (capital) study," 2009. 4, 6

[16] M. Naghavi, P. Libby, E. Falk, S. W. Casscells, S. Litovsky, J. Rumberger, J. J. Badimon, C. Stefanadis, P. Moreno, G. Pasterkamp *et al.*, "From vulnerable plaque to vulnerable patient a call for new definitions and risk assessment strategies: part i," *Circulation*, vol. 108, no. 14, pp. 1664–1672, 2003. 4

[17] T. Saam, T. S. Hatsukami, N. Takaya, B. Chu, H. Underhill, W. S. Kerwin, J. Cai, M. S. Ferguson, and C. Yuan, "The vulnerable, or high-risk, atherosclerotic plaque: Noninvasive mr imaging for characterization and assessment1," *Radiology*, vol. 244, no. 1, pp. 64–77, 2007. 4

[18] P. B. Gorelick, “Stroke prevention. an opportunity for efficient utilization of health care resources during the coming decade.” *Stroke*, vol. 25, no. 1, pp. 220–224, 1994. 4

[19] A. Landry, J. D. Spence, and A. Fenster, “Measurement of carotid plaque volume by 3-Dimensional ultrasound,” *Stroke*, vol. 35, no. 4, pp. 864–869, Apr. 2004. 4, 7, 14

[20] E. Ukwatta, J. Awad, A. D. Ward, D. Buchanan, J. Samarabandu, G. Parraga, and A. Fenster, “Three-dimensional ultrasound of carotid atherosclerosis: Semiautomated segmentation using a level set-based method,” *Medical Physics*, vol. 38, p. 2479, 2011. 4

[21] J. Spence and T. Rundek, “Toward clinical applications of carotid ultrasound: Intima-Media thickness, plaque area, and Three-Dimensional phenotypes,” *Ultrasound and Carotid Bifurcation Atherosclerosis*, pp. 431–448, 2012. 5

[22] J. D. Spence and D. G. Hackam, “Treating arteries instead of risk factors a paradigm change in management of atherosclerosis,” *Stroke*, vol. 41, no. 6, pp. 1193–1199, 2010. 5

[23] I. Shai, J. D. Spence, D. Schwarzfuchs, Y. Henkin, G. Parraga, A. Rudich, A. Fenster, C. Mallett, N. Liel-Cohen, A. Tirosh *et al.*, “Dietary intervention to reverse carotid atherosclerosis,” *Circulation*, vol. 121, no. 10, p. 1200, 2010. 5, 7, 16

[24] E. Bartlett, T. Walters, S. Symons, and A. Fox, “Quantification of carotid stenosis on ct angiography,” *American journal of neuroradiology*, vol. 27, no. 1, pp. 13–19, 2006. 5

[25] M. J. Koelemay, P. J. Nederkoorn, J. B. Reitsma, and C. B. Majoie, “Systematic review of computed tomographic angiography for assessment of carotid artery disease,” *Stroke*, vol. 35, no. 10, pp. 2306–2312, 2004. 5

[26] K. Nandalur, E. Baskurt, K. Hagspiel, M. Finch, C. Phillips, S. Bollampally, and C. Kramer, “Carotid artery calcification on ct may independently predict stroke risk,” *American Journal of Roentgenology*, vol. 186, no. 2, pp. 547–552, 2006. 5

[27] M. Wintermark, S. Jawadi, J. Rapp, T. Tihan, E. Tong, D. Glidden, S. Abedin, S. Schaeffer, G. Acevedo-Bolton, B. Boudignon *et al.*, “High-resolution ct imaging of carotid artery atherosclerotic plaques,” *American Journal of Neuroradiology*, vol. 29, no. 5, pp. 875–882, 2008. 5

[28] M. W. Lorenz, H. S. Markus, M. L. Bots, M. Rosvall, and M. Sitzer, “Prediction of clinical cardiovascular events with carotid intima-media thickness: a

systematic review and meta-analysis," *Circulation*, vol. 115, no. 4, p. 459, 2007. 6, 13

[29] M. Bots, A. Hoes, P. Koudstaal, A. Hofman, and D. Grobbee, "Common carotid intima-media thickness and risk of stroke and myocardial infarction: the rotterdam study," *Circulation*, vol. 96, no. 5, pp. 1432–1437, 1997. 6

[30] D. H. O'Leary, J. F. Polak, R. A. Kronmal, T. A. Manolio, G. L. Burke, and S. K. Wolfson Jr, "Carotid-artery intima and media thickness as a risk factor for myocardial infarction and stroke in older adults," *New England Journal of Medicine*, vol. 340, no. 1, pp. 14–22, 1999. 6, 12

[31] D. Baldassarre, M. Amato, A. Bondioli, C. R. Sirtori, and E. Tremoli, "Carotid artery intima-media thickness measured by ultrasonography in normal clinical practice correlates well with atherosclerosis risk factors," *Stroke; a Journal of Cerebral Circulation*, vol. 31, no. 10, pp. 2426–2430, Oct. 2000, PMID: 11022075. 6

[32] A. Fenster, D. Downey, and H. Cardinal, "Three-dimensional ultrasound imaging," *Physics in medicine and biology*, vol. 46, no. 5, p. R67, 2001. 6, 7, 8, 9

[33] D. B. Reid, E. B. Diethrich, P. Marx, and R. Wrasper, "Intravascular ultrasound assessment in carotid interventions," *Journal Information*, vol. 3, no. 2, 1996. 6

[34] C. V. Bourantas, K. K. Naka, S. Garg, S. Thackray, D. Papadopoulos, F. M. Alamgir, A. Hoye, and L. K. Michalis, "Clinical indications for intravascular ultrasound imaging," *Echocardiography*, vol. 27, no. 10, pp. 1282–1290, 2010. 6

[35] D. J. Clark, S. Lessio, M. O'Donoghue, R. Schainfeld, and K. Rosenfield, "Safety and utility of intravascular ultrasound-guided carotid artery stenting," *Catheterization and cardiovascular interventions*, vol. 63, no. 3, pp. 355–362, 2004. 6

[36] M. Robbin, M. Lockhart, T. Weber, J. Vitek, J. Smith, J. Yadav, A. Mathur, S. Iyer, and G. Roubin, "Carotid artery stents: early and intermediate follow-up with doppler us." *Radiology*, vol. 205, no. 3, pp. 749–756, 1997. 7

[37] M. Egger, J. D. Spence, A. Fenster, and G. Parraga, "Validation of 3D ultrasound vessel wall volume: an imaging phenotype of carotid atherosclerosis," *Ultrasound in medicine & biology*, vol. 33, no. 6, pp. 905–914, 2007. 7, 16

[38] P. S. Sidhu, "Ultrasound of the carotid and vertebral arteries," *British medical bulletin*, vol. 56, no. 2, pp. 346–366, 2000. 7

[39] E. G. Grant, C. B. Benson, G. L. Moneta, A. V. Alexandrov, J. D. Baker, E. I. Bluth, B. A. Carroll, M. Eliasziw, J. Gocke, B. S. Hertzberg *et al.*, "Carotid artery stenosis: Gray-scale and doppler us diagnosissociety of radiologists in ultrasound consensus conference1," *Radiology*, vol. 229, no. 2, pp. 340–346, 2003. 7

[40] E. Ukwatta, D. Buchanan, G. Parraga, and A. Fenster, "Three-dimensional ultrasound imaging of carotid atherosclerosis," in *Intelligent Computation and Bio-Medical Instrumentation (ICBMI), 2011 International Conference on.* IEEE, 2011, pp. 81–84. 7

[41] C. D. Ainsworth, C. C. Blake, A. Tamayo, V. Beletsky, A. Fenster, and J. D. Spence, "3D ultrasound measurement of change in carotid plaque volume: A tool for rapid evaluation of new therapies," *Stroke*, vol. 36, no. 9, pp. 1904–1909, Sep. 2005. 7, 9, 14

[42] D. N. Buchanan, T. Lindenmaier, S. McKay, Y. Bureau, D. G. Hackam, A. Fenster, and G. Parraga, "The relationship of carotid three-dimensional ultrasound vessel wall volume with age and sex: comparison to carotid intima-media thickness," *Ultrasound in medicine & biology*, 2012. 7, 14

[43] T. Nelson, D. Pretorius, A. Hull, M. Riccabona, M. Sklansky, and G. James, "Sources and impact of artifacts on clinical three-dimensional ultrasound imaging," *Ultrasound in obstetrics & gynecology*, vol. 16, no. 4, pp. 374–383, 2000. 7

[44] O. Oralkan, A. S. Ergun, C.-H. Cheng, J. A. Johnson, M. Karaman, T. H. Lee, and B. T. Khuri-Yakub, "Volumetric ultrasound imaging using 2-d cmut arrays," *Ultrasonics, Ferroelectrics and Frequency Control, IEEE Transactions on*, vol. 50, no. 11, pp. 1581–1594, 2003. 8

[45] A. Fenster, C. Blake, I. Gyacskov, A. Landry, and J. Spence, "3D ultrasound analysis of carotid plaque volume and surface morphology," *Ultrasonics*, vol. 44, no. Supplement 1, pp. e153–e157, Dec. 2006. 8, 14

[46] A. Fenster and D. B. Downey, "Three-dimensional ultrasound imaging," *Annual Review of Biomedical Engineering*, vol. 2, no. 1, pp. 457–475, Aug. 2000. 9

[47] C. Yuan, W. S. Kerwin, V. L. Yarnykh, J. Cai, T. Saam, B. Chu, N. Takaya, M. S. Ferguson, H. Underhill, D. Xu, F. Liu, and T. S. Hatsukami, "MRI of atherosclerosis in clinical trials," *NMR in Biomedicine*, vol. 19, no. 6, pp. 636–654, 2006. 9, 11, 13

[48] C. Yuan, M. Oikawa, Z. Miller, and T. Hatsukami, "MRI of carotid atherosclerosis," *J Nucl. Cardiol.*, vol. 15, no. 2, pp. 266–275, 2008. 9, 11

[49] A. Krasinski, B. Chiu, A. Fenster, and G. Parraga, "Magnetic resonance imaging and three-dimensional ultrasound of carotid atherosclerosis: Mapping regional differences," *J. Magn. Reson. Im.*, vol. 29, no. 4, pp. 901–908, 2009. 11, 13, 16

[50] H. Underhill and C. Yuan, "Carotid MRI: a tool for monitoring individual response to cardiovascular therapy?" *Expert Review of Cardiovascular Therapy*, vol. 9, no. 1, pp. 63–80, 2011. 11, 13

[51] W. S. Kerwin, K. D. O'Brien, M. S. Ferguson, N. Polissar, T. S. Hatsukami, and C. Yuan, "Inflammation in carotid atherosclerotic plaque: A dynamic contrast-enhanced MR imaging study1," *Radiology*, vol. 241, no. 2, p. 459, 2006. 11

[52] H. R. Underhill, T. S. Hatsukami, Z. A. Fayad, V. Fuster, and C. Yuan, "MRI of carotid atherosclerosis: clinical implications and future directions," *Nature Reviews Cardiology*, vol. 7, no. 3, pp. 165–173, 2010. 11

[53] M. L. Bots and D. E. Grobbee, "Intima media thickness as a surrogate marker for generalised atherosclerosis," *Cardiovascular drugs and therapy*, vol. 16, no. 4, pp. 341–351, 2002. 12

[54] M. L. Bots, G. W. Evans, W. A. Riley, and D. E. Grobbee, "Carotid intima-media thickness measurements in intervention studies design options, progression rates, and sample size considerations: a point of view," *Stroke*, vol. 34, no. 12, pp. 2985–2994, 2003. 12

[55] J. D. Spence, M. Eliasziw, M. DiCicco, D. G. Hackam, R. Galil, and T. Lohmann, "Carotid plaque area a tool for targeting and evaluating vascular preventive therapy," *Stroke*, vol. 33, no. 12, pp. 2916–2922, 2002. 12, 14

[56] D. Pretorius, T. Nelson, and J. Jaffe, "3-dimensional sonographic analysis based on color flow doppler and gray scale image data: a preliminary report." *Journal of ultrasound in medicine*, vol. 11, no. 5, pp. 225–232, 1992. 12

[57] S. H. Johnsen and E. B. Mathiesen, "Carotid plaque compared with intima-media thickness as a predictor of coronary and cerebrovascular disease," *Current cardiology reports*, vol. 11, no. 1, pp. 21–27, 2009. 12

[58] A. Landry, C. Ainsworth, C. Blake, J. D. Spence, and A. Fenster, "Manual planimetric measurement of carotid plaque volume using three-dimensional ultrasound imaging," *Medical Physics*, vol. 34, no. 4, pp. 1496–1505, Apr. 2007. 12, 14

[59] A. Krasinski, B. Chiu, J. D. Spence, A. Fenster, and G. Parraga, "Three-dimensional ultrasound quantification of intensive statin treatment of carotid

atherosclerosis," *Ultrasound in medicine & biology*, vol. 35, no. 11, pp. 1763–1772, 2009. 12, 16, 17

[60] B. Chiu, V. Beletsky, J. D. Spence, G. Parraga, and A. Fenster, "Analysis of carotid lumen surface morphology using three-dimensional ultrasound imaging," *Physics in Medicine and Biology*, vol. 54, p. 1149, 2009. 12

[61] B. Chiu, M. Egger, D. J. Spence, G. Parraga, and A. Fenster, "Area-preserving flattening maps of 3D ultrasound carotid arteries images," *Med. Image Anal.*, vol. 12, no. 6, pp. 676–688, 2008. 12, 17

[62] J. Spence and R. Hegele, "Non-invasive assessment of atherosclerosis risk," *Current Drug Targets-Cardiovascular & Hematological Disorders*, vol. 4, no. 2, pp. 125–128, 2004. 12

[63] G. Ferguson, M. Eliasziw, H. Barr, G. Clagett, R. Barnes, M. Wallace, D. Taylor, R. Haynes, J. Finan, V. Hachinski *et al.*, "The north american symptomatic carotid endarterectomy trial: surgical results in 1415 patients," *Stroke*, vol. 30, no. 9, pp. 1751–1758, 1999. 12

[64] H. Barnett, "Stroke prevention by surgery for symptomatic disease in carotid territory." *Neurologic clinics*, vol. 10, no. 1, p. 281, 1992. 13

[65] C. Warlow, "Mrc european carotid surgery trial: interim results for symptomatic patients with severe (70-99%) or with mild (0-29%) carotid stenosis," *The Lancet*, vol. 337, no. 8752, pp. 1235–1243, 1991. 13

[66] K. Al-Shali, A. A. House, A. J. Hanley, H. M. Khan, S. B. Harris, M. Mamakeesick, B. Zinman, A. Fenster, J. D. Spence, and R. A. Hegele, "Differences between carotid wall morphological phenotypes measured by ultrasound in one, two and three dimensions," *Atherosclerosis*, vol. 178, no. 2, pp. 319–325, 2005. 13, 14

[67] D. H. O'Leary and M. L. Bots, "Imaging of atherosclerosis: carotid intima–media thickness," *European heart journal*, vol. 31, no. 14, p. 1682, 2010. 13

[68] Y. Inaba, J. A. Chen, and S. R. Bergmann, "Carotid plaque, compared with carotid intima-media thickness, more accurately predicts coronary artery disease events: A meta-analysis," *Atherosclerosis*, 2011. 13

[69] E. Fosse, S. H. Johnsen, E. Stensland-Bugge, O. Joakimsen, E. B. Mathiesen, E. Arnesen, and I. Njølstad, "Repeated visual and computer-assisted carotid plaque characterization in a longitudinal population-based ultrasound study: the tromsø study," *Ultrasound in medicine & biology*, vol. 32, no. 1, pp. 3–11, 2006. 13

[70] S. H. Johnsen and E. B. Mathiesen, "Carotid plaque compared with intima-media thickness as a predictor of coronary and cerebrovascular disease," *Current cardiology reports*, vol. 11, no. 1, pp. 21–27, 2009. 13

[71] J. D. Spence, "Ultrasound measurement of carotid plaque as a surrogate outcome for coronary artery disease," *The American journal of cardiology*, vol. 89, no. 4, pp. 10–15, 2002. 13

[72] C. Mallett, A. A. House, J. D. Spence, A. Fenster, and G. Parraga, "Longitudinal ultrasound evaluation of carotid atherosclerosis in one, two and three dimensions." *Ultrasound in medicine & biology*, vol. 35, no. 3, p. 367, 2009. 13

[73] P. A. Barnett, J. D. Spence, S. B. Manuck, and J. R. Jennings, "Psychological stress and the progression of carotid artery disease," *Journal of hypertension*, vol. 15, no. 1, pp. 49–55, 1997. 14

[74] J. D. Spence, P. A. Barnett, D. E. Bulman, and R. A. Hegele, "An approach to ascertain probands with a non-traditional risk factor for carotid atherosclerosis," *Atherosclerosis*, vol. 144, no. 2, pp. 429–434, 1999. 14

[75] J. D. Spence, M. R. Malinow, P. A. Barnett, A. J. Marian, D. Freeman, and R. A. Hegele, "Plasma homocyst (e) ine concentration, but not mthfr genotype, is associated with variation in carotid plaque area," *Stroke*, vol. 30, no. 5, pp. 969–973, 1999. 14

[76] R. A. Hegele, M. R. Ban, C. M. Anderson, and J. D. Spence, "Infection-susceptibility alleles of mannose-binding lectin are associated with increased carotid plaque area," *Journal of Investigative Medicine*, vol. 48, no. 3, pp. 198–202, 2000. 14

[77] S. H. Johnsen, E. B. Mathiesen, O. Joakimsen, E. Stensland, T. Wilsgaard, M. Lchen, I. Njlstad, and E. Arnesen, "Carotid atherosclerosis is a stronger predictor of myocardial infarction in women than in men," *Stroke*, vol. 38, no. 11, pp. 2873–2880, Nov. 2007. 14

[78] E. B. Mathiesen, S. H. Johnsen, T. Wilsgaard, K. H. Bnaa, M. Lchen, and I. Njlstad, "Carotid plaque area and Intima-Media thickness in prediction of First-Ever ischemic stroke," *Stroke*, vol. 42, no. 4, pp. 972 –978, Apr. 2011. 14

[79] A. Landry, J. D. Spence, and A. Fenster, "Quantification of carotid plaque volume measurements using 3D ultrasound imaging," *Ultrasound in Medicine & Biology*, vol. 31, no. 6, pp. 751–762, Jun. 2005. 14

[80] T. Wannarong, G. Parraga, D. Buchanan, A. Fenster, A. A. House, D. G. Hackam, and J. D. Spence, "Progression of carotid plaque volume predicts cardiovascular events," *Stroke*, 2013. 14

[81] B. Chiu, M. Egger, J. D. Spence, G. Parraga, and A. Fenster, "Quantification of carotid vessel wall and plaque thickness change using 3D ultrasound images," *Medical physics*, vol. 35, p. 3691, 2008. 17

[82] N. Shammas, "Epidemiology, classification, and modifiable risk factors of peripheral arterial disease," *Vascular health and risk management*, vol. 3, no. 2, p. 229, 2007. 17

[83] B. Carabello, "Contemporary reviews in cardiovascular medicine," *Circulation*, vol. 112, pp. 432–437, 2005. 18

[84] J. Chi, B. Chiu, Y. Cao, X. Liu, J. Wang, N. Balu, C. Yuan, and J. Xu, "Assessment of femoral artery atherosclerosis at the adductor canal using 3d black-blood mri," *Clinical radiology*, 2013. 18, 20

[85] M. M. McDermott, K. Liu, M. H. Criqui, K. Ruth, D. Goff, M. F. Saad, C. Wu, S. Homma, and A. R. Sharrett, "Ankle-brachial index and subclinical cardiac and carotid disease the multi-ethnic study of atherosclerosis," *American journal of epidemiology*, vol. 162, no. 1, pp. 33–41, 2005. 18, 19

[86] A. B. I. Collaboration, F. Fowkes, G. Murray, I. Butcher, C. Heald, R. Lee, L. Chambless, A. Folsom, A. Hirsch, M. Dramaix *et al.*, "Ankle brachial index combined with framingham risk score to predict cardiovascular events and mortality," *JAMA: the journal of the American Medical Association*, vol. 300, no. 2, pp. 197–208, 2008. 18, 19, 20

[87] F. A. Arain and L. T. Cooper Jr, "Peripheral arterial disease: diagnosis and management," in *Mayo Clinic Proceedings*, vol. 83, no. 8. Elsevier, 2008, pp. 944–950. 19

[88] D. Isbell, C. Meyer, W. Rogers, F. Epstein, J. DiMaria, N. Harthun, H. Wang, and C. Kramer, "Reproducibility and reliability of atherosclerotic plaque volume measurements in peripheral arterial disease with cardiovascular magnetic resonance," *Journal of Cardiovascular Magnetic Resonance*, vol. 9, no. 1, pp. 71–76, 2007. 19, 20

[89] A. W. Pollak and C. M. Kramer, "Mri in lower extremity peripheral arterial disease: Recent advancements," *Current cardiovascular imaging reports*, vol. 6, no. 1, pp. 55–60, 2013. 20

[90] N. Balu, J. Wang, X. Zhao, T. Hatsukami, and C. Yuan, "Targeted multi-contrast vessel wall imaging of bilateral peripheral artery disease," in *Proc. Intl. Soc. Mag. Reson. Med*, vol. 18, 2010, p. 3685. 20

[91] N. Balu, V. L. Yarnykh, B. Chu, J. Wang, T. Hatsukami, and C. Yuan, "Carotid plaque assessment using fast 3d isotropic resolution black-blood mri," *Magnetic Resonance in Medicine*, vol. 65, no. 3, pp. 627–637, 2011. 20

[92] N. Bianda, M. Di Valentino, D. Périat, J. M. Segatto, M. Oberson, M. Moccetti, I. Sudano, P. Santini, C. Limoni, A. Froio *et al.*, "Progression of human carotid and femoral atherosclerosis: a prospective follow-up study by magnetic resonance vessel wall imaging," *European heart journal*, vol. 33, no. 2, pp. 230–237, 2012. 20

[93] R. Szeliski, *Computer vision: algorithms and applications.* Springer, 2010. 24

[94] R. Adams and L. Bischof, "Seeded region growing," *Pattern Analysis and Machine Intelligence, IEEE Transactions on*, vol. 16, no. 6, pp. 641–647, 1994. 25

[95] T. Pavlidis and Y.-T. Liow, "Integrating region growing and edge detection," *Pattern Analysis and Machine Intelligence, IEEE Transactions on*, vol. 12, no. 3, pp. 225–233, 1990. 25

[96] L. Rokach and O. Maimon, "Clustering methods," in *Data mining and knowledge discovery handbook.* Springer, 2005, pp. 321–352. 25

[97] R. M. Gray and D. L. Neuhoff, "Quantization," *Information Theory, IEEE Transactions on*, vol. 44, no. 6, pp. 2325–2383, 1998. 25

[98] D. Comaniciu and P. Meer, "Mean shift: A robust approach toward feature space analysis," *Pattern Analysis and Machine Intelligence, IEEE Transactions on*, vol. 24, no. 5, pp. 603–619, 2002. 25

[99] T. F. Chan and L. A. Vese, "Active contours without edges," *Image Processing, IEEE Transactions on*, vol. 10, no. 2, pp. 266–277, 2001. 26, 29

[100] Y. Boykov, O. Veksler, and R. Zabih, "Fast approximate energy minimization via graph cuts," *IEEE Transactions on Pattern Analysis and Machine Intelligence*, vol. 23, p. 2001, 2001. 26

[101] M. Kass, A. P. Witkin, and D. Terzopoulos, "Snakes: Active contour models," *IJCV*, vol. 1, no. 4, pp. 321–331, 1988. 26, 29

[102] S. Osher and J. A. Sethian, "Fronts propagating with curvature dependent speed: algorithms based on Hamilton-Jacobi formulations," 1988. 27

[103] V. Caselles, R. Kimmel, and G. Sapiro, "Geodesic active contours," *International Journal of Computer Vision*, vol. 22, no. 1, pp. 61–79, Feb. 1997. 27

[104] R. Malladi, J. A. Sethian, and B. C. Vemuri, “Shape modeling with front propagation: A level set approach,” *IEEE transactions on Pattern Analysis and machine intelligence*, vol. 17, pp. 158—175, 1995. 27

[105] J. Yuan, E. Ukwatta, X.-C. Tai, A. Fenster, and C. Schnoerr, “A fast global optimization-based approach to evolving contours with generic shape prior,” UCLA, Technical report CAM-12-38, 2012. 27, 28, 30, 31, 32

[106] Y. Boykov and G. Funka-Lea, “Graph cuts and efficient nd image segmentation,” *International Journal of Computer Vision*, vol. 70, no. 2, pp. 109–131, 2006. 27

[107] N. Paragios, Y. Chen, and O. D. Faugeras, *Handbook of mathematical models in computer vision.* Springer Publishing Company, Incorporated, 2010. 27

[108] T. Pock, A. Chambolle, D. Cremers, and H. Bischof, “A convex relaxation approach for computing minimal partitions,” in *Computer Vision and Pattern Recognition, 2009. CVPR 2009. IEEE Conference on.* IEEE, 2009, pp. 810–817. 27

[109] V. Kolmogorov and Y. Boykov, “What metrics can be approximated by geo-cuts, or global optimization of length/area and flux,” in *Computer Vision, 2005. ICCV 2005. Tenth IEEE International Conference on*, vol. 1. IEEE, 2005, pp. 564–571. 27

[110] K. Punithakumar, J. Yuan, I. B. Ayed, S. Li, and Y. Boykov, “A convex max-flow approach to distribution-based figure-ground separation,” *SIAM Journal on Imaging Sciences*, vol. 5, no. 4, pp. 1333–1354, 2012. 27, 28

[111] M. Klodt, T. Schoenemann, K. Kolev, M. Schikora, and D. Cremers, “An experimental comparison of discrete and continuous shape optimization methods,” in *Computer Vision–ECCV 2008.* Springer, 2008, pp. 332–345. 28

[112] J. Yuan, E. Bae, X.-C. Tai, and Y. Boykov, “A continuous max-flow approach to potts model,” in *Computer Vision–ECCV 2010.* Springer, 2010, pp. 379–392. 28

[113] E. Bae, J. Yuan, X. Tai, and Y. Boykov, “A study on continuous max-flow and min-cut approaches part ii: Multiple linearly ordered labels,” *UCLA CAM Report*, pp. 10–62, 2010. 28

[114] Y. Boykov, V. Kolmogorov, D. Cremers, and A. Delong, “An integral solution to surface evolution pdes via geo-cuts,” in *ECCV*, 2006, pp. 409–422. 28, 30

[115] Y. Boykov and V. Kolmogorov, “An experimental comparison of min-cut/max-flow algorithms for energy minimization in vision,” *IEEE Transactions on Pattern Analysis and Machine Intelligence*, vol. 26, pp. 359–374, 2001. 28

[116] V. Kolmogorov and R. Zabih, "What energy functions can be minimized via graph cuts," *IEEE Transactions on Pattern Analysis and Machine Intelligence*, vol. 26, pp. 65–81, 2004. 28

[117] A. Mitiche and I. B. Ayed, *Variational and level set methods in image segmentation*. Springer, 2010, vol. 5. 29

[118] R. T. Whitaker, "A Level-Set approach to 3D reconstruction from range data," *Int. J. Comput. Vision*, vol. 29, no. 3, pp. 203–231, 1998. 29

[119] S. Lankton, "Sparse field methods," Technical Report, Georgia Tech (July 2009), Tech. Rep., 2009. 29

[120] V. Caselles, R. Kimmel, and G. Sapiro, "Geodesic active contours," *IJCV*, vol. 22, no. 1, 1997. 29

[121] O. Michailovich, Y. Rathi, and A. Tannenbaum, "Image segmentation using active contours driven by the bhattacharyya gradient flow," *IEEE T. Image. Process.*, vol. 16, no. 11, pp. 2787–2801, 2007. 29

[122] S. Osher and R. Fedkiw, *Level set methods and dynamic implicit surfaces*, ser. Applied Mathematical Sciences. New York: Springer-Verlag, 2003, vol. 153. 30

[123] A. Chambolle, "An algorithm for mean curvature motion," *Interf. Free Bound.*, vol. 6, pp. 195–218, 2004. 30

[124] J. Yuan, E. Bae, and X. Tai, "A study on continuous max-flow and min-cut approaches," in *CVPR 2010*. 30, 32

[125] E. Ukwatta, J. Yuan, W. Qiu, M. Rajchl, and A. Fenster, "Efficient convex optimization-based curvature dependent contour evolution approach for medical image segmentation," in *SPIE Medical Imaging*. International Society for Optics and Photonics, 2013, pp. 866 902–866 902. 30

[126] T. F. Chan, S. Esedoglu, and M. Nikolova, "Algorithms for finding global minimizers of image segmentation and denoising models," *SIAM Journal on Applied Mathematics*, vol. 66, no. 5, pp. 1632–1648, 2006. 32

[127] K. Zou, S. Warfield, A. Bharatha, C. Tempany, M. Kaus, S. Haker, W. Wells, F. Jolesz, and R. Kikinis, "Statistical validation of image segmentation quality based on a spatial overlap index," *Academic Radiology*, vol. 11, no. 2, pp. 178–189, 2004. 35

[128] K. McGraw and S. Wong, "Forming inferences about some intraclass correlation coefficients." *Psychological methods*, vol. 1, no. 1, p. 30, 1996. 36

[129] J. R. Mitchell, S. J. Karlik, D. H. Lee, M. Eliasziw, G. P. Rice, and A. Fenster, "The variability of manual and computer assisted quantification of multiple sclerosis lesion volumes," *Medical Physics*, vol. 23, no. 1, pp. 85–97, 1996. 36

Chapter 2
3DUS of carotid atherosclerosis: Semi-automated segmentation using a level set-based method†

2.1 Introduction

3DUS of the carotid artery provides measurements of VWV that are complementary to one-dimensional measurements of the carotid artery as discussed in Section 1.4.5 of Chapter 1. One of the main issues in computing VWV is the requirement for time-consuming delineation of the carotid media-adventitia boundary (MAB) and lumen-intima boundary (LIB) in three-dimensions. Therefore, development and validation of an accurate and robust segmentation method to delineate the carotid MAB and LIB are required to alleviate the measurement burden from the user. In this chapter, we describe and evaluate a new semi-automated segmentation tool based on the level set method to delineate the MAB and LIB of the carotid arteries on a sequence of 2D US images (see Fig. 2.1 and 1.10(b) in Chapter 1) extracted from 3DUS images.

2.1.1 Previous work

Several investigations have been reported that rely on an expert observer to manually outline the MAB and LIB [2, 3, 4, 5, 6]. However, manual segmentation of these boundaries is labour intensive and time-consuming [6]. There are several studies that report on semi-automated segmentation methods for delineating the LIB and/or MAB on 2D US [7, 8, 9, 10, 11, 12], 3DUS [13, 14], MRI [15], and CTA [16, 17]. Here,

---

†. A version of this chapter has been published [1]: E. Ukwatta, J. Awad, A. D. Ward, D. Buchanan, J. Samarabandu, G. Parraga and A. Fenster, "A Three-dimensional ultrasound of carotid atherosclerosis: Semiautomated segmentation using a level set-based method," in *Medical physics*, 38(5), 2479–95 2011.

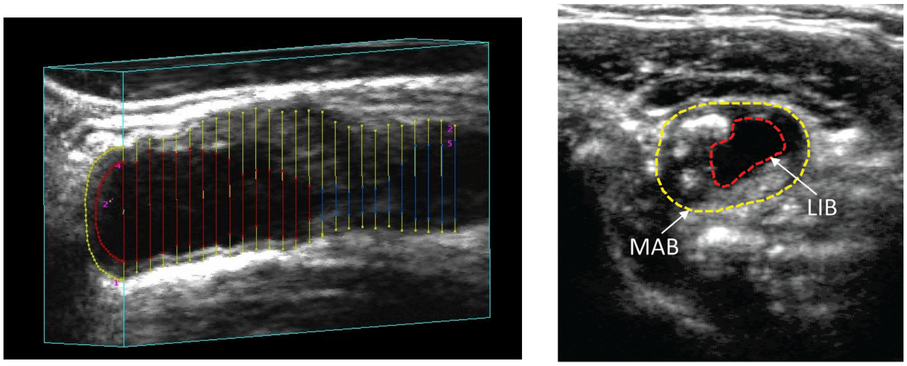

(a) (b)

Figure 2.1: (a) Sagittal cross-section of the common carotid artery (CCA) in a 3DUS image. The contours overlaid on the image represent the manual delineations done by an expert with an ISD of 1 mm; and (b) transverse view of a 3DUS image of the CCA showing expert-drawn contours delineating the MAB and LIB.

we focus on segmentation methods that aim to segment the LIB and/or MAB on US images. We classify the segmentation approaches developed for carotid US segmentation broadly into three categories based on the US imaging technique used: (1) 2D longitudinal US, (2) 2D transverse US, and (3) 3DUS. The majority of the existing literature on the segmentation of the carotid MAB and LIB focuses on obtaining IMT measurements from 2D US images passing through and parallel to the approximate central axis of the artery (henceforth referred to as “longitudinally oriented images”). These studies on the segmentation of the carotid artery boundaries included the application of dynamic programming [7], deformable snakes [8], Hough transforms [9], stochastic optimization [18] and classification approaches [10] to detect the carotid boundaries on longitudinally oriented images.

A number of other investigators have also described approaches for carotid LIB segmentation using the transverse view. Mao *et al.* [11] proposed a discrete dynamic contour model for extracting the carotid LIB from 2D transverse US images. They used a combination of local gradient difference and local gray level ratio between the outside and inside of the deformable contour to drive the evolution of the contour and validated their method using a total of seven transverse 2D slices. Abolmaesumi *et al.* [12] introduced a method based on the star algorithm improved by Kalman filtering to extract the LIB from transverse carotid US images, but did not validate the method using human patient images. Gill *et al.* [13] proposed a semi-automatic segmentation method based on a dynamic balloon model to extract the LIB in 3DUS, and validated the method using a single 3D US patient image. Their method requires placing a seed point within the carotid artery, which is initially inflated to determine the approximate LIB and then refined using image edge-based forces, which are susceptible to regions of poor image contrast at the boundary. Zahalka *et al.* [14] proposed a LIB segmentation method on 3DUS images using a geometrically deformable model with a stopping term based on the image gradient, which was validated using phantoms. In 3D carotid US images, the contrast is lower at boundaries parallel to the US beam, compared to boundaries orthogonal to the US beam. Image edge-based active contour methods may leak at low contrast boundaries as these methods assume the existence of image edges at the object boundary for the evolution to stop. For similar reasons, the applicability to 3DUS of techniques for MAB segmentation used for MRI and CTA images [15, 16] is unclear, and the assumption of elliptical vessel shape made by these techniques is tenuous, especially near the bifurcation (BF) (see Fig. 1.1(b) in Chapter 1). To the best of our knowledge, techniques for MAB segmentation on transverse images have not been previously reported for 2D or 3D carotid US images.

2.1.2 Contributions

The key innovation of this work was the incorporation of local and global image statistics with a boundary separation-based constraint and anchor points provided by the operator as high-level domain knowledge, enabling the accurate segmentation of the MAB and LIB. To our knowledge, no method has been previously reported for segmenting both the carotid artery LIB and MAB from 3DUS images. However, a preliminary study of this work has been published in a conference paper [19].

Out of the nine energies used for segmentation, we introduced the anchor point-based and boundary separation-based energies for level set methods. The developed algorithm would provide accurate quantification of VWV, thus enabling the accurate and noninvasive monitoring of progression and regression of carotid atherosclerosis.

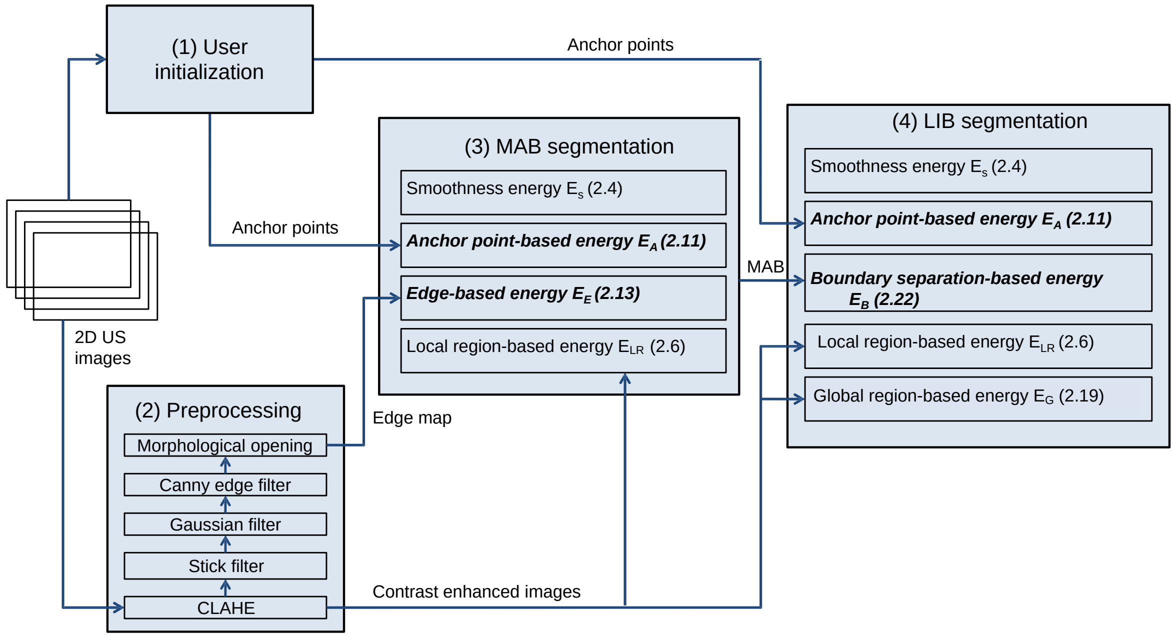
(1) User initialization
Anchor points
Anchor points
2D US images
(2) Preprocessing
Morphological opening
Canny edge filter
Gaussian filter
Stick filter
CLAHE
Edge map
Contrast enhanced images
(3) MAB segmentation
Smoothness energy E_s (2.4)
Anchor point-based energy E_A (2.11)
Edge-based energy E_E (2.13)
Local region-based energy E_{LR} (2.6)
MAB
(4) LIB segmentation
Smoothness energy E_s (2.4)
Anchor point-based energy E_A (2.11)
Boundary separation-based energy E_B (2.22)
Local region-based energy E_{LR} (2.6)
Global region-based energy E_G (2.19)

Figure 2.2: Block diagram of the workflow of the algorithm. Our contributions are shown in bold italic letters.

2.2 Materials and methods

2.2.1 Study subjects and imaging

3DUS images for 21 subjects were used, and all subjects provided written informed consent to the study protocol, which was approved by The University of Western Ontario Standing Board of Human Research Ethics. To better represent a diverse subject group, images were blindly selected from three subject groups: seven images from diabetes subjects, seven images from rheumatoid arthritis subjects, and seven images from atorvastatin subjects with carotid stenosis of 60% or more. The presence of stenosis was confirmed using carotid Doppler US flow velocities. Subjects were recruited from The Stroke Prevention Clinic at University Hospital (London Health Sciences Centre, London, Canada) and the Stroke Prevention and Atherosclerosis Research Centre (Robarts Research Institute, London, Canada).

The mechanical 3DUS system [20, 21, 22] used in this study has been described previously in Section 1.4.5.1. The voxel size of the 3DUS images was $\approx 0.1 \times 0.1 \times 0.15$ mm^3.

2.2.2 Overview and summary of approach

As shown in Fig. 2.2, the workflow consists of four main steps: (1) user initialization, (2) image preprocessing, (3) MAB segmentation, and (4) LIB segmentation. The first step involves an operator interactively placing manually selected points (henceforth referred to as "anchor points") on the MAB and LIB on each transverse cross-section. The MAB is segmented from contrast enhanced images using the level set approach by optimizing an objective function encoding smoothness energy, local region-based energy, edge-based energy utilizing the edge map obtained from preprocessing, and an energy which depends on the distance of the boundary to the anchor points (henceforth referred as "anchor point-based energy"). The motivation for the use of these energy terms is based on the observations that: (1) the parts of the MAB that are orthogonal to the US beam direction have relatively high image contrast, but poor contrast elsewhere (necessitating a region-based energy term to augment the edge-based term); and (2) this boundary has a smooth low-order shape. After the MAB has been segmented, lumen segmentation is performed, also using the level set method. The objective function for the LIB segmentation encodes smoothness energy, local and global region-based energies, an anchor point-based energy, and a boundary separation-based energy. The motivation for the use of these energy terms is based on the observations that: (1) the lumen region is relatively homogeneous and low intensity, (2) the LIB has missing edges, and (3) the LIB cannot be closer than some minimum distance from the MAB. The algorithm-generated contours were evaluated for accuracy and variability by comparison to contours delineated manually by an expert using volume-based, region-based, and boundary distance-based metrics on the 21 3DUS patient images, comprising 231 acquired 2D US frames.

2.2.3 User interaction

Rather than performing a fully manual outlining of the MAB and LIB, the operator initializes both boundaries by placing anchor points on each boundary on every transverse slice. The anchor points serve two purposes: (1) they attract the evolving curve to pass through them, and (2) they are used to define a spline that serves as the initialization boundary to the segmentation algorithm. In the clinical scenario, the operator would have full discretion over the number of anchor points to select, with the intent to select as few points as possible such that the algorithm provides a clinically acceptable segmentation.

2.2.4 Preprocessing

The preprocessing steps of the algorithm are shown in Figure 2.2. Contrast limited adaptive histogram equalization (CLAHE) [23] was applied to enhance the local contrast of the US images prior to the MAB and LIB segmentations. CLAHE partitions the image into contextual regions and applies histogram equalization by fitting a Rayleigh distribution to each local region. In this chapter, the values used for the CLAHE parameters [23]—number of image partitions, the contrast enhancement limit (CEL) to reduce the over-saturation of the image, and the mode of the Rayleigh distribution—are shown in Table 2.1.

The rest of the preprocessing steps were applied to obtain an edge map to aid in the MAB segmentation. Next, a cascaded stick filter [24] with stick length from 1 to 1.5 mm was applied to the contrast enhanced images to reduce the effect of image speckle. The stick filter employs line segments in different orientations and enhances edges by providing high response at the orientation that most likely represent an edge in the image. The stick filter lengths were chosen to correlate well with the MAB segments of the same length but large enough that it smoothes small-scale features and reduces the magnitude of edges with high curvature, which are not of interest. A Gaussian filter was then applied to smooth the image, followed by a Canny edge detection [25] to obtain an edge map that contains desired edges on the MAB and false edges corresponding to other structures. Morphological opening was used to remove edges that were smaller than 2 mm. The resulting filtered edge map

$$M(\mathbf{x}) = \begin{cases} 1 & \text{if } \mathbf{x} \text{ lies on an edge point} \\ 0 & \text{otherwise} \end{cases}, \tag{2.1}$$

was incorporated into the objective function of MAB segmentation.

In this chapter, values for the image preprocessing parameters were determined via a systematic search of the space of parameter values, which is described in Section 2.2.8. The parameters and their optimized values for preprocessing are shown in Table 2.1.

Table 2.1: Parameters and their optimized values for the preprocessing.

Operation	Parameters	Values
CLAHE	# Partitions, CEL, Rayleigh dist. mode	8, 0.02, 0.4
Stick filter	Stick length, interval	1–1.5 mm, 0.2 mm
Gaussian filter	Kernel size, SD	0.7 mm, 0.3 mm
Canny edge filter	High and low threshold	0.25, 0.08
Morphological opening	Element size	2 mm

2.2.5 Segmentation using level sets

We used active contours based on the level set method [26] to segment the MAB and LIB from 3DUS images. Our rationale for the use of the level set method, in contrast to, e.g., a parametric approach, is that it incorporates an implicit representation of contours and provides for the straightforward implementation of region-based segmentation, in addition to the edge-based segmentation [27]. US images suffer from artifacts, such as poor definition of the vessel boundaries, image speckle, and shadowing. These artifacts decrease the differentiation between the object of interest and background and pose a challenge to automated segmentation algorithms. Due to such challenges posed to image-based segmentation algorithms by plaque and US imaging artifacts, high-level user interaction and domain knowledge are incorporated into our proposed approach.

Let the bounded open subset $\Omega \subset \mathbb{R}^2$ represent the image domain. Each image is defined as $I : \Omega \to \mathbb{R}$, and $x \in \Omega$ is a spatial variable representing a single point. The level set is an implicit representation of a boundary defined by the function $\phi(\mathbf{x}) : \Omega \to \mathbb{R}$. The boundary is specified as the zero of the level set function, i.e., the set of spatial locations $\mathbf{x}$ for which $\phi(\mathbf{x}) = 0$. During the segmentation process, the function $\phi(\mathbf{x})$ is evolved according to the evolution equation given by

$$\frac{\partial \phi(\mathbf{x})}{\partial t} + F|\nabla \phi(\mathbf{x})| = 0, \tag{2.2}$$

where F is speed function. In our implementation, $\phi(\mathbf{x})$ is initially represented as a signed distance function of the boundary, and is evolved via the optimization of an objective function representing the goal of segmentation. The objective function contains two types of energy terms: external energy terms, derived from the (preprocessed) image data, and internal energy terms, derived from high-level knowledge about the expected shape of the boundaries as well as from user-specified anchor points.

In this chapter, we use sparse field level set (SFLS) method, which is a narrow-band level set implementation proposed by Whitaker [28]. Narrow-band methods update only the level set evolution around the neighbourhood of zero level set rather than computing $\phi(\mathbf{x})$ for the whole image domain. The narrow-band technique is required to implement the anchor-point based energy in our implementation.

The objective functions used in this work for the MAB and LIB are described below. Due to the differences in region and geometric features of the MAB and LIB two separate objective functions were used for their segmentations.

2.2.6 MAB segmentation

The MAB segments that are orthogonal to the US beam direction have high image contrast whereas the boundary segments that are parallel to the US beam direction have low image contrast. Moreover, the image intensity of the interior and exterior of the MAB (illustrated by the dashed outer contours in Fig. 2.1(b)) is heterogeneous. Therefore, a segmentation method solely based on region-based or edge-based energies may not yield an accurate segmentation. In addition, global region-based methods provide accurate segmentations, only when the interior and exterior of the object boundary can be accurately modeled by global statistics. Therefore, we use a hybrid geodesic energy combining local region-based and edge-based energies for the MAB segmentation. Edge-based forces drive the segmentation successfully in the presence of strong image gradients whereas the local region-based forces localize the boundary in the local neighbourhood without the presence of image gradients. The objective function E_{MAB} for MAB segmentation is defined as

$$E_{MAB} = \alpha_S E_S + \alpha_{LR} E_{LR} + \alpha_A E_A + \alpha_E E_E, \tag{2.3}$$

where E_S (2.4), E_{LR} (2.6), E_A (2.11), and E_E (2.13) are the regularization, local region-based, anchor point-based, and edge-based energies, respectively. To generate the results presented in this work, the parameters $\alpha_S, \alpha_{LR}, \alpha_A$, and α_E were set as shown in Table 2.2.

E_S promotes the smoothness of the boundary by minimizing its length and is given by [29]

$$E_S(\phi) = \int_\Omega |\nabla H(\phi(\mathbf{x}))| d\mathbf{x}, \tag{2.4}$$

where

$$H(x) = \begin{cases} 1 & \text{if } x < -\epsilon \\ 0 & \text{if } x > \epsilon \\ \frac{1}{2}\left[1 + \frac{x}{\epsilon} + \frac{1}{\pi}\sin(\frac{\pi x}{\epsilon})\right] & \text{if } |x| \leq \epsilon \end{cases}, \tag{2.5}$$

is the regularized Heaviside function [29] representing the interior region of the boundary. Similarly, the exterior region of the boundary is defined as $(1 - H(\phi(\mathbf{x})))$. ϵ is a small positive constant. The gradient of the Heaviside function within the integral (2.4) is the length of the boundary.

The local region based energy E_{LR} proposed by Lankton and Tannenbaum [30] assumes that at each point on the object boundary, the local interior and exterior neighbourhoods can be modeled by their mean intensities. Let $\hat{\mathbf{x}} \in \Omega$ be another independent spatial variable. The local region-based energy E_{LR} is

$$E_{LR}(\phi) = \int_\Omega \delta(\phi(\mathbf{x})) \int_\Omega B_L(\mathbf{x}, \hat{\mathbf{x}}) \left[H(\phi(\hat{\mathbf{x}}))(I(\hat{\mathbf{x}}) - u_x)^2 + (1 - H(\phi(\hat{\mathbf{x}})))(I(\hat{\mathbf{x}}) - v_x)^2\right] d\hat{\mathbf{x}} d\mathbf{x}, \tag{2.6}$$

where

$$\delta(x) = \begin{cases} 1 & \text{if } x = 0 \\ 0 & \text{if } |x| > \epsilon \\ \frac{1}{2\epsilon}\left[1 + \cos(\frac{\pi x}{\epsilon})\right] & \text{if } |x| \leq \epsilon \end{cases}, \tag{2.7}$$

is the regularized Dirac delta function and

$$B_L(\mathbf{x}, \hat{\mathbf{x}}) = \begin{cases} 1 & \text{if } ||\mathbf{x} - \hat{\mathbf{x}}|| < r_L \\ 0 & \text{otherwise} \end{cases} \tag{2.8}$$

is used to define a circular-shaped local region with localizing radius r_L.

$$u_x = \frac{\int_\Omega B_L(\mathbf{x}, \hat{\mathbf{x}}) H(\phi(\hat{\mathbf{x}}) I(\hat{\mathbf{x}}) d\hat{\mathbf{x}}}{\int_\Omega B_L(\mathbf{x}, \hat{\mathbf{x}}) H(\phi(\hat{\mathbf{x}})) d\hat{\mathbf{x}}}, \tag{2.9}$$

and

$$v_x = \frac{\int_\Omega B_L(\mathbf{x}, \hat{\mathbf{x}})(1 - H(\phi(\hat{\mathbf{x}}))) I(\hat{\mathbf{x}}) d\hat{\mathbf{x}}}{\int_\Omega B_L(\mathbf{x}, \hat{\mathbf{x}})(1 - H(\phi(\hat{\mathbf{x}}))) d\hat{\mathbf{x}}} \tag{2.10}$$

are the mean image intensities of the interior and exterior of the active contour within the region defined by $B_L(\mathbf{x}, \hat{\mathbf{x}})$. r_L is an important parameter that determines the degree of blending local statistics around the boundary to global statistics of the image. A small r_L essentially would act as an edge detector while an increasing r_L would cause convergence to global statistics.

Several previous segmentation methods have used user defined anchor points to guide the segmentation [31, 32]. Similarly, the energy E_A given by (2.11) encourages the contour to pass through each anchor point $\mathbf{x}_A^i$, placed by the expert if the evolving contour is within a distance r_A to the anchor point. When the contour points are away from the anchor point by more than r_A, there is no influence by this energy.

$$E_A(\phi) = \sum_{i=1}^{N_P} \int_\Omega \delta(\phi(\mathbf{x})) B_A^i(\mathbf{x}) (\phi(\mathbf{x}) - \phi(\mathbf{x}_A^i))^2 d\mathbf{x}, \tag{2.11}$$

where

$$B_A^i(\mathbf{x}) = \begin{cases} 1 & \text{if } ||\mathbf{x} - \mathbf{x}_A^i|| < r_A \\ 0 & \text{otherwise} \end{cases}, \tag{2.12}$$

is used to define a circular-shaped region around the anchor point with radius r_A and N_p is the number of anchor points. In our implementation, the curve evolution was started with an initial spline, which passed through the anchor points where E_A would be already at its minimum.

Caselles *et al.* [33] and Malladi *et al.* [34] introduced edge-based geometric active contours, which evolve an interface towards the desired object boundary under the assumption that there will be strong gradients at the object boundaries to stop the evolution. Here, we used an edge-based energy which utilizes the edge map $M(\mathbf{x})$ (2.1) generated during the preprocessing stage. The edge-based energy E_E is

$$E_E(\phi) = -\int_\Omega \delta(\phi(\mathbf{x})) \frac{B_E(\mathbf{x})}{\epsilon + |\phi(\mathbf{x}) - \phi(X_E(\mathbf{x}))|} d\mathbf{x}, \tag{2.13}$$

where

$$B_E(\mathbf{x}) = \begin{cases} 1 & \text{if } 0 < ||\mathbf{x} - X_E(\mathbf{x})|| < r_E \\ 0 & \text{otherwise} \end{cases}, \tag{2.14}$$

is the circular-shaped region around the point $\mathbf{x}$ with a radius r_E and ϵ is a small positive constant.

$$X_E(\mathbf{x}) = \arg\min_{\hat{\mathbf{x}}\in s} ||\mathbf{x} - \hat{\mathbf{x}}||, s = \{\hat{\mathbf{x}}; M(\hat{\mathbf{x}}) = 1\}; \tag{2.15}$$

is the nearest edge point from point $\mathbf{x}$. The edge force is non-zero when the contour is within a distance r_E to the closest edge point. According to (2.13), the energy E_E is minimum when the contour is placed on the edge.

By taking the first variation of the E_{MAB} (2.3) with respect to ϕ we obtain the evolving equation

$$\begin{aligned}\frac{\partial\phi(\mathbf{x})}{\partial t} =&\delta(\phi(\mathbf{x}))\Bigg\{\alpha_S \operatorname{div}\left(\frac{\nabla\phi(\mathbf{x})}{|\nabla\phi(\mathbf{x})|}\right)\\ &+\alpha_{LR}\int B_L(\mathbf{x},\hat{\mathbf{x}})\delta(\phi(\hat{\mathbf{x}}))\Big[(I(\hat{\mathbf{x}})-u_x)^2-(I(\hat{\mathbf{x}})-v_x)^2\Big]d\hat{\mathbf{x}}\\ &+\alpha_A\sum_{i=1}^{N_p} B_A^i(\mathbf{x})(\phi(\mathbf{x})-\phi(\mathbf{x}_A^i))+\alpha_E B_E(\mathbf{x})\\ &\times\frac{\operatorname{sgn}(\phi(\mathbf{x})-\phi(X_E(\mathbf{x})))}{(\epsilon+|\phi(\mathbf{x})-\phi(X_E(\mathbf{x}))|)^2}\Bigg\},\end{aligned} \tag{2.16}$$

where

$$\operatorname{sgn}(x) = \begin{cases} -1 & \text{if } x < 0 \\ 0 & \text{if } x = 0 \\ 1 & \text{if } x > 0 \end{cases}, \tag{2.17}$$

for the MAB segmentation. The stopping criteria of the MAB segmentation were based on the convergence test that terminates when the evolution does not change within bounds of 0.4 mm^2 on successive iterations and a maximum iteration criterion.

2.2.7 LIB segmentation

Unlike the MAB, the LIB has an irregular shape due to the presence of plaque and does not typically contain sharp, high contrast edges. However, the intensity distribution of the interior of the LIB is fairly homogeneous, whereas the outside region is heterogeneous. Therefore, we employed a combination of local region-based and global region-based forces to segment the LIB. The objective function E_{LIB} used to segment the LIB is given as

$$E_{LIB} = \lambda_S E_S + \lambda_{LR} E_{LR} + \lambda_G E_G + \lambda_A E_A + \lambda_E E_B, \tag{2.18}$$

where E_S (2.4), E_{LR} (2.6), E_G (2.19), E_A (2.11), and E_B (2.22) are the smoothness, local region-based, global region-based, anchor point-based, and boundary separation-based energies, respectively. To generate the results presented in this work, the parameters $\lambda_S, \lambda_{LR}, \lambda_G, \lambda_A$, and λ_B were set as given in Table 2.2. Similarly to MAB segmentation, the smoothness, local region-based, and the anchor point-based energies are used in lumen segmentation.

The global region-based energy (E_G) proposed by Chan and Vese [29] partitions the image into different regions based on their global distinct characteristics of the image region.

$$E_G(\phi) = \int_\Omega H(\phi(\mathbf{x}))(I(\mathbf{x}) - u)^2 + (1 - H(\phi(\mathbf{x})))(I(\mathbf{x}) - v)^2 d\mathbf{x}, \tag{2.19}$$

where

$$u = \frac{\int_\Omega H(\phi(\mathbf{x}))I(\mathbf{x})d\mathbf{x}}{\int_\Omega H(\phi(\mathbf{x}))d\mathbf{x}} \tag{2.20}$$

and

$$v = \frac{\int_\Omega (1 - H(\phi(\mathbf{x})))I(\mathbf{x})d\mathbf{x}}{\int_\Omega (1 - H(\phi(\mathbf{x})))d\mathbf{x}} \tag{2.21}$$

are the mean intensities of interior and exterior regions of the boundary. Equation (2.19) models the object and the background by mean intensities u and v.

Because the MAB and LIB are separated by the carotid media layer, they are encouraged to have a greater or equal separation distance (d_B) of 0.5 mm from each other [35]. We imposed d_B as a distance-based constraint to drive the LIB segmentation using the algorithm-generated MAB segmentation. The boundary separation-based energy E_B is given by

$$E_B(\phi) = \int_\Omega \delta(\phi(\mathbf{x}))B_B(\mathbf{x})d\mathbf{x}, \tag{2.22}$$

where

$$B_B(\mathbf{x}) = \begin{cases} 1 & \text{if } \min\limits_{\hat{\mathbf{x}}} D(\mathbf{x}, \hat{\mathbf{x}}) < d_T \\ 0 & \text{otherwise} \end{cases}, \tag{2.23}$$

and

$$D(\mathbf{x}, \hat{\mathbf{x}}) = ||\mathbf{x} - \hat{\mathbf{x}}||, \nabla H(\phi_{MAB}(\hat{\mathbf{x}})) = 1. \tag{2.24}$$

The term E_B discourages the intersection of the MAB and LIB. This energy is non-zero when the LIB moves closer to the MAB than distance d_B.

By taking the first variation of the E_{LIB} (2.18) with respect to ϕ, we obtain the evolving equation

$$\begin{aligned} \frac{\partial \phi(\mathbf{x})}{\partial t} =& \delta(\phi(\mathbf{x})) \Bigg\{ \lambda_S \operatorname{div}\left(\frac{\nabla \phi(\mathbf{x})}{|\nabla \phi(\mathbf{x})|} \right) \\ &+ \lambda_{LR} \int B_L(\mathbf{x}, \hat{\mathbf{x}}) \delta(\phi(\hat{\mathbf{x}})) \left[(I(\hat{\mathbf{x}}) - u_x)^2 - (I(\hat{\mathbf{x}}) - v_x)^2 \right] d\hat{\mathbf{x}} \\ &+ \lambda_G \left((I(\mathbf{x}) - u)^2 - (I(\mathbf{x}) - v)^2 \right) \\ &+ \lambda_A \sum_{i=1}^{N_p} \operatorname{sgn}(\phi(\mathbf{x}_A^i)) B_A^i(\mathbf{x}) (\phi(\mathbf{x}) - \phi(\mathbf{x}_A^i)) + \lambda_B B_B(\mathbf{x}) \Bigg\} \end{aligned} \tag{2.25}$$

for LIB segmentation. Similar to MAB segmentation, a narrow-band level set implementation was used for LIB segmentation with a stopping criteria based on the convergence test that the energy does not change within bounds of 0.4 mm^3 on successive iterations and a maximum iteration criterion.

2.2.8 Parameters of the segmentation

Initially, the parameter values were chosen empirically. Afterwards, the parameters were optimized sequentially for the MAB and LIB segmentations separately by changing a single parameter at a time for a range of its values while holding other parameters unchanged for 100 2D US images. For a given parameter, the parameter value corresponding to the highest overall Dice similarity coefficient (DSC) (1.14) was chosen as the optimized value. We used DSC as the metric for parameter optimization because it is a region-based metric that depends on spatial overlap, thus is more stringent than volume metrics. This procedure was repeated until convergence or until a maximum of five repetitions was met. It should be noted that this method is a local optimum search, thus the global optimum of the parameter values is not guaranteed. Table 2.2 shows the parameter values for the MAB and LIB segmentations after optimization. The parameter values were held constant during the validation experiments.

Table 2.2: Parameters and their optimized values for MAB and LIB segmentations.

Description	**MAB**		**LIB**	
	Parameter	**Value**	**Parameter**	**Value**
Local region radius	r_L	1.7 mm	r_L	1.4 mm
Anchor radius	r_A	2.5 mm	r_A	2.5 mm
Edge radius	r_E	2 mm	NA	_
Smoothness (E_S) weight	α_S	3.4	λ_S	1.2
Local region (E_{LR}) weight	α_{LR}	1	λ_{LR}	1
Anchor (E_A)weight	α_A	5.3	λ_A	4.7
Edge (E_E) weight	α_E	0.8	NA	_
Global region (E_G) weight	NA	_	λ_G	0.5
Boundary separation (E_B) weight	NA	_	λ_B	21

2.3 Validation

2.3.1 Experiment design

Expert manual segmentations were used as a surrogate for ground truth. The validation of the proposed algorithm was carried out by evaluating the accuracy of the algorithm-generated contours by comparison to the expert-drawn contours, as well as evaluating the reproducibility of the algorithm-generated contours. The manual segmentation method was previously described by Egger *et al.* [36] and is summarized here. Prior to contouring, the expert first located the bifurcation (BF) and defined an approximate medial axis of the carotid artery by choosing two points on the axis. The multi-planar 3D viewing software then presented 2D images of the artery by slicing through the 3D image orthogonally to the medial axis, in the inferior direction from the BF, with an inter-slice distance (ISD) of 1 mm. The expert then performed contouring of the MAB and LIB on each of these images. Figure 2.1 shows a sagittal cross-section of the CCA with manually annotated boundaries overlaid. An expert outlined the MAB and LIB boundaries five times repeatedly with a 24 hour period between repetitions on 231 transverse 2D slices extracted from 21 3DUS images. The images were randomized and the operator was blinded to the image order during each repetition to reduce memory bias. The operator also chose eight points on each boundary five times on each transverse slice with a 24 hour period between repetitions on the same data set. The user initialized the anchor points on the same image planes as for the manual segmentation to ensure that the algorithm segmented the same 2D images as segmented manually for direct comparison.

The reason behind selecting eight points initially on each boundary was to evaluate the sensitivity of the algorithm to the number of anchor points used for the segmentation. To determine the effect of choosing fewer than eight anchor points on the results of segmentation, we iteratively removed the anchor points one at a time, repeated the optimization, and calculated the validation metrics. Using this approach, we tested the proposed algorithm using four to eight anchor points. In the iterative removal process, anchor points capturing fine shape details (i.e., contributing little to the overall area covered by the shape) were removed first. In this paper, this ordering was achieved by the discrete contour evolution (DCE) algorithm [37]. The four points representing the coarsest representation of the shape were selected in advance from the eight anchor points by first numbering the eight points in order along the contour, and then considering the set of odd-numbered points, and the set of even numbered points. The set whose interpolating spline enclosed a region giving the greatest area overlap with that enclosed by the spline interpolating all eight points was selected as the coarsest, four-point representation of the shape. The DCE algorithm was then restricted to removing points only from the other set. This approach encourages a regular sampling of the boundary, avoiding the degenerate case where after anchor point removal, all of the remaining anchor points lie on one side of the shape.

2.3.2 Evaluation metrics

Metrics used in this dissertation were described in Section 1.10. Three types of metrics were used to evaluate the segmentations: volume-based, region-based, and boundary distance-based metrics. Volume-based metrics capture the aspect of the segmentation that is of greatest clinical interest: the VWV. Region- and boundary distance-based metrics describe in greater detail the spatial fidelity of the segmentations to those generated manually by the operator. The volumes were computed by multiplying the area enclosed by the boundary with the ISD of 1 mm.

We used six volume-based metrics: mean volume errors $\delta V_{VWV}, \delta V_{MAB}$, and δV_{LIB} (1.13) and mean absolute VWV errors $|\delta V_{VWV}|, |\delta V_{MAB}|$ and $|\delta V_{LIB}|$), all expressed as percentages. The mean VWV error δV_{VWV} for the 3DUS image set determines the overall VWV disagreement between the algorithm and manual segmentation.

A two-way mixed analysis of variance (ANOVA) with repeated measures was performed to determine the statistical significance of the measured performance differences between the algorithm and manual approach. The sources of variation in this design are: method (algorithm or manual) and repetitions. A two-way ANOVA test generates three p-values, one for each parameter independently, and one measuring the interaction between the parameters. The ANOVA study was performed using SPSS version 17.0 (SPSS Inc., Chicago, IL, USA).

We also computed the minimal detectable difference (MDD) (1.21) [38] for the algorithm and manual segmentation. The MDD is used to determine that the changes in VWV between two successive measurements is real and not a result of measurement variability. We used coefficient-of-variation (CV) (1.20) to compare the reproducibility of the algorithm and manual method for the generation of VWV. We also performed an F-test on the VWV estimates to determine the statistical significance of the difference between the standard deviations of the algorithm and manual segmentation.

The DSC (1.14) was used as a region-based measure to compare two segmentations for accuracy on slice-by-slice basis. The DSC quantifies the area overlap of two segmentations. For each transverse 2D image, the DSC was computed using the mean manual and mean algorithm boundaries. The approach to computing the mean boundary is given in Section 2.3.3. A mean DSC across patients was calculated to obtain an overall score determining the agreement between the algorithm and manual segmentations.

The mean absolute distance (1.17) (MAD) and maximum absolute distance (1.19) (MAXD) errors were used as boundary distance-based metrics. Mean boundaries were used to compute the MAD and MAXD. Boundary distance-based metrics depend on the establishment of a point-wise correspondence between the boundaries. We used

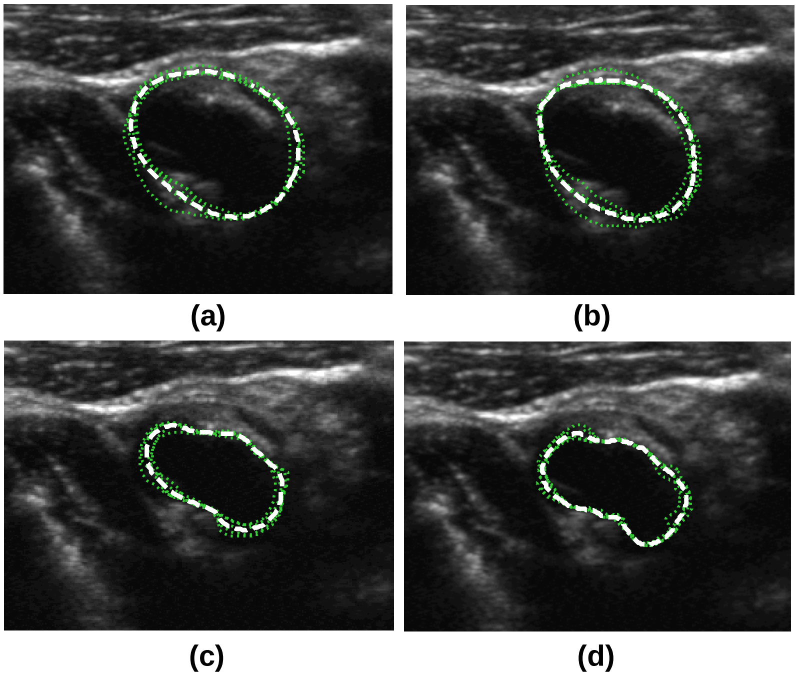

Figure 2.3: (a) Algorithm-generated boundaries for the MAB, (b) manually outlined boundaries for the MAB, (c) algorithm-generated boundaries for the LIB, and (d) manually outlined boundaries for the LIB. Legend: dotted contours - five segmented boundaries, dashed contour - corresponding mean boundary.

the symmetric correspondence method [39] described in Section 2.3.3 to establish correspondence. Averages of MAD and MAXD were computed across vessels to obtain an overall estimate of boundary disagreement. In addition to the accuracy and variability metrics, the time required to perform each manual delineation, each initialization of the algorithm, and the time required to execute the preprocessing steps and the level set method were recorded.

2.3.3 Mean boundary computation

We used a method similar to that of Chalana and Kim [40] to compute the mean boundary from the repeated manual segmentations and repeated algorithm-generated segmentations. Their method used closest point correspondence to establish correspondences. We used the symmetric correspondence method [3, 38], because it overcomes singularities (two points mapping to a single point) occurring in the closest point correspondence method. The symmetric correspondence method used in this paper is described in detail by Papademetris *et al.* [39]. The symmetric correspondence approach is well-motivated for use on this anatomy because the MAB and LIB are smooth and do not contain self intersections. In addition, we are establishing correspondence between multiple segmentations of the same artery. In this situation, the assumption that the boundaries to be corresponded are similar is stronger than in the scenario where the boundaries to be corresponded are derived from different objects/arteries.

Since the symmetric correspondence algorithm only establishes correspondence between a pair of boundaries, it was applied four times to establish correspondence between five boundaries. The boundary that was closest to the average boundary was chosen as the initial boundary and correspondences were established between this boundary and the other four boundaries. A point on the mean boundary was given by the centroid of the five corresponding points. A normal to the mean boundary was computed at each point on the mean boundary. The centroid of the intersection points of the normal and the five input boundaries were then determined. The resulting set of centroids gives a new mean boundary. The process was iterated until the mean boundary converged. Figure 2.3 shows the mean boundaries of the MAB and LIB generated using the manual delineations and algorithm-generated boundaries.

2.4 Results

We evaluated algorithm accuracy and reproducibility using 231 transverse slices from 21 carotid vessels. With the exception of the results described in Section 2.4.3, all of the results in this section were computed using four anchor points, chosen from the initially placed eight anchor points using the method described in Section 2.3.1. Figure 2.4 provides a qualitative overview of the results, showing the mean boundaries of the MAB and LIB computed using the algorithm-generated boundaries and manual delineations overlaid on 2D transverse images that are at a distance of 1, 4, 7, and 10 mm from the BF. Each column in Fig. 2.4 was extracted from a different vessel: one from each of diabetes, rheumatoid arthritis, and atorvastatin groups.

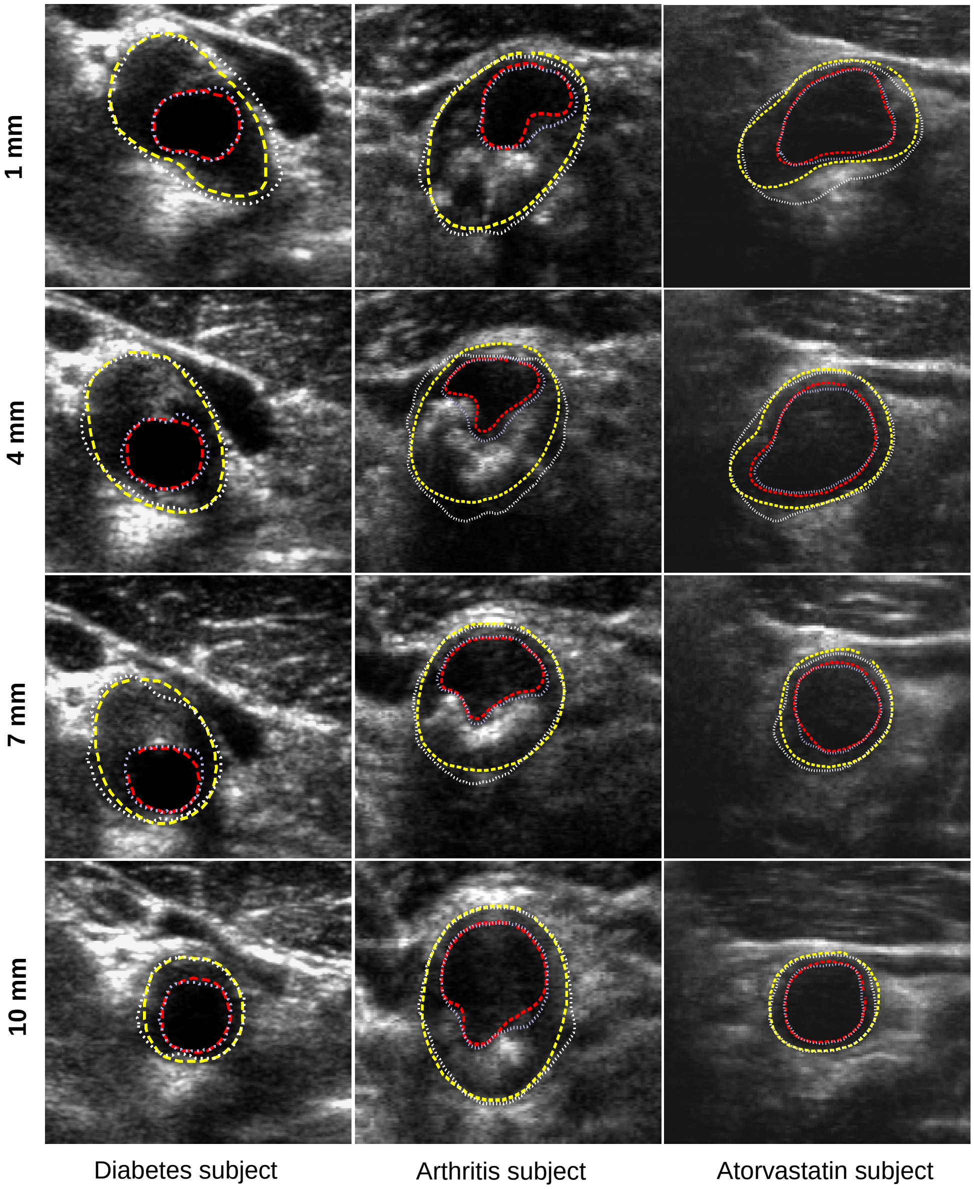
1 mm
4 mm
7 mm
10 mm
Diabetes subject
Arthritis subject
Atorvastatin subject

Figure 2.4: Sample results of the MAB and LIB segmentations for three patients using four anchor points chosen from the initial eight anchor points. (Dashed outer contour - manual MAB, dashed inner contour - manual LIB, dotted outer contour - algorithm-generated MAB, dotted inner contour - algorithm-generated LIB) 1, 5, 7, and 10 mm indicate the distance to the BF from each slice.

Table 2.3: Overall performance results of the algorithm for 231 2D slices extracted from the 21 3DUS images.

Metric	**MAB**	**LIB**
Volume error (%)	-1.3 ± 2.8	-1.0 ± 6.4
Absolute volume error (%)	2.5 ± 1.8	5.6 ± 3.0
95% CI (mm^3)	-23.1 to 0.3	-20.8 to 8.2
DSC (%)	95.4 ± 1.6	93.1 ± 3.1
MAD (mm)	0.2 ± 0.1	0.2 ± 0.1
MAXD (mm)	0.6 ± 0.3	0.7 ± 0.6

2.4.1 Accuracy

Bland-Altman plots [41] were used to examine the agreement between the VWVs generated from manual and algorithm segmentations. Figure 2.5 shows the Bland-Altman plot, which graphs the difference between manually computed and algorithm-generated VWV versus their average for each vessel. The mean bias and the 95% limit of agreement computed as the mean bias ± ($1.96 \times SD$ of the difference between two methods) are also shown in the figure. The mean bias for the algorithm was -5.1 mm^3.

The relationship between the algorithm and manual segmentation method was further examined using Pearson product-moment correlation analysis. Figure 2.6 graphs the VWV generated using the algorithm against the VWVs from manual method. The Pearson correlation coefficient of the two methods for generating VWV was highly significant ($r = 0.97, p < 0.01$).

In addition, we performed a two-way mixed repeated measures ANOVA on the mean VWVs of the two methods with an α value of 0.05. The p-value for the method (manual and algorithm) effect was 0.41, which indicates that the two methods were not statistically significantly different for the data used in this paper. The p-value for the repetition effect was 0.12, which indicates that repetition effect was also not significantly different. p-value of 0.31 for the interaction between the method and repetitions indicates no interaction between them.

We determined the 95% confidence interval (CI) of the difference between the algorithm and manual estimates of VWV. The average discrepancy (the bias) between the two methods was -5.1 mm^3 with a 95% CI of -17.4 mm^3 to 7.2 mm^3. The

MDDs [38] were computed for the segmentation methods using a level of significance (α) of 0.05 and power (β) of 0.8. The MDDs were 64.2 mm^3 and 50.3 mm^3 for the algorithm and manual segmentation, respectively.

The algorithm yielded an absolute VWV error $|\delta V_{VWV}|$ of $5.0 \pm 4.3\%$ with a segmentation bias of $-0.9 \pm 6.6\%$. Table 2.3 shows the overall evaluation results of the algorithm for 231 transverse 2D US images. The mean volume errors for the MAB and LIB indicate that the algorithm has a negative bias, thus the MAB and LIB volumes were underestimated. The algorithm reported a smaller absolute volume error for the MAB (2.5%) than the LIB (5.6%). Similarly, the algorithm yielded a higher DSC for the MAB (95.4%) than LIB (93.1%), although the algorithm reported similar MAD and MAXD errors for both boundaries.

Figure 2.7 graphs overall DSC, MAD, and MAXD as a function of distance to the BF for the MAB and LIB segmentations for 231 2D US images. The error bars represent one standard deviation above and below the mean. Note that the DSC is high ($\approx$ 96% for the MAB, $\approx$ 94% for the LIB) distal to the BF and decreases to $\approx$ 93% for the MAB and $\approx$ 90% for the LIB) proximal to the BF. Note that the standard deviation of the DSC is also higher near the BF. MAD and MAXD results agree with the DSC results such that the higher distance errors occur near the BF than distal to the BF.

2.4.2 Intra-observer variability

The CV was used to compare the intra-observer variability of the algorithm and manual method in estimating VWVs. The manual method and algorithm reported a CV of 3.9% and 5.1%, respectively. A two sample F-test was carried out to determine the statistical significance difference of the two variances. F-test gave a p-value of 0.93 ($N_I = 21$) indicating that we failed to show that the variances of the two methods are statistically significantly different for the sample used in this paper.

2.4.3 Number of initialized points

To determine the effect of initialization of the algorithm on accuracy and reproducibility, we used the algorithm five times for four, five, six, seven, and eight anchor points. Figure 2.8(a) shows the volume-based metrics δV_{VWV}, δV_{MAB} and δV_{LIB} versus the number of anchor points for the entire image data set. The algorithm gave a negative

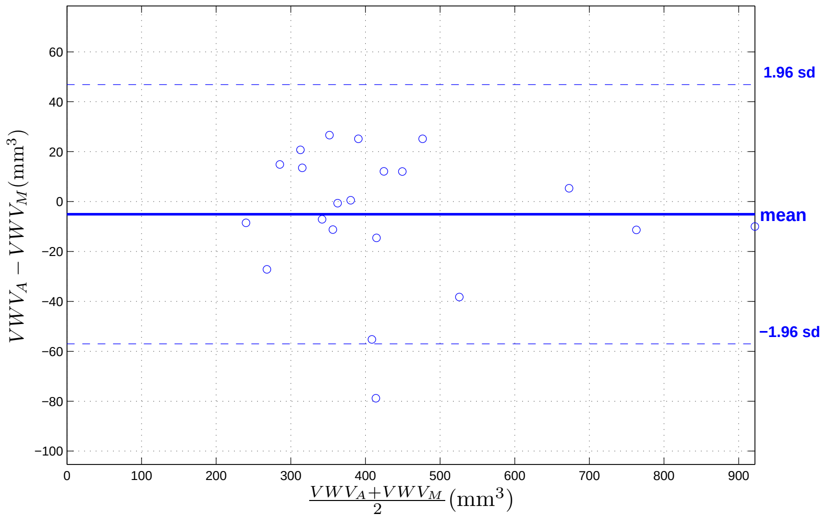

Figure 2.5: Bland-Altman plot of the VWVs generated using four anchor points chosen from the initial eight anchor points. The plot graphs the difference between the algorithm-generated and manual VWVs as a function of their mean.

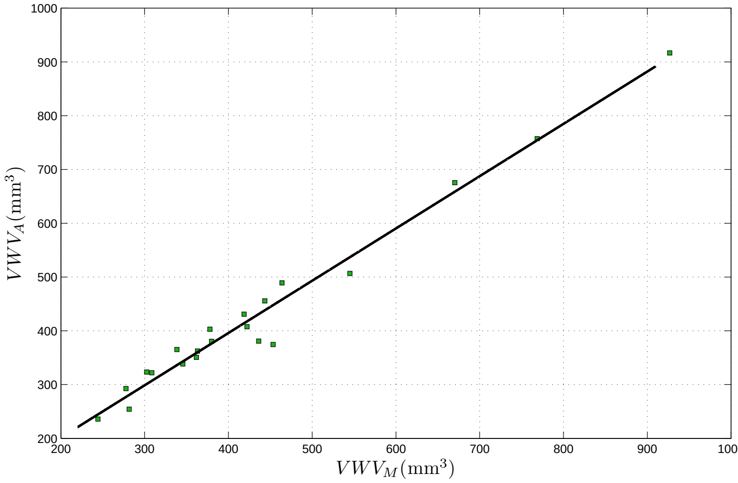

Figure 2.6: Correlation plot of VWV measurements for the algorithm and manual method. The VWVs were generated using four anchor points chosen from the initial eight anchor points for the algorithm.

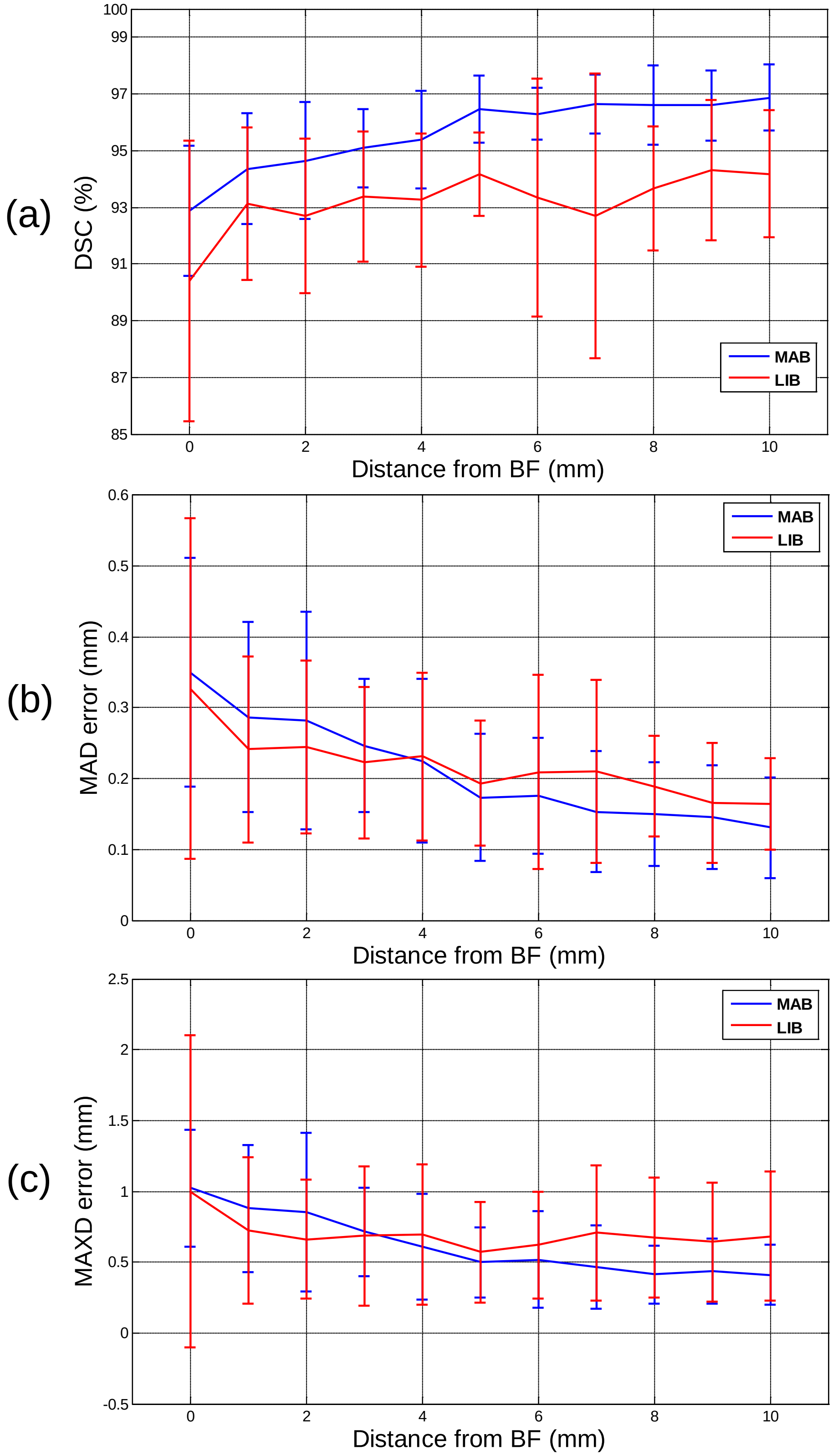

Figure 2.7: (a) Graph of DSC against distance to BF; (b) graph of MAD against distance to BF; and (c) graph of MAXD against distance to BF for the 231 images. The error bars represent one standard deviation.

للاستشارات المنارة

bias of -0.9% for δV_{VWV} using 4 anchor points and positive biases of 1.3, 1.1 and 1,8 % for using, 5, 6, 7, and 8 anchor points. The algorithm gave a similar pattern of biases for δV_{MAB} and δV_{LIB}. As shown in Figure 2.8(b), the absolute volume errors $|\delta V_{VWV}|$, $|\delta V_{MAB}|$, and $|\delta V_{LIB}|$ gradually decreased with the increasing number of anchor points.

Figure 2.8(c) plots the DSC as a function of number of anchor points. DSC gradually increased with the increasing number of anchor points for the MAB and LIB. Figure 2.8(d) graphs the CV in generating the VWV, MAB volume, and LIB volume versus the number of anchor points. The algorithm achieved a lower CV with an increasing number of anchor points for VWVs, MAB volumes, and LIB volumes.

2.4.4 Execution time

The reported times were calculated using the 231 images five times. 8.3 ± 1.5 min of operator time was required to manually delineate the MAB and LIB for a single 3DUS image (11 2D carotid images). In contrast, the algorithm required 1.6 ± 0.3 min of operator time to choose four anchor points. Moreover, the algorithm required a computational time of 1.2 ± 0.2 min to segment a single 3D image using a non-optimized Matlab (Natick, MA, USA) implementation on a single core of a PC with processor speed of 2.5 GHz.

2.5 Discussion

2.5.1 Discussion

Our goal was to develop and evaluate a semi-automated segmentation algorithm to delineate the MAB and LIB of the CCA for generating the measurement of 3DUS VWV [36]. Here, we report on: 1) the technical details of our 3DUS VWV segmentation algorithm, 2) measurement accuracy, 3) measurement reproducibility, and 4) execution speed on images from human subjects with a variety of underlying conditions. We also examined the effect of the number of anchor points used to initialize the algorithm.

We used a 2D segmentation method to delineate the carotid artery MAB and LIB on the same 2D slices used for manual segmentation to allow for a direct measurement of the benefit of the semi-automation to the existing manual procedure [2, 36, 42],

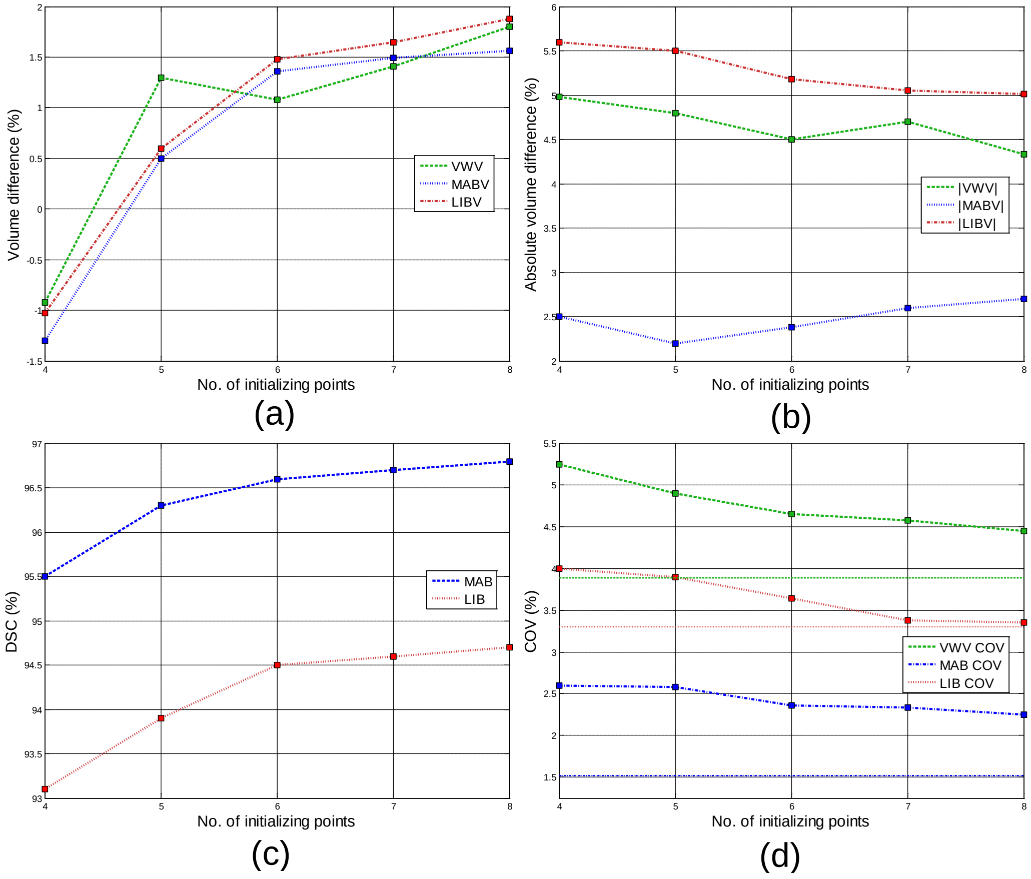

(a)

(b)

(c)

(d)

Figure 2.8: (a) Graph of $\delta V_{VWV}, \delta V_{MAB}$ and δV_{LIB} with varying number of initialized points; (b) graph of $|\delta V_{VWV}|, |\delta V_{MAB}|$ and $|\delta V_{LIB}|$ with varying number of initialized points; (c) graph of DSC for MAB and LIB with varying number of initialized points; and (d) graph of CV in computing VWV, MAB volume, and LIB volume with increasing number of initialized points.

while fixing other variables related to the operator interaction and workflow. We used a level set method, rather than, for example, a parametric approach, because the level set method enables the straightforward implementation of region-based energies. The objective function of the segmentation combined region-based and edge-based energies. Local region-based energies were incorporated to localize the boundary without the presence of edges. Energies derived from operator-placed contour anchor points were used to attract the boundary to pass through the anchor points, incorporating high-level direction given by the operator into the objective function. An energy term favouring a separation between the LIB and MAB boundaries was used to constrain the LIB, because without it LIB segmentation may leak through a low contrast boundary.

We then examined accuracy of the algorithm by comparing the algorithm results to manual segmentations. In the absence of histology images confirming the locations of the MAB and LIB, manual segmentations of the 3DUS images were used as a surrogate for truth. Bland-Altman plots (see Fig. 2.5) and the correlation coefficient of 0.97 (see Fig. 2.6) indicated a strong agreement of the two methods and ANOVA failed to detect a statistically significant difference between the methods. Based on our sample, there was a 95% chance that the VWV difference of the two methods ranges from -17.4 to 7.2 mm^3, which is not a clinically relevant difference [20]. The utility of the algorithm for monitoring plaque progression and regression in subjects depends on the MDD in VWV based on measurements given by of the algorithm. The algorithm is capable of detecting changes in VWV greater than or equal to the MDD of 64.2 mm^3. Knowledge of the MDD is essential in deciding on the follow-up times for the subjects. The follow-up time must be greater than the time required for VWV to progress or regress by 64.2 mm^3. This value is smaller than a previously reported VWV change of $\approx \pm 120$ mm$^3/yr$ [2, 42], which suggests that follow-up period of 7 months or more would be suitable using our method.

The accuracy of the algorithm was also examined using volume-based metrics. The overall VWV error δV_{VWV} of -0.9% (-5.1 mm^3) quantifies the segmentation bias of the algorithm. A bias of -0.9% implies that the algorithm underestimated the VWVs for the data set. However, a bias of -5.1 mm^3 may not be of clinical importance given the MDD of 64.2 mm^3. In addition, we used $|\delta V_{VWV}|$ to quantify the volume error of the algorithm. The mean absolute volume differences was $5.0 \pm 4.3\%$, which indicates that the algorithm provided equally good estimates of the VWVs when compared with the manual approach. The algorithm gave a smaller δV_{MAB} ($2.5 \pm 1.8\%$) for the MAB compared with for the LIB ($5.6 \pm 3.0\%$). Similarly, the standard deviation of the algorithm in generating MAB volume (2.8%) was smaller than LIB volume (6.4%). This may be due to the fact that four anchor points are adequate to segment the MAB due to its smooth low order shape.

Overall DSC values of $\approx 95\%$ and $\approx 93\%$ for the MAB and LIB, respectively, indicate that the algorithm-generated contours had a large amount of spatial overlap with manually-generated contours. The results of DSC are consistent with the volume-based metrics, that higher overall DSC was reported for the MAB than the LIB. Boundary distance-based metrics provide an even more detailed assessment of the accuracy of the segmentations, since they are more sensitive to undesirable spikes and protrusions of the algorithm-generated contours.

We also observed the variation of accuracy and error metrics as a function of distance to the BF (Fig. 2.7(a), (b) and (c)). The DSC was relatively small ($\approx 93\%$ for the MAB, 90% for the LIB) proximal to the BF and high ($\approx 96\%$ for the MAB, $\approx 94\%$ for the LIB) distal to the BF for both boundaries. The variability of MAD and MAXD versus the distance to the BF are also consistent with the DSC results. This may be due to the significant amount of plaque present proximal to the BF of the carotid artery. Large, calcified plaques create shadowing artifacts, making the MAB and LIB boundaries less prominent.

Chiu *et al.* [43] proposed a framework for evaluating our segmentation algorithm on a point-by-point basis. Their method [43] proposed statistical metrics to evaluate the difference of local vessel wall-thickness-plus-plaque (VWT) produced by manual and algorithm segmentations. The VWT maps for each subject can be pooled together to produce 2D standardized maps for the data set. Such 2D standardized maps can be used to improve the accuracy of the algorithm by identifying regions with larger errors.

The algorithm reported a higher CV (5.1%) compared to manual segmentation (3.9%) in estimating the VWV using four anchor points. However, a two-sample F-test failed to detect a statistically significant difference ($p = 0.9$). The small difference in variability (5.1% vs. 3.9%) may indicate that the variability of the algorithm is primarily caused by the observer selection of anchor points on the boundary rather than the variability introduced by the algorithm.

The average operator time saved using our algorithm (with 4 anchor points), compared with manual segmentation, was 5.5 min (8.3 min to 2.8 min), with 1.2 min spent on computation. Since our current implementation is in Matlab and is not optimized, we speculate that computation time may be substantially reduced by optimizing and parallelizing the implementation.

We also observed the effect of varying the number of anchor points (see Fig. 2.8) on accuracy and reproducibility. The segmentation bias varied from a small negative bias to a positive bias with the increasing number of points (see Fig. 2.8(a)) for VWV, MAB and LIB volumes. However, the segmentation biases were small ($\approx -1.2\%$ to $\approx 1.8\%$) and may not be of clinical significance. When we consider the MAB and LIB separately, δV_{LIB} showed a decreasing trend, although δV_{MAB} did not show a decreasing trend (see Fig. 2.8(b)). This may be due to that the MAB is a relatively smooth and low order curve, such that four points are sufficient to describe the shape. However, a gradual increase in the accuracy with the increasing number of points is noted for the DSC for both boundaries (see Fig. 2.8(c)). The CVs for VWV, MAB, and LIB volumes gradually decreased with the increasing number of anchor points (see Fig. 2.8(c)) to initialize the algorithm. For the LIB, the variability of the algorithm approaches the variability of the manual segmentation. We speculate that when increasing the number of anchor points to initialize the algorithm, the variability of the algorithm approaches the variability in manual delineations.

We compared the algorithm-generated contours to the contours drawn by a single operator. It is not known whether the regions of disagreement arise from inaccuracies in the algorithm, or from inaccuracies in the manual segmentation. Although phantoms with a known geometry may be used to establish a ground truth, it is not realistic to use traditional phantoms for the purposes of validating the accuracy of the algorithm, since they do not simulate the characteristics of patients' real 3DUS images with sufficient fidelity. Since the LIB is more challenging to segment, the algorithm uses segmented MAB to constrain the LIB segmentation from leaking. Therefore, the accuracy of the LIB segmentation depends to some extent on the accuracy of the MAB segmentation.

In this study, we only segmented a portion of the CCA. However, in the future we will investigate the segmentation of the internal and external carotid arteries as well. The developed algorithm segments each transverse slice independently and is a first step toward reducing the operator interaction for carotid segmentation.

As future work, we will investigate the use of both slice-by-slice propagation and direct 3D segmentation to reduce the operator interaction further by utilizing the image information along the out-of-plane direction as well. In the method, we used image intensity for the region-based energies, but energies based on image texture may improve the accuracy of the segmentation. In addition to generating VWV, the segmentations of the MAB and LIB can be used as a fundamental step in the analysis of carotid plaque composition [44] for the early identification of vulnerable plaques to prevent possible stroke.

References

[1] E. Ukwatta, J. Awad, A. D. Ward, D. Buchanan, J. Samarabandu, G. Parraga, and A. Fenster, "Three-dimensional ultrasound of carotid atherosclerosis: Semiautomated segmentation using a level set-based method," *Medical Physics*, vol. 38, p. 2479, 2011. 53

[2] I. Shai, J. D. Spence, D. Schwarzfuchs, Y. Henkin, G. Parraga, A. Rudich, A. Fenster, C. Mallett, N. Liel-Cohen, A. Tirosh *et al.*, "Dietary intervention to reverse carotid atherosclerosis," *Circulation*, vol. 121, no. 10, p. 1200, 2010. 53, 76, 78

[3] B. Chiu, M. Egger, J. D. Spence, G. Parraga, and A. Fenster, "Quantification of carotid vessel wall and plaque thickness change using 3D ultrasound images," *Medical physics*, vol. 35, p. 3691, 2008. 53, 69

[4] M. Egger, B. Chiu, J. D. Spence, A. Fenster, and G. Parraga, "Mapping spatial and temporal changes in carotid atherosclerosis from three-dimensional ultrasound images," *Ultrasound in medicine & biology*, vol. 34, no. 1, pp. 64–72, 2008. 53

[5] B. Chiu, V. Beletsky, J. D. Spence, G. Parraga, and A. Fenster, "Analysis of carotid lumen surface morphology using three-dimensional ultrasound imaging," *Physics in Medicine and Biology*, vol. 54, p. 1149, 2009. 53

[6] B. Chiu, M. Egger, D. J. Spence, G. Parraga, and A. Fenster, "Area-preserving flattening maps of 3D ultrasound carotid arteries images," *Med. Image Anal.*, vol. 12, no. 6, pp. 676–688, 2008. 53

[7] Q. Liang, I. Wendelhag, J. Wikstrand, and T. Gustavsson, "A multiscale dynamic programming procedure for boundary detectionin ultrasonic artery images," *IEEE Transactions on medical imaging*, vol. 19, no. 2, pp. 127–142, 2000. 53, 54

[8] C. P. Loizou, C. S. Pattichis, M. Pantziaris, T. Tyllis, and A. Nicolaides, “Snakes based segmentation of the common carotid artery intima media,” *Medical & Biological Engineering & Computing*, vol. 45, no. 1, pp. 35–49, Jan. 2007, PMID: 17203319. 53, 54

[9] S. Golemati, J. Stoitsis, E. G. Sifakis, T. Balkizas, and K. S. Nikita, “Using the hough transform to segment ultrasound images of longitudinal and transverse sections of the carotid artery,” *Ultrasound in Medicine & Biology*, vol. 33, no. 12, pp. 1918–1932, Dec. 2007. 53, 54

[10] F. Molinari, G. Zeng, and J. S. Suri, “An integrated approach to Computer-Based automated tracing and its validation for 200 common carotid arterial wall ultrasound images,” *Journal of Ultrasound in Medicine*, vol. 29, no. 3, p. 399, 2010. 53, 54

[11] F. Mao, J. Gill, D. Downey, and A. Fenster, “Segmentation of carotid artery in ultrasound images,” in *Engineering in Medicine and Biology Society, 2000. Proceedings of the 22nd Annual International Conference of the IEEE*, vol. 3, 2000, pp. 1734–1737. 53, 54

[12] P. Abolmaesumi, M. Sirouspour, and S. Salcudean, “Real-time extraction of carotid artery contours from ultrasound images,” in *Computer-Based Medical Systems, 2000. CBMS 2000. Proceedings. 13th IEEE Symposium on*, 2000, pp. 181–186. 53, 54

[13] J. D. Gill, H. M. Ladak, D. A. Steinman, and A. Fenster, “Accuracy and variability assessment of a semiautomatic technique for segmentation of the carotid arteries from three-dimensional ultrasound images,” *Medical Physics*, vol. 27, p. 1333, 2000. 53, 54

[14] A. Zahalka and A. Fenster, “An automated segmentation method for three-dimensional carotid ultrasound images,” *Physics in Medicine and Biology*, vol. 46, no. 4, pp. 1321–1342, Apr. 2001, PMID: 11324967. 53, 55

[15] I. M. Adame, R. J. van der Geest, B. A. Wasserman, and e. a. Mohamed, M. A., “Automatic segmentation and plaque characterization in atherosclerotic carotid artery MR images,” *Magn. Reson. Mater. Phy.*, vol. 16, no. 5, pp. 227–234, 2004. 53, 55

[16] D. Vukadinovic, T. Van Walsum, R. Manniesing, S. Rozie, R. Hameeteman, T. T. De Weert, A. Van Der Lugt, and W. J. Niessen, “Segmentation of the outer vessel wall of the common carotid artery in CTA,” *Medical Imaging, IEEE Transactions on*, vol. 29, no. 1, pp. 65–76, 2010. 53, 55

[17] R. Manniesing, M. Schaap, S. Rozie, R. Hameeteman, D. Vukadinovic, A. van der Lugt, and W. Niessen, “Robust CTA lumen segmentation of the atherosclerotic

carotid artery bifurcation in a large patient population," *Medical image analysis*, vol. 14, no. 6, pp. 759–769, 2010. 53

[18] F. Destrempes, J. Meunier, M.-F. Giroux, G. Soulez, and G. Cloutier, "Segmentation in ultrasonic b-mode images of healthy carotid arteries using mixtures of nakagami distributions and stochastic optimization," *IEEE Transactions on Medical Imaging*, vol. 28, no. 2, p. 215, 2009. 54

[19] E. Ukwatta, J. Awad, A. Ward, J. Samarabandu, A. Krasinski, G. Parraga, and A. Fenster, "Segmentation of the lumen and media-adventitia boundaries of the common carotid artery from 3d ultrasound images," *Proceedings of SPIE*, p. 79630G, 2011. 55

[20] C. D. Ainsworth, C. C. Blake, A. Tamayo, V. Beletsky, A. Fenster, and J. D. Spence, "3D ultrasound measurement of change in carotid plaque volume: A tool for rapid evaluation of new therapies," *Stroke*, vol. 36, no. 9, pp. 1904–1909, Sep. 2005. 56, 78

[21] A. Fenster, D. Downey, and H. Cardinal, "Three-dimensional ultrasound imaging," *Physics in medicine and biology*, vol. 46, no. 5, p. R67, 2001. 56

[22] A. Fenster and D. B. Downey, "Three-dimensional ultrasound imaging," *Annual Review of Biomedical Engineering*, vol. 2, no. 1, pp. 457–475, Aug. 2000. 56

[23] K. Zuiderveld, "Contrast limited adaptive histogram equalization," in *Graphics gems IV*. Academic Press Professional, Inc., 1994, pp. 474–485. 58

[24] S. D. Pathak, V. Chalana, D. R. Haynor, and Y. Kim, "Edge-guided boundary delineation in prostate ultrasound images," *IEEE Transactions on Medical Imaging*, vol. 19, no. 12, pp. 1211–1219, Dec. 2000, PMID: 11212369. 58

[25] J. Canny, "A computational approach to edge detection," *Pattern Analysis and Machine Intelligence, IEEE Transactions on*, no. 6, pp. 679–698, 1986. 58

[26] S. Osher and J. A. Sethian, "Fronts propagating with curvature dependent speed: algorithms based on Hamilton-Jacobi formulations," 1988. 59

[27] D. Cremers, M. Rousson, and R. Deriche, "A review of statistical approaches to level set segmentation: Integrating color, texture, motion and shape," *International Journal of Computer Vision*, vol. 72, no. 2, pp. 195–215, Aug. 2006. 59

[28] R. T. Whitaker, "A Level-Set approach to 3D reconstruction from range data," *Int. J. Comput. Vision*, vol. 29, no. 3, pp. 203–231, 1998. 60

[29] T. F. Chan and L. A. Vese, "Active contours without edges," *Image Processing, IEEE Transactions on*, vol. 10, no. 2, pp. 266–277, 2001. 61, 64

[30] S. Lankton and A. Tannenbaum, “Localizing Region-Based active contours,” *IEEE Transactions on Image Processing*, vol. 17, no. 11, pp. 2029–2039, Nov. 2008. 61

[31] T. Windheuser, T. Schoenemann, and D. Cremers, “Beyond connecting the dots: A polynomial-time algorithm for segmentation and boundary estimation with imprecise user input,” in *Computer Vision, 2009 IEEE 12th International Conference on*. IEEE, 2009, pp. 717–722. 62

[32] L. D. Cohen and R. Kimmel, “Global minimum for active contour models: A minimal path approach,” *International journal of computer vision*, vol. 24, no. 1, pp. 57–78, 1997. 62

[33] V. Caselles, R. Kimmel, and G. Sapiro, “Geodesic active contours,” *IJCV*, vol. 22, no. 1, 1997. 62

[34] R. Malladi, J. A. Sethian, and B. C. Vemuri, “Shape modeling with front propagation: A level set approach,” *IEEE transactions on Pattern Analysis and machine intelligence*, vol. 17, pp. 158—175, 1995. 62

[35] P. Touboul, M. Hennerici, S. Meairs, H. Adams, P. Amarenco, and e. a. Bornstein, N., “Mannheim carotid Intima-Media thickness consensus (2004-2006),” *Cerebrovascular Diseases*, vol. 23, no. 1, pp. 75–80, 2007. 64

[36] M. Egger, J. D. Spence, A. Fenster, and G. Parraga, “Validation of 3D ultrasound vessel wall volume: an imaging phenotype of carotid atherosclerosis,” *Ultrasound in medicine & biology*, vol. 33, no. 6, pp. 905–914, 2007. 66, 76

[37] X. Bai, L. J. Latecki, and W. Liu, “Skeleton pruning by contour partitioning with discrete curve evolution,” *IEEE Transactions on Pattern Analysis and Machine Intelligence*, vol. 29, no. 3, pp. 449–462, 2007. 67

[38] J. R. Mitchell, S. J. Karlik, D. H. Lee, M. Eliasziw, G. P. Rice, and A. Fenster, “The variability of manual and computer assisted quantification of multiple sclerosis lesion volumes,” *Medical Physics*, vol. 23, no. 1, pp. 85–97, 1996. 68, 69, 73

[39] X. Papademetris, A. J. Sinusas, D. P. Dione, and J. S. Duncan, “Estimation of 3D left ventricular deformation from echocardiography,” *Medical Image Analysis*, vol. 5, no. 1, pp. 17–28, Mar. 2001. 69, 70

[40] V. Chalana and Y. Kim, “A methodology for evaluation of boundary detection algorithms on medical images,” *Medical Imaging, IEEE Transactions on*, vol. 16, no. 5, pp. 642–652, 1997. 69

[41] D. Altman and J. Bland, "Measurement in medicine: the analysis of method comparison studies," *The statistician*, pp. 307–317, 1983. 72

[42] A. Krasinski, B. Chiu, J. D. Spence, A. Fenster, and G. Parraga, "Three-dimensional ultrasound quantification of intensive statin treatment of carotid atherosclerosis," *Ultrasound in medicine & biology*, vol. 35, no. 11, pp. 1763–1772, 2009. 76, 78

[43] B. Chiu, E. Ukwatta, S. Shavakh, and A. Fenster, "Quantification and visualization of carotid segmentation accuracy and precision using a 2d standardized carotid map," *Physics in medicine and biology*, vol. 58, no. 11, p. 3671, 2013. 79

[44] J. Awad, A. Krasinski, G. Parraga, and A. Fenster, "Texture analysis of carotid artery atherosclerosis from three-dimensional ultrasound images," *Medical Physics*, vol. 37, no. 4, pp. 1382–1391, Apr. 2010. 81

Chapter 3

3D segmentation of 3DUS carotid atherosclerosis using sparse field level sets[†]

3.1 Introduction

As described in Section 1.8, delineations of the carotid MAB and LIB are required in generating 3DUS VWV and VWT measurements and are helpful in generating the TPV measurement. Although, VWV has been shown to be more sensitive to temporal changes in carotid atherosclerosis than the more widely used IMT, 3DUS VWV is not used because manual segmentation of the carotid MAB and LIB is tedious and time-consuming. Previously developed semi-automated algorithms [2, 3] including the 2D algorithm described in Chapter 2, also require user interactions on every slice. Therefore, VWV measurements are still mainly generated using manual segmentations [4], and a few attempts [2, 3, 5] have been reported for developing semi-automated algorithms. Therefore, the objective of this work is to develop and evaluate a semi-automated 3D algorithm for segmenting the MAB and LIB of the CCA from 3DUS images with fewer user interactions.

3.1.1 Previous studies

Some carotid ultrasound-based segmentation techniques reported in the literature are two-dimensional and are used to determine the IMT measurements in longitudinal views from carotid 2DUS images [13, 14, 15, 16]. However, for the purpose of obtaining volumetric measurements, the entire MAB and LIB surfaces need to be delineated

---

[†] A version of this chapter has been published [1]: E. Ukwatta, J. Yuan, D. Buchanan, B. Chiu, J. Awad, W. Qiu, G. Parraga, and A. Fenster "Three-dimensional segmentation of three-dimensional ultrasound carotid atherosclerosis using sparse field level sets," in *Medical Physics,* 40(5) 2903–20, 2013.

Table 3.1: Previous papers describing carotid LIB and/or MAB segmentations from 3DUS/B-mode images.

Paper	Year	Dimension	LIB	MAB	Time (min)	No. of images (type)	Other information
Ukwatta [6]	2011	2D	Coupled level set	Coupled level set	3.7 ± 0.4	21 (3DUS)	-Anchor points on the boundary on each slice.
Ukwatta [3]	2011	2D	Level set	Level set	2.8 ± 0.4	21 (3DUS)	-Anchor points on the boundary on each slice.
Yang [2]	2011	2D	Active shape model	Active shape model	4.4 ± 0.6	68 (3DUS)	-Initializing a shape model on each slice. -Requires training data
Solovey [7]	2010	3D	Level set	–	–	2 (3DUS)	-Seed points inside the lumen.
Gill [8]	2000	3D	Dynamic	–	30 s	1 (3DUS)	-Initializing the balloon model inside the LIB.
Guerrero [9]	2007	2D	Star Kalman filters	–	23 s	3 (B-mode sequence)	-Seed point inside the LIB.
Abolmaesumi [10]	2000	2D	Star algorithm/ Kalman filtering	–	–	1 (B-mode sequence)	-Seed point inside the LIB.
Zahalka [11]	2001	2D	Active contours	–	25s/	2 (3DUS)	-Seed point inside the LIB. -Results not reported.
Mao [12]	2000	2D	Active contours	–	0.8 s/ slice	7 (B-mode)	-Seed point inside the LIB.

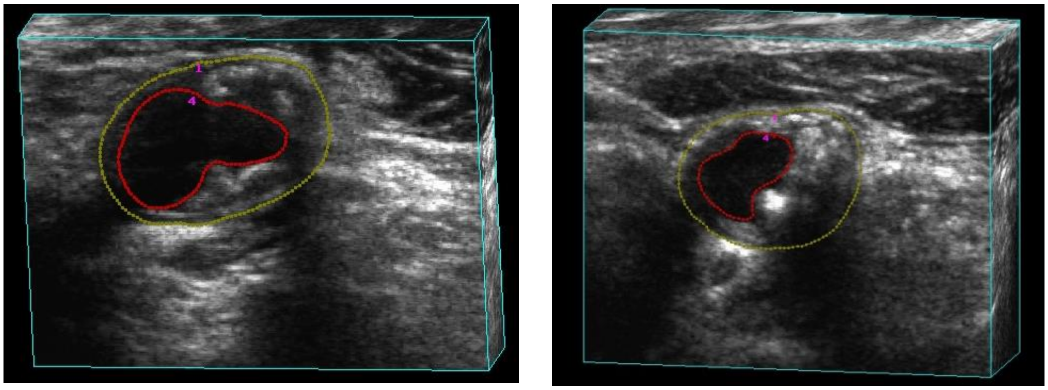

Figure 3.1: Two example transverse views of the CCA with overlaid manual segmentations of the MAB and LIB from 3DUS images of two subjects with carotid stenosis of more than 60%. Note that although the MAB has a relatively low order convex shape, the LIB may have a nonconvex shape.

in either transverse views or in 3D combining both transverse and longitudinal views. In this chapter, we specifically focus on 2D and 3D algorithms that have been developed for segmenting the entire surface of carotid MAB and/or LIB from 3DUS images as shown in Table 3.1. The algorithms can be divided into two main categories as shown in Table 3.1: Techniques [7, 8, 9, 10, 11, 12] that only segment the carotid LIB and ones [2, 3, 6] that segment both the carotid MAB and LIB. For example, Gill *et al.* [8] and Solovey [7] proposed direct 3D segmentation methods only for LIB segmentation. Gill *et al.* [8] used a 3D dynamic balloon model that is inflated to coarsely locate the boundary and then refined using edge-based energies for LIB segmentation. However, edge-based segmentation alone is not adequate to stop leaking at low-contrast boundaries in US images [17]. Solovey [7] proposed a level set-based method to segment the LIB by incorporating a region term that minimizes the probability distribution overlap and a weak geometric prior, which encourages convexity of the boundary in a level set framework. However, the carotid LIB may not have a convex shape due to the presence of plaque, which is most prominent close to the bifurcation, as shown in Fig. 3.1. Another limitation of some of the studies [10, 11, 12] for LIB segmentation is that they validated their algorithm on only seven 2D B-mode patient images [12], few phantom images [11], or did not report on a quantitative segmentation validation [10].

Three previous methods have been reported for segmenting both the carotid MAB and LIB from 3DUS images [2, 3, 6]. Yang *et al.* [2] used active shape models to segment the carotid LIB and MAB slice-wise, which involved a large number of training images to generate models. However, the shape of the LIB could be different between subjects, which is also affected by the degree of stenosis, as shown in Fig. 3.1. Ukwatta *et al.* [3] proposed a 2D segmentation method for delineating the carotid arteries on a slice-by-slice basis on transverse slices extracted from 3DUS images. Ukwatta *et al.* [6] used a coupled level set approach to simultaneously segment the MAB and LIB. For both techniques, the areas from individual segmentations are summed together to generate the VWV measurement. Since each slice is segmented independently at an ISD of 1 mm, the methods require user interaction on every slice. Although the slice thickness of our 3DUS images is approximately 0.15 mm, the 2D methods [3, 6] make an assumption of no considerable change in the vessel morphology within an ISD of 1 mm.

3.1.2 Contributions

In this chapter, we describe and evaluate a direct 3D segmentation algorithm to delineate the MAB and LIB of the CCA from 3DUS images. The algorithm uses a similar boundary-based initialization approach used previously for the 2D segmentation [3], but requires initialization only on a smaller subset of transverse slices than the number of slices used in the 2D method [3]. However, the proposed method does not hold the assumption of constant vessel morphology within an ISD of 1 mm, as it provides a direct 3D segmentation of the entire 3DUS image at a slice thickness of 0.15 mm. The 3D method uses nine energy functionals in total, out of which eight were used in the 2D method [3].

The main contribution of this chapter is the extension of the energy functions [3] to 3D. To the best of our knowledge, the proposed algorithm is the first direct 3D segmentation method for segmenting both the carotid MAB and LIB from 3DUS images for the purpose of computing the VWV. A direct 3D segmentation method has the potential for reducing user interaction over a 2D method, while increasing the robustness of the segmentation by integrating out-of-plane image information.

A preliminary study of this work has been previously described in a conference paper [18]. The algorithm was briefly described and validated only for accuracy using 15 3DUS images in the conference paper [18]. In this chapter, we provide comprehensive details of the proposed algorithm and provide a thorough analysis of the accuracy and intra-observer variability on 21 3DUS images with five repeated algorithm segmentations. In addition, initialization of the algorithm is investigated with respect to accuracy and variability with ISD of 1, 2, 3, 4, and 10 mm.

3.2 Materials and methods

Our segmentation pipeline consists of four main steps as shown in Fig. 3.2: Algorithm initialization, 3D image preprocessing, MAB segmentation, and LIB segmentation. Each of the steps is described below.

3.2.1 Algorithm initialization

A boundary-based initialization approach is used in our algorithm as opposed to a region-based initialization, where the observer chooses “anchor points” on the MAB

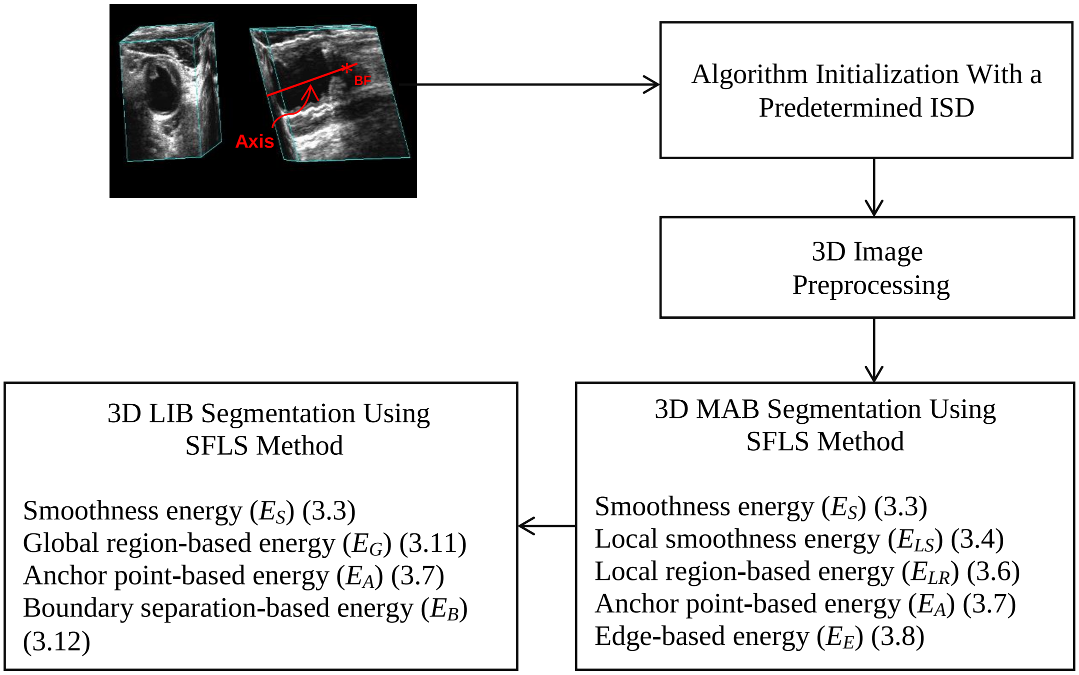
Axis
BF
Algorithm Initialization With a Predetermined ISD
3D Image Preprocessing
3D MAB Segmentation Using SFLS Method
Smoothness energy (E_S) (3.3)
Local smoothness energy (E_{LS}) (3.4)
Local region-based energy (E_{LR}) (3.6)
Anchor point-based energy (E_A) (3.7)
Edge-based energy (E_E) (3.8)
3D LIB Segmentation Using SFLS Method
Smoothness energy (E_S) (3.3)
Global region-based energy (E_G) (3.11)
Anchor point-based energy (E_A) (3.7)
Boundary separation-based energy (E_B) (3.12)

Figure 3.2: Block diagram of the workflow of the 3D algorithm.

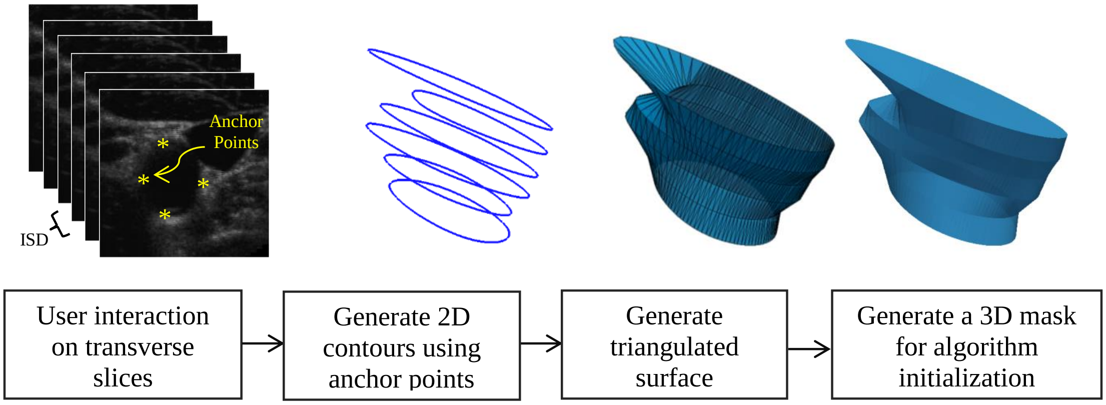
Anchor Points
ISD
User interaction on transverse slices
Generate 2D contours using anchor points
Generate triangulated surface
Generate a 3D mask for algorithm initialization

Figure 3.3: The process of creating a 3D mask from anchor points as the initial surface for the algorithm with an ISD of 2 mm.

and LIB. The anchor points are used to generate the initial mask for the segmentation and constrain the evolving surface to always pass through them.

The observer first locates the BF and defines the long axis of the artery as shown in Fig. 3.2. Then, the observer chooses four anchor points each on the MAB and LIB on a set of transverse slices, which are orthogonal to the long axis of the artery, with a pre-defined ISD. For example, ISD of 1, 2, 3, 4, and 10 mm are used in this chapter, where large ISDs result in fewer user interactions. In comparison to the 2D method [3], which requires user initializations on every slice at an ISD of 1 mm, our 3D method uses fewer slices for initialization.

Figure 3.3 shows the steps for generating a 3D mask to represent the initial surface for the segmentation algorithm for the LIB or MAB. For the set of 2D planes with user-initialized anchor points, 2D contours are first generated by cubic spline interpolation with approximately 0.2 mm interval between adjacent points using the four anchor points on each plane. The 2D contours are then corrected for any intersections of the MAB and LIB automatically, by correcting the LIB to have a minimum separation of 0.5 mm from the carotid MAB [19]. The contour points between two adjacent parallel slices are then corresponded using the similarity correspondence algorithm [20]. The symmetric correspondence algorithm provides an improvement to the closest point algorithm by avoiding multiple points being mapped to the same point [20]. A triangular surface is generated using the corresponding points, which

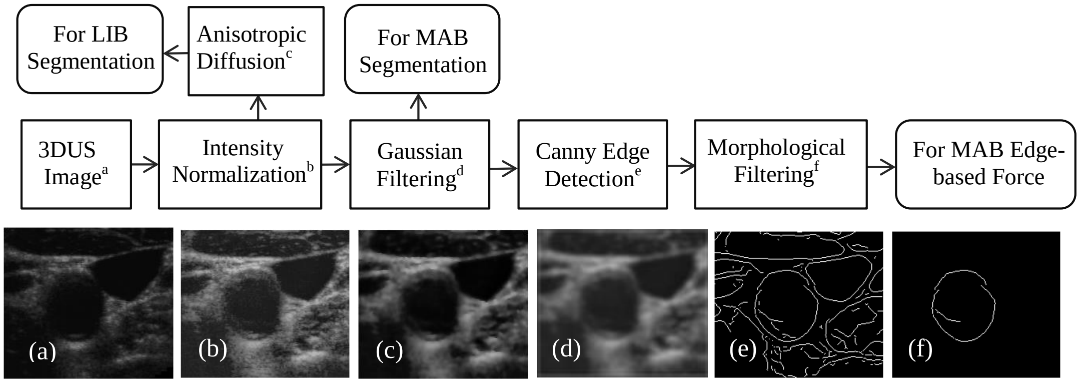
For LIB Segmentation
Anisotropic Diffusion^c
For MAB Segmentation
3DUS Image^a
Intensity Normalization^b
Gaussian Filtering^d
Canny Edge Detection^e
Morphological Filtering^f
For MAB Edge-based Force
(a)
(b)
(c)
(d)
(e)
(f)

Figure 3.4: 3D image preprocessing steps of the algorithm. The results here are shown for a single slice of the 3DUS image.

is then converted to a 3D binary mask. Any voxel inside the triangular surface is assigned label one and any voxel outside the surface is labeled zero.

3.2.2 3D image preprocessing

The preprocessing steps of our algorithm are shown in Fig. 3.4. Initially, a region-of-interest (ROI) is chosen by using a 7 mm margin in all three directions from the minimum and maximum values of x, y, and z coordinates of the initial surface. Two separate preprocessing pipelines are used for the MAB and LIB as shown in Fig. 3.4. The 3DUS image is first normalized using the minimum and maximum intensity of the image to reduce the effect of different image contrast of each image. Then, edge-preserving anisotropic diffusion filtering [21] is applied to reduce the effect of image speckle, as shown in previous studies [17, 22, 23]. This method enhances the 3DUS image by diffusing image regions with low or no image gradient while preserving image edges. In addition, it provides the filtered output image within a few seconds for 3DUS images. The output from the diffusion filtering is used as the input 3DUS image for LIB segmentation. For MAB segmentation, filtered output from the Gaussian filter with a kernel size of 0.7 mm is used as the input 3DUS image. The rest of the preprocessing steps are applied to obtain an edge map to aid in MAB segmentation. We apply Canny edge detector [24] on the filtered 3DUS images to obtain an edge map, as previously used in US segmentation tasks [23]. Morphological operations are then used on the edge map to remove edge segments that are smaller than 2 mm, and edges that are more than a distance of 10 mm from the initial surface. The resulting filtered edge map is incorporated into the objective function of MAB segmentation. In this chapter, values for image preprocessing parameters are determined via a systematic search of the space of parameter values. The parameters and their optimized values for preprocessing are shown in Table 3.2.

3.2.3 Sparse field level set (SFLS) method

In this chapter, we used a sparse field level set (SFLS) implementation [25] for both LIB and MAB segmentations. The SFLS method updates only the level set evolution around the neighborhood of zero level set rather than computing for the whole image domain to speed up the evolution by reducing the amount of computation. Let the bounded open subset $\Omega \in \mathbb{R}^3$ represent the image domain, where the image $I : \Omega \to \mathbb{R}$ and $\mathbf{x} \in \Omega$ is a spatial variable. The level set is an implicit representation of a surface defined by the Lipschitz function $\phi(\mathbf{x}) : \Omega \to \mathbb{R}$, where the zero level of $\phi(\mathbf{x})$ represents the segmented surface. $\phi(\mathbf{x})$ is represented as a signed distance function at the beginning, where $\phi(x) < 0$ inside the surface. The level set evolution equation is given by

$$\frac{\partial \phi(\mathbf{x})}{\partial t} + \nabla E |\nabla \phi(\mathbf{x})| = 0 \tag{3.1}$$

where E is the objective function representing the goal of segmentation [26, 27]. $\phi(\mathbf{x})$ is evolved based on the objective function, until it converges to an energy minimum. The objective function contains two types of energy terms: external energy terms, derived from the (preprocessed) image data, and internal energy terms, derived from high-level knowledge about the expected shape of the boundaries as well as from user-specified anchor points.

3.2.4 MAB segmentation

At first, we segment the MAB using the 3D SFLS method. The segmentation task of the MAB from 3DUS carotid images is challenging due to the following reasons: Low image contrast of the MAB especially on the surface that is parallel to the US beam, presence of calcified plaque creating shadowing and signal dropouts, heterogeneous intensities on the interior and exterior of the MAB (contain both hypo-echoic and hyper-echoic regions), and overlapping intensity PDFs with each other as shown in Fig. 1.10(c) in Chapter 1. To address these challenges in the segmentation, we incorporated five types of energy criteria into the objective functional (E_{MAB}) for the MAB (see Fig. 3.2):

$$E_{MAB} = \alpha_S E_S + \alpha_{LS} E_{LS} + \alpha_{LR} E_{LR} + \alpha_A E_A + \alpha_E E_E, \tag{3.2}$$

where weights $\alpha_S, \alpha_{LS}, \alpha_{LR}, \alpha_A, \alpha_E$ are positive constants.

The smoothness energy [27, 28] (3.3) is the standard regularization used in level sets that penalizes the length of the segmentation surface and is given by

$$E_S(\phi) = \int_\Omega |\nabla H(\phi(\mathbf{x}))| d\mathbf{x}, \tag{3.3}$$

where $H(\mathbf{x})$ is the regularized Heaviside function [27] representing interior of the segmentation surface, whereas the exterior region of the surface is defined as $(1 - H(\mathbf{x}))$. ϵ is a small positive constant.

The local smoothness energy [29] (E_{LS}) reduces the convexity and concavity of a local neighborhood region defined by a spherical mask. Let $\hat{\mathbf{x}} \in \Omega$ be another independent spatial variable:

$$E_{LS}(\phi) = \int_\Omega \delta(\phi(\mathbf{x}))(A_v(\mathbf{x}) - A_u(\mathbf{x}))^2 d\mathbf{x}, \tag{3.4}$$

where

$$B_L(\mathbf{x}, \hat{\mathbf{x}}) = \begin{cases} 1 & \text{if } ||\mathbf{x} - \hat{\mathbf{x}}|| < r_L \\ 0 & \text{otherwise} \end{cases}, \tag{3.5}$$

is used to define a spherical region with localizing radius r_L. $A_u(\mathbf{x}) = \int_\Omega B_L(\mathbf{x}, \hat{\mathbf{x}}) H(\phi(\hat{\mathbf{x}})) d\hat{\mathbf{x}}$ and $A_v(\mathbf{x}) = \int_\Omega B_L(\mathbf{x}, \hat{\mathbf{x}})(1 - H(\phi(\hat{\mathbf{x}}))) d\hat{\mathbf{x}}$ are the volume of the inside and outside regions of the $B_L(\mathbf{x}, \hat{\mathbf{x}})$. $\delta(\mathbf{x})$ is the regularized Dirac delta function, which is the derivative of $H(\mathbf{x})$.

The local region-based energy (E_{LR}) [28] minimizes the intensity inhomogeneity of the local interior and exterior regions:

$$E_{LR}(\phi) = \int_\Omega \delta(\phi(\mathbf{x})) \int_\Omega B_L(\mathbf{x}, \hat{\mathbf{x}}) \left[H(\phi(\hat{\mathbf{x}}))(I(\hat{\mathbf{x}}) - u_x)^2 + (1 - H(\phi(\hat{\mathbf{x}})))(I(\hat{\mathbf{x}}) - v_x)^2 \right] d\hat{\mathbf{x}} d\mathbf{x} \tag{3.6}$$

where $u(\mathbf{x})$ and $v(\mathbf{x})$ are the mean image intensities of the interior and exterior of the active contour within the local region defined by $B_L(\mathbf{x}, \hat{\mathbf{x}})$ [28]. The parameter r_L determines the degree of blending local statistics around the boundary to global statistics of the image.

The anchor point-energy [3] (E_A) encourages the contour to pass through each anchor point $\mathbf{x}_A^i$, placed by the observer if the evolving contour is within a distance r_A to the anchor point:

$$E_A(\phi) = \sum_{i=1}^{N_P} \int_\Omega \delta(\phi(\mathbf{x})) B_A^i(\mathbf{x})(\phi(\mathbf{x}) - \phi(\mathbf{x}_A^i))^2 d\mathbf{x}, \tag{3.7}$$

where $B_A^i(\mathbf{x}) = \begin{cases} 1 & \text{if } ||\mathbf{x} - \mathbf{x}_A^i|| < r_A \\ 0 & \text{otherwise} \end{cases}$ is used to define a spherical mask around the anchor point with radius r_A and N_P is the number of anchor points. When the contour points are away from the anchor point by more than r_A there is no influence of this energy term. In our implementation, the segmentation is started with the initial mask that already passes through the anchor points, where E_A would be already at its minimum. With initializing the segmentation close to the MAB using the anchor points, we reduce the possibility of the evolving contour to be trapped in local minima due to the heterogeneity of the region and also reduce the computational time for segmentation.

The edge-based level set framework was initially proposed by Caselles *et al.* [30]. We use a modified edge-based energy [3] term (E_E) to complement the region-based forces, especially at locations of the surface that are orthogonal to the US beam:

$$E_E(\phi) = -\int_\Omega \delta(\phi(\mathbf{x})) \frac{B_E(\mathbf{x})}{\epsilon + |\phi(\mathbf{x}) - \phi(X_E(\mathbf{x}))|} d\mathbf{x}, \tag{3.8}$$

where $B_E(\mathbf{x}) = \begin{cases} 1 & \text{if } 0 < ||\mathbf{x} - X_E(\mathbf{x})|| < r_E \\ 0 & \text{otherwise} \end{cases}$ is the spherical region around the point $\mathbf{x}$ with a radius r_E and $X_E(x) = \arg\min_{\hat{x} \in s} ||\mathbf{x} - \hat{\mathbf{x}}||$, $s = \{\hat{\mathbf{x}}; M(\hat{\mathbf{x}}) = 1\}$ being the nearest edge point from point $\mathbf{x}$ and $M(\mathbf{x}) = \begin{cases} 1 & \text{if } \mathbf{x} \text{ lies on an edge point} \\ 0 & \text{otherwise} \end{cases}$ is the edge map obtained from preprocessing. The edge force is nonzero when the contour is within a distance r_E to the closest edge point and minimum when the contour is placed on the edge.

By taking the first variation of E_{MAB} (3.2) with respect to ϕ, we obtain the evolving equation function for MAB segmentation where $\operatorname{sgn}(\mathbf{x})$ is the signum function [3]:

$$\begin{aligned}\frac{\partial\phi(\mathbf{x})}{\partial t} =& \delta(\phi(\mathbf{x}))\Bigg\{\alpha_S \operatorname{div}\left(\frac{\nabla\phi(\mathbf{x})}{|\nabla\phi(\mathbf{x})|}\right) \\ &+ \alpha_{LS}(A_v(\mathbf{x}) - A_u(\mathbf{x})) \\ &+ \alpha_{LR}\int B_L(\mathbf{x},\hat{\mathbf{x}})\delta(\phi(\hat{\mathbf{x}}))\Big[(I(\hat{\mathbf{x}}) - u_x)^2 - (I(\hat{\mathbf{x}}) - v_x)^2\Big]d\hat{\mathbf{x}} \\ &+ \alpha_A\sum_{i=1}^{N_p} B_A^i(\mathbf{x})(\phi(\mathbf{x}) - \phi(\mathbf{x}_A^i)) + \alpha_E B_E(\mathbf{x}) \\ &\times \frac{\operatorname{sgn}(\phi(\mathbf{x}) - \phi(X_E(\mathbf{x})))}{\epsilon + |\phi(\mathbf{x}) - \phi(X_E(\mathbf{x}))|}\end{aligned} \tag{3.9}$$

3.2.5 LIB segmentation

After the MAB has been segmented, LIB segmentation is performed also using the 3D SFLS method. The challenges in the LIB segmentation are low image-contrast edges of the LIB and its irregular shape in some subjects due to the presence of plaque. For LIB segmentation, we use a global region-based energy, high-level knowledge provided by the observer, and previously obtained MAB segmentation to constrain the LIB. The objective functional (E_{LIB}) for the LIB comprises of four energies (see Fig. 3.2):

$$E_{LIB} = \lambda_S E_S + \lambda_A E_A + \lambda_G E_G + \lambda_B E_B \tag{3.10}$$

where weights $\lambda_S, \lambda_A, \lambda_G, \lambda_B$ are positive constants. E_S is the smoothness energy (3.3), and E_A is the anchor point-based energy (3.7) as defined previously.

The global region-based energy [27]

$$E_G(\phi) = \int_\Omega H(\phi(\mathbf{x}))(I(\mathbf{x}) - u_m)^2 + (1 - H(\phi(\mathbf{x})))(I(\mathbf{x}) - v_m)^2 d\mathbf{x}, \tag{3.11}$$

partitions the image into different regions based on their global distinct characteristics of the image region. u_m and v_m are the mean intensities of interior and exterior regions of the boundary [3, 27]. The use of a combination of local region-based and global region-based forces to segment the LIB is motivated by the fact that the intensity of the interior of the lumen is fairly homogeneous while outside of the LIB the intensity is heterogeneous.

Because the MAB and LIB are separated by the intima-media layer, we constrained them to have a minimum distance (d_B) of 0.5 mm from each other [19]. The algorithm-generated MAB is used to reduce leaking of the LIB at a weak boundary. We imposed d_B as a distance-based constraint to drive the LIB segmentation using the algorithm-generated MAB segmentation. The boundary separation-based energy (E_B) is given by

$$E_B(\phi) = \int_{\Omega} \delta(\phi(\mathbf{x})) B_B(\mathbf{x}) d\mathbf{x}, \tag{3.12}$$

$$B_B(\mathbf{x}) = \begin{cases} 1 & \text{if } \min\limits_{\hat{\mathbf{x}}} D(\mathbf{x}, \hat{\mathbf{x}}) < d_B \\ 0 & \text{otherwise} \end{cases} \quad \text{and } D(\mathbf{x}, \hat{\mathbf{x}}) = ||\mathbf{x} - \hat{\mathbf{x}}||, \nabla H(\phi_{MAB}(\hat{\mathbf{x}})) = 1.$$

The term E_B discourages the intersection of the MAB and LIB. This energy is nonzero when the LIB moves closer to the MAB than distance d_B.

By taking the first variation of the E_{LIB} (3.10) with respect to ϕ we obtain the evolving equation for the LIB segmentation:

$$\begin{aligned} \frac{\partial \phi(\mathbf{x})}{\partial t} =& \delta(\phi(\mathbf{x})) \Bigg\{ \lambda_S \operatorname{div}\left(\frac{\nabla \phi(\mathbf{x})}{|\nabla \phi(\mathbf{x})|} \right) \\ &+ \lambda_G \Big((I(\mathbf{x}) - u)^2 - (I(\mathbf{x}) - v)^2 \Big) \\ &+ \lambda_A \sum_{i=1}^{N_p} B_A^i(\mathbf{x})(\phi(\mathbf{x}) - \phi(\mathbf{x}_A^i)) + \lambda_B B_B(\mathbf{x}) \Bigg\} \end{aligned} \tag{3.13}$$

The stopping criteria for MAB and LIB segmentation is based on the convergence test that terminates when the evolution does not change within bounds of 0.4 mm^3 on successive iterations and a maximum iteration criterion, which is set to be 250 iterations.

Initially, the parameter values were chosen empirically, which were then optimized for the MAB and LIB segmentations using DSC. The optimization was performed by changing a single parameter over a range of possible values, while holding the other parameters fixed for ten 3DUS images. We used DSC as the metric for parameter optimization, as it is a region-based metric that depends on spatial overlap, which is thus more stringent than volume metrics. This procedure was repeated until either convergence or a maximum of five repetitions were met. It should be noted that we performed only a local optimum search, thus the global optimum of the parameter values is not guaranteed. Table 3.3 shows the parameter values for the MAB and LIB segmentations after optimization. The parameter values were held constant during the validation experiments.

Table 3.2: Parameters and their optimized values for the preprocessing

Operation	**Parameters**	**Values**
Diffusion filtering	No. of iterations, time step, conductance	4, 0.2, 1.0
Gaussian filter	Kernel size, SD	0.7, 0.3 mm
Canny edge filter	High and low threshold	0.25, 0.08
Morphological opening	Element size, minimum size maximum distance	2.5, 2, 10 2 mm

Table 3.3: Parameters and their optimized values for MAB and LIB segmentations.

Description	**MAB**		**LIB**	
	Parameter	**Value**	**Parameter**	**Value**
Local region radius	r_L	0.7 mm	–	–
Anchor radius	r_A	0.8 mm	r_A	0.9 mm
Edge radius	r_E	0.8 mm	–	–
Smoothness (E_S) weight	α_S	0.4	λ_S	0.6
Local smoothness (E_{LS}) weight	α_{LS}	0.8	–	–
Local region (E_{LR}) weight	α_{LR}	3.1	–	–
Anchor (E_A)weight	α_A	1.9	λ_A	1.8
Edge (E_E) weight	α_E	0.4	–	–
Global region (E_G) weight	–	–	λ_G	0.7
Boundary separation (E_B) weight	–	–	λ_B	1.9

3.3 Validation

The algorithm was evaluated for accuracy and reproducibility by comparison to user-drawn contours. Manual segmentations of the MAB and LIB were performed using 3D multi-planar viewing software [31] on transverse views up to a distance of 1 cm of the artery from the bifurcation with an ISD of 1 mm. For further information about the manual segmentations the readers are referred to Egger *et al.* [32]. The images were first randomized to the observer for both repeated manual and algorithm segmentation rounds. An observer outlined the carotid MAB and LIB five times repeatedly with a 24 h period between repetitions on 21 3DUS images. The observer initialized the anchor points on the same image planes as for the manual segmentation to ensure that the algorithm segmented the same 2D slices with an ISD of 1 mm as segmented manually for direct comparison. For the five repeated algorithm segmentations, four anchor points were chosen for both the MAB and LIB on each slice for each 3DUS image for each round with a 24 h period between repetitions on the same data set as described by Ukwatta *et al.* [3].

We also evaluated the algorithm accuracy and reproducibility with different ISDs for initialization on the same data set. ISD of 1, 2, 3, 4, and 10 mm were used in the experiments, where larger ISDs require fewer user interaction. For example, for an ISD of 2 mm, user initializations on every other slice is used as anchor points and are used to generate initial mask.

3.3.1 Evaluation metrics

The algorithm-generated surfaces were resliced at 1 mm intervals, for a direct comparison to manual segmentation. Similar to the 2D method [3], we used the same volume-based, region-based, and distance-based metrics to evaluate the accuracy of our segmentation method. Volume-based metrics capture the aspect of the segmentation that is of greatest clinical interest: the VWV. Region- and boundary distance-based metrics describe in greater detail the spatial fidelity of the segmentations to those generated manually by the observer.

The evaluation metrics were described in Section 1.10 of Chapter 1. The volumes were computed by multiplying the area enclosed by the boundary with the ISD. We used volume error (δV) and absolute volume error ($|\delta V|$) as the volume-based metrics. We computed δV and $|\delta V|$ for the MAB (δV_{MAB} and $|\delta V_{MAB}|$), LIB (δV_{LIB} and $|\delta V_{LIB}|$), and VWV (δV_{VWV} and $|\delta V_{VWV}|$). The overall mean volume error for the 3DUS image set is obtained by averaging the δV, whereas the overall absolute mean volume error is considered as the geometric mean of the $|\delta V|$.

We used CV to compare the reproducibility of the algorithm and manual method for the generation of VWV. We also computed the MDD [33] of VWV for the algorithm and manual segmentation. The MDD is used to determine the change in the VWV between two successive measurements that can be detected at a given confidence level.

Average boundaries were computed from repeated segmentations and were used for computing region-based and distance-based metrics. Similar to evaluation of the 2D method [3], the DSC was used as a region-based measure to compare two segmentations for accuracy on slice-by-slice basis, and MAD and MAXD were used as as boundary distance-based metrics.

3.4 Results

The algorithm was evaluated for accuracy and intra-observer variability using 21 3DUS images with a fixed set of parameters as shown in Table 3.3. All of the results in this section were computed using four anchor points per slice. We report the results in terms of computational time, accuracy, and repeatability as follows.

3.4.1 Computational time and user interaction

The reported times were calculated as a mean of the 21 3DUS images, which have been segmented five times. A mean observer time of 8.3 ± 1.5 min was required to manually delineate the MAB and LIB from a 3DUS image on 11 transverse 2D slices. The algorithm required mean observer time of 1.6 ± 0.3 min for choosing four anchor points on the MAB and LIB with an ISD of 1 mm for a 3DUS image with 11 2D slices for segmentation. For the proposed 3D algorithm with an ISD of 1 mm for initialization, the observer is required to choose 88 points in total to segment the MAB and LIB from a 1 cm portion of the CCA similar to the 2D method [3]. However, the number of points required to initialize the algorithm is reduced to 48, 32, 24, and 16 points for ISDs of 2, 3, 4, and 10 mm for initialization, respectively.

In addition to the observer time for initialization, the algorithm required a mean computational time of 1.14 ± 0.83 min to segment a 3DUS image using a nonoptimized Matlab (Natick, MA, USA) implementation on a PC with Intel core i7 processor (Intel corporation, Santa Clara, CA) with a speed of 3.0 GHz. From the total computational time, mean computational time of 0.91 ± 0.8 min is used for computing local region-based image force for MAB segmentation.

3.4.2 Accuracy

The slice-by-slice comparison of the algorithm to manual segmentations for two 3DUS images is shown in Fig. 3.5 and 3.6, one with mild stenosis and one with moderate stenosis. Each column corresponds to the algorithm segmentation results generated with the corresponding ISD. The mean manual segmentations are shown as yellow continuous contours and the mean algorithm segmentations are shown as purple dashed contours. A single round of algorithm segmentations, along with the anchor points used for initialization, are shown as cyan dashed contours. For instance, for an ISD of 2 mm, every other slice is initialized, whereas for an ISD of 10 mm only the first and last slices are initialized. For the 3DUS image with a mild stenosis (see Fig. 3.5), even for an ISD of 10 mm, the algorithm contours for both the MAB and LIB are in good agreement with manual contours. However, for the 3DUS image with a moderate stenosis (see Fig. 3.6), the accuracy in terms of DSC for the entire slice set decreased with the increase of ISD, where the lowest DSC was reported for the ISD of 10 mm for both the MAB and LIB.

The comparison of the algorithm-generated MAB and LIB surfaces with an ISD of 3 mm to the manual segmentations for the same two 3DUS images used in Fig. 3.5 and 3.6 are shown in Fig. 3.7. The algorithm-generated surfaces (shown in purple) are overlaid with the manually-generated surfaces (shown in yellow), where the algorithm surfaces appear smoother than the manual segmentations. This is due to incorporation of an smoothness energy in the algorithm, and 3D segmentation of every slice at slice thickness of 0.15 mm, while manual segmentations were generated at an ISD of 1 mm.

The corresponding flattened VWT maps [34] for the algorithm and the manual segmentations for the same two 3DUS images are shown in Fig. 3.8. In the flattened VWT map, the colour encodes the thickness between the MAB and LIB. Visually, the algorithm-generated flattened VWT map closely resembles the manual flattened VWT map.

The region-based and distance-based metrics results for the MAB and LIB for the 21 3DUS images are shown in Table 3.4. The results of the 2D segmentation

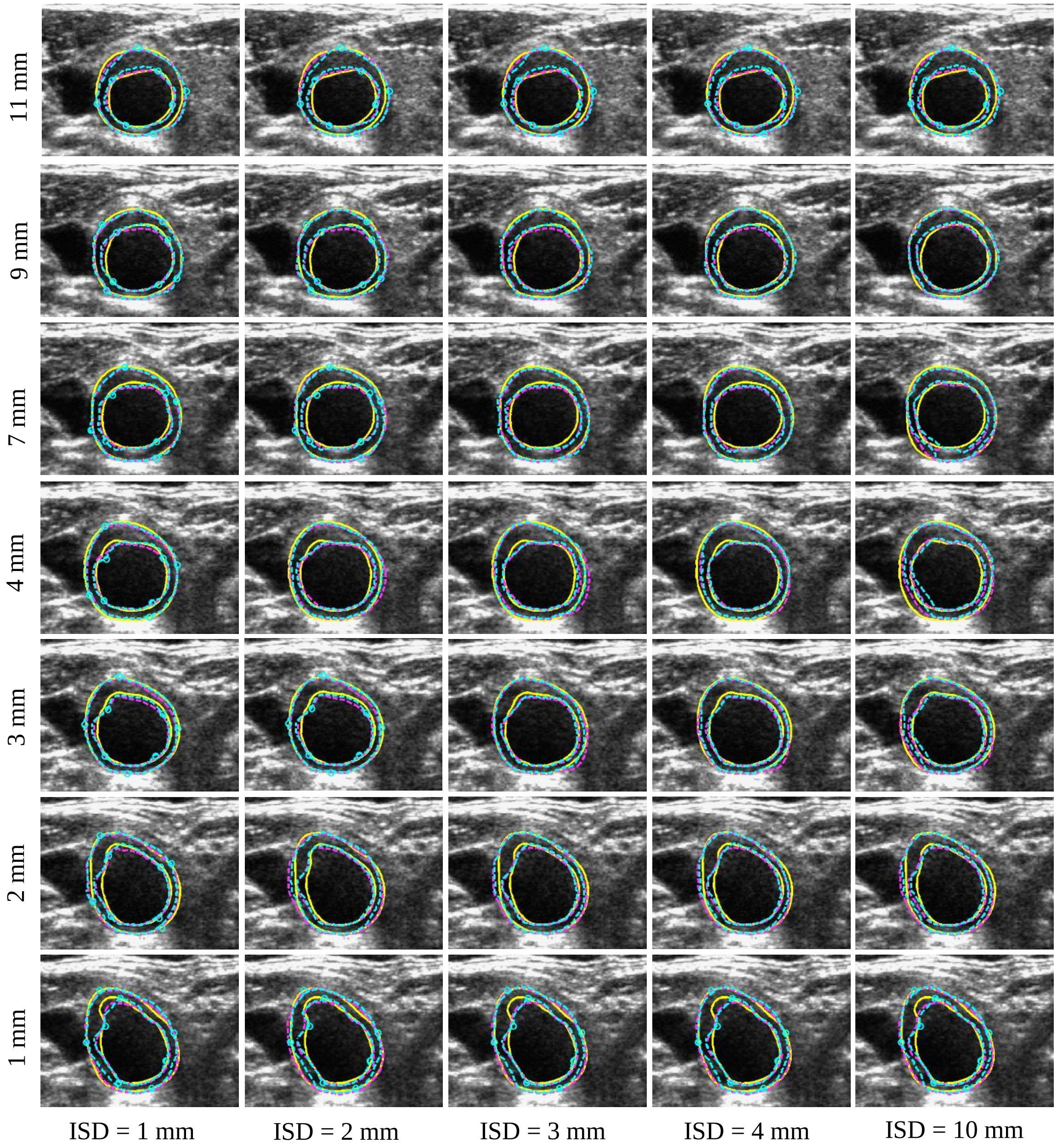
11 mm
9 mm
7 mm
4 mm
3 mm
2 mm
1 mm
ISD = 1 mm
ISD = 2 mm
ISD = 3 mm
ISD = 4 mm
ISD = 10 mm

Figure 3.5: 2D slice-by-slice comparisons of algorithm segmentations to manual segmentations for a subject with a mild stenosis. Results for ISD from 1–4, and 10 mm are shown. The contours are as follows: Continuous yellow contour mean manual MAB and LIB, dashed purple contour mean algorithm MAB and LIB, and cyan dashed contour one round of algorithm MAB and LIB. Each row corresponds to the distance from the BF and each column corresponds to the ISD used for initialization.

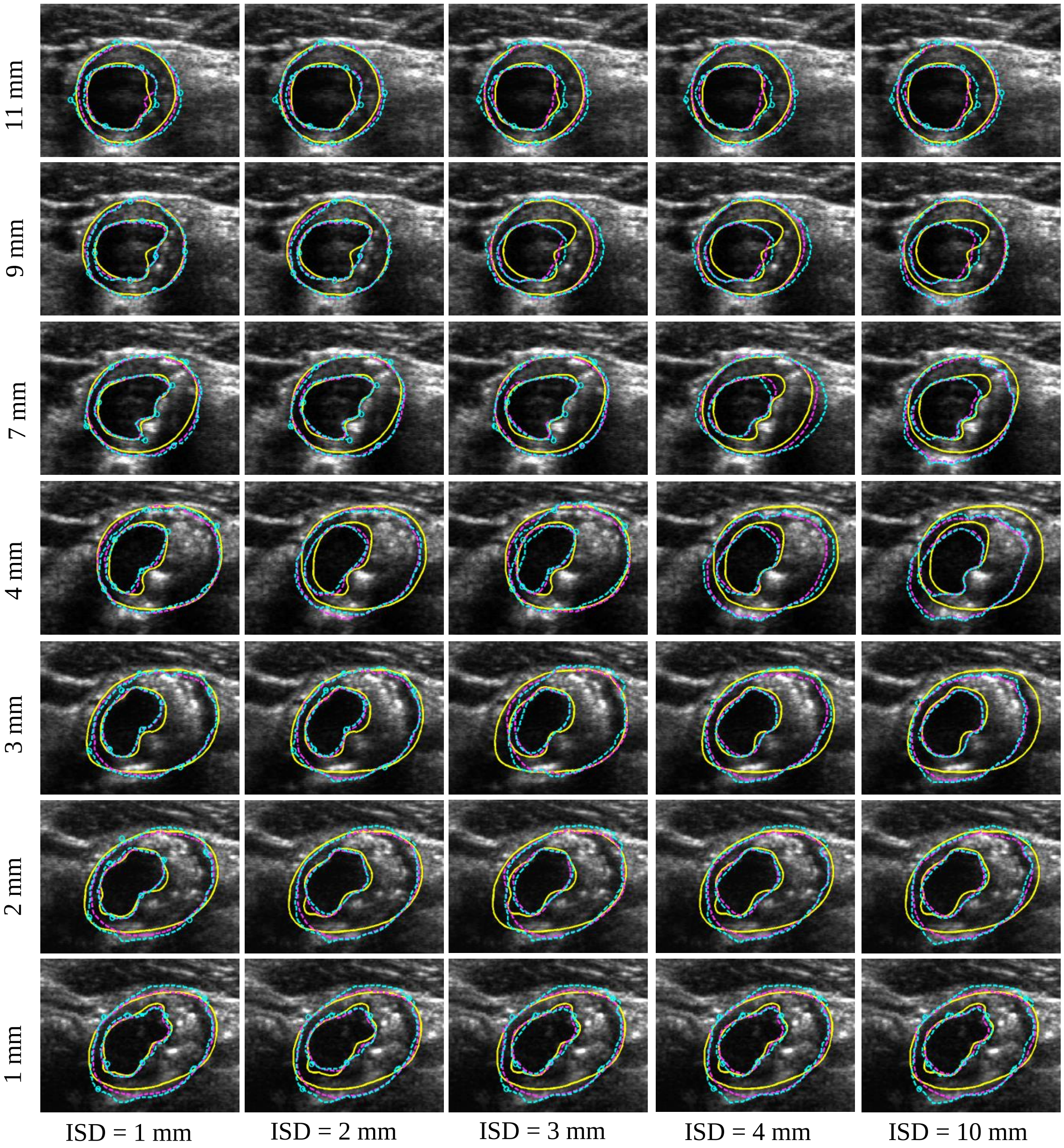
11 mm
9 mm
7 mm
4 mm
3 mm
2 mm
1 mm
ISD = 1 mm
ISD = 2 mm
ISD = 3 mm
ISD = 4 mm
ISD = 10 mm

Figure 3.6: 2D slice-by-slice comparisons of algorithm segmentations to manual segmentations for a subject with a moderate stenosis (stenosis is between 30% and 70%). Results for ISD from 1–4 mm, and 10 mm are shown. The accuracy dropped at 4 and 10 mm. The contours are as follows: Continuous yellow contour mean manual MAB and LIB, dashed purple contour mean algorithm MAB and LIB, and cyan dashed contour one round of algorithm MAB and LIB. Each row corresponds to the distance from the BF and each column corresponds to the ISD used for initialization.

method [3] are also included in Table 3.4 for a direct comparison with the proposed 3D algorithm. We evaluated the accuracy of the algorithm with varying ISDs from 1 to 4 and 10 mm. The metrics were computed by comparing the mean algorithm boundary with the mean manual boundary obtained from five repeated segmentations. The highest mean DSC for the MAB and LIB for the proposed 3D algorithm was reported for the ISD of 1 mm. As expected, the DSC gradually decreased with the increasing ISD for both the carotid MAB and LIB. At all ISDs, the MAB yielded a higher DSC than the LIB. The SD of DSC were small and gradually increased with the ISD for both the MAB and LIB, except at ISD of 4 mm for the LIB. Paired t-tests have been performed to evaluate the significance of the DSC measurements of the 2D [3] and 3D methods. The 3D algorithm is significantly different from the 2D method at all the tested ISDs.

Similar to the trend in DSC results, both MAD and MAXD errors increased with increasing ISD for both the MAB and LIB. Similar to the 2D method [3], the 3D algorithm yielded sub-millimeter errors for MAD and its SDs for all ISDs. Except for MAD at ISD of 1 mm, MAD errors of the 3D algorithm were statistically significantly different from MAD errors of the 2D method [3]. MAXD errors ranged from 0.75 to 1.19 mm for the MAB and 0.3 to 1.49 mm for the LIB, where the highest MAXD was reported for ISD of 10 mm. Except for MAXD errors for the MAB at the ISD of 1 mm, MAXD errors of the 3D algorithm were significantly different from MAXD errors of the 2D method [3].

Table 3.5 shows the volume-based evaluation results for the 3D algorithm for ISDs from 1 to 4 and 10 mm. The results of the 2D segmentation method [3] are also included in Table 3.5 for direct comparison. For the VWV measurements, the algorithm underestimated the volumes for ISD of 1, 4, and 10 mm and slightly overestimated for ISD of 2 and 3 mm. Similar to the trend in the region-based and distance-based evaluation results, the absolute VWV error $|\delta V_{VWV}|$ gradually increased from 4.32% to 13.28% with the increase of ISD. The absolute volumes errors ($|\delta V_{VWV}|$, $|\delta V_{MAB}|$, and $|\delta V_{LIB}|$) for the proposed 3D algorithm were not significantly different from the results of the 2D segmentation for the ISDs of 1 to 3 mm. However, the $|\delta V_{VWV}|$ results for the ISDs of 4 and 10 mm were significantly different.

The p-values for the hypothesis test that compares the mean VWV of the algorithm and manual segmentation using a two-way repeated measures ANOVA are shown in Table 3.6, along with the mean difference and the CI of the mean differ-

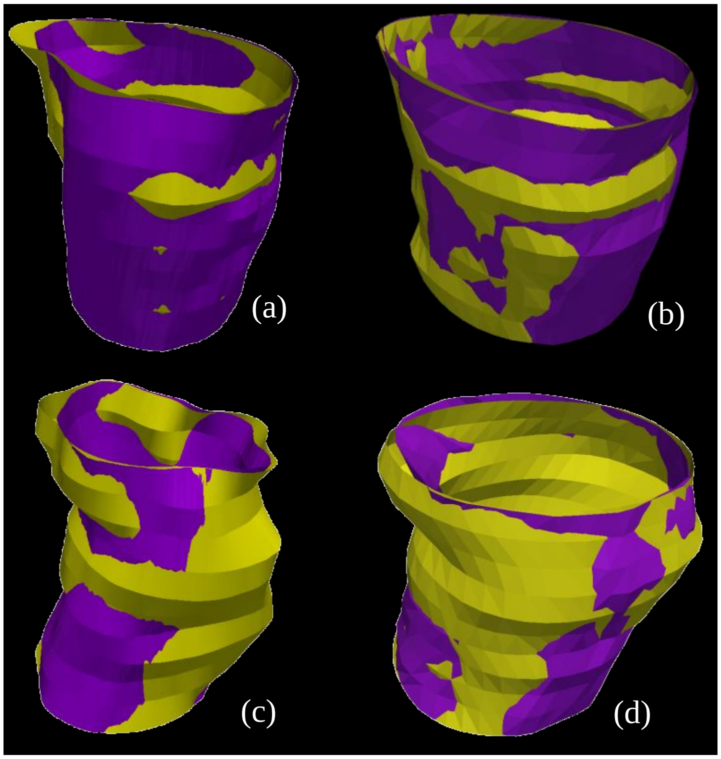

Figure 3.7: Comparison of the MAB and LIB algorithm segmentations to manual segmentations for an ISD of 3 mm for two example 3DUS images that were used for Fig. 6 and 7. The algorithm-generated surfaces are shown in purple and the manually-generated surfaces are shown in yellow. (a) LIB surface comparison with manual segmentation for a subject with a mild stenosis; (b) MAB surface comparison with manual segmentation of the same subject; (c) LIB surface comparison with manual segmentation for a subject with a moderate stenosis; and (d) MAB surface comparison with manual segmentation of the same subject.

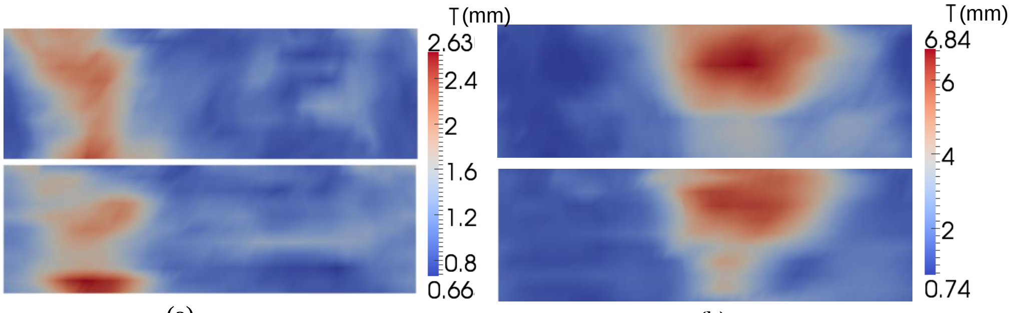

(a) (b)

Figure 3.8: Algorithm and manually-generated flattened VWT maps of the surfaces shown in Fig. 8 for the same two example 3DUS images. The first row corresponds to algorithm-generated flattened VWT maps, whereas second row corresponds to manually-generated flattened VWT maps. (a) Subject with a mild stenosis; and (b) Subject with a moderate stenosis.

ence of the algorithm- and manually-generated VWV. As indicated by the p-values in Table 3.6, the algorithm failed to show a significant difference for ISDs of 1, 2, 3, and 4 mm, with respect to the manually generated VWV. However, manually and algorithm-generated VWVs at ISD of 10 mm are significantly different. In comparison to the 2D method [3], the 3D algorithm also failed to show a significant difference for ISDs of 1, 2, and 3 mm, while there was significant difference for ISDs of 4 and 10 mm.

Figure 3.9 shows the Bland-Altman plot [35] for the comparison of algorithm- and manually-generated VWV for an ISD of 3 mm. The algorithm had a small bias (0.64 mm^3) and a small CI of -23.5–22.7 mm^3, which is relatively small compared to the 244–926 mm^3 range of the VWV. An example correlation plot for algorithm- and manually-generated VWV is shown for ISD of 3 mm in Fig. 3.10. The black dashed line indicates 95% CI of Pearson correlation coefficient (r). The Pearson correlation coefficient is also shown in Table 3.10, along with their p-values and 95% CI. The correlation of algorithm- and manually-generated VWVs were in the range of 0.95 to 0.97 for ISDs of 1 to 4 mm and 0.89 for ISD of 10 mm. They were also significantly correlated ($p < 0.0001$) with manually-generated VWVs for all tested ISDs.

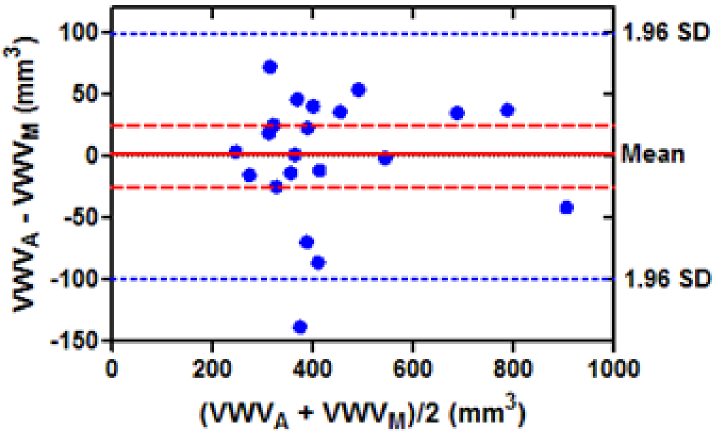

Figure 3.9: Bland-Altman plot for comparing algorithm- and manually-generated 3DUS VWV, where ISD of 3 mm is used for the algorithm initialization. The red continuous line indicates the bias, the blue dotted lines indicate the level of agreement, and the red dashed lines indicate the 95% CI.

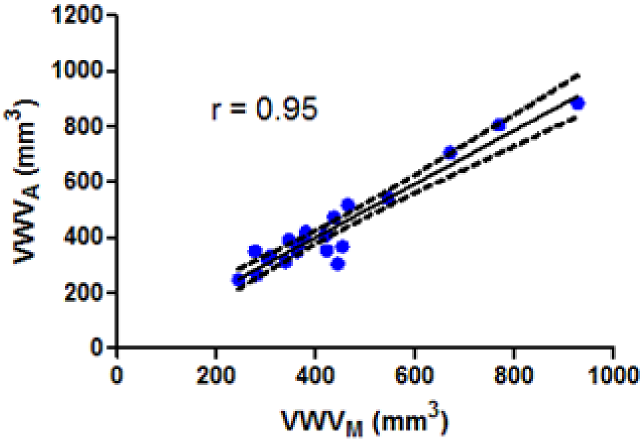

Figure 3.10: Correlation plot for algorithm- and manually-generated 3DUS VWV, where ISD of 3 mm is used for the algorithm initialization. The dashed lines indicate the 95% CI of the best fit line.

Table 3.4: Results for the MAB and LIB segmentation using region-based and distance-based metrics for the 21 3DUS images using the average boundaries. The results of the 3D algorithm are given for ISD of 1, 2, 3, 4, and 10 mm.

Metric	2D method	3D method (ISD varied from 1–4 mm and 10 mm)				
		1 mm	2 mm	3 mm	4 mm	10 mm
DSC_{MAB} (%)	95.4 ± 1.6	95.03 ± 1.77	94.57 ± 2.01	94.4 ± 2.24	93.53 ± 3.83	90.4 ± 4.3
DSC_{LIB} (%)	93.1 ± 3.1	92.09 ± 4.23	91.08 ± 4.46	90.64 ± 4.97	89.24 ± 5.87	84.85 ± 5.6
MAD_{MAB} (mm)	0.2 ± 0.1	0.24 ± 0.08	0.27 ± 0.10	0.28 ± 0.18	0.31 ± 0.19	0.46 ± 0.23
MAD_{LIB} (mm)	0.2 ± 0.1	0.22 ± 0.10	0.34 ± 0.16	0.35 ± 0.16	0.40 ± 0.19	0.54 ± 0.26
$MAXD_{MAB}$ (mm)	0.6 ± 0.3	0.75 ± 0.69	0.83 ± 0.85	0.89 ± 0.82	0.92 ± 1.00	1.19 ± 0.87
$MAXD_{LIB}$ (mm)	0.7 ± 0.6	0.3 ± 1.05	0.91 ± 0.51	0.97 ± 0.62	1.13 ± 0.82	1.49 ± 0.97

Table 3.5: Results for the VWV, MAB, and LIB using volume-based metrics for the 21 3DUS images. The results of the 3D algorithm are given for ISD of 1, 2, 3, 4, and 10 mm.

Metric	2D method	3D method (ISD varied from 1–4 mm and 10 mm)				
		1 mm	2 mm	3 mm	4 mm	10 mm
δV_{VWV} (%)	-0.9± 6.6	-3.22 ± 9.65	1.02 ± 12.32	0.56 ± 12.42	-5.5 ± 13.1	-12.7 ± 17.65
δV_{VWV} (mm^3)	-5.08± 26.5	-15.45± 38.9	2.28± 47.44	0.64± 49.54	-23.60± 52.47	-59.8 ± 73.5
δV_{MAB} (%)	-1.3± 2.8	-0.03± 3.08	2.28 ± 3.1	0.85 ± 9.25	-2.97 ± 4.12	-9.91± 7.11
δV_{LIB} (%)	-1.0 ± 6.4	3.60± 8.60	3.10 ± 4.0	-0.37 ± 49.5	-0.75 ± 12.42	-6.65± 17.16
$\lvert\delta V_{VWV}\rvert$ (%)	5.0± 4.3	4.32± 7.20	5.6 ± 8.5	5.64 ± 8.1	6.29± 9.78	13.28 ± 12.30
$\lvert\delta V_{MAB}\rvert$ (%)	2.5± 1.8	1.92± 1.69	2.53 ± 2.17	1.55± 2.45	2.79± 2.93	8.12 ± 6.50
$\lvert\delta V_{LIB}\rvert$ (%)	5.6± 3.0	2.8± 7.18	3.79± 7.54	4.43± 6.26	6.10 ± 8.56	10.63 ± 10.46

Table 3.6: Comparison of algorithm- and manually-generated VWV for 21 3DUS images using statistical testing and Pearson r. The results of the 3D algorithm are given for ISD of 1, 2, 3, 4, and 10 mm.

Metric	2D method	3D method (ISD varied from 1–4 mm and 10 mm)				
		1 mm	2 mm	3 mm	4 mm	10 mm
p-value	0.41	0.09	0.82	0.97	0.058	0.002
Mean (mm^3)	-5.1	-15.45	2.28	0.64	-23.6	-59.8
95% CI (mm^3)	$-17.4 - 7.2$	$-33.6 - 2.7$	-19.8–24.4	-23.5–22.7	-48.1–0.86	-94.1–25.5
Pearson r	0.97	0.97	0.96	0.95	0.95	0.89
p-value	< 0.0001	< 0.0001	< 0.0001	< 0.0001	< 0.0001	< 0.0001
95% CI for r	0.94–0.99	0.93–0.99	0.91–0.98	0.89–0.98	0.88–0.98	$0.75 - 0.95$

Table 3.7: Standard deviation (SD), coefficient-of-variation (CV), and minimum detectable difference (MDD) of volume measurements for 21 3DUS images computed using the repeated measurements of algorithm and manual segmentations. The results of the 3D algorithm are given for ISD of 1, 2, 3, 4, and 10 mm.

Metric	Manual	2D method	3D method (ISD from 1-4 mm and 10 mm)				
			1 mm	2 mm	3 mm	4 mm	10 mm
SD_{VWV} (mm^3)	18.1	23.2	20.85	24.35	27.13	34	40.7
CV_{VWV} (%)	3.89	5.1	4.97	5.57	6.8	8.23	10.82
CV_{MAB} (%)	1.53	2.36	2.47	2.78	3.4	3.6	5.25
CV_{LIB} (%)	3.3	3.5	3.12	2.34	3.7	4.88	6.18
MDD_{VWV} (mm^3)	50.3	64.2	57.8	67.5	75.2	94.2	112.9

3.4.3 Reproducibility

The intra-observer variability results of generating MAB and LIB volumes and VWV are shown in Table 3.7. The results of the previous 2D method [3] are also shown in Table 3.7 for direct comparison. The manual segmentation yielded the smallest CV_{VWV} and CV_{MAB}, although the proposed 3D algorithm reported the smallest CV_{LIB} at 2 mm. The CV_{VWV}, and CV_{MAB}, and MDD gradually increased with the increase in ISD for the proposed algorithm. The CV_{LIB} has a similar trend, except at 2 mm. The CVs for the 3D algorithm, especially for ISDs of 1 and 2 mm, are comparable to the CVs of the 2D algorithm. The MDDs of the proposed 3D algorithm were in the range of 57.8 to 112.9 mm^3, and the MDD increased with the increasing ISD. The MDD of the 3D algorithm at ISD of 1 mm is smaller than the 2D method, although the 3D algorithm reported slightly higher MDDs for ISD of 2 and 3 mm.

3.5 Discussion

In this chapter, we developed and evaluated a 3D semi-automated segmentation algorithm based on SFLS method to delineate the MAB and LIB of the CCA for the measurement of the VWV, which is a previously developed 3DUS-based measurement [32] of carotid atherosclerosis. As such, the purpose of the algorithm is to generate VWV measurements for monitoring patients being managed for risk of stroke using non-surgical methods [4, 5, 36]. In addition, the proposed algorithm may also be used for generation of VWT change maps [37] and analysis of vessel wall region for plaque characterization [38, 39]. Here, we discuss the technical details of our 3DUS VWV segmentation algorithm, computational time, measurement accuracy, measurement reproducibility, and comparison to previous methods.

3.5.1 Methodology

The proposed algorithm is an extension of the 2D slice-wise segmentation method [3] that we have described previously. We chose SFLS method over other level set methods for two main reasons. The SFLS method is an improvement to the narrow-band level set method [40], which is relatively less computationally expensive than classical level set methods [26, 28], which compute the level set function for the entire image.

Moreover, the SFLS method does not split the segmentation into multiple regions away from the zero level, thus disjoint regions are not generated in the segmentation.

In this chapter, we used the minimum and maximum intensity values of the 3DUS image for normalization of the entire image at once, due to both its simplicity and the ability to perform the normalization without any additional user interactions to identify bright intensities around adventitia. However, for a subsequent analysis of the segmented vessel wall region, which is very sensitive to variations in image intensity, such as texture analysis to differentiate plaque components [38], a more sophisticated normalization would be required to normalize the images [41, 42].

In the experiments, the observer chose four anchor points on initialization boundaries for any chosen ISD. However, in practice, the observer can choose more anchor points on each initialization boundary. The observer can also vary the ISD for each 3DUS image depending on the amount of plaque and the complexity of the plaque surface. We speculate that the accuracy and reproducibility of the segmentation may increase with the increasing number of anchor points, as indicated by the Fig. 9 in the 2D segmentation paper [3].

The 3D algorithm has been validated on 3DUS images from a single ultrasound device. However, different scanners could generate 3DUS images with different voxel sizes. The differences in voxel size across images do not affect the segmentation, because the thresholds and parameters of the algorithm are defined in millimeters. Such millimeter values are converted to voxel values of the current 3DUS image during the segmentation procedure.

The proposed 3D algorithm has some limitations. Although, the 3D algorithm reduces user interactions required for segmentation with an ISD greater than 1 mm in contrast to the 2D method [3], the 3D algorithm is still far from full automation due to the challenges in the segmentation of very low-contrast boundaries. In addition, the initial surface for the MAB is required to be close to the actual MAB for obtaining accurate segmentations, because the effect of the local region-based term is limited by its local radius r_L.

3.5.2 Computational time

The algorithm required lesser user time and fewer interactions to generate segmentations than manual delineations. The algorithm required a mean time of 1.6 min to initialize the MAB and LIB of the CCA from a 3DUS image for a portion of 1 cm with an ISD of 1 mm. In our experiments, the observer provided anchor points with an ISD of 1 mm. For ISDs more than or equal to 2 mm, the anchor points corresponding to the given ISD are chosen from the anchor point set generated with the ISD of 1 mm. If we assume that number of points used for initialization is linearly proportional to the time taken for the observer to actually choose anchor points, an observer would take approximately 0.58 min to initialize a 1 cm portion of the CCA with an ISD of 3 mm. In this case, the algorithm would require only 1.72 min of total time, which comprises of user interaction time of 0.58 min and SFLS algorithm computational time of 1.14 min. This is approximately 79% reduction in time (1.72 min vs. 8.3 min) in comparison manual segmentation.

In comparison to the previous 2D method [3], the 3D algorithm was able to reduce user interaction further, when ISD of more than or equal to 2 mm is used for the initialization. For example, with an ISD of 3 mm, the observer is required to initialize only 32 points in total on four slices for both the MAB and LIB as opposed to 88 points in 11 slices for segmenting the MAB and LIB from a 1 cm section of the CCA from a given 3DUS image. However, with the current nonoptimized Matlab implementation of the SFLS method, the proposed 3D algorithm required approximately similar computational time to the 2D method [3] (1.14 ± 0.83 min vs 1.2 ± 0.2 min). The main time-consuming task for the 3D algorithm is the local region-based force computation for the MAB segmentation, which requires about 80% (0.92 min out of 1.14 min) of the computational time. However, the local region-based force calculation can be performed independently for each point on the zero level set, thus the computation can be parallelized in a graphics processing unit (GPU), which may be able to substantially speed up the segmentation.

3.5.3 Accuracy

For 3DUS images with mild stenosis (see Fig. 3.5 for an example), accurate segmentations could be obtained even at ISD of 10 mm, because the CCA is more regular from one slice to the next over a 1 cm distance of the CCA. However, when the subject has moderate (see Fig. 3.6) or severe stenosis, the morphology of the artery could differ from one slice to its adjacent slice. Therefore, when an ISD, such as 10 mm is used, the generated initial surface for the 3D segmentation could be too far from the desired boundary for the algorithm to converge to the desired boundary.

The accuracy of the algorithm was evaluated with respect to distance-based, region-based, and volume-based metrics. The algorithm yielded DSCs in the range of 90.4–95.0 mm^3 for the MAB and 84.8–92.1 mm^3 for the LIB, where the DSC was highest for the ISD of 1 mm, for both the MAB and LIB, and then gradually decreased with the increase of ISD (see Table 3.4). Moreover, the 3D algorithm is statistically significantly different from the 2D method [3] at all the ISDs tested.

Similar to the trend in DSC results, both the MAD and MAXD errors were small and increased with increasing ISD for both the MAB and LIB (see Table 3.4). This may be due to the fact that the initial surface could be further away from desired segmentation with an increasing ISD, thus the algorithm could be trapped in local minima providing suboptimal results. To investigate the reduction in accuracy with increasing ISD, we computed the MAD error between the initial contours and the manual segmentation. The results show an increase in the MAD error with the ISD, with the highest being at an ISD of 10 mm. Except for the MAD at ISD of 1 mm, the MAD errors of the 3D algorithm were statistically significantly different from the MAD errors of 2D method [3]. The MAXD errors of the 3D algorithm were statistically significantly different from the MAXD errors of 2D method [3], except for the MAB at the ISD of 1 mm. The MAB always yielded a higher DSC than the LIB, because the observer may be able to locate anchor points for the MAB more robustly than for the LIB due to its regular shape. This is further supported by the fact that manual CV_{MAB} was smaller than manual CV_{LIB} (1.53% vs. 3.30% as shown in Table 3.7).

The main purpose of the 3D algorithm is for generating VWV measurements for monitoring plaque burden. Therefore, we extensively validated the accuracy and reproducibility of the algorithm for generating the VWV. The algorithm-generated VWV was significantly correlated ($p < 0.0001$) with the manually-generated VWV ($r > 0.95$ for ISDs of 1 to 4 mm, and $r = 0.89$ for ISD of 10 mm) with small 95% CI for Pearson r (see Table 3.6). We failed to detect a statistically significant difference ($p > 0.05$) between algorithm- and manually-generated VWV for ISD of 1 to 4 mm, although they were statistically significant for ISD of 10 mm. The values within the 95% CIs (i.e., CI of −23.5–22.7 mm^3 for ISD of 3 mm) of the VWV difference were small for ISDs of 1 to 4 mm, in comparison to their VWV range of 244–926 mm^3.

We computed both absolute and signed volume errors (see Table 3.5) as volume-based metrics to evaluate the algorithm. The signed volume error provides an indication of the bias of the algorithm, whereas the absolute volume error is a more stringent measure of the discrepancy between algorithm and manual measurements. The absolute VWV errors ($|\delta V_{VWV}|$) of the proposed 3D algorithm were in the range of 4.32–13.28%. However, $|\delta V_{VWV}|$ of the 3D algorithm were not significantly different from $|\delta V_{VWV}|$ of the 2D method for the ISDs of 1–3 mm. However, $|\delta V_{VWV}|$ results for the ISDs of 4 and 10 mm were significantly different. For the ISD of 1, 4, and 10 mm, the algorithm underestimated the VWV. The underestimation of VWV could be mainly due to either the MAB volume is underestimated and/or the LIB volume is overestimated, except for ISD of 10 mm, where both the MAB and LIB volumes were underestimated (see Table 3.5). For ISD of 1 mm, the underestimation of VWV occurred mainly due to the overestimation of the LIB. For ISD of 4 and 10 mm, the underestimation occurred due to the underestimation of the MAB (see Table 3.5). We observed that for ISDs more than 2 mm, the initial surface is mostly enclosed within the desired surface. When the initial surface is further away from the desired boundary, the MAB segmentation could be trapped in local minima because its region-based energy is dependent only on local statistics, which finally leads to underestimating the MAB volume. Although global-region based energy is used for LIB segmentation to avoid this issue, it is not used for MAB segmentation, because of inhomogeneity of the inside and outside intensities for the MAB. However, since LIB is constrained by the MAB segmentation, when the MAB volume is underestimated, the LIB volume may also be underestimated.

3.5.4 Reproducibility

We used CV and the MDD (see Table 3.7) to evaluate the intra-observer variability of the algorithm for computing VWV from repeated measurements. The algorithm yielded small CV_{VWV} (e.g., 5.57% for ISD of 3 mm) that are comparable with the CVs for manual segmentation and the 2D method [3]. The CV_{VWV} also increased with the increase of ISD, which may be due to larger differences in initial surfaces between repetitions for large ISD than for small ISD. Two sample F-tests were carried out to determine the statistical significant difference of the variance of the proposed method with manual segmentation and the 2D method [3]. The F-tests failed to show that the variances of the proposed methods are significantly different from the variances of the manual segmentation and the 2D method [3] for all the ISDs.

Manual CV_{VWV} (3.89%) was comparable with the previously reported manual intra-observer CV_{VWV} values of 4.6% by Egger *et al.* [32] and 4.7% by Egger *et al.* [43]. Apart from the effect caused by different datasets, the reason for slightly lower manual CV_{VWV} of ours could be due to two main reasons. In our study, the observer set the BF and axis for each 3DUS image only once and used them for other repetitions, as opposed to setting different BF and axis for each repetition. In addition, our study used only VWV of the CCA, whereas their study used VWV of the ICA and ECA in addition to VWV of CCA.

Manual CV_{VWV} was also smaller than the algorithm CV_{VWV} (3.9% vs. 4.97–10.82%). Although, manual CV_{MAB} was smaller than algorithm CV_{MAB}, manual CV_{LIB} is larger than the algorithm CV_{LIB} for ISD of 1 and 2 mm. In addition, CV_{MAB} was always smaller than the corresponding CV_{LIB}. This could be due to the fact that the observer can more accurately locate the MAB for choosing anchor points, because of its smooth and low order shape. The MDD values (see Table 3.7) of the proposed algorithm increased with increased ISD. Although algorithm MDDs were larger than the manual MDD, the MDD results of the proposed algorithm was smaller than a previously reported VWV change of $\approx 120\ \text{mm}^3/\text{yr}$ [36], which suggests that a follow up period of 1 yr could be used for any ISD, although, for ISD of 1 and 2 mm, even seven month period may be suitable as follow up.

3.5.5 Comparison to previous methods

There are three previous 2D segmentation methods [2, 3, 6], reported in the literature that segment both the MAB and LIB from 3DUS images as shown in Table 3.1. Out of these three methods, the one proposed by Ukwatta *et al.* [3] is currently used in clinical trials [5]. Therefore, in this paper, we compared the accuracy, intra-observer variability, user interaction, and the computational time of the proposed method to the 2D segmentation method [3]. Although the accuracy, intra-observer variability, and computational time of the proposed 3D algorithm is comparable to the 2D method [3], there are two main advantages of the proposed 3D algorithm over previous methods [2, 3, 6]. One advantage is the reduction of number of anchor points for initialization, which translates into overall reduction of total segmentation time.

For instance for ISD of 3 mm, the number of anchor points required for segmenting 1 cm section of the CCA from a 3DUS image is 32, as opposed to 88 with an ISD of 1 mm. The other advantage is the ability to generate the segmentation at each voxel interval (typically 0.15 mm) along the long axis direction in much less time than a 2D segmentation method. For example, for segmentation of a 1 cm section of the CCA at ISD of 0.15 mm, the 2D method [3] would require 17 min (67 slices where 11 slices require 2.8 min). However, the proposed algorithm would require about 1.72 min to segment the image at ISD of 0.15 mm with an initialization ISD of 3 mm.

The 2D segmentation method proposed by Ukwatta *et al.* [3] requires a total segmentation time of 2.8 min and the one proposed by Yang *et al.* [2] reported 4.4 min to segment the CCA from a 3DUS image. The total segmentation time for the proposed algorithm with an ISD of 3 mm is approximately 1.72 min, which is less than the previous methods. However, note that the algorithm computational times of the proposed 3D method are not directly comparable to the computational times proposed by Yang *et al.* [2], due to differences in hardware and datasets used in the papers.

3.5.6 Selection of proper ISD

Based on the evaluation results, more suitable ISDs for initialization are 2 and 3 mm, which use fewer user interactions for initialization than the 2D method [3], while maintaining a DSC of more than 90%, CV_{VWV} less than or equal to 6.8%, $|\delta V_{VWV}|$ less than or equal to 5.64%, and a bias as small as 2.28 and 0.64 mm^3, in comparison to VVWs in the range of 244–926 mm^3 for VWV computation. After selecting an ISD for a study computing VWV, our results can also be used to estimate the number of subjects that must be monitored in a clinical trial to detect a desired average regression in VWV at a desired power and significance [33, 44]:

$$n \geq \frac{2(Z_\alpha + Z_\beta)^2 SD_{VWV}^2}{M_d^2}, \tag{3.14}$$

where n is the number of subjects, M_d is the desired mean difference in VWV, Z_α is the standard normal deviate exceeded in either direction with probability α, and Z_β is the standard normal deviate exceeded in one direction with probability β, where $1 - \beta$ is the desired power [33]. SD_{VWV} is the standard deviation of the repeated measurements of VWV as shown in Table 3.7. For example for an ISD of 3 mm, $SD_{VWV} = 27.13$ mm^3, $\alpha = 0.05$, and $\beta = 0.2$ (hence, $Z_\alpha = 1.96$ and $Z_\beta = 0.842$) to measure a mean VWV regression of 30 mm^3 with a 95% confidence interval, which was in fact the mean VWV regression of a patient group in a statin drug trial [36] of 3 months, the minimum number of patients required is 13.

References

[1] E. Ukwatta, J. Yuan, D. Buchanan, B. Chiu, J. Awad, W. Qiu, G. Parraga, and A. Fenster, “Three-dimensional segmentation of three-dimensional ultrasound carotid atherosclerosis using sparse field level sets,” *Medical physics*, vol. 40, p. 052903, 2013. 86

[2] X. Yang, J. Jin, W. He, M. Yuchi, and M. Ding, “Segmentation of the common carotid artery with active shape models from 3d ultrasound images,” in *Proc. of SPIE Vol*, vol. 8315, 2012, pp. 83 152H–1. 86, 87, 88, 115, 116

[3] E. Ukwatta, J. Awad, A. D. Ward, D. Buchanan, J. Samarabandu, G. Parraga, and A. Fenster, “Three-dimensional ultrasound of carotid atherosclerosis: Semiautomated segmentation using a level set-based method,” *Medical Physics*, vol. 38, p. 2479, 2011. 86, 87, 88, 89, 91, 95, 96, 99, 100, 104, 106, 110, 111, 112, 113, 114, 115, 116

[4] I. Shai, J. D. Spence, D. Schwarzfuchs, Y. Henkin, G. Parraga, A. Rudich, A. Fenster, C. Mallett, N. Liel-Cohen, A. Tirosh *et al.*, “Dietary intervention to reverse carotid atherosclerosis,” *Circulation*, vol. 121, no. 10, p. 1200, 2010. 86, 110

[5] D. N. Buchanan, T. Lindenmaier, S. McKay, Y. Bureau, D. G. Hackam, A. Fenster, and G. Parraga, “The relationship of carotid three-dimensional ultrasound vessel wall volume with age and sex: comparison to carotid intima-media thickness,” *Ultrasound in medicine & biology*, 2012. 86, 110, 115

[6] E. Ukwatta, J. Awad, A. D. Ward, D. Buchanan, G. Parraga, and A. Fenster, “Coupled level set approach to segment carotid arteries from 3D ultrasound images,” in *Biomedical Imaging: From Nano to Macro, 2011 IEEE International Symposium on*, 2011, pp. 37–40. 87, 88, 115

[7] I. Solovey, “Segmentation of 3d carotid ultrasound images using weak geometric priors,” *M. S. thesis, The University of Waterloo, Canada*, 2010. 87, 88

[8] J. D. Gill, H. M. Ladak, D. A. Steinman, and A. Fenster, “Accuracy and variability assessment of a semiautomatic technique for segmentation of the carotid

arteries from three-dimensional ultrasound images," *Medical Physics*, vol. 27, p. 1333, 2000. 87, 88

[9] J. Guerrero, S. Salcudean, J. McEwen, B. Masri, and S. Nicolaou, "Real-Time vessel segmentation and tracking for ultrasound imaging applications," *IEEE Transactions on Medical Imaging*, vol. 26, no. 8, pp. 1079–1090, Aug. 2007. 87, 88

[10] P. Abolmaesumi, M. Sirouspour, and S. Salcudean, "Real-time extraction of carotid artery contours from ultrasound images," in *Computer-Based Medical Systems, 2000. CBMS 2000. Proceedings. 13th IEEE Symposium on*, 2000, pp. 181–186. 87, 88

[11] A. Zahalka and A. Fenster, "An automated segmentation method for three-dimensional carotid ultrasound images," *Physics in Medicine and Biology*, vol. 46, no. 4, pp. 1321–1342, Apr. 2001, PMID: 11324967. 87, 88

[12] F. Mao, J. Gill, D. Downey, and A. Fenster, "Segmentation of carotid artery in ultrasound images," in *Engineering in Medicine and Biology Society, 2000. Proceedings of the 22nd Annual International Conference of the IEEE*, vol. 3, 2000, pp. 1734–1737. 87, 88

[13] F. Molinari, G. Zeng, and J. S. Suri, "A state of the art review on intima-media thickness (IMT) measurement and wall segmentation techniques for carotid ultrasound," *Computer methods and programs in biomedicine*, vol. 100, no. 3, pp. 201–221, 2010. 86

[14] C. P. Loizou, C. S. Pattichis, M. Pantziaris, T. Tyllis, and A. Nicolaides, "Snakes based segmentation of the common carotid artery intima media," *Medical & Biological Engineering & Computing*, vol. 45, no. 1, pp. 35–49, Jan. 2007, PMID: 17203319. 86

[15] F. Molinari, G. Zeng, and J. S. Suri, "An integrated approach to Computer-Based automated tracing and its validation for 200 common carotid arterial wall ultrasound images," *Journal of Ultrasound in Medicine*, vol. 29, no. 3, p. 399, 2010. 86

[16] S. Golemati, J. Stoitsis, E. G. Sifakis, T. Balkizas, and K. S. Nikita, "Using the hough transform to segment ultrasound images of longitudinal and transverse sections of the carotid artery," *Ultrasound in Medicine & Biology*, vol. 33, no. 12, pp. 1918–1932, Dec. 2007. 86

[17] J. Noble and D. Boukerroui, "Ultrasound image segmentation: a survey," *Medical Imaging, IEEE Transactions on*, vol. 25, no. 8, pp. 987–1010, 2006. 88, 92

[18] E. Ukwatta, J. Awad, D. Buchanan, G. Parraga, and A. Fenster, "Three-dimensional semi-automated segmentation of carotid atherosclerosis from three-dimensional ultrasound images," in *Proc. of SPIE Vol*, vol. 8315, 2012, pp. 83 150O–1. 89

[19] P. Touboul, M. Hennerici, S. Meairs, H. Adams, P. Amarenco, and e. a. Bornstein, N., "Mannheim carotid Intima-Media thickness consensus (2004-2006)," *Cerebrovascular Diseases*, vol. 23, no. 1, pp. 75–80, 2007. 91, 97

[20] X. Papademetris, A. J. Sinusas, D. P. Dione, and J. S. Duncan, "Estimation of 3D left ventricular deformation from echocardiography," *Medical Image Analysis*, vol. 5, no. 1, pp. 17–28, Mar. 2001. 91

[21] P. Perona and J. Malik, "Scale-space and edge detection using anisotropic diffusion," *Pattern Analysis and Machine Intelligence, IEEE Transactions on*, vol. 12, no. 7, pp. 629–639, 1990. 92

[22] Y. Yu and S. T. Acton, "Speckle reducing anisotropic diffusion," *Image Processing, IEEE Transactions on*, vol. 11, no. 11, pp. 1260–1270, 2002. 92

[23] S. D. Pathak, V. Chalana, D. R. Haynor, and Y. Kim, "Edge-guided boundary delineation in prostate ultrasound images," *IEEE Transactions on Medical Imaging*, vol. 19, no. 12, pp. 1211–1219, Dec. 2000, PMID: 11212369. 92

[24] J. Canny, "A computational approach to edge detection," *Pattern Analysis and Machine Intelligence, IEEE Transactions on*, no. 6, pp. 679–698, 1986. 92

[25] R. T. Whitaker, "A Level-Set approach to 3D reconstruction from range data," *Int. J. Comput. Vision*, vol. 29, no. 3, pp. 203–231, 1998. 93

[26] S. Osher and J. A. Sethian, "Fronts propagating with curvature dependent speed: algorithms based on Hamilton-Jacobi formulations," 1988. 93, 110

[27] T. F. Chan and L. A. Vese, "Active contours without edges," *Image Processing, IEEE Transactions on*, vol. 10, no. 2, pp. 266–277, 2001. 93, 94, 96

[28] S. Lankton and A. Tannenbaum, "Localizing Region-Based active contours," *IEEE Transactions on Image Processing*, vol. 17, no. 11, pp. 2029–2039, Nov. 2008. 94, 95, 110

[29] J. Awad, A. Owrangi, L. Villemaire, E. ORiordan, G. Parraga, and A. Fenster, "Three-dimensional lung tumor segmentation from x-ray computed tomography using sparse field active models," *Medical Physics*, vol. 39, p. 851, 2012. 94

[30] V. Caselles, R. Kimmel, and G. Sapiro, "Geodesic active contours," *International Journal of Computer Vision*, vol. 22, no. 1, pp. 61–79, Feb. 1997. 95

[31] A. Fenster, D. Downey, and H. Cardinal, "Three-dimensional ultrasound imaging," *Physics in medicine and biology*, vol. 46, no. 5, p. R67, 2001. 99

[32] M. Egger, J. D. Spence, A. Fenster, and G. Parraga, "Validation of 3D ultrasound vessel wall volume: an imaging phenotype of carotid atherosclerosis," *Ultrasound in medicine & biology*, vol. 33, no. 6, pp. 905–914, 2007. 99, 110, 115

[33] J. R. Mitchell, S. J. Karlik, D. H. Lee, M. Eliasziw, G. P. Rice, and A. Fenster, "The variability of manual and computer assisted quantification of multiple sclerosis lesion volumes," *Medical Physics*, vol. 23, no. 1, pp. 85–97, 1996. 100, 116

[34] B. Chiu, M. Egger, D. J. Spence, G. Parraga, and A. Fenster, "Area-preserving flattening maps of 3D ultrasound carotid arteries images," *Med. Image Anal.*, vol. 12, no. 6, pp. 676–688, 2008. 101

[35] D. Altman and J. Bland, "Measurement in medicine: the analysis of method comparison studies," *The statistician*, pp. 307–317, 1983. 106

[36] A. Krasinski, B. Chiu, J. D. Spence, A. Fenster, and G. Parraga, "Three-dimensional ultrasound quantification of intensive statin treatment of carotid atherosclerosis," *Ultrasound in medicine & biology*, vol. 35, no. 11, pp. 1763–1772, 2009. 110, 115, 117

[37] B. Chiu, M. Egger, J. D. Spence, G. Parraga, and A. Fenster, "Quantification of carotid vessel wall and plaque thickness change using 3D ultrasound images," *Medical physics*, vol. 35, p. 3691, 2008. 110

[38] J. Awad, A. Krasinski, G. Parraga, and A. Fenster, "Texture analysis of carotid artery atherosclerosis from three-dimensional ultrasound images," *Medical Physics*, vol. 37, no. 4, pp. 1382–1391, Apr. 2010. 110, 111

[39] F. Molinari, W. Liboni, P. Giustetto, E. Pavanelli, S. Giordano, and J. S. Suri, "Use of ultrasound contrast agents in plaque characterization," in *Atherosclerosis Disease Management*. Springer, 2011, pp. 195–219. 110

[40] D. Adalsteinsson and J. A. Sethian, "A fast level set method for propagating interfaces," *Journal of Computational Physics*, vol. 118, no. 2, pp. 269 – 277, 1995. 110

[41] C. P. Loizou, C. S. Pattichis, M. Pantziaris, T. Tyllis, and A. Nicolaides, "Quality evaluation of ultrasound imaging in the carotid artery based on normalization and speckle reduction filtering," *Medical and Biological Engineering and Computing*, vol. 44, no. 5, pp. 414–426, 2006. 111

[42] F. Molinari, G. Krishnamurthi, U. R. Acharya, S. V. Sree, G. Zeng, L. Saba, A. Nicolaides, and J. S. Suri, “Hypothesis validation of far-wall brightness in carotid-artery ultrasound for feature-based imt measurement using a combination of level-set segmentation and registration,” *Instrumentation and Measurement, IEEE Transactions on*, vol. 61, no. 4, pp. 1054–1063, 2012. 111

[43] M. Egger, A. Krasinski, B. K. Rutt, A. Fenster, and G. Parraga, “Comparison of b-mode ultrasound, 3-dimensional ultrasound, and magnetic resonance imaging measurements of carotid atherosclerosis,” *Journal of Ultrasound in Medicine*, vol. 27, no. 9, p. 1321, 2008. 115

[44] P. Armitage, G. Berry, and J. N. S. Matthews, *Statistical methods in medical research*. Wiley-Blackwell, 2008. 116

Chapter 4

3D carotid multi-region MRI segmentation by globally optimal evolution of coupled surfaces†

4.1 Introduction

Excellent soft-tissue contrast and noninvasiveness of MR imaging make it ideally suited for *in vivo* carotid imaging; as well as obtaining volumetric and morphological measurements for monitoring carotid atherosclerosis [2]. Numerous studies have established the application of MRI in quantifying measurements including VWV [3], plaque composition [4, 5], and inflammation [6] etc. In order to compute such measurements, it is required to accurately delineate the carotid adventitia (AB) and lumen-intima (LIB) boundaries of the CCA, ICA, and ECA (as illustrated in Fig. 4.1 and 1.11 in Chapter 1) from 3D carotid MR images.

The main objective of this chapter is to introduce a novel 3D multi-region segmentation approach for delineating the AB and LIB surfaces from T1-weighted (T1w) black-blood carotid MR images (also known as "vessel wall images") efficiently and robustly. A fast and robust identification of the carotid AB and LIB from MR images may greatly assist a comprehensive analysis of carotid atherosclerosis, and accelerate the translation of these measurements to clinical researches and applications.

4.1.1 Previous studies

We summarize the previous studies of LIB and/or AB segmentation from the 3D black-blood carotid MR images into two categories (see Table 4.1): methods that segment both the carotid AB and LIB, and ones that segment only the LIB.

---

†. A version of this chapter has been published [1]: E. Ukwatta, J. Yuan, M. Rajchl, W. Qiu, D. Tessier, and A. Fenster, "3D carotid multi-region MRI segmentation by globally optimal evolution of coupled surfaces," in *IEEE Transactions on Medical Imaging,* 32(4), 770-85 2013.

Table 4.1: Previous studies describing carotid LIB and/or AB segmentation methods for black-blood MR imaging.

Paper	Year	Dim.	LIB	AB	Artery	# of images	Time (s)	Other information
Adame [7]	2004	2D	Fuzzy clustering	Ellipse fitting	CCA	50 slices	25s/slice /boundary	User interaction on each slice.
Klooster [8]	2011	3D	Surface fitting	Surface fitting	CCA	45	48 s	MRA images & registration required.
Kerwin [9]	2007	2D	B-spline snakes	B-spline snakes	CCA, ICA	26	–	ICA & ECA segmented separately.
Ladak [10]	2001	2D	Parametric deformable model	Parametric deformable model	CCA, ICA	4	–	CCA & ICA segmented separately.
Yuan [11]	1999	2D	Snakes	Snakes	CCA, ICA	5	20s-2min/slice /boundary	User interaction on each slice.
Tang [12]	2010	3D	Active contours	–	CCA, ICA, ECA	76	–	MRA images required.
Ladak [13]	2000	3D	Parametric deformable model	–	CCA, ICA, ECA		60 s	Accuracy results not reported.
Jin [14]	2004	3D	Parametric deformable model	–	CCA, ICA, ECA	5	3 min	Manually drawn centerline.

Most previous techniques [7, 9, 10, 11] that segment both the AB and LIB from 3D carotid MR images are performed in a 2D slice-by-slice manner. For example, Adame *et al.* [7] and Kerwin *et al.* [9] proposed to segment the carotid AB and LIB separately on each transverse (also referred to as "short-axis") slice of the carotid CCA and ICA based on 2D parametric deformable models. Their methods were also used in clinical studies [15, 16]. Recently, Klooster *et al.* [8] introduced a five-step approach, where the carotid LIB surface of the CCA was first extracted in MR angiography (MRA) images using a 3D deformable model, then registered and refined to allow LIB segmentation of the 2D vessel wall MR image sequence. The carotid AB was finally segmented by fitting a 3D surface using information on image gradients. However, their method [8] segmented only the carotid CCA and required MRA images to segment vessel wall MR images. On the other hand, the 2D slice-by-slice methods [7, 9, 10, 11] require user interaction on each slice, which results in substantial user efforts. Moreover, their numerical schemes are based on local optimization techniques, which are sensitive to user initialization and image quality. Kerwin *et al.* [9] and Liu *et al.* [17] proposed methods that segment the carotid AB and LIB separately and propagate the segmentation result from one slice to the next, in order to reduce the amount of user interaction. However, these methods also rely on the local optimization-based 2D parametric contour evolution models, such as deformable snakes. Due to the fact that the segmentations are propagated slice-wise, the segmentation error could also propagate from one slice to the next and bias the segmentation of its successive slices. In addition, it is challenging for such methods to handle deformations of multiple regions jointly, especially at the bifurcation, where changes to the topology of the contour are required to be incorporated into the segmentation of the carotid CCA, ICA, and ECA (see Fig. 1.11(a)).

Some other studies [12, 13, 14] (see also Table 4.1) demonstrated only segmentation of the carotid LIB. However, segmentation of both the carotid AB and LIB are essential for a quantitative analysis of carotid atherosclerosis plaque burden [4].

4.1.2 Contributions

In this paper, we propose a novel global optimization-based approach for delineating the carotid AB and LIB surfaces of the CCA, ICA, and ECA from 3D T1w black blood MR images. The main contributions of this work can be summarized as follows.

- We introduce a new global optimization-based contour evolution method, which jointly segments a 3D carotid MR image into three regions: wall, lumen, and background. It simultaneously propagates the two contours of the AB and LIB based on matching region related intensity PDF to their respective intensity PDF models, while preserving the inter-surface order constraint (4.1) of the AB and LIB. In practice, enforcing such inter-surface prior improves the accuracy and reliability of segmentation.

- We show that the optimization problem for the simultaneous evolution of the two ordered surfaces of the AB and LIB during each discrete time frame can be solved globally and exactly by means of convex relaxation, i.e. the two surfaces of AB and LIB can be evolved to their globally best positions, while keeping their inter-surface order, at each evolution step.

- We introduce the dual/equivalent formulation of the resulting convex relaxation problem of evolving the two ordered contours of the AB and LIB and derive a new continuous max-flow-based algorithm. The continuous max-flow algorithm enforces the inter-surface order constraint implicitly, through optimizing the directed flows without additional computational cost. In addition, a new parallelized version of the continuous max-flow-based algorithm is implemented on a GPU to achieve high computational performance.

- We demonstrate that the algorithm achieves high accuracy and precision with fewer user interactions. The algorithm requires the initialization of *only a single transverse slice* for extracting the AB and LIB surfaces from a 3D MR image.

The proposed approach is based on the recent developments of convex relaxation methods. The readers are referred to the studies [18, 19, 20] for a detailed description of the convex relaxation and continuous max-flow methods. Distinct from the discrete global optimization methods [21], the convex relaxation methods are employed in a spatially continuous setting, which provide sub-pixel accuracy while avoiding metrication artifacts.

Yuan *et al.* [22] proposed a similar global optimization-based framework for evolving a single contour by efficiently solving a sequence of continuous min-cut problems. Their method [22] outperforms the other contour evolution methods, such as level set, in terms of efficiency and robustness to poor initialization. The proposed global optimization-based evolution of the coupled surfaces AB and LIB of this paper is motivated by their method [22].

A preliminary study of this work was described in a conference paper [23]. In this work, we describe both the comprehensive theory of the proposed approach and its detailed implementations. We also propose an improvement to the segmentation accuracy of the carotid ICA and ECA by incorporating new inter-surface separation-based priors of the AB and LIB. Moreover, in comparison to the preliminary study [23], the proposed algorithm is validated extensively over a large number of images, in terms of accuracy, intra- and inter-observer variability and computing vessel wall volume measurements. Additionally, we compare the results to those found in the existing literature.

4.2 Method

In this section, a novel multi-region segmentation method is proposed, which partitions a 3D MR image into three regions: the lumen region $\mathcal{R}_l$, the outer wall region $\mathcal{R}_w$, and the background region $\mathcal{R}_b$ (see Fig. 4.1 and 4.2(a)), by simultaneously

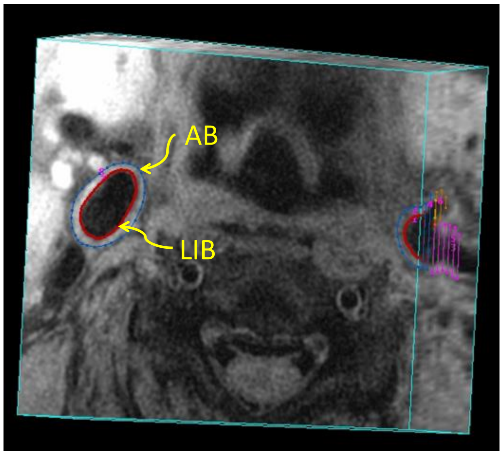

Figure 4.1: A 3D view of a T1-weighted 3T carotid MR image showing the transverse and sagittal cross sections of the CCA with overlaid manual segmentations. The manual segmentations are performed on each transverse slice.

evolving the two coupled surfaces, the lumen-intima (LIB) $\mathcal{C}_{LIB}$ and the adventitia (AB) $\mathcal{C}_{AB}$ to their optimal locations. In particular, we utilize the prior knowledge of anatomy that the region enclosed by the surface $\mathcal{C}_{LIB}$ always resides within the region enclosed by the surface $\mathcal{C}_{AB}$, i.e.

$$\mathcal{C}_{LIB} \subset \mathcal{C}_{AB}\,,^{1} \tag{4.1}$$

which acts as an additional geometrical or order constraint on the proposed joint optimization of $\mathcal{C}_{LIB}$ and $\mathcal{C}_{AB}$. In practice, enforcing such inter-surface prior or order (4.1) further improves the accuracy and reliability of the segmentation.

When the two surfaces $\mathcal{C}_{LIB}$ and $\mathcal{C}_{AB}$ are computed, the three regions $\mathcal{R}_l$, $\mathcal{R}_w$, and $\mathcal{R}_b$ of the input 3D MR image can be determined by (see Fig. 4.2(a))

$$\mathcal{R}_l := \mathcal{C}_{LIB}\,, \;\; \mathcal{R}_w := \mathcal{C}_{AB} \backslash \mathcal{C}_{LIB}\,, \;\; \mathcal{R}_b := \Omega \backslash \mathcal{C}_{AB}\,. \tag{4.2}$$

The proposed method is distinct from the previous local optimization-based contour evolution solutions, such as level set, such that the two surfaces $\mathcal{C}_{LIB}$ and $\mathcal{C}_{AB}$ are evolved to their globally optimal positions during each discrete time-frame, sub-

---

[1] In this paper, the two "surfaces" $\mathcal{C}_{LIB}$ and $\mathcal{C}_{AB}$ may also refer to their respective enclosed regions or volumes based on the context.

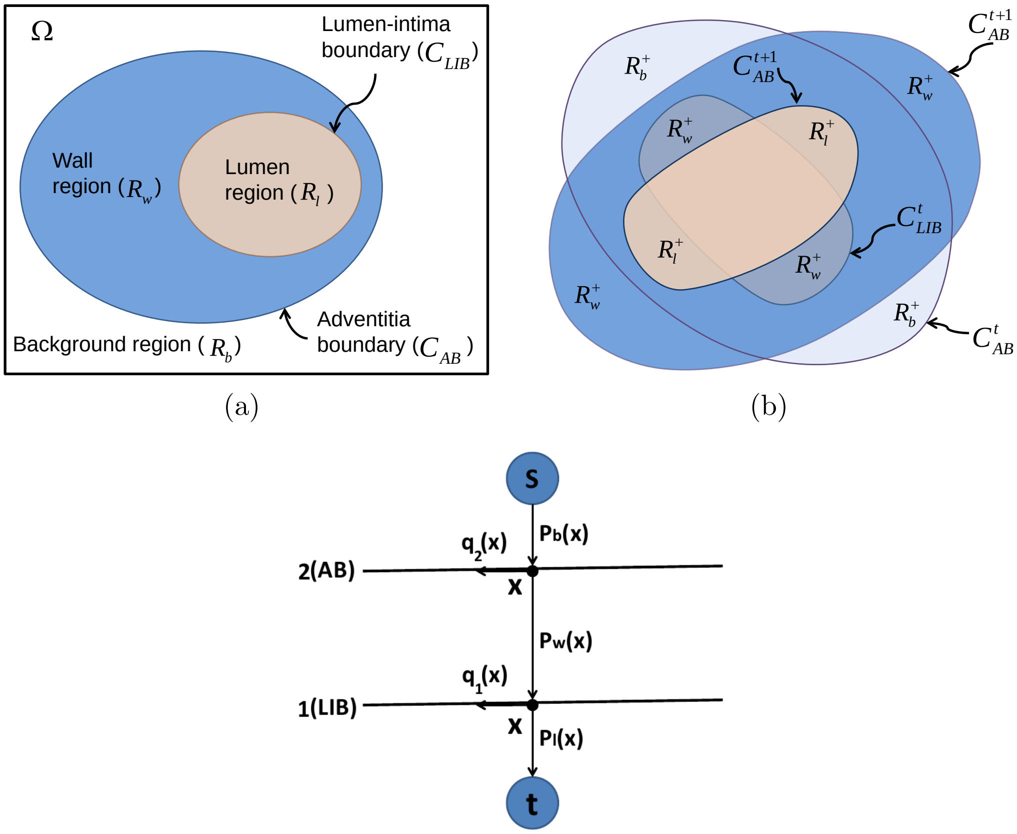
Ω
Lumen-intima boundary (C_{LIB})
Wall region (R_w)
Lumen region (R_l)
Adventitia boundary (C_{AB})
Background region (R_b)
C_{AB}^{t+1}
R_b^+
C_{AB}^{t+1}
R_w^+
R_w^+
R_l^+
C_{LIB}^t
R_l^+
R_w^+
R_w^+
R_b^+
C_{AB}^t
S
$P_b(x)$
$q_2(x)$
2(AB)
x
$P_w(x)$
$q_1(x)$
1(LIB)
x
$P_l(x)$
t

(a) (b)

(c)

Figure 4.2: (a) Pictorial representation of image domain Ω and its sub-domains: Lumen region (R_l), wall region (R_w), and background (R_b); (b) region differences by the evolution of the two surfaces $\mathcal{C}_{AB}$ and $\mathcal{C}_{LIB}$; and (c) the spatially continuous flow configurations used in the continuous max-flow formulation.

ject to the inter-surface order constraint (4.1) by means of convex optimization. This results in a time-implicit surface evolution scheme, which allows a large discrete-time step-size that in turn substantially speeds up evolution of the surfaces.

Moreover, matching the estimated intensity PDFs of the three regions $\mathcal{R}_l$, $\mathcal{R}_w$, and $\mathcal{R}_b$ to their corresponding intensity PDF models is explored as the global statistical criterion to guide evolving $\mathcal{C}_{LIB}$ and $\mathcal{C}_{AB}$.

4.2.1 Optimization model with geometrical constraint

The PDF of intensities, i.e. the intensity histogram, is a global descriptor of the object of interest, such that matching the intensity PDF models of the object regions provides a robust mechanism to guide the evolution of contours [24, 25].

Let $I(x) \in \mathcal{Z}$ be a given 3D carotid MR image, where $\mathcal{Z}$ is the set of image intensity values; $u_1(x)$ and $u_2(x)$ be the indicator or labeling functions of the regions enclosed by $\mathcal{C}_{LIB}$ and $\mathcal{C}_{AB}$ respectively, such that

$$u_1(x) := \begin{cases} 1\,, & \text{where } x \text{ is inside } \mathcal{C}_{LIB} \\ 0\,, & \text{otherwise} \end{cases}\,, \tag{4.3}$$

and

$$u_2(x) := \begin{cases} 1\,, & \text{where } x \text{ is inside } \mathcal{C}_{AB} \\ 0\,, & \text{otherwise} \end{cases}\,. \tag{4.4}$$

Given the inter-surface order constraint (4.1) of the surfaces $\mathcal{C}_{LIB}$ and $\mathcal{C}_{AB}$, the binary region labeling functions $u_1(x)$ and $u_2(x)$ must satisfy the following linear inequality:

$$u_1(x) \,\leq\, u_2(x)\,, \quad \forall x \,\in\, \Omega\,, \tag{4.5}$$

which is also referred to as the linear order of the labeling functions $u_1(x)$ and $u_2(x)$. In fact, preserving such a linear order constraint of the labeling functions is essential to gain the global optimality not only for the optimization step studied in the following sections, but also for a series of multi-labeling problems in computer vision, e.g. [26, 27, 28] etc.

Given (4.2), the indicator or labeling functions $u_{l,w,b}(x) \in \{0, 1\}$ and their label values, for $\forall x \in \Omega$, of the three regions $\mathcal{R}_{l,w,b}$ can be expressed as follows:

$$u_l = u_1\,, \quad u_w = u_2 - u_1\,, \quad u_b = 1 - u_2\,. \tag{4.6}$$

In this work, the two surfaces $\mathcal{C}_{LIB}$ and $\mathcal{C}_{AB}$ are propagated by minimizing the total Bhattacharyya distance [29, 30, 31] between the estimated PDFs $h_{l,w,b}(z)$, where $z \in \mathcal{Z}$, of the three object regions $\mathcal{R}_{l,w,b}$ and their respective PDF models $\hat{h}_{l,w,b}(z)$:

$$E_{\mathrm{m}}(u) \;=\; -\sum_{i=l,w,b}\,\sum_{z\in\mathcal{Z}}\sqrt{h_i(z)\,\hat{h}_i(z)}\,, \tag{4.7}$$

such that the intensity PDF models $\hat{h}_{l,w,b}$, where $z \in \mathcal{Z}$, of the three object regions are calculated from the sampled voxels of the 3D carotid MR image. However, the intensity PDF models can also be generated from a training data set and the other statistical divergences, such as the symmetric Kullback-Leibler distance [32] etc., can also be used.

By the Parzen method [33] and (4.6), the intensity PDFs $h_{l,w,b}(z)$, where $z \in \mathcal{Z}$, for the respective three object regions $\mathcal{R}_{l,w,b}$ can be estimated by

$$h_i(z) \;=\; \frac{\int_\Omega K(z - I(x))\, u_i(x)\, dx}{\int u_i(x)\, dx}\,, \quad i \;=\; l, w, b\,,$$

where $K(\cdot)$ is the Gaussian kernel function such that

$$K(x) \;=\; \frac{1}{\sqrt{2\pi\sigma^2}} \exp(-x^2/2\sigma^2)\,.$$

With the combination of the global statistical criterion (4.7) of matching the intensity PDF models $\hat{h}_{l,w,b}(z)$ of three regions $\mathcal{R}_{l,w,b}$ and the geometrical constraint (4.5) on the labeling functions, we propose to segment the input 3D carotid MR image $I(x)$ by minimizing the following energy function

$$\min_{u_{1,2}(x) \in \{0,1\}} E_{\mathrm{m}}(u) \;+\; \sum_{i=1,2} \int_\Omega g(x)\, |\nabla u_i(x)|\; dx\,, \tag{4.8}$$
$$\text{s.t.} \quad u_1(x) \;\leq\; u_2(x)\,. \quad \forall x \in \Omega$$

The second term is an image gradient-weighted total-variation-based (TV) smoothness term, which corresponds to the segmentation with the minimum geodesic length. In this paper, the weight function $g(x)$ in (4.8) is positive and is given by

$$g(x) \;=\; \lambda_1 + \lambda_2 \exp(-\lambda_3\, |\nabla I(x)|)\,, \quad \lambda_{1,2,3} \;\geq\; 0\,. \tag{4.9}$$

Note that, the values of $g(x)$ fall within the range $[\lambda_1, \lambda_1 + \lambda_2]$.

4.2.2 Global optimization-based coupled contour evolution

It is challenging to solve the combinatorial optimization problem (4.8) directly, due to its highly nonlinear and non-convex energy function and the discrete-valued unknown functions. To this end, we propose to minimize (4.8) while preserving the associated geometrical constraint (4.5), by evolving the coupled surfaces $\mathcal{C}_{LIB}$ and $\mathcal{C}_{AB}$. The current surfaces $\mathcal{C}^t_{LIB}$ and $\mathcal{C}^t_{AB}$ at time t are propagated to their new positions $\mathcal{C}^{t+1}_{LIB}$ and $\mathcal{C}^{t+1}_{AB}$ during each discrete time frame t to $t+1$. Finally, they are converged to the desired position of the AB and LIB.

Motivated by the recent developments proposed by Yuan *et al.* [22], we introduce a novel global optimization-based approach to propagate the coupled contours $\mathcal{C}_{LIB}$ and $\mathcal{C}_{AB}$ to their globally optimal positions during each discrete time frame. In comparison to the classical contour evolution methods, the joint optimization of the AB and LIB surfaces, subject to the inter-surface constraint (4.1), during each discrete time step can be solved globally by the proposed convex optimization algorithm, where the inter-surface constraint (4.1) is implicitly adapted in the optimization scheme. The resulting time-implicit contour evolution approach provides high numerical efficiency.

In the following section, we first review the recent progress of the global optimization-based single contour evolution methods. We then introduce the global optimization-based approach for the evolution of coupled contours $\mathcal{C}_{LIB}$ and $\mathcal{C}_{AB}$.

4.2.2.1 Single contour evolution by convex optimization

The conventional contour evolution methods, e.g. [25, 34, 35, 36] etc., gradually propagate a contour subject to the minimization of a certain energy function, while the associated time-explicit convection equations are often solved by local-optimization methods. In practice, the computational result and efficiency of such approaches have the following limitations. The contour may be trapped in a locally optimal position during each time frame. The final result depends heavily on the initial position of the segmentation. The discrete time-step has an upper bound to achieve numerical stability, such as the CFL condition for explicitly solving the convection PDEs [37]. The nonlinear high-order derivatives, such as curvature, are also highly affected by image noise.

In contrast, the global optimization-based contour evolution approaches [38, 39] overcome such challenges and generate simple, efficient, and robust algorithms for computation. For instance, the convex relaxation-based approach proposed by Yuan *et al.* [22] propagates a contour to its globally optimal position at each discrete time frame by solving a sequence of convex optimization problems, for which an efficient continuous max-flow algorithm [18] is available. In addition, the new contour position at each evolution step is computed in a fully time-implicit manner, which allows a large time-step and substantially speeds up contour propagation [22].

For the given contour $\mathcal{C}^t$ at the current time t, its new position $\mathcal{C}^{t+1}$ at the next discrete time $t+1$ can be achieved by solving the following optimization problem [22]:

$$\min_{\mathcal{C}} \int_{\mathcal{C}^+} e^+(x)\,dx \;+\; \int_{\mathcal{C}^-} e^-(x)\,dx \;+\; \int_{\partial\mathcal{C}} g(s)\,ds\,, \tag{4.10}$$

where $\mathcal{C}^+$ and $\mathcal{C}^-$ are the expansion and shrinkage regions with respect to $\mathcal{C}^t$, and the functions $e^+(x)$ and $e^-(x)$ define the cost corresponding to the pixel x in $\mathcal{C}^+$ and $\mathcal{C}^-$. In summary, the contour evolution during each time frame is performed with the minimum total cost with respect to region changes, i.e. expansion $\mathcal{C}^+$ and shrinkage $\mathcal{C}^-$, and total region perimeter. When the cost functions $e^+(x)$ and $e^-(x)$ are given by the distance between x and the boundary of $\mathcal{C}^t$, the contour evolution given by (4.10), is equivalent to the well-known mean-curvature driven contour motion [22]. Moreover, the other typical contour evolutions applied in image processing can also be well described by (4.10) with different configurations of $e^+(x)$ and $e^-(x)$.

In particular, the optimization problem (4.10) can be equivalently formulated as a spatially continuous min-cut problem

$$\min_{u(x)\in\{0,1\}} \left\langle 1-u, D^1 \right\rangle + \left\langle u, D^2 \right\rangle + \int_{\Omega} g(x)\,|\nabla u|\;dx\,, \tag{4.11}$$

where $u(x) \in \{0,1\}$ is the indicator function of the contour $\mathcal{C}$, and the two label assignment functions $D^1(x)$ and $D^2(x)$ are given by

$$D^1(x) \;:=\; \begin{cases} e^-(x)\,, & \text{where } x \in \mathcal{C}^t \\ 0\,, & \text{otherwise} \end{cases} \tag{4.12}$$

$$D^2(x) \;:=\; \begin{cases} e^+(x)\,, & \text{where } x \notin \mathcal{C}^t \\ 0\,, & \text{otherwise} \end{cases} \quad . \tag{4.13}$$

In this regard, the efficient continuous max-flow algorithm [18] is employed to solve the continuous min-cut (4.11) globally and exactly, which implies that the new contour $\mathcal{C}^{t+1}$ at the next time step $t+1$ is globally optimal. In addition, the solution of (4.10) provides exactly a fully time-implicit scheme of the contour evolution, for which a large time evolution step-size is allowed to substantially speed up the evolution process [22].

4.2.2.2 Global optimization-based evolution of coupled contours

Here, we extend the optimization theory introduced by Yuan *et al.* [22] to evolve the two contours $\mathcal{C}_{LIB}$ and $\mathcal{C}_{AB}$, which minimizes the energy function (4.8).

To motivate the evolution theory of coupled contours $\mathcal{C}_{LIB}$ and $\mathcal{C}_{AB}$, we utilize the key observation of the single contour evolution: For the region $\mathcal{C}$ and its complementary $\Omega \backslash \mathcal{C}$ during each discrete time frame, the region shrinkage $\mathcal{C}^-$ actually corresponds to the expansion of the complementary region $\Omega \backslash \mathcal{C}$. Hence, the optimization principle (4.10) amounts to achieving the minimum total cost of the two region expansions w.r.t. $\mathcal{C}$ and $\Omega \backslash \mathcal{C}$, which can be applied for the evolution of the coupled contours $\mathcal{C}_{LIB}$ and $\mathcal{C}_{AB}$. Note that, $\mathcal{C}_{LIB}$ and $\mathcal{C}_{AB}$ partition the given image domain Ω into three regions $R_{l,w,b}$ (see Fig. 4.2(a)). Given the current contours $\mathcal{C}^t_{LIB}$ and $\mathcal{C}^t_{AB}$ at time t, the region changes w.r.t. $\mathcal{C}^t_{LIB}$ and $\mathcal{C}^t_{AB}$ can be expressed using the region expansions $R^+_{l,w,b}$ w.r.t. the current regions $\mathcal{R}^t_{l,w,b}$ (see Fig. 4.2(b)). Let $e^+_{l,w,b}(x)$ be the cost functions corresponding to the region expansions $R^+_{l,w,b}$, such that $e^+_{l,w,b}(x)$ are the first-order derivatives of the intensity PDF matching function (4.7) [29] w.r.t. $u_{l,w,b}(x)$, i.e.

$$e_i^+(x) = \frac{1}{2V_i} \sum_{z \in \mathcal{Z}} \left\{ \sqrt{h_i(z)\,\hat{h}_i(z)} - \sqrt{\frac{\hat{h}_i(z)}{h_i(z)}} K(z - I(x)) \right\} \tag{4.14}$$

where $V_i = \int_\Omega u_i \, dx$, $i = l, w, b$, is the volume of the current region $\mathcal{R}^t_i$. Similar to the method proposed by Yuan *et al.* [22], an additional distance term $\mathrm{dist}(x, \mathcal{R}_{l,w,b})(x)$, which is the distance from x to the boundary of the region $\mathcal{R}_{l,w,b}$, is added to the cost $e^+_{l,w,b}(x)$, respectively to constrain the contour movements during each time step. The cost functions (4.14) guide the evolution of the contours towards the minimization of the intensity PDF matching function (4.7).

We propose to propagate the two contours $\mathcal{C}^t_{LIB}$ and $\mathcal{C}^t_{AB}$ to their new positions from time t to $t+1$ by achieving the minimum total cost of region expansions, i.e.

$$\begin{aligned} \min_{\mathcal{C}_{LIB}, \mathcal{C}_{AB}} & \int_{\mathcal{R}^+_l} e^+_l(x)\, dx + \int_{\mathcal{R}^+_w} e^+_w(x)\, dx + \int_{\mathcal{R}^+_b} e^+_b(x)\, dx \\ & + \int_{\partial \mathcal{C}_{LIB}} g(s)\, ds + \int_{\partial \mathcal{C}_{AB}} g(s)\, ds \end{aligned} \tag{4.15}$$

subject to the geometrical inter-surface constraint (4.1). As shown in Fig. 4.2(b), the shrinkage region of the wall matches the union of the expansion region of the lumen and the expansion region of the background. However, we formulated (4.15) based on its current label after the evolution. For example, a voxel that moved to the lumen region pays the cost $e_l^+(x)$ irrespective of whether it is changed from the wall region or background region, which is counted once in the final energy function.

We show the optimization problem (4.15) can be globally and exactly solved by means of convex relaxation. In order to achieve this, we first show that (4.15) can be equally reformulated as a spatially continuous min-cut problem with the linearly ordered labels proposed in [27].

We define the label assignment functions

$$D_i(x) \;:=\; \begin{cases} e_i^+(x)\,, & \text{where } x \notin \mathcal{R}_i^t \\ 0\,, & \text{otherwise} \end{cases}\;, \quad i = l, w, b\,. \tag{4.16}$$

In view of the labeling functions (4.3) and (4.4) of the two contours $\mathcal{C}_{LIB}$ and $\mathcal{C}_{AB}$, we have

Proposition 1 *The optimization problem* (4.15) *can be equivalently expressed by the following continuous min-cut problem with the linearly ordered labels:*

$$\min_{u_{1,2}(x)\in\{0,1\}} \; \langle u_1, D_l\rangle + \langle u_2 - u_1, D_w\rangle + \langle 1 - u_2, D_b\rangle + \sum_{i=1,2}\int_\Omega g(x)|\nabla u_i|\,dx \tag{4.17}$$

subject to the label order constraint (4.5)*, i.e.* $u_1(x) \le u_2(x)$.

proof 2 *In view of* (4.16)*, the label assignments functions* $D_{l,w,b}(x) = 0$*, for any* $x \in \mathcal{R}_{l,w,b}^t$*; and* $D_{l,w,b}(x) = e_{l,w,b}^+(x)$*, otherwise.*

Hence, the integral $\langle u_i, D_i\rangle$*,* $i = l, w, b$*, provides the exact value* $\int_{\mathcal{R}_i^+} e_i^+(x)\,dx$*. Moreover, the weighted total-variation functions in* (4.17) *correspond to the weighted perimeter/area of the contour* $\mathcal{C}_{LIB}$ *and* $\mathcal{C}_{AB}$*. Then, the proposition is proved.*

4.2.3 Convex relaxation and continuous max-flow approach

Bae *et al.* [27] proved that the combinatorial optimization problem (4.17) can be solved globally and exactly by its convex relaxation

$$\min_{u_{1,2}(x)\in[0,1]} \quad \langle u_1, D_l\rangle + \langle u_2 - u_1, D_w\rangle + \langle 1 - u_2, D_b\rangle$$
$$+ \sum_{i=1,2} \int_\Omega g(x)|\nabla u_i|\, dx \tag{4.18}$$

subject to the ordered label constraint $u_1(x) \leq u_2(x)$.

Note that, the binary constraint $u_{1,2}(x) \in \{0,1\}$ on the values of the labeling functions $u_1(x)$ and $u_2(x)$ in (4.17) is relaxed to be $u_{1,2}(x) \in [0,1]$ in (4.18), which amounts to the convex optimization problem (4.18). Moreover, we have the following.

Proposition 3 *Given the global optimum* $u^*_{1,2}(x)$ *of the convex relaxation problem* (4.18), *the threshold of* $u^*_{1,2}(x)$ *by any value* $\gamma \in (0,1]$ *provides the global binary optimum of the combinatorial optimization problem* (4.17) *using the thresholding theorem proposed by Chan et al. [40].*

proof 4 *Its proof directly follows [27].*

The existence of the global and exact optimum to (4.17) indicates that the two contours $\mathcal{C}^t_{LIB}$ and $\mathcal{C}^t_{AB}$ can be propagated to their globally optimal positions from the discrete time t to $t+1$, while preserving the inter-surface order constraint (4.1).

4.2.3.1 Continuous max-flow model

We introduce the continuous max-flow theory proposed by Bae *et al.* [27] to compute the proposed convex optimization problem (4.18) globally, and the original combinatorial optimization problem (4.17) in turn (by Prop. 3).

We adapt the flow configuration introduced in [27] for the specified three region segmentation case (see Fig. 4.2(c)). Note that, two image domains representing AB and LIB and two additional terminals s and t are given. s is linked to any pixel x in the image domain AB, then linked to the same pixel in the image domain LIB, and then linked to t. The flows $p_b(x)$, $p_w(x)$, and $p_l(x)$ are directed and attached to the corresponding links. Within the image domains AB and LIB, there then exists corresponding spatial flows $q_2(x)$ and $q_1(x)$ around the pixel x.

With such flow settings, we propose the associated continuous max-flow model as follows:

$$\max_{p_b, p_l, p_w} \quad \int_\Omega p_b(x)\, dx \tag{4.19}$$

subject to the flow capacities

$$|q_i(x)| \, \le \, g_i(x)\,, \quad i \, = \, 1, 2\,; \tag{4.20}$$

$$p_i(x) \, \le \, D_i(x)\,, \quad i \, = \, b, l, w\,; \tag{4.21}$$

and the flow conservation conditions

$$\begin{aligned} (\operatorname{div} q_1 - p_w + p_l)(x) \, &= \, 0\,, \\ (\operatorname{div} q_2 - p_b + p_w)(x) \, &= \, 0\,. \end{aligned} \tag{4.22}$$

It can be proven that the continuous max-flow model (4.19) is dual/equivalent to the convex relaxation problem (4.18) [27]. The main advantage of such a continuous max-flow formulation (4.19) is that it results in an efficient continuous max-flow-based algorithm through the modern convex optimization theory, which embeds the labeling constraints $u_{1,2}(x) \in [0, 1]$ and $u_1(x) \le u_2(x)$ implicitly in the algorithm. Moreover, the proposed algorithm avoids implementing the non-smooth and nonlinear total-variation terms in (4.18), directly.

4.2.3.2 Continuous max-flow based algorithm

We propose a new continuous max-flow based algorithm, which explores flow maximization over all the dual flows $p_{l,w,b}(x)$ and $q_{1,2}(x)$ during each iteration simultaneously. In practice, such new parallelized scheme achieves a faster convergence and can be easily parallelized on a GPU. The update equations of the continuous max-flow algorithm are provided in Appedix A.

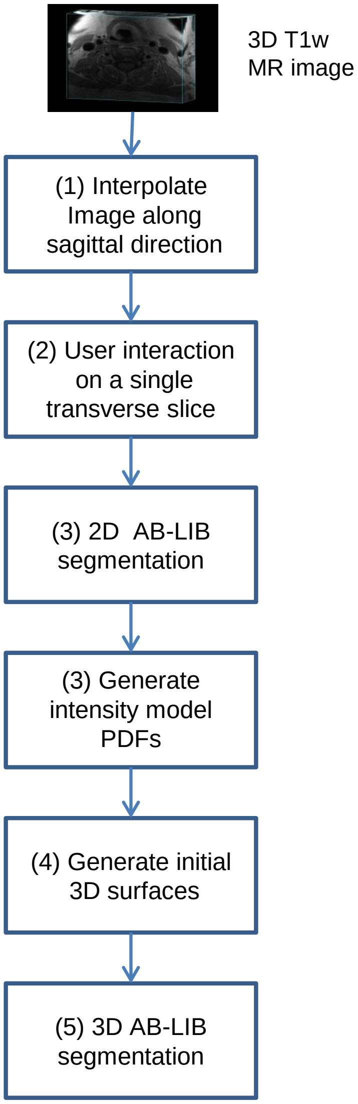
3D T1w
MR image
(1) Interpolate Image along sagittal direction
(2) User interaction on a single transverse slice
(3) 2D AB-LIB segmentation
(3) Generate intensity model PDFs
(4) Generate initial 3D surfaces
(5) 3D AB-LIB segmentation

Figure 4.3: Block diagram of our segmentation pipeline. The proposed continuous max-flow algorithm with ordered geometric constraints is used in two occasions: It is used initially for a 2D segmentation on a single transverse slice to for the purpose of generating intensity PDFs of the three regions to aid in the 3D segmentation. It is then used to segment the carotid arteries in 3D. The only user interaction required is to mark seed points on the lumen, wall, and background regions prior to 2D coupled evolution.

4.3 Experiment design and implementations

4.3.1 Study subjects and image acquisition

The data comprise of 38 left and right carotid artery black blood MR images from ten subjects: 12 3T T1-weighted (voxel size $\approx 0.2 \times 0.2 \times 2$ mm^3), and 26 1.5T T1-weighted (voxel size $\approx 0.5 \times 0.5 \times 2$ mm^3) MR images. The ten subjects were recruited from the Premature Atherosclerosis Clinic and Stroke Prevention Clinic at University Hospital, London Health Sciences Centre (London, ON, Canada). Each subject provided written informed consent, which has been approved by the Research Ethics Board at The University of Western Ontario. For this study, the subjects had moderate stenosis (30% - 50%) and were enrolled with carotid TPA of 0.5 cm^2 or greater as measured previously with B-mode ultrasound.

Subjects were scanned at 1.5T and 3.0T with GE Excite HD MRI systems (Milwaukee, WI, USA) operating at a 12x software level as previously described by Krasinski *et al.* [3] with fat saturation and without cardiac gating. Identical pulse sequences and identical custom-build six-element carotid bifurcation-optimized receive-only phase-array coils were used in the two systems. The images consisted of a multislice 2D black-blood acquisition, with T1w contrast, using double inversion recovery (DIR with 180° pulse). Table 4.2 shows the MR imaging parameters for both 1.5T and 3T MR images. Localized shimming was performed before each sequence to ensure good performance of fat saturation pulses.

4.3.2 Segmentation pipeline

Figure 4.3 shows a block diagram of the proposed segmentation pipeline, which is described in detail in the following sections.

4.3.2.1 Interpolation

The 3D MR images were interpolated initially to obtain a 3D image with approximately isotropic voxel dimensions using B-spline interpolation [41]. For the 3T MR images, nine additional slices were interpolated in the axial direction between each adjacent pair of original slices to obtain a voxel dimension of $0.2 \times 0.2 \times 0.2$ mm^3.

Table 4.2: Magnetic Resonance Imaging Parameters for T1-weighted Double Inversion Recovery scans at 1.5T and 3.0T.

Acquisition Parameter	**1.5T**	**3.0T**
Echo Time, TE (ms)	12	11.4
Recovery Time, TR	1RR	1RR
Receiver Bandwidth, RBW (kHz)	41.67	41.67
Field of View, FOV (cm)	11	11
Thickness (mm)	2	2
Matrix	224×224	224×224
Number of Excitations, NEX	3	3
Scan Time (minutes)	8:48	8:48
Fat Saturation	Yes	Yes
Spacing Overlap	0	0
Number of Slices	16	16
Pulse Sequence	FSE	FSE

Similarly, for the 1.5T MR images, three additional slices were interpolated in the axial direction between each adjacent pair of original slices to obtain a voxel dimension of $0.5 \times 0.5 \times 0.5$ mm^3.

This step ensures the direct applicability of the classical 3D total-variation function to equally regularize along each spatial direction. However, it is also possible to weight regularization in each spatial direction independently to account for anisotropic images.

4.3.2.2 User interaction

The sole user interaction in our approach was choosing some sampled voxels of the carotid wall, lumen, and background regions *on a single transverse slice* of the interpolated input 3D MR image. The voxels were chosen by the user using a paint brush user interface tool, as shown in Fig. 4.4(a)-(d). Such region-based user interaction techniques have been used previously for medical image segmentation [42, 43]. The sampled voxels marked by green, red, and blue correspond to lumen, wall, and background regions, respectively. In our experiments, the transverse slice was chosen to be the furthest from the carotid bifurcation. However, this choice is arbitrary and the user can also choose any other image slice for initialization. The purpose of the sampled voxels is threefold: I) the sampled voxels are used to approximate the intensity

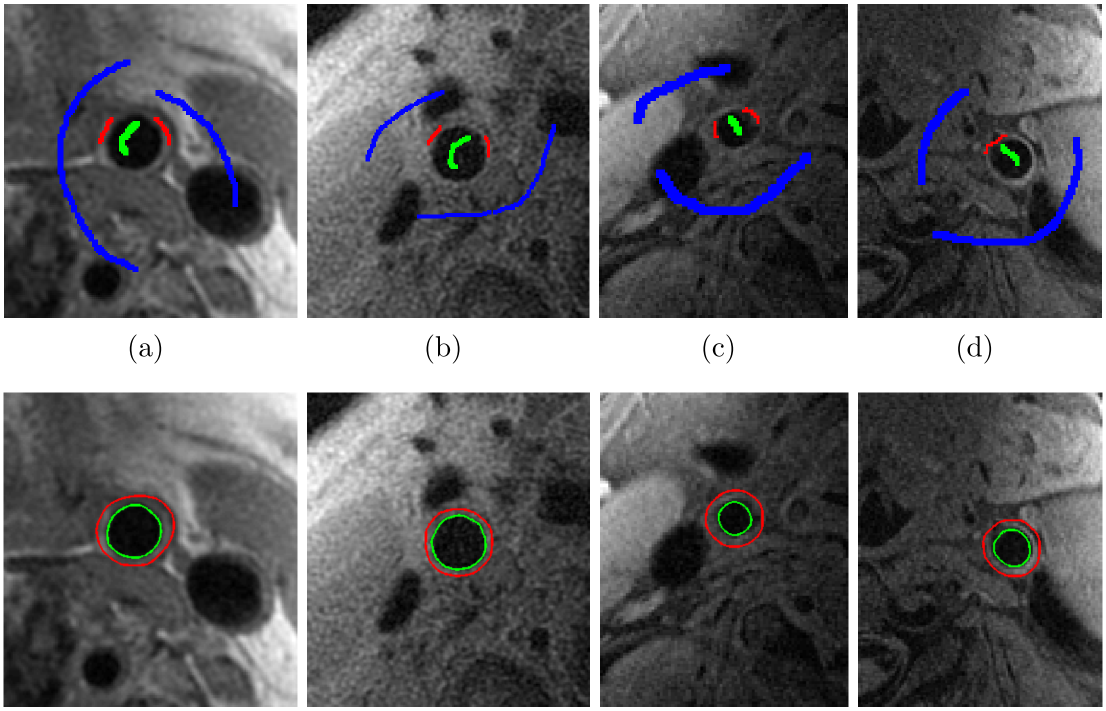

Figure 4.4: Example user initializations and the 2D AB-LIB segmentations using the proposed continuous max-flow algorithm. The only user interaction in the pipeline is choosing the sampled voxels on a single transverse slice. The voxels marked by green, red, and blue correspond to the lumen, wall and background regions respectively. (a) and (b): Initializations for two 3T MR images, (c) and (d): Initializations for two 1.5T MR images. (e) and (f): 2D Segmentations for two 3T MR images, (g) and (h): 2D segmentations for two 1.5T MR images.

PDF models for distribution matching in the 2D AB-LIB segmentation step; II) they are used as the hard constraints of segmentation regions such that the sampled voxels are fixed to be in their corresponding regions, which can be readily implemented in the introduced continuous max-flow framework (as described below); and III) they are also used as the initial regions for the 2D AB-LIB segmentation step (as described below).

4.3.2.3 2D AB-LIB segmentation and generation of intensity PDF models

A 2D segmentation of the carotid AB and LIB was performed on the same transverse slice that the user initialized, in order to further refine the intensity PDF models

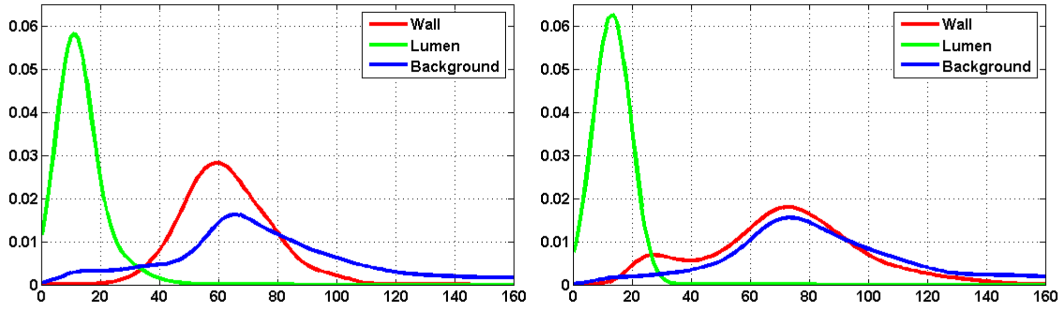

(a) PDF models (b) Estimated PDFs at Iter #1

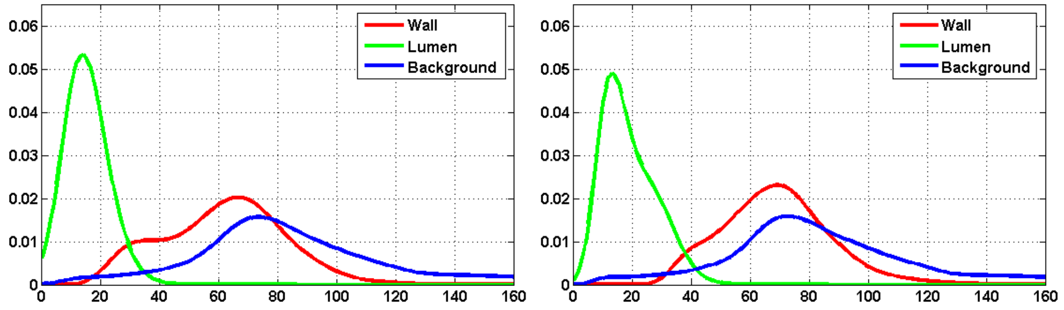

(c) Final result PDFs (d) Ground truth PDFs

Figure 4.5: Normalized intensity probability density functions (PDF) used in 3D AB-LIB segmentation for Bhattacharyya distance matching for a single 3D image. Gaussian kernel width of seven is used to generated the PDFs.

using the 2D segmentation result. The 2D AB-LIB segmentation was obtained using the proposed coupled surface evolution approach with the inter-surface order constraint. The optimization problem of the coupled surface evolution is solved using the proposed continuous max-flow approach by minimizing the objective function (4.18). Four criteria were used for 2D AB-LIB segmentation: The Bhattacharyya distribution matching (4.7), gradient-based smoothness term (4.9), hard constraints for user marked voxels (4.23), and minimum AB-LIB separation-based prior (4.24). The last two terms are described below.

Hard constraints for user sampled voxels: The sampled voxels (see Fig. 4.4(a)-(d)) by the user were used both as the initial regions and as the hard region constraints for the 2D AB-LIB segmentation step. For example, the blue voxels marked on the background region are fixed to the background region during the whole computation procedure (see Fig. 4.4(a)-(d)). Such region-based hard constraints can be easily implemented into the proposed continuous flow-maximization scheme as the following flow capacity constraints, which are standard in a max-flow procedure (see [21] etc.):

$$\begin{aligned} D_w(x) &= +\infty\,, \quad D_b(x) = +\infty\,, \quad x \in S_l \\ D_l(x) &= +\infty\,, \quad D_b(x) = +\infty\,, \quad x \in S_w \\ D_l(x) &= +\infty\,, \quad D_w(x) = +\infty\,, \quad x \in S_b \end{aligned} \tag{4.23}$$

where S_i, $i = l, w, b$, denote the sampled voxel regions within the lumen, wall, and background regions, respectively. Note that, when $x \in S_l$, the voxel x retains its status in the lumen region, because it would otherwise incur an infinite cost to change its status to be within either the wall or background regions.

Minimum AB-LIB separation-based prior: The lumen region usually appears uniformly in intensity and has well defined image edges at the LIB. However, the wall region is relatively heterogeneous in intensity and has overlapping image intensities with the background region, which is challenging for the segmentation task. We incorporated an anatomically motivated separation of the carotid AB and LIB by the intima-media layer, in order to prevent the AB from collapsing to the LIB, when the carotid AB is weakly defined in the image. Because, the AB and LIB are separated by the carotid media layer, they are encouraged to have a greater or equal separation distance (d_{min}) of 0.5 mm from each other [44]. We used hard constraints to implement the minimum AB-LIB separation-based prior, such that the minimum distance between the AB and LIB should be larger than some constant d_{min} in order to maintain the separation of the AB and LIB. This can be implemented as follows

$$D_b(y) = +\infty \,, \quad \text{s.t. } d(y, \mathcal{R}_l) < d_{min}; \tag{4.24}$$

where $d(y, \mathcal{R}_l)$ denotes the Euclidean distance from voxel $y \in \mathcal{R}_w$ to the lumen region $\mathcal{R}_l$.

Using the computed 2D AB-LIB segmentation result, more representative intensity PDF model for each region were constructed to aid in the 3D AB-LIB segmentations, as shown in Fig. 4.5.

4.3.2.4 Generation of initial surfaces for 3D segmentation

Two initial surfaces are required for the AB and LIB to initialize the proposed coupled surface evolution algorithm. To obtain a crude estimate of the LIB surface as shown in Fig. 4.6(a) and 4.6(c), a region growing segmentation [45] was performed on the lumen region. A region growing method was used due to its simplicity to quickly obtain a crude segmentation. Alternatively, other initialization methods can also be used, such as defining a center line along long-axis views. Inputs to the region growing method include the minimum intensity of the lumen region obtained from the previous 2D segmentation and a threshold level defined as the percentage of the difference between minimum and maximum intensity (I_{max}). In this paper, we used 20% and 15% as the I_{max} for 3T and 1.5T MR images for all the experiments, which were chosen empirically. To obtain an initial surface for the AB, we dilated the surface generated from the region growing method by 2.5 mm.

4.3.2.5 3D AB-LIB segmentation

Finally, the two initial surfaces were simultaneously evolved with the inter-surface geometric constraint using the proposed global continuous max-flow algorithm for segmentation of the carotid AB and LIB by minimizing the objective function (4.18). We used four criteria for the segmentation: Bhattacharyya distribution matching (4.7), gradient-based smoothness term (4.9), minimum AB-LIB separation-based

Table 4.3: Algorithm parameters values for the experiments.

Parameter **(Equation #)**	**3T MR images** **LIB**	 **AB**	**1.5T MR images** **LIB**	 **AB**
λ_1 (4.9)	0.05	0.05	0.05	0.1
λ_2 (4.9)	0.7	0.1	0.7	0.1
λ_3 (4.9)	3	3	2	2
λ_4 (4.26)	–	0.01	–	0.02

prior (4.24), and a maximum AB-LIB separation-based prior (4.25).

Maximum AB-LIB separation prior: We introduced an additional criterion for the 3D segmentation, due to the fact that in some images the AB surface maintains a smooth single surface without splitting into the ICA and ECA at the bifurcation. This is more apparent when the AB has weak image gradient and/or wall region has substantially overlapping intensity distributions (see Fig. 4.5(d)) with the background. In order to encourage the splitting, we used a criterion that penalizes the separation between the carotid AB and LIB, when the distance between them is higher than their average separation plus one standard deviation. The maximum AB-LIB separation-based prior is defined as

$$D_w^{'}(x) = \begin{cases} d(x, R_l), & \text{if } d(x, R_l) \geq (d_{mean} + sd) \\ 0, & \text{otherwise} \end{cases} \tag{4.25}$$

where $x \in R_w$, and $d(x, R_l)$ denotes the distance from voxel x to the lumen region R_l. d_{mean} and sd are the mean separation and standard deviation of separation between the AB and LIB for the current segmentation. The new cost that a pixel must incur to retain its status in the wall region is now given by

$$D_w(x) = D_w(x) + \lambda_4 D_w^{'}(x), \tag{4.26}$$

where $\lambda_4 > 0$. Note that unlike the minimum-separation-based prior, this term is controlled using a weight parameter λ_4.

4.3.3 Validation

The performance of the algorithm was evaluated with respect to manual segmentations by an expert in terms of accuracy and reproducibility. Manual segmentations were performed on a slice-by-slice basis on transverse views using a multi-planar reformatting software with a 2 mm inter-slice distance (ISD) up to 4 cm along carotid arteries. The CCA was outlined about 2 cm below the bifurcation, whereas the ICA and ECA were outlined by about 1 cm above the bifurcation. For a direct comparison, we compared the algorithm-generated segmentations to manual segmentations on a slice-by-slice basis. For this purpose, we sliced the algorithm-generated surfaces on the same planes as the ones that the manual segmentations were performed.

We used volume-based, region-based, and boundary distance-based metrics to evaluate the accuracy of the algorithm. We used volume error δV_E and percentage volume error (δV_P) (1.13) for volume-based metrics. In addition, we also computed absolute volume error $|\delta V_E|$ and absolute volume error $|\delta V_P|$ as a percentage.

The Dice similarity coefficient (DSC) (1.14) [46] was used as a region-based metric. The root-mean-squared-error (RMSE) of distance (1.18) and the Hausdorff distance (MAXD) (1.19) were used as distance-based metrics. Averages of DSC, RMSE, and MAXD were computed for the entire data set to obtain overall estimates of each metric.

A subset of our dataset was used to evaluate the intra- and inter-observer variability of the proposed algorithm. We randomly selected 8 3D images from 12 3T MR images and 8 3D images from 26 1.5T MR images. Five users participated in this study; one user (U1 a trained graduate student by a radiologist) performed a single round of manual segmentations and four different users (U2 a graduate student, U3 post-doctoral fellow, U4 a graduate student, U5 a research assistant) performed algorithm segmentations of the same data set five times. Four users performed repeated algorithm segmentations in order to assess the intra- and inter-observer variability. We used the coefficient-of-variation (CV) (1.20) and intra-class correlation coefficient (ICC) [47] to evaluate the precision of the algorithm in computing the clinically relevant VWV. The intra-observer CVs were computed to evaluate the variability (relative to the mean) among five measurement repetitions of each of the four observers, whereas inter-observer CV was computed to evaluate the variability among users. The ICC measures the reliability by computing the proportion of variance between observations. A single measure of absolute agreement using a two-way mixed study was used to compute ICC. We computed the minimum detectable difference (MDD) (1.21) [48] for the algorithm segmentation in generating VWV. The MDD provides an indication of the change in volume between two successive measurements that can be detected at a given confidence level [48]. Paired t-tests and Pearson correlation tests were also performed to compare algorithm-generated and manual VWV.

All statistical analyses were performed using IBM SPSS Statistical version 19 (IBM Corporation, 2010), in which results were considered significant when the probability of making a type I error was less than 5% ($p < 0.05$).

4.4 Experiment results

Two parameter sets were used for the 1.5T and 3T images, respectively, as shown in Table 4.3. The parameters were initially chosen empirically, and then optimized one parameter at a time using 5 images from the 3T MR images, and 5 images from 1.5T MR images, which were chosen randomly from the entire dataset. The DSC (1.14) was used as the evaluation metric in the experiments for the choice of the parameters. These parameters were kept constant during the evaluation experiments. The segmentation was terminated when the difference between successive iterations for both the AB and LIB was less than 10 voxels.

Figure 4.5 shows the model, estimated, and final intensity PDFs of the algorithm and the intensity PDF from manual segmentations for a sample 3D MR image. During the evolution, the estimated PDFs of the current segmentation were matched with the PDF models obtained from the 2D segmentation. As can be observed from Fig. 4.5, the intensity PDF of the final result is very similar to the intensity PDF from the manual segmentation.

4.4.1 Computational time

The convex max-flow algorithm was implemented using parallel computing architecture (CUDA, NVIDIA Corp., Santa Clara, CA). The user interface for initialization, preprocessing and cost calculation were performed using Matlab (Mathworks Inc., Natick, MA). The experiments were conducted on a Quad core Windows workstation with 3.0 GHz, 32GB RAM and a GPU of NVDIA GTX670. Initialization for our algorithm required a mean time of 21.0 ± 2.7 s, including the time required to run the

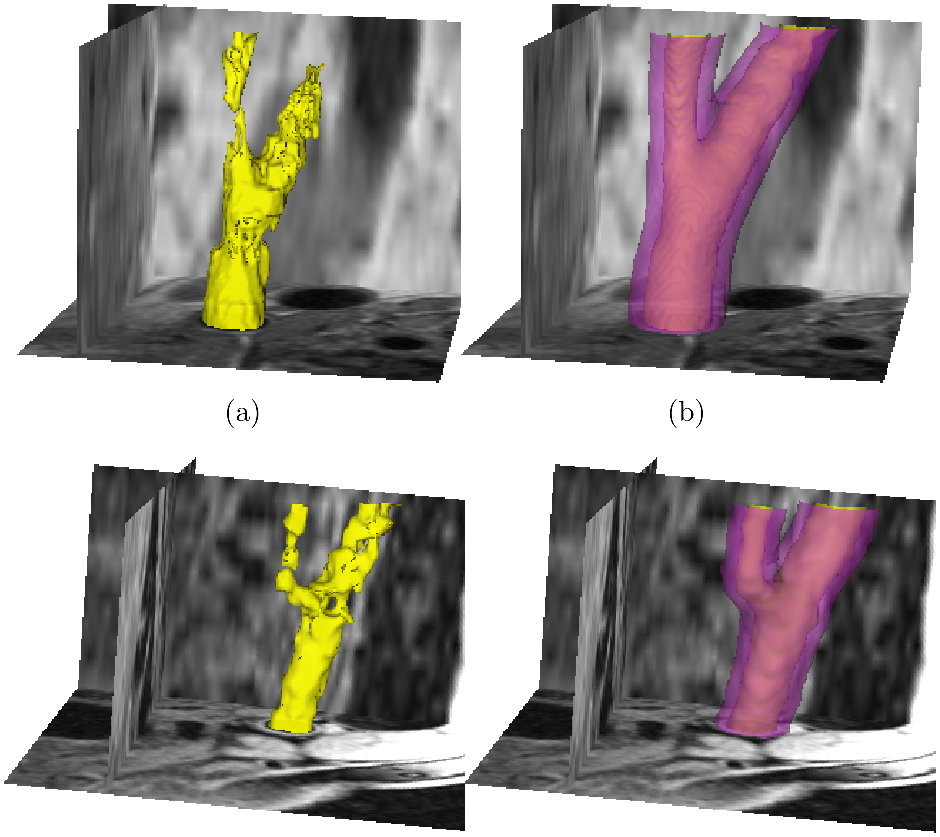
(a) (b)

(c) (d)

Figure 4.6: Example segmentations of a T1-weighted 3T image: (a) Initial surface for LIB obtained using region growing, (b) algorithm generated AB and LIB surfaces. Example segmentations of a T1-weighted 1.5T image: (c) Initial surface for LIB obtaining using region growing, (d) algorithm generated AB and LIB segmented surfaces.

2D max-flow algorithm, which took 6.4 s (2 s for the max-flow computation and 4.4 s for the cost computation using a nonoptimized Matlab code). The 2D algorithm required on average 4 iterations to obtain the final result. The average computational time for one iteration of the max-flow solver was 4 s. For a 3T image, the time for convergence of the 3D algorithm was $\approx$ 26 s (6 s for the max-flow computation and 20 s for the cost computation using a nonoptimized Matlab code), which was achieved within 5-12 iterations for a single 3D MR image. For a 1.5T image, the convergence time of the 3D algorithm was $\approx$ 5 s (1.4 s for the max-flow computation and 3.6 s for the cost computation using a nonoptimized Matlab code), which was achieved within 10 iterations.

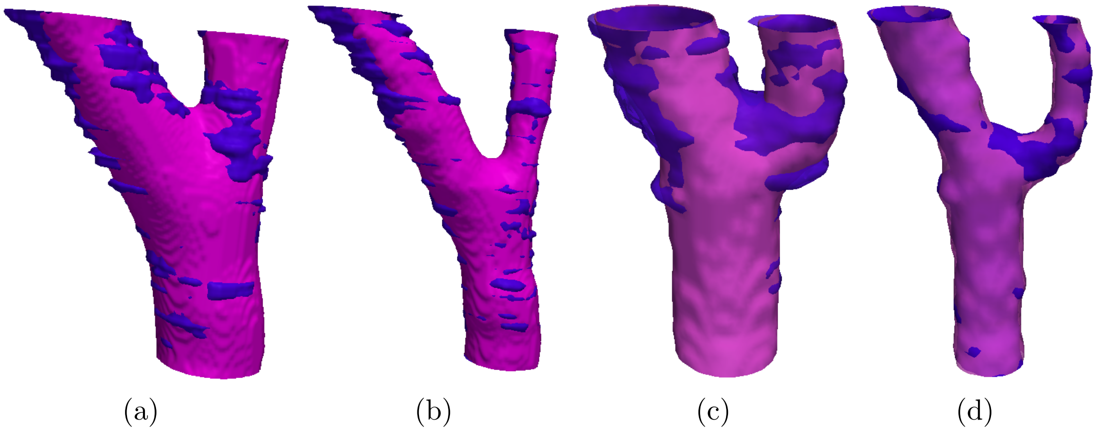

Figure 4.7: Visual surface comparisons of some example algorithm-generated AB and LIB surfaces to manually generated surfaces. The manually segmented surface is shown in blue color whereas the algorithm generated surface is shown in purple color. (a) AB surface segmented from a T1-weighted 3T MR image, (b) LIB surface segmented from the same T1-weighted 3T MR image, (c) AB surface segmented from a T1-weighted 1.5T MR image, and (d) LIB surface segmented from the same T1-weighted 1.5T MR image.

4.4.2 Accuracy

Segmentation results of two example 3D MR images are shown in Fig. 4.6. The carotid AB and LIB surfaces generated using the proposed algorithm for 3T and 1.5T MR images are shown in Fig. 4.6(b) and (d), whereas the initial surfaces generated from region growing method are shown in Fig. 4.6(a) and (c). The comparison of the algorithm-generated AB and LIB surfaces to the manual segmentations are shown in Fig. 4.7. The manually segmented surface is rendered in blue, whereas the algorithm surface is rendered in purple. Greater disagreement between the algorithm and manual delineations is present at the bifurcation of the carotid AB surface by visual comparison. Figure 4.8 shows the slice-by-slice comparisons of the algorithm to the manual segmentations for the carotid AB and LIB of the CCA, ICA, and ECA. Algorithm segmentations are shown in green continuous contours, whereas manual segmentations corresponds to the red dashed lines. As observed in Fig. 4.8, the algorithm segmentations are in good agreement with the manual segmentations.

The performance results of the algorithm for 12 3T MR images are shown in Table 4.5. The algorithm yielded more than 90% DSCs for the AB and LIB of the CCA and ICA. The DSC of ≈93% yielded for the CCA AB and LIB is the highest.

Table 4.4: Confidence intervals (CI) and Pearson correlation coefficients for computing VWV.

	Artery	Pearson r	p-value	95% CI (mm^3)	p-value
3T	CCA	0.82	0.001	-80.5–67.3	0.998
	ICA	0.76	0.006	-46.8–26.7	0.634
	ECA	0.74	0.004	-13.2–20.7	0.560
1.5T	CCA	0.94	< 0.001	-16.5–54.8	0.279
	ICA	0.87	< 0.001	15.9–54.7	0.020
	ECA	0.73	< 0.001	4.7–39.5	0.015

In addition, the lowest and highest standard deviations were reported for the CCA and for the ECA, respectively. The absolute volume errors follows a similar trend, where the lowest volume errors were obtained for the CCA, even though the actual difference in mm^3 is higher for the CCA, due to its larger size than the ICA and ECA. The volume errors (δV_E) obtained for the algorithm were small and negative (≤ 35 mm^3).

The RMSEs for the segmentation and their standard deviation are sub-millimeter for both the AB and LIB of the CCA, ICA, and ECA. For example, RMSEs for the AB and LIB of the CCA were 0.5 mm and 0.3 mm, respectively, which is equivalent to 2.5 and 1.5 times the width of a voxel (0.2 mm). The MAXD errors reported for the LIB were lower than for the AB for all three sections of the CA.

Table 4.6 shows performance results of the algorithm for 26 1.5T T1-weighted MR images. The algorithm yielded more than 90% DSCs for the AB and LIB of the carotid CCA and ICA. The DSC of 91%±1.6% and 92%±2.1% were the highest DSC for the CCA AB and LIB. The lowest DSCs were reported for the ECA AB and LIB, which were ≈87% and ≈86%. Similar to the previous results with 3T MR images, the algorithm underestimated the volumes relative to the manual segmentations except for the ECA AB.

The RMSEs were sub-millimeter for the 1.5T MR images. For example, RMSEs for the CCA AB and LIB were 0.6±0.1 mm and 0.5±0.2 mm, respectively. The algorithm also yielded small MAXD errors (0.9 to 2.1 mm). For example for the CCA, MAXD errors were 1.3±0.4 mm and 1.3±0.8 mm for the AB and LIB, respectively.

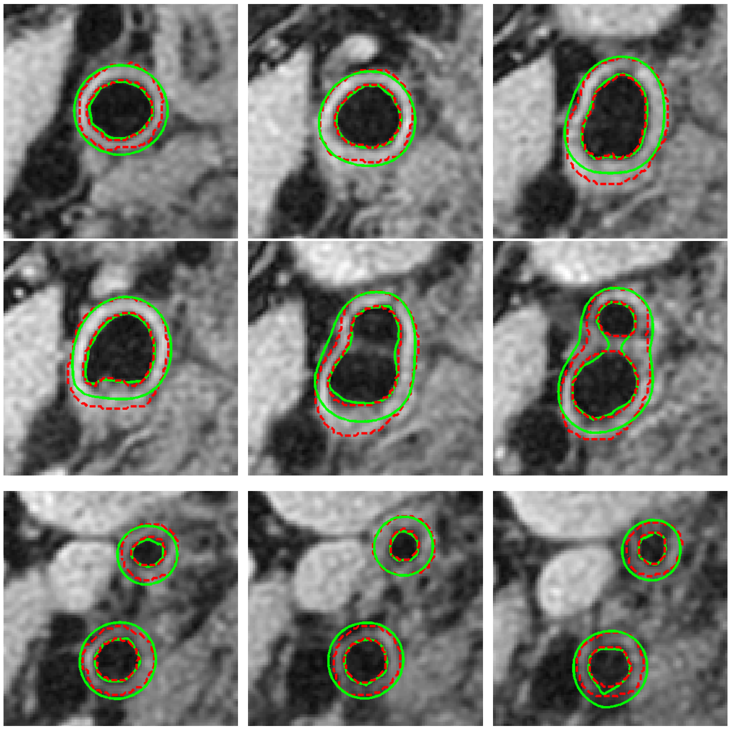

(a) Slice-by-slice comparisons for a T1w 3T image

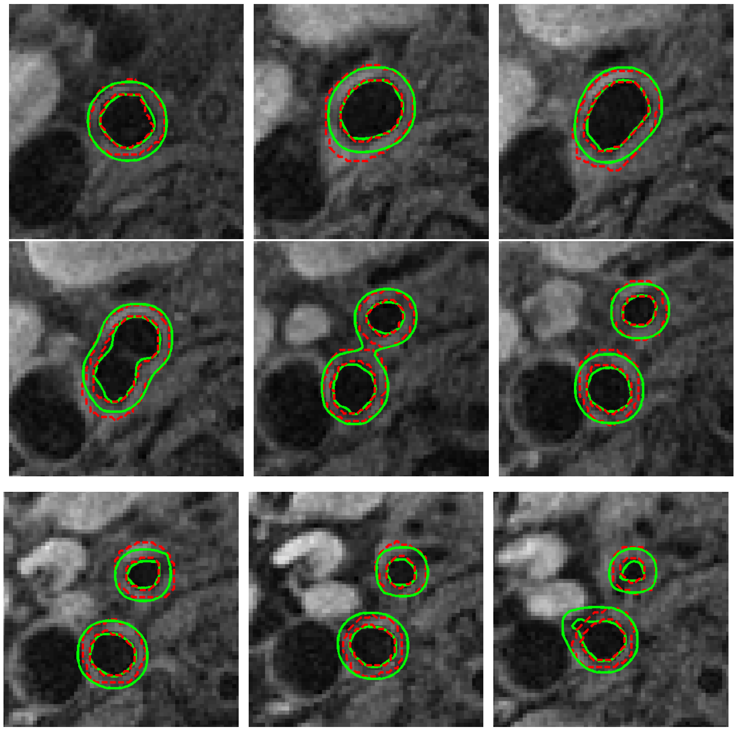

(b) Slice-by-slice comparisons for a T1w 1.5T image

Figure 4.8: 2D slice-by-slice comparisons of algorithm-generated surface to manual segmentations for two example images. The algorithm generated surface is sliced on the same planes as the 2D manual segmentations. Algorithm segmentations are shown as a green continuous line whereas the manual segmentations are shown in red dashed lines.

للاستشارات المنارة

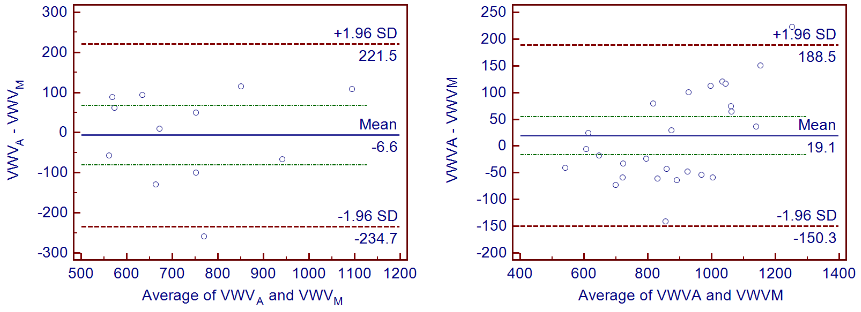

(a) CCA (b) CCA

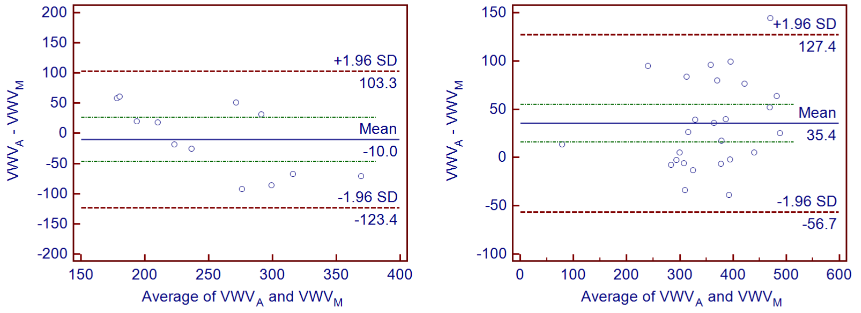

(c) ICA (d) ICA

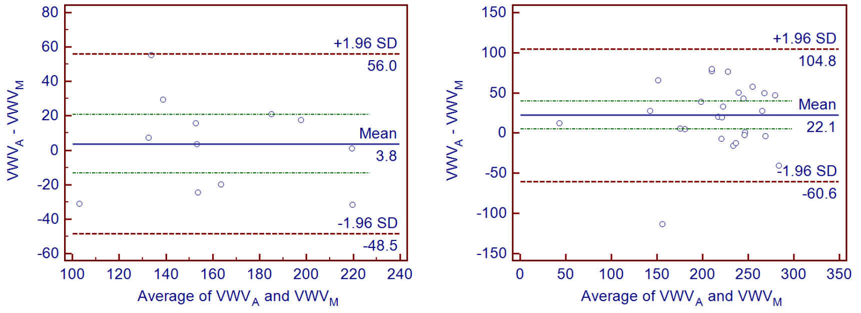

(e) ECA (f) ECA

Figure 4.9: Bland-Altman plots [49] of the vessel wall volume (VWV) measurements. Confidence interval (CI) of mean of differences between the VWVs are also indicated by the green dotted line. **1st Column:** Graph for 12 3T images, **2nd Column:** Graph for 26 1.5T images.

Table 4.5: Accuracy results for 12 T1-weighted 3T MR images using the proposed algorithm.

		DSC (%)	**RMSE** (mm)	**MAXD** (mm)	$\lvert\delta\mathbf{V_E}\rvert$ (mm^3)	$\lvert\delta\mathbf{V_P}\rvert$ (%)	$\delta\mathbf{V_E}$ (mm^3)	$\delta\mathbf{V_P}$ (%)
CCA	AB	93.0 ± 1.9	0.5 ± 0.7	1.1 ± 0.9	83.0 ± 93.9	5.8 ± 5.4	-34.3 ± 122.6	-1.7 ± 8.0
	LIB	93.3 ± 1.4	0.3 ± 0.2	0.8 ± 0.5	50.7 ± 33.8	7.4 ± 5.7	-27.7 ± 55.8	-4.0 ± 10.1
ICA	AB	90.1 ± 3.3	0.5 ± 0.5	1.6 ± 1.4	61.0 ± 46.2	11.9 ± 7.4	-34.6 ± 69.8	-4.9 ± 14.5
	LIB	90.4 ± 3.2	0.2 ± 0.1	0.6 ± 0.2	25.1 ± 17.4	14.5 ± 6.0	-24.5 ± 18.2	-14.1 ± 6.7
ECA	AB	88.4 ± 4.6	0.7 ± 0.7	2.0 ± 2.1	23.8 ± 24.2	10.1 ± 9.7	-13.0 ± 32.0	-4.2 ± 13.9
	LIB	84.1 ± 6.0	0.2 ± 0.1	0.6 ± 0.1	17.2 ± 11.0	23.6 ± 10.9	-16.8 ± 11.8	-23.1 ± 12.2

Table 4.6: Accuracy results for 26 T1-weighted 1.5T MR images using the proposed algorithm.

		DSC (%)	**RMSE** (mm)	**MAXD** (mm)	$\lvert\delta\mathbf{V_E}\rvert$ (mm^3)	$\lvert\delta\mathbf{V_P}\rvert$ (%)	$\delta\mathbf{V_E}$ (mm^3)	$\delta\mathbf{V_P}$ (%)
CCA	AB	91.3 ± 1.6	0.6 ± 0.1	1.3 ± 0.4	111.0 ± 88.0	6.7 ± 5.3	-16.0 ± 142.3	-1.1 ± 8.7
	LIB	92.4 ± 2.1	0.5 ± 0.2	1.3 ± 0.8	91.6 ± 82.4	12.8 ± 11.2	-35.1 ± 119.3	-3.9 ± 17.1
ICA	AB	91.1 ± 2.1	0.6 ± 0.4	2.1 ± 1.4	56.7 ± 40.5	10.0 ± 8.5	-7.9 ± 70.2	-0.1 ± 13.3
	LIB	90.0 ± 4.4	0.3 ± 0.1	1.1 ± 0.6	48.0 ± 48.0	16.0 ± 12.4	-45.3 ± 50.6	-15.4 ± 13.8
ECA	AB	87.4 ± 4.2	0.6 ± 0.5	2.0 ± 1.6	38.2 ± 24.6	13.9 ± 10.6	1.5 ± 46.1	3.5 ± 17.4
	LIB	85.7 ± 6.6	0.3 ± 0.2	0.9 ± 0.5	28.4 ± 22.9	25.3 ± 14.6	-20.6 ± 30.4	-20.5 ± 25.6

4.4.3 Vessel wall volume (VWV) computation

The VWV quantifies the vessel wall thickness plus plaque, which is used as a biomarker for carotid atherosclerosis [50]. The VWV for each image is obtained by subtracting the total volume of the lumen region from the total volume enclosed by the carotid AB of the CCA, ICA, and ECA separately. In this paper, we validate our algorithm for the purpose of generating VWV. The Bland-Altman plots [49] shown in Fig. 4.9, show the difference of the manual and algorithm measurements as a function of their mean. The algorithm shows a bias of -6.6, -10.0, and 3.8 mm^3 for the CCA, ICA, and ECA for 3T MR images and a bias of 19.1, 35.4, and 22.1 mm^3 for the CCA, ICA, and ECA for 1.5T MR images. The Pearson correlation coefficients of algorithm-generated VWV for each artery indicate a significant correlation (range for r: 0.73–0.94, $p<0.001$), with the manually-generated VWV as shown in Table 4.4. For the 3T MR images, there was no statistically significant difference ($p>0.05$) between the algorithm- and manually-generated VWV. Similarly, there was no statistically significant difference for CCA VWVs of the 1.5T MR images, although, there is a

Table 4.7: Results of inter- and intra-observer variability of the algorithm for 8 T1-weighted 3T MR images using the proposed algorithm.

User ID	CCA			ICA			ECA		
	CV (%)	*ICC*	MDD (mm^3)	CV (%)	*ICC*	MDD (mm^3)	CV (%)	*ICC*	MDD (mm^3)
U2	0.9	0.992	17.2	1.1	0.995	7.6	1.9	0.996	9.0
U3	0.7	0.996	13.3	2.0	0.983	13.6	2.7	0.993	12.4
U4	2.4	0.949	45.8	3.3	0.952	23.2	5.6	0.966	26.6
U5	0.8	0.994	14.7	2.0	0.983	14.1	3.1	0.990	14.7
Inter -observer	2.9	0.995	52.9	4.1	0.996	31.4	6.6	0.997	34.2

Table 4.8: Results of inter- and intra-observer variability of the algorithm for 8 T1w 1.5T MR images using the proposed algorithm.

User ID	CCA			ICA			ECA		
	CV (%)	*ICC*	MDD (mm^3)	CV (%)	*ICC*	MDD (mm^3)	CV (%)	*ICC*	MDD (mm^3)
U2	0.4	0.999	11.9	0.4	0.999	2.8	0.4	0.999	2.0
U3	0.5	0.999	9.6	0.4	0.999	3.4	0.5	0.999	2.5
U4	0.6	0.999	17.0	0.7	0.997	5.9	0.8	0.999	4.8
U5	0.4	0.999	11.0	0.5	0.999	3.7	0.4	0.999	2.3
Inter -observer	0.9	0.998	22.9	1.0	0.987	9.6	1.3	0.996	7.0

significant difference ($p<0.05$) between the ICA VWV and ECA VWV. The 95% confidence intervals of the mean difference between algorithm- and manually-generated VWV are also shown in Table 4.4. For example, the CI of the CCA for 1.5T MR images indicates that the mean difference of the population may fall within -16.5 to 54.8 mm^3.

4.4.4 Precision

We assessed the intra- and inter-observer variability of our algorithm for computing the VWV by repeatedly segmenting the same image set five times with different initializations by four users. Eight T1w 3T MR images, and eight 1.5T MR images were used for the analysis. Figure 4.10(a) and (b) show bar graphs of the DSC for 5 repeated segmentations of a single user for each section of the carotid artery, for which the user (U3 for the experiments of this paper) was selected randomly. The error bar on the plots represents the standard deviation of DSC measurements. Similarly, Fig. 4.10(c) and (d) show bar graphs of the DSC of four experts for each section of the carotid artery. By visual comparison of the intra- and inter-observer measurements, the DSC values are consistent and show very small variations across different repetitions and different users.

The intra- and inter-observer variability analysis results of the algorithm for computing VWV for T1w 3T images are shown in Table 4.7. We used CV, ICC, and MDD to assess the precision. The intra- and inter-observer CV values were small for all three sections of the artery as shown in Table 4.7. For example, the intra-observer CV ranged from 0.7% to 2.4% for the CCA and inter-observer CV is 2.9%. The algorithm yielded small intra- and inter-observer MDDs in the range of 7.6 to 52.9 mm^3, although, the inter-observer MDDs were slightly larger than the intra-observer MDDs. In accordance with the CV and MDD results, the algorithm also yielded high intra- and inter-observer ICCs that are more than 0.94 in all occasions.

Table 4.8 shows the results of intra- and inter-observer variability in computing VWV for 1.5T MR images. Small CVs were observed for 1.5T MR images. For example, the CV ranged from 0.4% to 0.7% for the CCA. Similar to the results for T1w 3T images, our algorithm obtained small intra- and inter-observer CVs in the range of 0.4-1.3%. The MDD values also had a small range of 2.0 - 22.9 mm^3, while ICC values were more than 0.996 for all three sections of the artery.

4.5 Discussion

We described and validated a novel global optimization-based approach for jointly segmenting the carotid lumen and wall by evolving the two coupled surfaces of AB and LIB, which integrates an inter-surface order constraint to improve the segmentation accuracy and robustness, especially in the absence of strong image information. Here we discuss the algorithm in terms of experimental methodology, computational time, accuracy, and precision in detail.

The algorithm is initialized by sampling a single 2D slice of the 3D MR image. Although it is important to sufficiently sample the intensities, especially in the back-

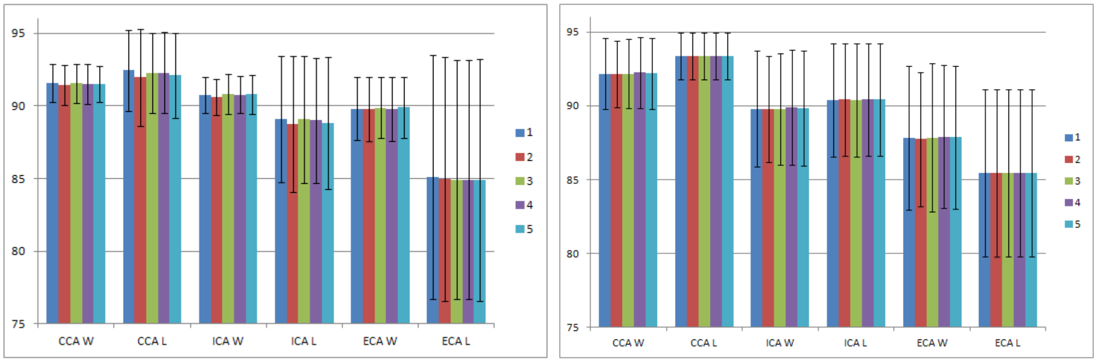

(a) Intra-observer variability of DSC for 8 3T images

(b) Intra-observer variability of DSC for 8 1.5T images

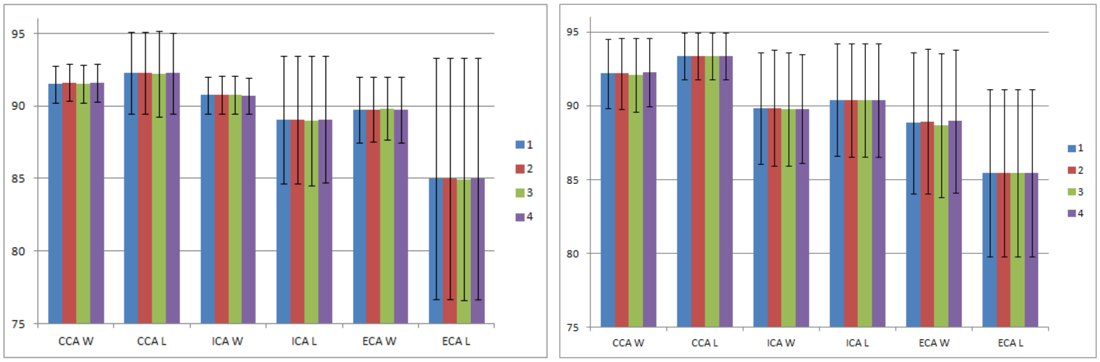

(c) Inter-observer variability of DSC for 8 3T images

(d) Inter-observer variability of DSC for 8 1.5T images

Figure 4.10: The evaluation of intra- and inter-observer variability of DSC of the proposed method. The error bars indicate the standard deviation.

ground for a robust segmentation, the algorithm is not sensitive to the background initialization. The main reason for this is that the intensity PDF model generated from the sampled background voxels is used only for the 2D AB-LIB segmentation of only a single transverse slice, together with the application of the inter-contour priors of the AB and LIB. Once the 2D AB-LIB segmentation is obtained, the intensity PDF model corresponding to the background is re-computed from the entire background region of the transverse slice instead of the sampled background voxels.

4.5.1 Computational time

The parallelized implementation of the algorithm using a GPU required only about 26 s for 3D AB-LIB segmentation from a 3T carotid MR image, within which 6 s was taken for the continuous max-flow algorithm, and 20 s was required for the unoptimized Matlab program. The algorithm required only 5 s in total for segmenting the AB and LIB from a 1.5T 3D carotid MR image, for which a substantial amount of time was spent on the distance transform function and the kernel density function in Matlab. The main purpose of the algorithm is for monitoring of carotid atherosclerosis longitudinally and not for an OR application. Therefore, the computation speed of the algorithm is adequate. However, the proposed approach can be further sped up by optimizing the Matlab program, implementing the distance transforms on a GPU, and using faster hardware.

4.5.2 Accuracy

We used region-based, volume-based, and boundary distance-based metrics for algorithm evaluation. The algorithm yielded high accuracy (i.e.: DSC For the AB and LIB of the CCA $\approx 93\%$ for 3T MR images) for the AB and LIB of the CCA and ICA. The algorithm reported a higher accuracy for the CCA, for both 1.5T and 3T MR images, than for the ICA and ECA. Within the ICA and ECA, the ICA achieved higher accuracy than the ECA. The reduced accuracy for the ECA may be due to its smaller size in comparison to the CCA and ICA, as well as the weak image information of the ECA AB; such that the algorithm attempts to maintain a minimum length on the surface without splitting at the carotid bifurcations. Clinically, CCA and ICA segmentations are more important than ECA segmentation, because the plaque tends to be present mostly in the CCA and ICA [4].

The distance RMSEs and their standard deviations were sub-millimeter, which indicates a good agreement with the manual segmentations. The MAXD errors were less than 2.1 mm for all boundaries, which also indicates a strong agreement with the manual method. In most cases, MAXD errors (see Table 4.5 and 4.6) for the AB were higher than the LIB, especially for the ECA and ICA. The reason may be due to the fact that in some images the AB surface may split slightly above the actual bifurcation region, because of the poor image quality.

The algorithm yielded comparable errors for the volume-based metrics (see Table 4.5 and 4.6). The algorithm segmentation resulted in small absolute volume errors in the range of 17 to 111 mm^3 for the entire data set. The absolute volume errors were largest for the CCA AB (111 mm^3) and CCA LIB (91.6 mm^3), where CCA AB volumes were in the range of 900 - 2129 mm^3 and CCA LIB volumes were in the range of 399 - 1026 mm^3. The volume errors (δV_E and δV_P) indicate that the proposed method slightly underestimates the manually generated volumes, even though the difference is not statistically significant. For the computation of VWV, the algorithm-generated VWV showed a high agreement with manual VWV, as indicated by the high Pearson correlation coefficients (see Table 4.4). The CIs provide an estimated interval of the mean difference between algorithm-generated and manual VWV with 95% confidence level. Note that, the values within the CIs (see Table 4.4) reported for our algorithm were small. However, the CI are affected by the sample size, where larger sample sizes lead to a tight estimate of the CI.

For 1.5T MR images, the algorithm overestimated the VWV for the CCA, ICA, and ECA (see Fig. 8(b), (d), and (f)). The overestimation of the VWV could occur due to the underestimation of the LIB volume and/or overestimation of the AB volume. According to the results for signed volume error δV_p (see Table 4.6), the algorithm underestimated the LIB volume for all sections of the CA, while δV_p for the AB volumes were small. Therefore, the bias arises from the underestimation of the LIB volume for these images.

In some cases, disagreements with the manual segmentations are due to the fact that the user did not follow the image boundaries at finer scale. In addition, quantization may also introduce errors in the volume computation.

4.5.3 Precision

An algorithm used in practice should yield low intra- and inter- observer variability in addition to high accuracy. We evaluated the variability of our algorithm for computation of the VWV. Our algorithm yielded small intra-observer CVs (see Table 4.7 and 4.8) for all three arteries for both 3T and 1.5T MR images, which indicates that the algorithm is robust to user interaction. Because of using region-based sample points as opposed to using boundary-based sample points, our algorithm is not subject to the operator variability that arises from identifying object boundaries for choosing boundary-based sample points. The low inter-observer CV and the high inter-observer ICC of our algorithm suggests a high reproducibility. This is particularly useful in multi-center clinical trials, where the measurements may be made by multiple observers in different locations at different times. The intra- and inter-observer MDDs (see Table 4.7 and 4.8) were smaller (2.0 to 52.9 mm^3) than the annual change ($\approx$ 120 mm^3/ year) of VWV change in a patient with moderate stenosis [51, 52].

4.5.4 Other potential applications

In addition to computing VWV for monitoring plaque burden, segmentations of the carotid AB and LIB surfaces by the proposed method may also be employed for MR plaque component analysis [2] and for carotid stent simulation [53], where the visibility of the carotid AB and some plaque components in MR images [2] can be used in determining the stress distribution in the vessel wall and degree of straightening for carotid stenting simulation. The proposed coupled-surface evolution approach may also be investigated for use with other image segmentation tasks, such as the segmentation of abdominal aortic aneurysms (AAA) and myocardial segmentation in cinematic MR images. For the segmentation of AAA, it is expected that the lumen and thrombus regions, including bifurcations, can be computed in a similar manner using the proposed algorithm. For the myocardial segmentation, the epi- and endocardial boundaries may also be simultaneously segmented using the proposed coupled contour evolution approach.

4.5.5 Comparison to previous studies

Some previous studies have described coupled contour evolution approaches for medical imaging [54, 55, 56, 57, 58] etc., and natural imaging [59, 60] etc. Approaches proposed by Paragios *et al.* [55, 60] and Yezzi *et al.* [59] were 2D segmentation methods and used local optimization methods, such as level sets or snakes for curve evolution. Zeng *et al.* [56] proposed a 3D level set method for coupled surface segmentation of 3D MR brain images. Delong *et al.* [58] and Schmidt *et al.* [57] used graph-cut based coupled 2D/3D coupled contour segmentation algorithms. Li *et al.* [54] proposed a 2D/3D single-shot graph-cut approach to segment coupled surfaces based on the combinatorial optimization technique. They [54] first unwrap the image by casting rays from the center-line of the object to obtain a polar representation of the image, which allows their method to segment multiple nested surfaces along the resulting columns. They [54] use smoothness constraints δ_x and δ_y to regularize the stiffness of the surfaces, which is achieved via the TV-based smoothness term in our approach. Their surface separation realized using constraints δ^l and δ^u, is achieved via the minimum- and maximum separation forces in our approach. However, a limitation of their approach is the need for unwrapping the image domain, which may introduce distortions. In addition, handling carotid bifurcations and changes in topology are challenging, because their method also assumes that each surface intersects each ray at only one location.

To our knowledge, public data are not available for the validation of the carotid vessel wall images. Therefore, we used data acquired in our center for algorithm validation. The closest previous studies to our work were by Adame *et al.* [7], Kerwin *et al.* [9], Ladak *et al.* [10], and Yuan *et al.* [11] as shown in Table 4.1. Note that, here we considered only the techniques that do not require the acquisition of other modalities such as MR angiography (e.g. work from Klooster *et al.* [8]) to assist the segmentation. All the above methods are slice-by-slice methods that require user interaction on each slice to segment the LIB and AB sequentially. In addition, these methods may be required to initialize and segment the ICA and ECA for each boundary separately. However, our proposed algorithm segments both the AB and LIB simultaneously and requires expert interaction only on a single slice. From the methods that have reported the computational time, the method proposed by Adame *et al.* [7] requires 25 s per boundary per slice, whereas the method proposed by Yuan *et al.* [11] requires a time of 20 s to 2 min per slice per boundary. Our method provides substantial improvement in speed (26 s for a 3D image with 110 slices; 6 s for max-flow in a GPU and 20 s for cost computation using non-optimized Matlab code) for segmenting 3D carotid MR images.

The method proposed by Adame *et al.* [7] has been used in clinical trials [15]. They [7] segmented only the carotid CCA and reported accuracy in terms of area difference but not DSC. For the CCA, our method yielded absolute volume errors of 6.1% and 7.3% for the AB and LIB; whereas, their method yielded area errors of 6% and 8% for the AB and LIB. As for the precision, their method reported intra-observer CV of 4.3% and 3.5% and inter-observer CV of 9.5% and 5.3% for computing luminal and wall areas of the CCA, which are more than the intra- and inter-observer CVs reported by our method for the CCA (see Table 4.7 and 4.8 for CV values for the CCA). However, note that the two studies used different data sets and different users, so quantitative comparison is not meaningful. In the study proposed by Krasinski *et al.* [3] a single observer performed manual VWV measurements repeatedly five times and reported an intra-observer CV of 6.4% to 7.7% on the same dataset as ours. In comparison to their results, our algorithm yielded a smaller intra-observer CVs (see Table 4.7 and 4.8 for CV values) for generating VWV measurements.

References

[1] E. Ukwatta, J. Yuan, M. Rajchl, D. Tessier, and A. Fenster, “3D carotid multi-region MRI segmentation by globally optimal evolution of coupled surfaces,” *IEEE Transactions of medical imaging*, vol. 32, no. 4, pp. 770–85, 2013. 122

[2] C. Yuan, W. S. Kerwin, V. L. Yarnykh, J. Cai, T. Saam, B. Chu, N. Takaya, M. S. Ferguson, H. Underhill, D. Xu, F. Liu, and T. S. Hatsukami, “MRI of atherosclerosis in clinical trials,” *NMR in Biomedicine*, vol. 19, no. 6, pp. 636–654, 2006. 122, 157

[3] A. Krasinski, B. Chiu, A. Fenster, and G. Parraga, “Magnetic resonance imaging and three-dimensional ultrasound of carotid atherosclerosis: Mapping regional differences,” *J. Magn. Reson. Im.*, vol. 29, no. 4, pp. 901–908, 2009. 122, 137, 159

[4] C. Yuan, M. Oikawa, Z. Miller, and T. Hatsukami, “MRI of carotid atherosclerosis,” *J Nucl. Cardiol.*, vol. 15, no. 2, pp. 266–275, 2008. 122, 124, 155

[5] H. Underhill and C. Yuan, “Carotid MRI: a tool for monitoring individual response to cardiovascular therapy?” *Expert Review of Cardiovascular Therapy*, vol. 9, no. 1, pp. 63–80, 2011. 122

[6] W. S. Kerwin, K. D. O’Brien, M. S. Ferguson, N. Polissar, T. S. Hatsukami, and C. Yuan, “Inflammation in carotid atherosclerotic plaque: A dynamic contrast-enhanced MR imaging study1,” *Radiology*, vol. 241, no. 2, p. 459, 2006. 122

[7] I. M. Adame, R. J. van der Geest, B. A. Wasserman, and e. a. Mohamed, M. A., “Automatic segmentation and plaque characterization in atherosclerotic carotid artery MR images,” *Magn. Reson. Mater. Phy.*, vol. 16, no. 5, pp. 227–234, 2004. 123, 158, 159

[8] R. van’t Klooster, P. de Koning, R. Dehnavi, and J. e. a. Tamsma, “Automatic lumen and outer wall segmentation of the carotid artery using deformable 3D models in MR angiography and vessel wall images,” *J. Magn. Reson. Im.*, vol. 35, 2011. 123, 158

[9] W. Kerwin, D. Xu, F. Liu, T. Saam, H. Underhill, N. Takaya, B. Chu, T. Hatsukami, and C. Yuan, “Magnetic resonance imaging of carotid atherosclerosis,” *Top. Magn. Reson. Imag.*, vol. 18, no. 5, pp. 371–378, 2007. 123, 158

[10] H. M. Ladak, J. B. Thomas, J. R. Mitchell, B. K. Rutt, and D. A. Steinman, “A semi-automatic technique for measurement of arterial wall from black blood MRI,” *Med. Phys.*, vol. 28, no. 6, pp. 1098–1107, Jun. 2001. 123, 158

[11] C. Yuan, E. Lin, J. Millard, and J. Hwang, “Closed contour edge detection of blood vessel lumen and outer wall boundaries in black-blood MR images,” *Magn. Reson. Imaging.*, vol. 17, no. 2, pp. 257–266, Feb. 1999. 123, 158

[12] H. Tang, R. van Onkelen, T. van Walsum, R. Hameeteman, M. Schaap, and F. e. a. Tori, “A semi-automatic method for segmentation of the carotid bifurcation and bifurcation angle quantification on black blood MRA,” *MICCAI*, pp. 97—104, 2010. 123, 124

[13] H. M. Ladak, J. S. Milner, and D. A. Steinman, “Rapid three-dimensional segmentation of the carotid bifurcation from serial MR images,” *J. Biomed. Eng.*, vol. 122, pp. 96–9, 2000. 123, 124

[14] Y. Jin and H. M. Ladak, “Software for interactive segmentation of the carotid artery from 3D black blood magnetic resonance images,” *Comput. Meth. Prog. Bio.*, vol. 75, no. 1, pp. 31–43, Jul. 2004. 123, 124

[15] R. Duivenvoorden, E. de Groot, B. M. Elsen, J. S. Lamris, R. J. van der Geest, E. S. Stroes, J. J. Kastelein, and A. J. Nederveen, “In vivo quantification of

carotid artery wall dimensions: 3.0 tesla MRI versus b-mode ultrasound imaging." *Circulation: Cardiovascular Imaging*, 2009. 123, 159

[16] I. Adame, P. de Koning, B. Lelieveldt, B. Wasserman, J. Reiber, and R. van der Geest, "An integrated automated analysis method for quantifying vessel stenosis and plaque burden from carotid mri images," *Stroke*, vol. 37, no. 8, pp. 2162–2164, 2006. 123

[17] W. Liu, N. Balu, J. Sun, and e. a. Zhao, X., "Segmentation of carotid plaque using multicontrast 3D gradient echo MRI," *J. Magn. Reson. Im.*, 2011. 123

[18] J. Yuan, E. Bae, and X. Tai, "A study on continuous max-flow and min-cut approaches," in *CVPR 2010*. 125, 130, 131

[19] E. Bae, J. Yuan, and X.-C. Tai, "Global minimization for continuous multiphase partitioning problems using a dual approach," *Int. J. Comput. Vision.*, vol. 92, no. 1, pp. 112–129, 2011. 125

[20] D. Cremers, T. Pock, K. Kolev, and A. Chambolle, "Convex relaxation techniques for segmentation, stereo and multiview reconstruction," *Markov Random Fields for Vision and Image Processing. The MIT Press, Boston*, 2011. 125

[21] Y. Boykov, O. Veksler, and R. Zabih, "Fast approximate energy minimization via graph cuts," *IEEE T. Pattern. Anal.*, vol. 23, no. 11, pp. 1222–1239, 2001. 125, 141

[22] J. Yuan, E. Ukwatta, X.-C. Tai, A. Fenster, and C. Schnoerr, "A fast global optimization-based approach to evolving contours with generic shape prior," UCLA, Technical report CAM-12-38, 2012. 125, 130, 131, 132

[23] E. Ukwatta, J. Yuan, M. Rajchl, and A. Fenster, "Efficient global optimization based 3D carotid AB-LIB MRI segmentation by simultaneously evolving coupled surfaces," in *MICCAI*, ser. LNCS, N. Ayache, H. Delingette, P. Golland, and K. Mori, Eds., vol. 7512, 2012, pp. 377–384. 125

[24] G. Aubert, M. Barlaud, O. Faugeras, and S. Jehan-Besson, "Image segmentation using active contours: calculus of variations or shape gradients?" *SIAM J. Appl. Math.*, vol. 63, no. 6, pp. 2128–2154, 2003. 128

[25] O. Michailovich, Y. Rathi, and A. Tannenbaum, "Image segmentation using active contours driven by the bhattacharyya gradient flow," *IEEE T. Image. Process.*, vol. 16, no. 11, pp. 2787–2801, 2007. 128, 130

[26] H. Ishikawa, "Exact optimization for markov random fields with convex priors," *IEEE T. Pattern. Anal.*, vol. 25, pp. 1333–1336, 2003. 128

[27] E. Bae, J. Yuan, X.-C. Tai, and Y. Boycov, “A fast continuous max-flow approach to non-convex multilabeling problems,” UCLA, Technical report CAM-10-62, 2010. 128, 133, 134, 135

[28] T. Pock, A. Chambolle, H. Bischof, and D. Cremers, “A convex relaxation approach for computing minimal partitions,” in *PROC CVPR IEEE*, Miami, Florida, 2009. 128

[29] D. Freedman and T. Zhang, “Active contours for tracking distributions,” *Image Processing, IEEE Transactions on*, vol. 13, no. 4, pp. 518–526, 2004. 128, 132

[30] I. B. Ayed, H.-m. Chen, K. Punithakumar, I. Ross, and S. Li, “Graph cut segmentation with a global constraint: Recovering region distribution via a bound of the bhattacharyya measure,” in *Computer Vision and Pattern Recognition (CVPR), 2010 IEEE Conference on*. IEEE, 2010, pp. 3288–3295. 128

[31] K. Punithakumar, J. Yuan, I. B. Ayed, S. Li, and Y. Boykov, “A convex max-flow approach to distribution-based figure-ground separation,” *SIAM Journal on Imaging Sciences*, vol. 5, no. 4, pp. 1333–1354, 2012. 128

[32] D. Johnson and S. Sinanovic, “Symmetrizing the kullback-leibler distance,” *IEEE T. Inform. Theory*, vol. 1, no. 1, pp. 1–10, 2001. 129

[33] E. Parzen, “On estimation of a probability density function and mode,” *The Annals of Mathematical Statistics*, vol. 33, no. 3, pp. pp. 1065–1076, 1962. 129

[34] M. Kass, A. P. Witkin, and D. Terzopoulos, “Snakes: Active contour models,” *IJCV*, vol. 1, no. 4, pp. 321–331, 1988. 130

[35] V. Caselles, R. Kimmel, and G. Sapiro, “Geodesic active contours,” *IJCV*, vol. 22, no. 1, 1997. 130

[36] T. F. Chan and L. A. Vese, “Active contours without edges,” *Image Processing, IEEE Transactions on*, vol. 10, no. 2, pp. 266–277, 2001. 130

[37] S. Osher and R. Fedkiw, *Level set methods and dynamic implicit surfaces*, ser. Applied Mathematical Sciences. New York: Springer-Verlag, 2003, vol. 153. 130

[38] Y. Boykov, V. Kolmogorov, D. Cremers, and A. Delong, “An integral solution to surface evolution pdes via geo-cuts,” in *ECCV*, 2006, pp. 409–422. 130

[39] A. Chambolle, “An algorithm for mean curvature motion,” *Interf. Free Bound.*, vol. 6, pp. 195–218, 2004. 130

[40] T. F. Chan, S. Esedoglu, and M. Nikolova, “Algorithms for finding global minimizers of image segmentation and denoising models,” *SIAM Journal on Applied Mathematics*, vol. 66, no. 5, pp. 1632–1648, 2006. 134

[41] P. Thévenaz, T. Blu, and M. Unser, “Interpolation revisited [medical images application],” *IEEE T. Med. Imaging*, vol. 19, no. 7, pp. 739–758, 2000. 137

[42] Y. Y. Boykov and M.-P. Jolly, “Interactive graph cuts for optimal boundary & region segmentation of objects in nd images,” in *Computer Vision, 2001. ICCV 2001. Proceedings. Eighth IEEE International Conference on*, vol. 1. IEEE, 2001, pp. 105–112. 138

[43] D. Freedman and T. Zhang, “Interactive graph cut based segmentation with shape priors,” in *Computer Vision and Pattern Recognition, 2005. CVPR 2005. IEEE Computer Society Conference on*, vol. 1. IEEE, 2005, pp. 755–762. 138

[44] P. Touboul, M. Hennerici, S. Meairs, H. Adams, P. Amarenco, and e. a. Bornstein, N., “Mannheim carotid Intima-Media thickness consensus (2004-2006),” *Cerebrovascular Diseases*, vol. 23, no. 1, pp. 75–80, 2007. 142

[45] R. Adams and L. Bischof, “Seeded region growing,” *Pattern Analysis and Machine Intelligence, IEEE Transactions on*, vol. 16, no. 6, pp. 641–647, 1994. 142

[46] K. Zou, S. Warfield, A. Bharatha, C. Tempany, M. Kaus, S. Haker, W. Wells, F. Jolesz, and R. Kikinis, “Statistical validation of image segmentation quality based on a spatial overlap index,” *Academic Radiology*, vol. 11, no. 2, pp. 178–189, 2004. 144

[47] K. McGraw and S. Wong, “Forming inferences about some intraclass correlation coefficients.” *Psychological methods*, vol. 1, no. 1, p. 30, 1996. 144

[48] J. R. Mitchell, S. J. Karlik, D. H. Lee, M. Eliasziw, G. P. Rice, and A. Fenster, “The variability of manual and computer assisted quantification of multiple sclerosis lesion volumes,” *Medical Physics*, vol. 23, no. 1, pp. 85–97, 1996. 145

[49] D. Altman and J. Bland, “Measurement in medicine: the analysis of method comparison studies,” *The statistician*, pp. 307–317, 1983. xxi, 150, 151

[50] M. Egger, J. D. Spence, A. Fenster, and G. Parraga, “Validation of 3D ultrasound vessel wall volume: an imaging phenotype of carotid atherosclerosis,” *Ultrasound in medicine & biology*, vol. 33, no. 6, pp. 905–914, 2007. 151

[51] A. Krasinski, B. Chiu, J. D. Spence, A. Fenster, and G. Parraga, “Three-dimensional ultrasound quantification of intensive statin treatment of carotid atherosclerosis,” *Ultrasound in medicine & biology*, vol. 35, no. 11, pp. 1763–1772, 2009. 157

[52] I. Shai, J. D. Spence, D. Schwarzfuchs, Y. Henkin, G. Parraga, A. Rudich, A. Fenster, C. Mallett, N. Liel-Cohen, A. Tirosh *et al.*, “Dietary intervention to reverse carotid atherosclerosis,” *Circulation*, vol. 121, no. 10, p. 1200, 2010. 157

[53] F. Auricchio, M. Conti, M. De Beule, G. De Santis, and B. Verhegghe, "Carotid artery stenting simulation: From patient-specific images to finite element analysis," *Medical engineering & physics*, vol. 33, no. 3, pp. 281–289, 2011. 157

[54] K. Li, X. Wu, D. Chen, and M. Sonka, "Optimal surface segmentation in volumetric images-a graph-theoretic approach," *IEEE T. Pattern. Anal.*, vol. 28, no. 1, pp. 119–134, 2006. 158

[55] N. Paragios, "A variational approach for the segmentation of the left ventricle in cardiac image analysis," *International Journal of Computer Vision*, vol. 50, no. 3, pp. 345–362, 2002. 158

[56] X. Zeng, L. H. Staib, R. T. Schultz, and J. S. Duncan, "Volumetric layer segmentation using coupled surfaces propagation," in *Computer Vision and Pattern Recognition, 1998. Proceedings. 1998 IEEE Computer Society Conference on.* IEEE, 1998, pp. 708–715. 158

[57] F. R. Schmidt and Y. Boykov, "Hausdorff distance constraint for multi-surface segmentation," in *Computer Vision–ECCV 2012.* Springer, 2012, pp. 598–611. 158

[58] A. Delong and Y. Boykov, "Globally optimal segmentation of multi-region objects," in *Computer Vision, 2009 IEEE 12th International Conference on.* IEEE, 2009, pp. 285–292. 158

[59] A. Yezzi, A. Tsai, and A. Willsky, "A fully global approach to image segmentation via coupled curve evolution equations," *Journal of Visual Communication and Image Representation*, vol. 13, no. 1, pp. 195–216, 2002. 158

[60] N. Paragios and R. Deriche, "Coupled geodesic active regions for image segmentation: A level set approach," *ECCV*, pp. 224–240, 2000. 158

Chapter 5

Joint segmentation of 3D femoral artery lumen and outer wall from 3D black-blood MR images[†]

5.1 Introduction

Peripheral arterial disease (PAD) is a common circulatory disease, which occludes the arteries with long term accumulation of plaque due to atherosclerosis. Although PAD causes morbidity ranging from intermittent claudication to critical limb ischemia, it has long been underdiagnosed and undertreated [2, 3] and may have been overshadowed by cardio- and cerebro-vascular events and mortality [4]. Coronary and cerebrovascular diseases coexist with PAD [5, 6, 7] and asymptomatic and symptomatic PAD are consistent and powerful independent predictors of coronary artery and cerebrovascular diseases [4]. Therefore, reproducible and sensitive measurements of PAD are important for evaluating patient's response to medical treatment for improved management of patients with PAD. Some previous investigations have shown that the most occluded location due to PAD is the adductor canal region of the superficial femoral artery (SFA) [8]. Therefore, in this work, we focus on PAD of the SFA.

Currently, ankle-brachial index (ABI), an approximate estimate of the relative blood flow in the ankle compared to the brachial artery, is used for diagnosis and assessment of the severity of PAD [9]. Patients with ABIs less than 0.9 may be followed up with a MRI or CTA. However, similar to other luminographic techniques, it has limited capabilities for assessing the progression of the disease and prediction of clinical events [4]. Assessment of PAD using cardio-vascular MR imaging has been continued to develop [10], due to its non-invasiveness and its ability to image the femoral artery vessel wall with high image contrast. In this paper, we use 3D black-blood MR images (see Fig. 5.1(a) and (b)) acquired using the 3D motion-sensitized driven equilibrium (MSDE) prepared rapid gradient echo sequence (3D MERGE) [11, 12], which enables evaluation of the femoral artery vessel wall up to a length of 50 cm.

[†]. A preliminary version [1] of this chapter has been accepted for publication at *International Conference on Medical Image Computing and Computer Assisted Intervention 2013 (MICCAI)*. A complete version of this chapter has been submitted for publication: E. Ukwatta, J. Yuan, M. Rajchl, W. Qiu, B. Chiu, and A. Fenster, "Joint segmentation of lumen and outer wall from 3D femoral artery MR images: Towards volumetric phenotypes of peripheral arterial disease," in *IEEE Transactions on Medical Imaging,* submitted on August 26, 2013.

Due to the high vessel wall image contrast, MR imaging facilitates morphological and volumetric measurements of plaque burden, which may be more sensitive to clinical outcomes [4, 8, 10, 13]. However, one of the current challenges for obtaining volumetric/morphological measurements is the delineation of the femoral lumen and outer wall surfaces (see Fig. 1.12(a) in Chapter 1) from 3D femoral MR images comprising of about 500–1000 slices per dataset. The manual segmentations of the femoral outer wall and lumen are performed slice-wise on transverse view (see Fig. 5.2(a)). However, it is usually performed at an ISD greater than the slice thickness to alleviate measurement burden from a time-consuming and tedious process. For example, manual segmentation of the lumen and outer wall from a 3D femoral MR image at an ISD of 10 mm requires about 80 min [14] of user time. Therefore, the objective of this work is to develop and validate an algorithm for segmenting the femoral lumen and outer wall surfaces robustly and efficiently from 3D black-blood MR images. The major challenges for a segmentation algorithm of the femoral lumen and outer wall are the thin and elongated shape appearance of the femoral artery (see Fig. 1.12(a)) and the lack of distinctive image boundary at the outer wall boundary, and strong overlapping of intensity appearance between the outer wall and its surrounding region.

5.1.1 Previous studies

To our knowledge, only one study [14] has been reported for describing a semi-automated method for segmentation of both the femoral artery lumen and wall boundaries from MR images. Although, some previous studies have been reported for segmentation of the carotid artery lumen and outer wall from carotid MR images [15, 16]

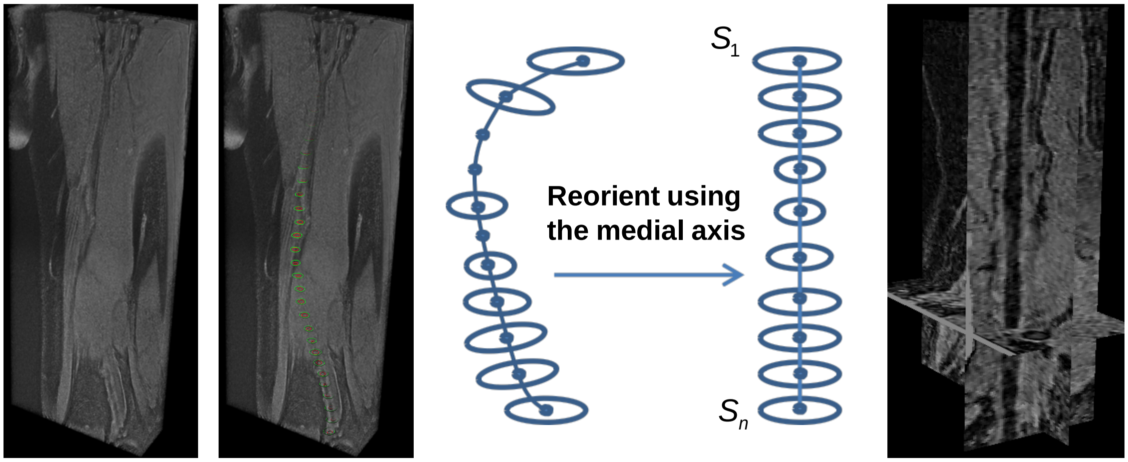

(a) (b) (c) (d)

Figure 5.1: (a) An example femoral MR image of a patient; (b) same image with overlaid manual annotations of the femoral artery lumen and outer wall; (c) reorientation of the femoral MR image using the medial axis of the artery. The reorientation procedure is described in Section 5.3.2; and (d) Long axis view of reoriented 3D MR image.

these methods may not be directly applicable to femoral artery segmentation from MR images due to its thin and elongated appearance in the MR images and the relative inferior quality of the femoral MR images.

Chiu *et al.* [14] proposed a 2D slice-by-slice B-spline snake segmentation procedure, where the segmentation of the current slice is propagated as the initial contour to assist segmenting its succeeding slice. As well, this method first segments the lumen region, then the outer wall region. Initially, the segmentation of the first slice is performed manually. For the subsequent slice, the segmentation boundary of the first slice was propagated and transformed using the transformation obtained by registering the first transverse slice to the second transverse image slice using an optical flow-based registration procedure. When the ratio between the luminal areas of adjacent slices is outside the range of 0.5 and 1.5, the segmentation pauses and requires further user interaction to proceed. After the lumen segmentation had been obtained, the outer wall was then segmented using a two-pass process with forward and backward passes. Two such propagations were performed using a conditional shape model, where two outer wall segmentations are obtained for each slice. Afterwards, a gradient-based decision rule was applied to the two contours to determine the final

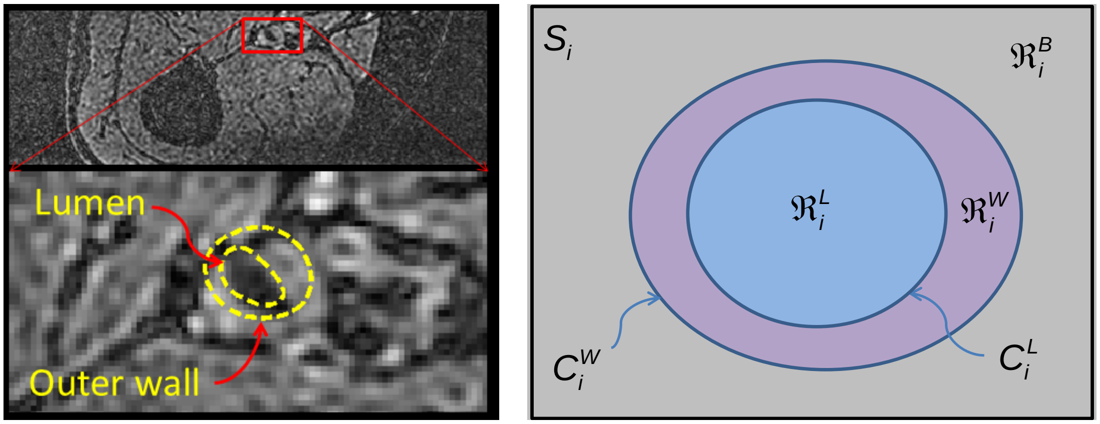

(a) (b)

Figure 5.2: (a) A transverse slice of a 3D femoral MR image with manual delineations; and (b) schematic diagram denoting the notation used for lumen and outer wall contours C_i^L, C_i^W and lumen, outer wall, and backgound regions $\mathcal{R}_i^L, \mathcal{R}_i^W, \mathcal{R}_i^B$.

contour. The outer wall result is then formatted using a curved planar reformatting view. The 2D method [14] requires about 8–10 min of user time for the lumen and outer wall segmentations. In addition, such slice-by-slice technique does not globally enforce the inherent spatial coherence of the contours along the medial axis of the artery, hence segmentation errors in one slice can be propagated and accumulated in the segmentation of the next slices.

5.1.2 Contributions

In this chapter, we describe a novel and efficient global optimization-based 3D algorithm to jointly segment the outer wall and lumen of the femoral artery from 3D black-blood MR images, while enforcing the spatial consistency of the re-oriented slice sequence (see Fig. 5.1(c) and (d)) along the medial axis of the artery. We demonstrate that the resulting combinatorial optimization problem can be solved globally and exactly by means of convex relaxation, and propose the new *coupled continuous max-flow (CCMF) model*, which presents the dual formulation to the studied convex relaxation model and allows a fast numerical algorithm. In addition, the new spatially continuous max-flow model directly leads to an efficient continuous max-flow based algorithm based on modern convex optimization theories. The algorithm is implemented in a GPU to obtain high computational efficiency.

To our knowledge, the proposed approach is the first 3D algorithm for segmenting the femoral lumen and outer wall from 3D black-blood MR images. The results of the experiments demonstrate that our method provides high accuracy and repeatability with significantly less user interaction. The proposed method outperforms the previous method [14] in terms of computational time, and amount of user interaction needed.

A preliminary study of this work has been previously submitted to a conference paper [1]. However, this paper is substantially extended from the previous submission with the following information: (1) a comprehensive description of the algorithm is included; (2) a validation of the area and volumetric segmentation results; and (3) the algorithm is implemented in a GPU to increase the computational efficiency.

5.2 Methods

We propose a global optimization approach to simultaneously segment the femoral artery lumen and outer wall surfaces from an input 3D femoral MR image $\mathcal{V}$. Let $\mathcal{V}_R$ be the reoriented 3D MR image with n 2D transverse slices $\mathcal{S}_1 \ldots \mathcal{S}_n$, reoriented using the medial axis of the femoral artery. When the artery is straightened using the medial axis as shown in Fig. 5.1(c), it appears as an approximate cylindrical shape. The process of obtaining the medial axis and the artery straightening process are described in detail in Section 5.3.2. As an alternative to a direct 3D segmentation of $\mathcal{V}$, the proposed segmentation is performed on the reoriented image $\mathcal{V}_r$ to enforce the tubular-like shape of the femoral artery, which entails spatial consistency between adjacent transverse slices. The proposed algorithm simultaneously segments the reoriented MR image $\mathcal{V}_r$ into lumen, outer wall, and background by jointly enforcing *tubular prior* on both the femoral lumen and outer wall. We first describe briefly the multi-region segmentation formulation of the femoral lumen and outer wall in Section 5.2.1 and describe the integration of the *tubular prior* into the multi-region segmentation formulation in Section 5.2.2.

5.2.1 Muti-region segmentation formulation

Here we decompose the segmentation of the reoriented image $\mathcal{V}_r$ as a problem of segmenting n 2D slices $\mathcal{S}_i, i = 1 \ldots n$, simultaneously. Let $\mathcal{C}_i^L$ and $\mathcal{C}_i^W$ denote the lumen and outer wall contours and $\mathcal{R}_i^B$, $\mathcal{R}_i^W$ and $\mathcal{R}_i^L$, $i = 1 \dots n$, denote background, outer wall, and lumen regions within the 2D slice $\mathcal{S}_i$, respectively. Let $u_i^1(x)$ and $u_i^2(x) \in \{0, 1\}$, $i = 1 \dots n$, be the corresponding indicator labeling functions of $\mathcal{C}_i^W$ and $\mathcal{C}_i^L$ such that

$$u_i^1(x) = \begin{cases} 1\,, & \text{for } \forall x \text{ within } \mathcal{C}_i^W \\ 0\,, & \text{otherwise} \end{cases} \quad , \quad i = 1 \dots n\,.$$

and

$$u_i^2(x) = \begin{cases} 1\,, & \text{for } \forall x \text{ within } \mathcal{C}_i^L \\ 0\,, & \text{otherwise} \end{cases} \quad ; \quad i = 1 \dots n\,.$$

Since the lumen region $\mathcal{R}_i^L$ is located within the outer wall region $\mathcal{R}_i^W$ (see Fig. 1(b)) in each slice $\mathcal{S}_i$, $i = 1 \dots n$, the following labeling order can be enforced in the segmentation as follows:

$$u_i^2(x) \,\leq\, u_i^1(x)\,, \quad \forall x \,\in\, \mathcal{S}_i\,; \quad i = 1 \dots n\,. \tag{5.1}$$

Then the binary labeling functions $u_i^{L,W,B} \in \{0, 1\}$ for $\mathcal{R}_i^{L,W,B}$ can be obtained as follows:

$$u_i^L = u_i^2\,, \;\; u_i^W = u_i^1 - u_i^2\,, \;\; u_i^B = 1 - u_i^1\,. \tag{5.2}$$

The segmentation of each slice $\mathcal{S}_i$, $i = 1 \dots n$, into the three regions of $\mathcal{R}_i^{B,W,L}$ can be formulated as a coupled continuous min-cut problem [17], which minimizes the following energy function

$$\begin{aligned} E_i(u_i^1, u_i^2) :=& \Big\{ \int u_i^B D_i^B \, dx + \int u_i^W D_i^W \, dx \\ & + \int u_i^L D_i^L \, dx \Big\} + \Big\{ \int_\Omega g_i(x) \left|\nabla u_i^W\right| \, dx \\ & + \int_\Omega g_i(x) \left|\nabla u_i^L\right| \, dx \Big\} \end{aligned} \tag{5.3}$$

over the binary labeling functions $u_i^{1,2}(x) \in \{0, 1\}$, subject to constraint (5.1).

In (5.3), the functions $D_i^B(x)$, $D_i^W(x)$, and $D_i^L(x)$ evaluate the cost to label pixel $x \in \mathcal{S}_i$, $i = 1 \dots n$, as the background region $\mathcal{R}_i^B$, the wall region $\mathcal{R}_i^W$ and the lumen region $\mathcal{R}_i^L$ respectively. For example when the intensity log likelihood terms

$$D_i^j(x) = -\ln\left(Pr^j\ \left(I(x)\,|\,\mathcal{R}_i^j\right)\right)\,,\quad j = L, W, B \tag{5.4}$$

are used as data terms for segmentation [18, 19, 19], for pixel x to be labeled within the region $\mathcal{R}_i^j$, it incurs cost $D_i^j(x)$, which is based on how well the intensity of x matches the model/prior intensity histogram Pr $(I(x))$ of R_i^j. Hence, the sum of the first three terms provides the total cost of labeling each pixel with slice $\mathcal{S}_i$. The two weighted total-variation functions of (5.3) measure the smoothness of the two contours $\mathcal{C}_i^W$ and $\mathcal{C}_i^L$ w.r.t. the labeling functions $u_i^1(x), u_i^2(x) \in \{0, 1\}$, where $g_i(x)$ is a positive weight function of the image gradient as follows:

$$g_i(x) = \lambda_1 + \lambda_2 \exp(-\lambda_3|\nabla I(x)|)\,,\quad \lambda_{1,2,3} \geq 0 \tag{5.5}$$

where the values of $g_i(x)$ fall within the range of $[\lambda_1, \lambda_1 + \lambda_2]$.

5.2.2 Spatial consistency prior between adjacent slices

The n slices $\mathcal{S}_1 \ldots \mathcal{S}_n$ of $\mathcal{V}_r$ are aligned along the medial axis of the femoral artery (see the blue dotted line in Fig. 5.1(c)). Due to the tubular shape of the femoral artery, the wall or lumen boundaries of two adjacent transverse slices appear similar in size. In other words, the boundaries of adjacent slices have strong spatial consistency between them. With this regard, we propose to enforce such *spatial consistency prior* of the segmented contours $\mathcal{C}_i^W$ and $\mathcal{C}_i^L$, $i = 1 \ldots n$, by penalizing the total spatial/area differences of the contours between two neighbouring slices, i.e. minimizing

$$\begin{aligned}\pi_i(u) := \Bigg\{ &\int_\Omega \left|u_{i+1}^1 - u_i^1\right| dx \\ &+ \int_\Omega \left|u_{i+1}^2 - u_i^2\right| dx \Bigg\}\,,\quad i = 1 \ldots n-1\,.\end{aligned} \tag{5.6}$$

Here, the first and second terms of (5.6) correspond to the spatial consistency terms for the femoral outer wall and lumen.

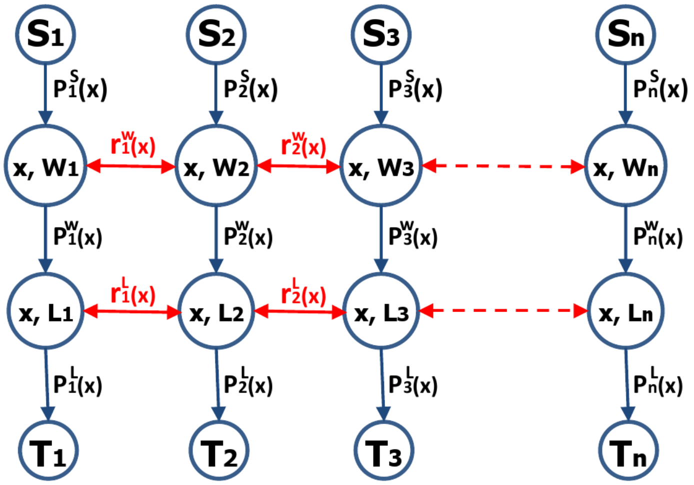
S_1
S_2
S_3
S_n
$P_1^S(x)$
$P_2^S(x)$
$P_3^S(x)$
$P_n^S(x)$
x, W_1
$r_1^W(x)$
x, W_2
$r_2^W(x)$
x, W_3
x, W_n
$P_1^W(x)$
$P_2^W(x)$
$P_3^W(x)$
$P_n^W(x)$
x, L_1
$r_1^L(x)$
x, L_2
$r_2^L(x)$
x, L_3
x, L_n
$P_1^L(x)$
$P_2^L(x)$
$P_3^L(x)$
$P_n^L(x)$
T_1
T_2
T_3
T_n

Figure 5.3: Flow configurations of the proposed *coupled continuous max-flow model.*

5.2.3 Optimization formulation

In view of (5.3) and (5.6), we propose to segment the 3D surfaces of the femoral artery outer wall and lumen by segmenting the n 2D image slices while incorporating inter-slice consistency (5.6), which can be formulated with a balancing weight $\alpha > 0$ as

$$\min_{u^{1,2}(x)\in\{0,1\}} \sum_{i=1}^{n} E_i(u_i) + \alpha \sum_{i=1}^{n-1} \pi_i(u)\,; \qquad \text{s.t.} \;\; u_i^2(x) \leq u_i^1(x)\,, \;\; i = 1 \ldots n\,. \tag{5.7}$$

5.2.4 Convex relaxation and coupled continuous max-flow model

In this study, we show that the proposed optimization problem (5.7) can be globally and exactly solved by its convex relaxation

$$\min_{u^{1,2}(x)\in[0,1]} \sum_{i=1}^{n} E_i(u_i) + \alpha \sum_{i=1}^{n-1} \pi_i(u)\,; \qquad \text{s.t.} \;\; u_i^L(x) \leq u_i^W(x)\,, \;\; i = 1 \ldots n\,, \tag{5.8}$$

where the binary-valued constraints $u_i^{1,2}(x) \in \{0,1\}$ in (5.7) are replaced by their convex relaxation $u_i^{1,2}(x) \in [0,1]$ [20]. Clearly, (5.8) amounts to a convex optimization problem for which a global optimum exists. Here, we study (5.8) by introducing its dual formulation, i.e., the novel *CCMF model*, and show the thresholding of the computed optimum of the convex relaxation problem (5.8) solves its original combinatorial optimization problem (5.7) globally and exactly.

5.2.5 Coupled continuous max-flow (CCMF) model

We introduce the new flow configuration based on the studies in [17] (as illustrated in Fig. 5.3). For each image slice $\mathcal{S}_i$, $i = 1 \dots n$, we add two image copies Ω_i^W and Ω_i^L w.r.t. the regions $\mathcal{R}_i^W$ and $\mathcal{R}_i^L$; two additional flow terminals: the source s_i and the sink t_i, are added; link the source s_i to each pixel x in Ω_i^W, along which the directed source flow $p_i^s(x)$ is defined; link each pixel $x \in \Omega_i^W$ to the same pixel x at Ω_i^L, along which the directed outer wall flow $p_i^W(x)$ is defined; link each pixel $x \in \Omega_i^L$ to the sink t_i, along which the directed lumen flow $p_i^L(x)$ is defined; within Ω_i^W and Ω_i^L, the local vector flow fields $q_i^W(x), q_i^L(x) \in \mathbb{R}^2$ are given around each pixel x. Between two adjacent Ω_i^W and Ω_{i+1}^W, $i = 1 \dots n-1$, we link $x \in \Omega_i^W$ to the same position $x \in \Omega_{i+1}^W$, along which a coupled flow $r_i^W(x)$ streaming in both directions is defined. Between two adjacent Ω_i^L and Ω_{i+1}^L, $i = 1 \dots n-1$, we link $x \in \Omega_i^L$ to the same position $x \in \Omega_{i+1}^L$, along which a coupled flow $r_i^L(x)$ streaming in both directions is defined.

With the above flow configuration, we introduce the novel *CCMF model*, which maximizes the total flow streaming from the n sources:

$$\max_{p^s, p^t, q, r} \sum_{i=1}^{n} \int_\Omega p_i^s(x)\, dx \tag{5.9}$$

subject to the flow capacity constraints

$$\begin{aligned} p_i^s(x) \,\le\, C_i^s(x)\,,\;\; p_i^W(x) \,\le\, C_i^W(x)\,, \\ p_i^L(x) \,\le\, C_i^L(x)\,;\;\; i \,=\, 1 \dots n\,; \end{aligned} \tag{5.10}$$

$$\left|q_i^W(x)\right| \,\le\, g_i(x)\,,\;\; \left|q_i^L(x)\right| \,\le\, g_i(x)\,;\;\; i \,=\, 1 \dots n\,; \tag{5.11}$$

$$\left|r_i^W(x)\right| \,\le\, \alpha\,, \;\; \left|r_i^L(x)\right| \,\le\, \alpha\,; \;\; i \,=\, 1\ldots n-1\,; \tag{5.12}$$

and the flow conservation constraints within each $\Omega_i^{W,L}$, $i = 1\ldots n$:

$$\rho_1^W(x) := \big(\operatorname{div} q_1^W - p_1^s + p_1^W + r_1^W\big)(x) = 0\,; \tag{5.13}$$

$$\rho_1^L(x) := \big(\operatorname{div} q_1^L - p_1^W + p_1^L + r_1^L\big)(x) = 0\,; \tag{5.14}$$

$$\rho_i^W(x) := \big(\operatorname{div} q_i^W - p_i^s + p_i^W + r_i^W - r_{i-1}^W\big)(x) = 0\,; \;\; i = 2\ldots n-1\,; \tag{5.15}$$

$$\rho_i^L(x) := \big(\operatorname{div} q_i^L - p_i^W + p_i^L + r_i^L - r_{i-1}^L\big)(x) = 0\,; \;\; i = 2\ldots n-1\,; \tag{5.16}$$

$$\rho_n^W(x) := \big(\operatorname{div} q_n^W - p_n^s + p_n^W - r_{n-1}^W\big)(x) = 0\,; \tag{5.17}$$

$$\rho_n^L(x) := \big(\operatorname{div} q_n^L - p_n^W + p_n^L - r_{n-1}^L\big)(x) = 0\,. \tag{5.18}$$

- *Capacity constraints on source and sink flows:*

$$p_i^s(x) \,\le\, C_i^s(x)\,, \; p_i^t(x) \,\le\, C_i^t(x)\,; \; i \,=\, 1\ldots n\,; \tag{5.19}$$

- *Capacity constraints on spatial flows:*

$$|q_i(x)| \,\le\, g_i(x)\,, \; i \,=\, 1\ldots n\,; \tag{5.20}$$

- *Capacity constraints on coupled flows:*

$$|r_i(x)| \,\le\, \alpha\,, \; i \,=\, 1\ldots n\,; \tag{5.21}$$

- *Flow conservation constraints:* all the flows at each pixel of every slice are balanced, i.e., for each of the last $n-1$ slices $\mathcal{S}_i$, $i = 2\ldots n$, at each position $x \in \mathcal{S}_i$, it must suffice

$$\rho_i(x) := \big(\operatorname{div} q_i - p_i^s + p_i^t + r_i - r_{i-1}\big)(x) = 0\,; \tag{5.22}$$

  and for the first slice $\mathcal{S}_1$, at each position $x := (x_1, x_2) \in \mathcal{S}_1$, the total flow balance is evaluated by

$$\rho_1(x) := \big(\operatorname{div} q_1 - p_1^s + p_1^t + r_1\big)(x) - r_n(L - x_1, x_2)$$

and it must suffice

$$\rho_1(x) \, = \, 0 \, . \tag{5.23}$$

5.2.6 Global and exact optimization of (5.7)

By introducing the multiplier functions $u_i^{W,L}(x)$, $i = 1 \dots n$, to the linear equalities (5.22) - (5.18), we then have the equivalent primal-dual model of (5.9) such that

$$\min_{u^{W,L}} \max_{p,q,r} \sum_{i=1}^{n} \int_{\Omega} p_i^s(x)\, dx + \sum_{i=1}^{n} \left\langle u_i^W, \rho_i^W \right\rangle + \sum_{i=1}^{n} \left\langle u_i^L, \rho_i^L \right\rangle \tag{5.24}$$

subject to the flow capacity constraints (5.19) - (5.21).

By variational analysis, the following results can be proven. The readers are referred to [17, 21, 22] for proofs.

Proposition 1 *The* coupled continuous max-flow model (5.9)*, the convex relaxation model* (5.8) *and the primal-dual model* (5.24) *are equivalent to each other:*

$$(5.9) \iff (5.8) \iff (5.24) \, . \tag{5.25}$$

Proposition 2 *Let* $(u_1^{W,L}(x), \dots u_n^{W,L}(x))^* \in [0,1]$ *be the global optimum of the convex relaxation problem* (5.8)*, the thresholds* $\tilde{u}_i^{W,L}(x) \in \{0,1\}$*,* $i = 1 \dots n$*, by any* $\gamma \in [0,1)$*, where*

$$\tilde{u}_i^W(x) = \begin{cases} 1\,, & (u_i^W)^*(x) > \gamma \\ 0\,, & (u_i^W)^*(x) \leq \gamma \end{cases} \, , \tag{5.26}$$

$$\tilde{u}_i^L(x) = \begin{cases} 1\,, & (u_i^L)^*(x) > \gamma \\ 0\,, & (u_i^L)^*(x) \leq \gamma \end{cases} \quad i = 1 \dots n \, , \tag{5.27}$$

solves the original combinatorial optimization problem (5.7) *globally and exactly.*

5.2.7 Coupled continuous max-flow (CCMF) algorithm

By Prop. 2, the global optimum of the proposed challenging segmentation problem (5.7) can be achieved by thresholding the optimum of its convex relaxation (5.8) with any $\gamma \in [0,1)$. On the other hand, Prop. 1 shows that the optimum of such convex relaxation problem (5.8) is given by the optimal multipliers to the corresponding linear

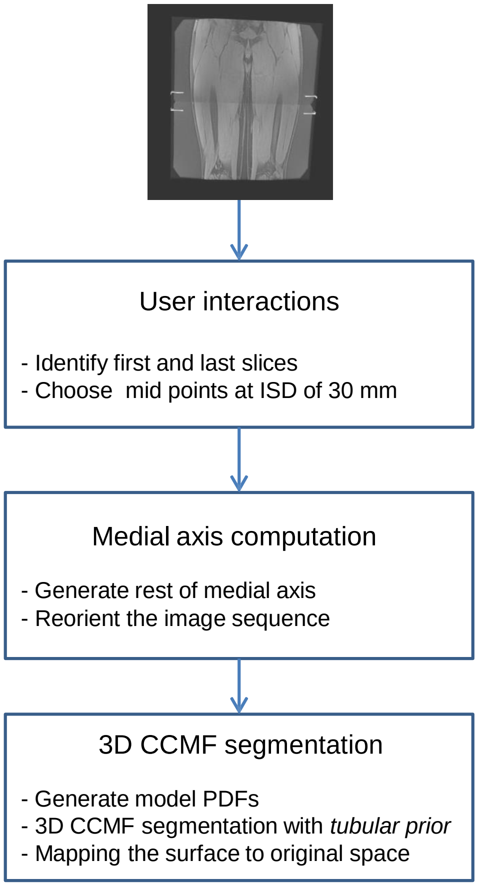
User interactions
- Identify first and last slices
- Choose mid points at ISD of 30 mm
Medial axis computation
- Generate rest of medial axis
- Reorient the image sequence
3D CCMF segmentation
- Generate model PDFs
- 3D CCMF segmentation with *tubular prior*
- Mapping the surface to original space

Figure 5.4: The block diagram of the segmentation pipeline. User interaction is performed only in the first step.

equality conditions (5.22)-(5.18). Indeed, this directly derives the *CCMF algorithm* based on the modern augmented Lagrangian algorithm [22], see also [17, 21] for the detailed algorithmic scheme. The proposed *CCMF algorithm* avoids directly solving the non-smooth function terms in (5.8) and performs at high efficiency in the experiments of this work.

5.3 Implementation and data

The segmentation pipeline of the proposed algorithm is shown in Fig. 5.4. Each step is described in detail below.

5.3.1 User initialization

Using multi-planar reformatting software, the user chooses approximately a 300 mm section of the femoral artery by identifying the first and last transverse slices for segmentation. The observer manually delineates the femoral lumen and outer wall boundaries in the first and last slices similar to [14]. The observer is then presented with a set of transverse cross-sections of the artery with an inter-slice distance (ISD) of 30 mm, where the observer chooses an approximate mid point of the femoral lumen amounting to about 10–12 points in total for the entire 3D image.

5.3.2 Medial axis computation

An approximate medial axis of the femoral artery is required to reorient the transverse slices as shown in Fig. 5.1(c). The user selected points from the initialization are then connected using the live-wire algorithm [23] to find the rest of the points on the medial axis. The live-wire algorithm sequentially generates the minimum cost path from one point to the other from the starting slice to the end slice. The Frangi vesselness filter [24] with a kernel size of 3 to 5 pixels is applied to the 3D MR image and its output is used as a cost map for the live-wire algorithm, where high vesselness response corresponds to low cost in the cost map. The user then examines the medial axis for its correctness. In severe stenosis cases, the user may need to introduce additional points and to recompute the medial axis. The transverse slices are then reoriented based on the medial axis of the artery in order for the lumen and outer wall images to appear as cylinders as shown in Fig. 5.1(c) and (d). This is performed as a straightening operation where the axis is straightened according to starting point of the medial axis.

5.3.3 3D CCMF segmentation

We use manual segmentation of the first and last slices as initialization for 3D segmentation. An intensity log-likelihood term is used as the data term for the segmentation. The model PDFs for the intensity log-likelihood matching are generated from the manual segmentation of the first and last slices. For the wall, lumen and background regions, the corresponding intensity PDFs are

$$Pr^j(z) = \frac{\int_\Omega K(z - I(x))\, u^j(x) dx}{\int_\Omega u^j(x)\, dx} \quad j = L, W, B \tag{5.28}$$

where the input image $I(x) \in \mathcal{Z}$, u^j, $j = L, W, B$ (5.2), and $K(.)$ is the Gaussian kernel function such that

$$K(x) = \frac{1}{\sqrt{2\pi\sigma^2}} \exp(-x^2/2\sigma^2)\,.$$

σ of 5 is used to generate the PDFs with 256 intensity bin sizes. We then apply the *CCMF* algorithm with the spatial consistency prior and the inter-surface label order constraint to jointly segment the femoral lumen and outer wall in 3D from reoriented femoral MR image V_r. The femoral lumen and outer wall surfaces generated using the algorithm are then mapped to the original space using the inverse transformation, which can be used for further analysis of the vessel wall boundaries.

5.3.4 Data and acquisition

To our knowledge, a public data set with ground truth is not available for T1w femoral artery images. Therefore, we used a data set acquired in by the Department of Radiology, Renji Hospital (Shanghai Jiao Tong University, Shanghai, China). All the subjects had provided written informed consent. The study protocol had been approved by the ethical review board of Renji Hospital.

Our data set comprises of 10 3D motion-sensitized driven equilibrium (MSDE) prepared rapid gradient echo sequence (3D MERGE) images from seven subjects. Five of these subjects were symptomatic with intermittent claudication. The MR images were acquired using two stations with field-of-view of $400 \times 40 \times 250$ mm^3 to cover up to 500 mm longitudinally with isotropic voxel size of 1.0 mm. Image acquisition time was $\approx$ 7 min. The imaging parameters were TR $=$ 10 ms, TE $=$ 4.8 ms, flip angle $= 6°$, turbo factor $=$ 100 and one excitation (NEX). In this study, 300 mm length of the SFA was analyzed starting from the femoral bifurcation to the end of the femur and the segment that is upstream from the femoral bifurcation is ignored due to poor image quality.

5.3.5 Validation

Manual segmentation of the femoral MR images is used as ground truth to evaluate the algorithm. Manual segmentation of the femoral outer wall and lumen boundaries were performed using a multi-planar software platform [25]. Manual segmentations were performed on transverse views with an ISD of 10 mm. Since the algorithm provides 3D segmentation, the algorithm-generated surfaces were sliced and were compared to manual segmentations with an ISD of 10 mm.

Both the accuracy and reproducibility of the algorithm were evaluated. We used regional-, area- and boundary distance-based metrics to assess the accuracy of the algorithm for the femoral lumen and outer wall separately. We used Dice similarity coefficient (DSC) [26], area overlap (1.15) (AO), and area difference (1.16) (AD) as region-based metrics. Mean absolute distance (MAD) (1.17) and maximum absolute distance errors (MAXD) (1.19) are used as boundary-distance based metrics. MAD and MAXD were computed by establishing point-by-point correspondence of the manual and algorithm-generated boundaries. VWA is the area of the region enclosed between the femoral artery outer wall and lumen regions. We used VWA as the clinical measure of evaluation for this study. We computed the mean VWA errors (δVWA_{Mean}) and root mean square VWA errors (δVWA_{RMSE}) [14] as area-based metrics.

Six femoral 3D MR images were chosen randomly from the entire data set to evaluate the intra-observer variability of the proposed algorithm. To assess the reproducibility of the algorithm in generating VWA, the user repeatedly segmented six femoral MR images five times, each on a different day. Coefficient-of-variation (CV) and standard deviation (SD) were used to assess the intra-observer variability of the algorithm. We also used intra-class correlation coefficient (ICC) [27], which measures reliability of the algorithm by computing the proportion of variance between observations. A single measure of absolute agreement using a two-way mixed study was used to compute ICC. Statistical analyses were performed using IBM SPSS Statistical version 19 (IBM Corporation, 2010), in which results were considered significant when the probability of making a type I error was less than 5%.

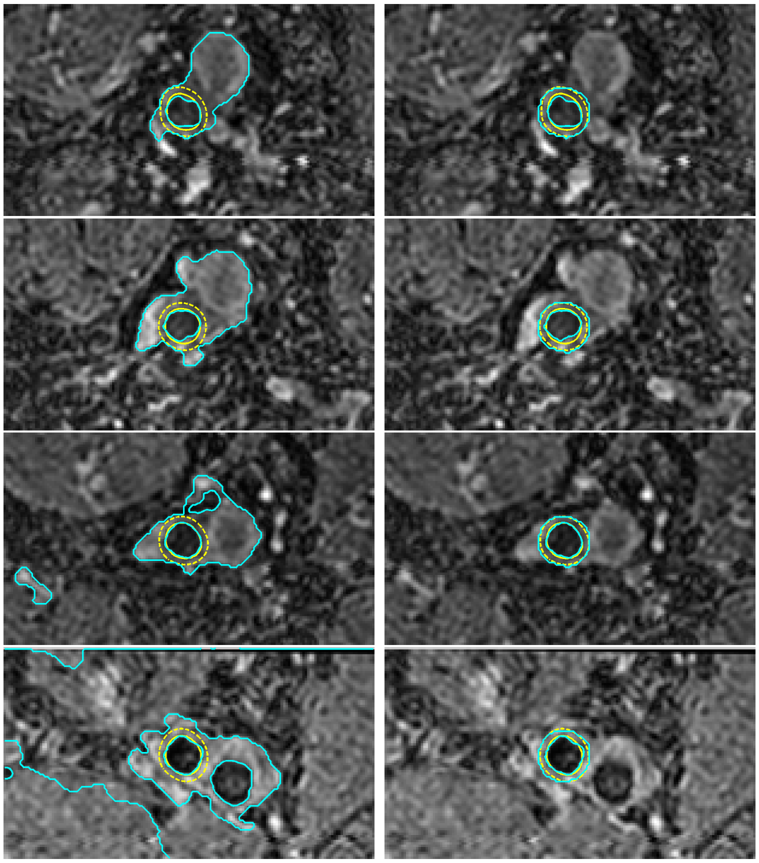

Figure 5.5: The impact of the proposed spatial consistency prior is illustrated here: **Column 1:** Algorithm results without the spatial consistency prior. **Column 2:** Algorithm results with the spatial consistency prior. The algorithm generated-contours are shown as cyan continuous lines whereas the manual contours are shown as dashed yellow lines.

5.4 Results

For slice-by-slice validation, our data set consisted of 355 2D slices extracted from 10 3D femoral MR images. The parameters (i.e., $\alpha = 18$, $\lambda_{1,2,3} = 0.1, 1.7, 3$) were optimized sequentially by varying one parameter at a time and evaluating accuracy using DSC. The optimized parameters were held constant during experiments for the entire dataset.

Fig. 5.5 illustrates the usefulness of the *tubular prior* in femoral MR segmentation. Algorithm contours are shown as cyan continuous lines, whereas manual contours are shown as yellow dashed lines. The results are shown for a set of transverse slices extracted from the segmented 3D surfaces. The segmented contours in the first column of Fig. 5.5 correspond to the output of the algorithm without the *tubular prior*. The segmented boundary leaked into other surrounding regions partially due to the low image contrast of the outer wall boundary. The segmentation results of the algorithm with the *tubular prior* are shown in the second column of Fig. 5.5, where the tubular prior was able to constrain the segmentation from leaking at low contrast boundaries.

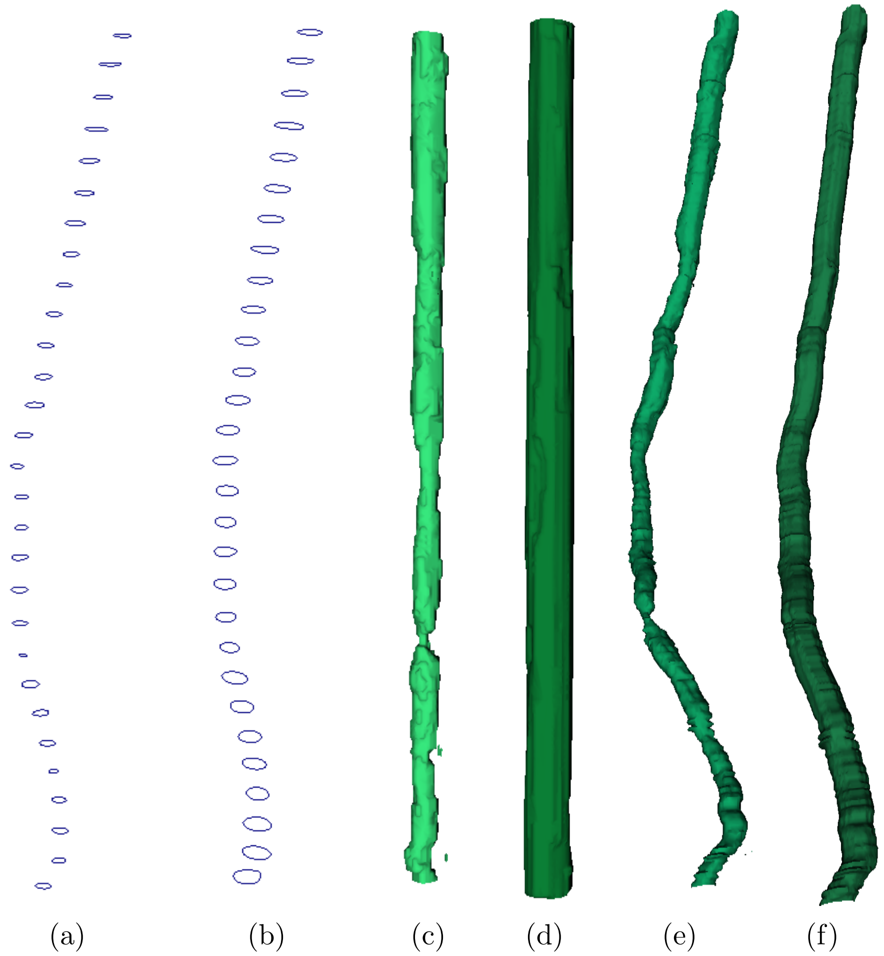

Figure 5.6: Surfaces. (a) Manual segmented boundaries of the lumen; (b) manual segmented boundaries of the wall; (c) algorithm-generated lumen surface; (d) algorithm-generated wall surface; (e) reoriented algorithm-generated lumen surface; and (f) reoriented algorithm-generated wall surface.

5.4.1 Computational time

The experiments were performed on a Windows PC with an Intel Core i7 CPU and 16GB RAM. The continuous max-flow algorithm was implemented on a GPU using CUDA (NVIDIA Corp., Santa Clara, CA). The user interface and image preprocessing were implemented using Matlab (Mathworks Inc., Natick, MA). The proposed method required about 98 s of user time for initialization and preprocessing, out of which most of the time was required for manual interactions to compute the medial axis of the SFA. In addition, the algorithm required $\approx$10 s of computational time for the *CCMF* solver.

5.4.2 Accuracy

Figure 5.6 shows the femoral lumen and outer wall surfaces generated for an example femoral 3D MR image. The algorithm generated surfaces are shown in Fig. 5.6(c) and (d). Segmentation results of the reoriented slices were used to reconstruct the 3D lumen and outer wall surfaces by applying the inverse transform as shown in Fig. 5.6(e) and (f), which were compared to manual segmentations on a slice-by-slice basis.

Segmentation results of the reoriented slices were used to reconstruct the 3D lumen and outer wall surfaces, which were compared to manual segmentations on a slice-by-slice basis. Some example results of the algorithm for three femoral MR images are shown in Fig. 5.7. The manual segmented boundaries for the outer wall and lumen are shown as a dashed lines whereas the algorithm-generated boundaries are shown as a continuous lines. Visual comparison of the manual and algorithm segmented boundaries shows good agreement. Most of the disagreement of the outer wall boundary is due to lack of image contrast (see bottom left image in Fig. 5.7 as an example).

Table 5.1 shows accuracy evaluation of the proposed algorithm for 355 2D slices extracted from the 10 femoral 3D MR images. The algorithm yielded DSC of 89.1% for the outer wall and 85.4% for the lumen, but yielded lower DSC of 75.1% for the vessel wall region. The algorithm reported AO of over 80% for both the lumen and outer wall. For distance-based metrics, the algorithm also yielded sub-millimeter errors for MAD and distance errors smaller than 1 mm for MAXD. The average area error (A_{AVG}) for the wall was 5.03 mm^2, which indicates that the algorithm

Table 5.1: Performance results of the proposed algorithm for 355 2D slices extracted from the 10 femoral 3D MR images. The voxel size of the MR images is $\approx 1.0\times1.0\times1.0$ mm^3.

Metric	Wall	Lumen
DSC (%)	89.1±3.70	85.4±3.39
AO (%)	81.2±3.88	80.4±10.74
MAD (mm)	0.44±0.10	0.40±0.08
MAXD (mm)	0.97±0.23	0.87±0.13
A_{AVG} (mm^2)	5.03±7.90	-1.15 ± 3.74
A_{RMSE} (mm^2)	9.07	3.73
Metric	Vessel wall region	
DSC (%)	75.1 ± 8.9	
VWA_{AVG} (mm^2)	6.18±5.11	
VWA_{RMSE} (mm^2)	7.8	

Table 5.2: Intra-observer variability of the algorithm using five repetitions of the same observer for 176 2D slices extracted from six femoral 3D MR images, which were chosen randomly from the entire data set.

Metric	Lumen	Wall	VWA
CV(%)	6.43	4.88	6.69
ICC	0.969	0.937	0.949
SD (mm^2)	1.9	2.6	2.3

overestimated the outer wall area. In addition, A_{AVG} for the lumen was -1.15 mm^2, which indicates that the algorithm has slightly underestimated the lumen area. For the vessel wall region, the algorithm overestimated the VWA (i.e., VWA_{AVG} of 6.18 mm^2).

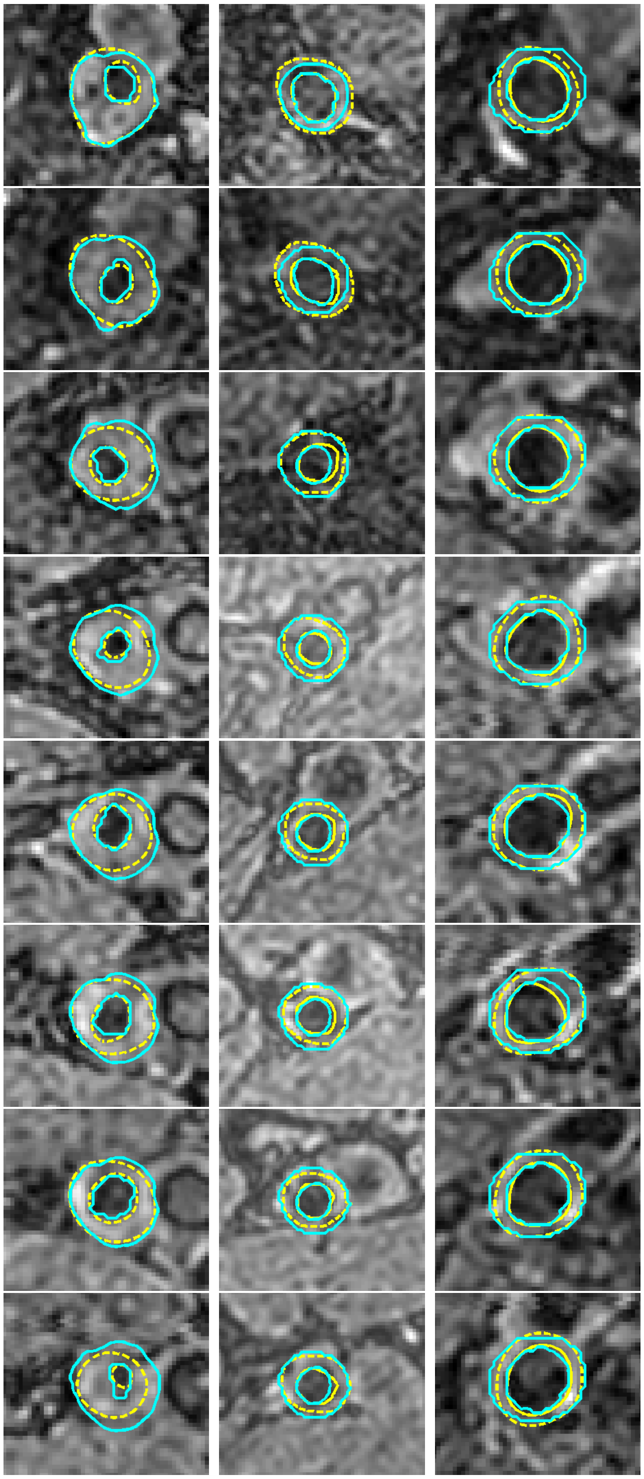

Figure 5.7: Slice-wise comparison of the computation results (cyan) to the manual segmentation (yellow) for the femoral wall and lumen boundaries for three 3D MR images. Each column corresponds to images for a different patient. The slices are separated by 30 mm from each other.

Table 5.3: Comparison of the algorithm to Chiu *et al.* [14] using 176 2D slices extracted from six femoral 3D MR images used in their study.

Metric	Proposed method		Chiu *et al.* [14]	
	Wall	Lumen	Wall	Lumen
AO (%)	82.9±4.72	81.3±8.46	84.7±9.46	85.6±9.36
AD (%)	23.5±8.21	24.9±9.32	12.9±12.95	9.8±9.78
MAD (mm)	0.43±0.13	0.42±0.09	0.32±0.23	0.20±0.17
MAXD (mm)	0.89±0.16	0.86±0.16	0.77±0.52	0.55±0.48
Metric	Vessel wall region		Vessel wall region	
VWA_{AVG} (mm^2)	4.77±5.12		4.58±7.10	
VWA_{RMSE} (mm^2)	6.29		8.45	

The algorithm was compared to the 2D segmentation method proposed by Chiu *et al.* [14] and the comparison is shown in Table 5.3. Their method [14] was evaluated with six femoral 3D MR images. The same data of their study [14] were used here for a direct comparison of the two algorithms. Compared to the 2D method [14], the algorithm yielded lower AO and higher AD for both the femoral artery lumen and outer wall. However, the SDs of the algorithm for AO were smaller than the 2D method. Similar to the region-based metrics, the algorithm also yielded higher MAD and MAXD errors than the 2D method [14]. Both algorithms yielded comparable VWA_{AVG} (4.77 vs. 4.58 mm^2) for the VW region. The algorithm yielded a smaller VWV_{RMSE} compared to the 2D method [14].

5.4.3 Precision

A user repeatedly segmented six femoral MR images five times to assess the reproducibility of the algorithm in generating VWA. Table 5.2 shows the reproducibility results of the algorithm using CV, ICC, and SD. The algorithm yielded a CV of 6.69% for VWA and a smaller CV for the outer wall than the lumen. In addition, the SDs for the lumen, outer wall, and VWA were in the range of 1.9–2.6 mm^2. The intra-observer ICCs of the algorithm for the lumen, outer wall, and VWV were greater than 0.93, which indicates high reproducibility of the area measurements.

5.5 Discussion

In this chapter, a novel algorithm was described and evaluated for 3D segmentation of the femoral artery lumen and outer wall from black-blood MR images. Here, the technical aspects of the algorithm and its results are discussed as follows.

The algorithm was based on a *CCMF* model, which simultaneously segments the femoral artery lumen and outer wall surfaces by enforcing two priors, i.e., the spatial consistency between the adjacent 2D reoriented MR slices and the anatomical order between the femoral artery lumen and outer wall surfaces, in a global optimization manner. The user is required to segment the first and last slices of the slice stack and then providing control points to identify the medial axis of the artery for initialization. Accurate computation of the femoral medial axis is crucial for the subsequent segmentation of the outer wall and lumen.

Direct 3D segmentation of a femoral MR image ($\approx$ 400 slices) without a spatial consistency prior had two problems: Segmentation for the outer wall leaked due to its high similarity to background, and (2) the segmentation surface shrunk due to shrinking bias, especially when there was a large stenosis in the artery. The algorithm with a spatial consistency prior overcame both of these problems. The proposed approach to reorient the 2D MR stack based on the medial axis of the artery and performing the segmentation with a *tubular prior* avoid leakage at the boundaries with weak contrast of the femoral outer wall boundary and speeds up the segmentation.

The main strengths of the algorithm are fast computational speed and requirement for only few user interactions. The proposed algorithm required only 1–2% of the total time (1.67 min vs. 70–80 min [14]) for segmenting the femoral outer wall and lumen compared to manual segmentation.

In addition to femoral artery segmentation, the proposed algorithm can be applied to segment objects with some symmetry. For instance, the method can be applied to segment the prostate boundaries from MR images.

5.5.1 Accuracy

The algorithm yielded a DSC $\geq$ 85% (see Table 5.1) for both the lumen and outer wall. Although previous algorithms reported in this dissertation yielded DSC greater than 90% for the lumen and outer wall boundaries of the carotid artery, it is challenging to obtain such DSCs for femoral MR segmentations, due to its coarse resolution of the femoral MR images, which in turn leads to fewer voxels representing the femoral artery. Although, the femoral lumen has a high agreement by visual comparison, DSC for the lumen was smaller than DSC for the outer wall. Moreover, DSC of 75.1% for the VW region was smaller than DSCs for the lumen and outer wall. This may be due to its small size, where a disagreement of few pixels may lead to a smaller DSC. AO is a more stringent measure of regional overlap than DSC, which is reflected by the smaller AO values reported.

Sub-millimeter error values for MAD (see Table 5.1) for both the lumen and outer wall indicate a high agreement between the manual and algorithm boundaries. MAXD errors smaller than 1 mm indicate that the segmentation boundary did not leak and create isolated regions further from the desired boundary, due to the spatial consistency prior.

As for the area-based measurements (see Table 5.1), the algorithm overestimated (A_{AVG} of 5.03 mm^2) the outer wall boundary, while slightly underestimating (A_{AVG} of -1.15 mm^2) the lumen boundary. This is reflected by the higher A_{RMSE} for the outer wall boundary. The algorithm overestimated (A_{AVG} of 6.18 mm^2) the VW region, which is mostly attributed by the overestimation of the outer wall. The algorithm yielded comparable A_{RMSE} to the A_{RMSE} (6.29 vs. 6.6 mm^2) between repeated manual segmentations.

5.5.2 Precision

Precision is one of the most important aspect of the algorithm for longitudinal monitoring of PAD plaque burden, because a systematic bias may cancel out when VWA change is measured from baseline to follow-up. The sensitivity to initialization was computed using five repeated segmentations with different initializations. The algorithm yielded ICC greater than 0.93% (ICC of 0.949 for VW region), which indicates a high consistency between repeated measurements. CV of 6.69% (see Table 5.2) for VWA indicates that the algorithm was robust to initialization and selection of first and last slices. One of the main strengths of the algorithm is that SD of the algorithm (2.3 mm^2) is smaller than the V_{RMSE} of 6.6 mm^2 [14] between two repeated manual segmentations.

5.5.3 Comparison to previous methods

Here we briefly describe the algorithmic differences of the proposed method to comparative methods and then focus on comparison of algorithms for femoral artery MR segmentation. Although, comparable segmentation algorithms to the proposed segmentation algorithm have been reported for carotid artery segmentation, the proposed method is distinct from the prior studies [16, 28] both in application and theory. The proposed CCMF is a novel flow-maximization framework with n coupled sources and sinks, which solves n coupled min-cut problems efficiently, whereas prior studies [16, 17, 21] describe a single min-cut problem with a single source-sink max-flow scheme.

Numerous algorithms [29, 30, 31, 32] have been developed specifically for segmenting tubular structures. Unlike our proposed algorithm, most of these algorithms were developed for segmenting only the vessel lumen.

To our knowledge, only one study [14] has been reported for femoral artery lumen and outer wall segmentation, which was performed in 2D, one boundary and one slice at a time. However, the proposed algorithm segments both boundaries simultaneously in 3D by enforcing spatial consistency prior. Our algorithm yielded comparably accurate results to Chiu *et al.* [14] for VWA while requiring fewer user interactions and less computation time ($\approx$ 10 s vs. 230–290 s). Currently, most of the observer time is used for identifying the medial axis of the artery, which may be further improved by a centerline detection algorithm with minimal user interactions.

References

[1] E. Ukwatta, J. Yuan, B. Chiu, Q. Qu, M. Rajchl, and A. Fenster, "Joint segmentation of 3d femoral lumen and outer wall surfaces from MR images," in *MICCAI*, 2013. 165, 169

[2] F. A. Arain and L. T. Cooper Jr, "Peripheral arterial disease: diagnosis and management," in *Mayo Clinic Proceedings*, vol. 83, no. 8. Elsevier, 2008, pp. 944–950. 165

[3] N. Shammas, "Epidemiology, classification, and modifiable risk factors of peripheral arterial disease," *Vascular health and risk management*, vol. 3, no. 2, p. 229, 2007. 165

[4] D. Isbell, C. Meyer, W. Rogers, F. Epstein, J. DiMaria, N. Harthun, H. Wang, and C. Kramer, “Reproducibility and reliability of atherosclerotic plaque volume measurements in peripheral arterial disease with cardiovascular magnetic resonance,” *Journal of Cardiovascular Magnetic Resonance*, vol. 9, no. 1, pp. 71–76, 2007. 165, 166

[5] M. H. Criqui, “Systemic atherosclerosis risk and the mandate for intervention in atherosclerotic peripheral arterial disease,” *The American journal of cardiology*, vol. 88, no. 7, pp. 43–47, 2001. 165

[6] Z.-J. Zheng, A. R. Sharrett, L. E. Chambless, W. D. Rosamond, F. J. Nieto, D. S. Sheps, A. Dobs, G. W. Evans, and G. Heiss, “Associations of ankle-brachial index with clinical coronary heart disease, stroke and preclinical carotid and popliteal atherosclerosis: the atherosclerosis risk in communities (aric) study.” *Atherosclerosis*, vol. 131, no. 1, p. 115, 1997. 165

[7] B. A. Golomb, T. T. Dang, and M. H. Criqui, “Peripheral arterial disease morbidity and mortality implications,” *Circulation*, vol. 114, no. 7, pp. 688–699, 2006. 165

[8] J. Chi, B. Chiu, Y. Cao, X. Liu, J. Wang, N. Balu, C. Yuan, and J. Xu, “Assessment of femoral artery atherosclerosis at the adductor canal using 3d black-blood mri,” *Clinical radiology*, 2013. 165, 166

[9] A. B. I. Collaboration, F. Fowkes, G. Murray, I. Butcher, C. Heald, R. Lee, L. Chambless, A. Folsom, A. Hirsch, M. Dramaix *et al.*, “Ankle brachial index combined with framingham risk score to predict cardiovascular events and mortality,” *JAMA: the journal of the American Medical Association*, vol. 300, no. 2, pp. 197–208, 2008. 165

[10] A. W. Pollak and C. M. Kramer, “Mri in lower extremity peripheral arterial disease: Recent advancements,” *Current cardiovascular imaging reports*, vol. 6, no. 1, pp. 55–60, 2013. 166

[11] N. Balu, J. Wang, X. Zhao, T. Hatsukami, and C. Yuan, “Targeted multi-contrast vessel wall imaging of bilateral peripheral artery disease,” in *Proc. Intl. Soc. Mag. Reson. Med*, vol. 18, 2010, p. 3685. 166

[12] N. Balu, V. L. Yarnykh, B. Chu, J. Wang, T. Hatsukami, and C. Yuan, “Carotid plaque assessment using fast 3d isotropic resolution black-blood mri,” *Magnetic Resonance in Medicine*, vol. 65, no. 3, pp. 627–637, 2011. 166

[13] N. Bianda, M. Di Valentino, D. Périat, J. M. Segatto, M. Oberson, M. Moccetti, I. Sudano, P. Santini, C. Limoni, A. Froio *et al.*, “Progression of human carotid and femoral atherosclerosis: a prospective follow-up study by magnetic resonance

vessel wall imaging," *European heart journal*, vol. 33, no. 2, pp. 230–237, 2012. 166

[14] B. Chiu, J. Sun, X. Zhao, J. Wang, N. Balu, J. Chi, J. Xu, C. Yuan, and W. Kerwin, "Fast plaque burden assessment of the femoral artery using 3d black-blood mri and automated segmentation," *Medical Physics*, vol. 38, p. 5370, 2011. xv, 166, 167, 168, 169, 177, 179, 185, 186, 187, 188

[15] R. van't Klooster, P. de Koning, R. Dehnavi, and J. e. a. Tamsma, "Automatic lumen and outer wall segmentation of the carotid artery using deformable 3D models in MR angiography and vessel wall images," *J. Magn. Reson. Im.*, vol. 35, 2011. 166

[16] E. Ukwatta, J. Yuan, M. Rajchl, D. Tessier, and A. Fenster, "3D carotid multi-region MRI segmentation by globally optimal evolution of coupled surfaces," *IEEE Transactions of medical imaging*, vol. 32, no. 4, pp. 770–85, 2013. 166, 188

[17] E. Bae, J. Yuan, X.-C. Tai, and Y. Boycov, "A fast continuous max-flow approach to non-convex multilabeling problems," UCLA, Technical report CAM-10-62, 2010. 170, 173, 175, 176, 188

[18] Y. Boykov and G. Funka-Lea, "Graph cuts and efficient nd image segmentation," *International Journal of Computer Vision*, vol. 70, no. 2, pp. 109–131, 2006. 171

[19] M. Rajchl, J. Yuan, J. A. White, C. M. Nambakhsh, E. Ukwatta, F. Li, J. Stirrat, and T. M. Peters, "A fast convex optimization approach to segmenting 3d scar tissue from delayed-enhancement cardiac mr images," in *Medical Image Computing and Computer-Assisted Intervention–MICCAI 2012*. Springer, 2012, pp. 659–666. 171

[20] J. Yuan, E. Ukwatta, X.-C. Tai, A. Fenster, and C. Schnoerr, "A fast global optimization-based approach to evolving contours with generic shape prior," UCLA, Technical report CAM-12-38, 2012. 173

[21] J. Yuan, E. Bae, and X. Tai, "A study on continuous max-flow and min-cut approaches," in *CVPR 2010*. 175, 176, 188

[22] D. P. Bertsekas, *Nonlinear Programming*. Athena Scientific, September 1999. 175, 176

[23] W. A. Barrett and E. N. Mortensen, "Interactive live-wire boundary extraction," *Medical Image Analysis*, vol. 1, no. 4, pp. 331–341, 1997. 177

[24] A. Frangi, W. Niessen, K. Vincken, and M. Viergever, "Multiscale vessel enhancement filtering," *Medical Image Computing and Computer-Assisted InterventationMICCAI98*, pp. 130–137, 1998. 177

[25] W. Kerwin, D. Xu, F. Liu, T. Saam, H. Underhill, N. Takaya, B. Chu, T. Hatsukami, and C. Yuan, "Magnetic resonance imaging of carotid atherosclerosis: plaque analysis," *Topics in Magnetic Resonance Imaging*, vol. 18, no. 5, pp. 371–378, 2007. 179

[26] K. Zou, S. Warfield, A. Bharatha, C. Tempany, M. Kaus, S. Haker, W. Wells, F. Jolesz, and R. Kikinis, "Statistical validation of image segmentation quality based on a spatial overlap index," *Academic Radiology*, vol. 11, no. 2, pp. 178–189, 2004. 179

[27] K. McGraw and S. Wong, "Forming inferences about some intraclass correlation coefficients." *Psychological methods*, vol. 1, no. 1, p. 30, 1996. 179

[28] E. Ukwatta, J. Yuan, M. Rajchl, and A. Fenster, "Efficient global optimization based 3D carotid AB-LIB MRI segmentation by simultaneously evolving coupled surfaces," in *MICCAI*, ser. LNCS, N. Ayache, H. Delingette, P. Golland, and K. Mori, Eds., vol. 7512, 2012, pp. 377–384. 188

[29] F. Benmansour and L. D. Cohen, "Tubular structure segmentation based on minimal path method and anisotropic enhancement," *International Journal of Computer Vision*, vol. 92, no. 2, pp. 192–210, 2011. 188

[30] H. Li and A. Yezzi, "Vessels as 4-d curves: Global minimal 4-d paths to extract 3-d tubular surfaces and centerlines," *Medical Imaging, IEEE Transactions on*, vol. 26, no. 9, pp. 1213–1223, 2007. 188

[31] D. Lesage, E. D. Angelini, I. Bloch, and G. Funka-Lea, "A review of 3d vessel lumen segmentation techniques: Models, features and extraction schemes," *Medical image analysis*, vol. 13, no. 6, pp. 819–845, 2009. 188

[32] T. Pock, C. Janko, R. Beichel, and H. Bischof, "Multiscale medialness for robust segmentation of 3d tubular structures," in *Proc. Comp. Vis. Winter Workshop, Austria*, 2005. 188

Chapter 6

Summary and future directions

6.1 Summary

With improved strategies to treat atherosclerosis non-surgically and cost effectively, sensitive and non-invasive imaging modalities that allow quantification of the plaque burden are becoming more important in the management of patients who suffer from atherosclerosis. The work of this dissertation was motivated by the need for more informative measurements of the plaque burden (e.g., VWV). For translating such volumetric measurements to clinical research and subsequently to clinical care, development and validation of semi-automated algorithms for segmentation of the artery lumen and outer wall that reduce the overall observer time and observer variability are vital.

In this dissertation, four semi-automated algorithms were described for segmenting the lumen and outer wall boundaries from: (1) 3D carotid US images, (2) 3D carotid MR images, and (3) 3D femoral MR images. Development of the segmentation algorithms described in this dissertation are aimed toward alleviating measurement burden of the observer, which is a main requirement for use of 3D measurements in practice. Algorithms for each segmentation problem were developed by integrating information extracted from the image with domain knowledge and user interactions. Domain knowledge of the minimal separation between surfaces were used as an inter-surface constraint in all the cases, while the amount of user interaction was dependent on the degree of distinguishable features of each boundary in each modality. The algorithms were finally validated by comparison to manual delineations made by trained observers.

An ideal algorithm is expected to yield high accuracy, high precision, and fast computation time, and require fewer interactions and less expertise than manual segmentation. While it's challenging to develop methods that yield all five criteria for medical image segmentation problems of this dissertation, some of the criteria was achieved as described below.

6.2 2D slice-wise segmentation of carotid 3DUS images (Chapter 2)

A semi-automated algorithm based on the SFLS method was described for segmentation of the carotid artery lumen and outer wall from 3DUS images. To our knowledge, this was the first published method to segment both the carotid outer wall and lumen boundaries from 3DUS images for the purpose of generating VWV. To address the challenges of the MAB and LIB segmentations from 3DUS images, user interactions on each slice and inter-surface constraints were integrated into the segmentation method. In total, nine energy functions were used for the segmentation: four energies for the outer wall and five energies for the lumen. We introduced two of the anchor-point based and boundary-separation based energies and the other energies were proposed previously.

The algorithm was validated with respect to volume-, region-, and boundary distance-based metrics using 21 3DUS images. The algorithm reduced the need for operator interaction, and generated VWV measurements with high precision (CV $<$ 6%) and accuracy (DSC $>$ 95%). The user was required to choose only four anchor points on each boundary for each transverse slice. The algorithm was able to reduce the operators time by 66% (2.8 min from 8.3 min) compared to manual segmentation for segmenting 1 cm length of the artery. The MDD of VWV was determined to be less than the average anticipated change within seven months, permitting clinical use of our tool after a seven-month interval between baseline and follow-up to monitor treatment response. The algorithm has been integrated into an in-house software platform, 3D Quantify, which is currently being used in clinical trials.

6.3 3D segmentation of carotid 3DUS images (Chapter 3)

To reduce the number of interactions further, the 2D algorithm was extended into 3D. The 3D algorithm is also based on the SFLS method and uses ten energy functions. Initialization of the algorithm requires the observer to choose anchor points on each boundary on a set of transverse slices with a user-specified ISD, in which larger ISD requires fewer user interactions than smaller ISD. To our knowledge, this method is the first published 3D algorithm for segmenting both the MAB and LIB of the CCA from 3DUS images for the purpose of generating VWV. Similar to the 2D method, we integrated regional- and boundary-based image statistics, expert initializations, and anatomically motivated boundary separation into the segmentation.

The 3D algorithm was evaluated using the same data set used in Chapter 2 and was compared to the 2D algorithm. The 3D segmentation algorithm provided high accuracy (i.e., DSC $>$ 90% for ISDs of 1, 2, and 3 mm) in terms of volume-, region-, and distance-based metrics. The algorithm reduced user time by $\approx$ 79% compared to manual segmentation. The algorithm also reported MDD smaller than previously reported VWV change of 120 mm^3/yr in generating VWV. The method provided comparable accuracy and intra-observer variability (CV of 6.8 % for ISD of 3 mm) results to previous 2D segmentation method [1], with fewer user interactions and shorter segmentation time, when ISD of 2 mm or more is used for the initialization.

6.4 3D segmentation of carotid MR images (Chapter 4)

A novel multi-region segmentation algorithm based on convex max-flow was described to segment the carotid artery lumen and outer wall from black-blood MR images. Unlike the level set algorithms described in Chapter 4 and 5, this algorithm simultaneously segments the outer wall and lumen surfaces, while enforcing an inter-surface constraint implicitly. As opposed to the boundary-based interactions in our previous algorithms, The initialization of the algorithm performed is by choosing voxels inside the lumen, outer wall, and background regions. The proposed global optimization approach for simultaneous propagation of the outer wall and lumen surfaces provides a fast segmentation of carotid, hence the measurement of carotid atherosclerosis. The algorithm required user interaction only on a single slice of the 3D image compared to previous methods [2, 3] requiring interactions on every slice. The algorithm was parallelized using GPU to increase the computational speed, thus reducing user time by 93% (0.78 vs. 12 min) compared to manual segmentations.

The algorithm yielded high accuracy (DSC $>$90%). Experiments show the proposed method is faster and reproducible, in terms of intra- and inter- observer variability (intra-observer CV $<$ 5.6% and inter-observer CV $<$ 6.6%), and requires fewer user interactions than the previous methods [2, 3]. It can be used in clinical trials involving the monitoring of carotid atherosclerosis using 3D MR imaging-based biomarkers.

6.5 3D segmentation of femoral MR images (Chapter 5)

We developed and validated a novel algorithm based on convex max-flow to segment the femoral arteries that enforces a tubular shape prior and an inter-surface consistency of the outer wall and lumen to maintain a minimum separation distance between the two surfaces. The developed algorithm is the first 3D segmentation algorithm for delineating the femoral lumen and outer wall from MR images. The algorithm required the observer to choose only about ten points on the medial axis of the artery to yield the 3D surfaces of the lumen and outer wall, which reduced the operator time by 97% (1.8 vs. 70–80 min) compared to the manual segmentation.

Our algorithm yielded high accuracy (i.e., DSC $\geq$ 85% and sub-millimeter error values for MAD and MAXD) for both the femoral lumen and outer wall. The algorithm also yielded high reproducibility (i.e., ICC of 0.95 and CV as low as 6.69% for VWA) for generating VWA, which is the most important aspect of the algorithm for longitudinal monitoring of PAD plaque burden, because a systematic bias may cancel out when VWA change is measured from baseline to follow-up.

6.6 Limitations

One of main limitations of this dissertation is the lack of ground truth for evaluating the algorithms. We used manual segmentation as a surrogate of ground truth, as commonly reported in other image segmentation studies. However, it is not known whether the regions of disagreement arise from inaccuracies in the algorithm, or from inaccuracies in manual segmentation. Although phantoms with a known geometry may be used to establish a ground truth, it is not realistic to use phantoms for the purposes of validating accuracy of the algorithm, since they do not simulate characteristics of patients' real 3DUS and MR images with sufficient fidelity. Moreover, the algorithm may be validated with digital histology images of excised carotid specimens as ground truth. However, such validation process is prone to many sources of errors including the registration error of *in-vivo* images to digital histopathology images of excised specimens, and the shrinking and deformation that occurs in fixing and slicing the excised specimens.

In this dissertation, we have used 21 3DUS images in Chapter 2 and 3, 38 MR images in Chapter 4, and 10 MR images in Chapter 5 for validation. While it is important to include a larger number of images in the studies for a rigorous validation, the number of images is limited by the requirement for repeated manual segmentations.

The limitations specific to each algorithm described in this dissertation are described as follows:

Chapter 2 and 3: The 3DUS segmentation algorithms [4, 5] reported a comparable intra-observer CVs to manual segmentation. Since a boundary-based initialization approach is used to initialize those algorithms, variability of the user is introduced into segmentation results. However, the multi-region MR segmentation algorithm [6] reported smaller intra-observer CVs due to a region-based initialization approach.

Since the outer wall segmentation uses localized region- and edge- based energies, the initial model needs to be close to the desired segmentation boundary for obtaining accurate segmentations. When the initial spline generated from the anchor points are away from the effect of the local-region based forces, the algorithm might not converge to the desired boundary. Moreover, since the lumen boundary is more challenging to segment, both the 2D and 3D algorithms use segmented the outer wall boundary to constrain the lumen segmentation from leaking. Therefore, the accuracy of lumen segmentation depends to some extent on the accuracy of outer wall segmentation.

Both 2D and 3D algorithms for 3DUS images use a large number of energies, thus have a large number of parameters. When the parameter space is large, obtaining a optimal set of parameter values is challenging.

Chapter 4: For this study, the subjects had moderate stenosis (30–50%) as measured previously with B-mode ultrasound. None of the subjects had ultrasound evidence of hemodynamically severe carotid artery stenosis. Thus, the maximum AB-LIB separation prior (see Section 4.3.2.5) may pose problems for segmentation of severely diseased arteries with the current methodology of initializing just a single transverse slice, especially when wall intensities of the diseased region may be more similar to the background. These cases would require additional user inputs in the form of hard constraints for the critical regions, and then a repeated segmentation. The combinatorial and continuous max-flow techniques can readily integrate such user interactions into the repeated optimization process as an editing/refinement step [7, 8].

Chapter 5: Due to the reorientation step of the femoral MR images (see Section 5.3.2), the femoral MR segmentation algorithm relies on accurate extraction of the medial axis of the femoral artery. Therefore, we currently employ a semi-automated approach to extract the medial axis. If the medial axis is not accurate, it will substantially affect the segmentation results. To avoid this, the observer can visually verify the medial axis for correctness before the segmentation is performed.

6.7 Future directions

Since the number of patients suffering from carotid atherosclerosis, and the number of novel treatments for carotid atherosclerosis are expected to grow rapidly, it is important to continue to develop and validate non-invasive, cost-effective, and direct measurements of atherosclerosis for more accurately stratifying risk of stroke. As such, several future directions that would benefit from the developed segmentation methods are discussed below.

6.7.1 Towards automated segmentation

An immediate future direction is automating the developed semi-automated segmentation algorithms. While it is challenging to fully automate 3DUS segmentation approaches, the user interactions may be reduced further. However, segmentation algorithms for carotid and femoral MR images may be fully automated.

For 3DUS carotid segmentation, when the segmentation of the baseline 3DUS image is obtained using the developed approach in Chapter 3, the segmentation process may be automated for follow-up 3DUS images. This may be achieved by registering the follow-up 3DUS image to the baseline 3DUS image using a deformable registration algorithm [9]. The baseline segmentation model can then be registered to the follow-up 3DUS image using the same transform, which can then be used as the initialization for segmentation.

For carotid MR segmentation, a large set of training MR images could be used to generate the intensity model PDFs for the lumen, outer wall, and background regions, an average MR image, and a multi-organ atlas. An atlas based approach can then be employed to segment the carotid artery and surrounding structures. A new patient MR image would be first registered to the average MR image and the model would then be transformed to the new image as the initialization. When the initialization model is created for the new image, the segmentation can be performed using the coupled surface segmentation algorithm described in Chapter 4.

Similar to carotid MR segmentation, intensity model PDFs can be generated from a training data set for femoral MR segmentation. When the user specifies the first and last transverse slices for segmentation, an automated centerline extraction method [10] may be applied to generated the centerline. When the centerline is extracted, the rest of the approach in Chapter 5 can be applied to generate the femoral lumen and outer wall surfaces.

6.7.2 Adaptive parameters and parameter optimization

In the segmentation algorithms presented in this dissertation, a fixed set of parameters were used for algorithm evaluation. The parameters were empirically optimized by perturbing one parameter at a time while holding other parameters constant. However, this parameter optimization method may not necessarily lead to optimal set of parameter values. To avoid this issue, the parameters can be optimized using the Powell's method [11] by finding and optimizing along the conjugate directions.

For each algorithm presented in this dissertation, set of algorithm parameters were empirically optimized using a small set of training data. However, due to the inherent variations in medical images, fixed set of parameters may not be able to address the variations in medical image datasets and yield accurate segmentations for each image. Therefore, a method to adaptively adjust parameters based on information derived from the current image may improve the accuracy of segmentation [12, 13].

6.7.3 3DUS carotid ICA segmentation

The 3DUS segmentation methods described in Chapter 2 and 3 are validated only for segmenting the carotid CCA. Since quantifying plaque burden in the carotid ICA is also clinically important, the algorithms for 3DUS segmentation can be extended to include segmentation of the carotid ICA, similar to the carotid MR segmentation algorithm described in Chapter 4.

6.7.4 Plaque composition and inflammation

A plaque could remodel from a vulnerable plaque to a stable plaque, without essentially change in size during medical treatment [14]. Therefore, volumetric measurements alone are not adequate to stratify plaque vulnerability to rupture and cause ischemic stroke. The pathophysiology of carotid plaques dictates that morphological and compositional characterization are required for identification of vulnerable plaques [15].

Plaque composition measurements and inflammation are strong indicators of plaque vulnerability [16]. Collagen rich plaques are more stable and respond well to interventions such as angioplasty and stent deployment. Lipid rich plaques are heterogeneous in texture, are relatively unstable, but are more likely to regress with dietary changes and drug therapy [17]. Ulcerated plaques and plaques with a thin fibrous cap and a large lipid core have been known to have a high risk for stroke. Plaques with high calcium content, especially when located superficially, are considered to be less vulnerable to rupture [18]. Thus, plaque characterization is useful in selecting the appropriate clinical intervention. Moreover, sensitive plaque characterization will provide valuable information in longitudinal studies of progression or regression following lipid lowering drug and diet modification strategies.

Although the ability of MR imaging for plaque composition [19, 20] and inflammation analysis [21] have been validated, the ability of 3DUS to identify individual plaque components such as fibrous, necrotic core, loose connective tissue, and calcifications is still unclear. Therefore, future work lies in investigating the capability of 3DUS imaging to identify plaque components, which could be validated using digital histopathology images of endarterectomy specimens and *in vivo* MR imaging.

Existing literature suggests that grey-scale texture analysis of carotid US images can distinguish between types of plaques [22]. Collagen rich plaques are echogenic and homogeneous in US images, while lipid rich plaques are heterogeneous in texture and echolucent in US images [23]. As such, 3DUS imaging of carotid arteries may provide non-invasive and cost-effective way of analyzing the plaque composition within the segmented VW regions. With the on-going carotid atherosclerosis imaging network

(CAIN) study [24], the developed algorithm can be used as a first step to generate VW regions for further analysis.

6.7.5 Morphological analysis

In this dissertation, we validated our methods for computing VWV. However, the proposed algorithms may also be used for computing vessel wall thickness and plaque (VWT) maps to investigate localized plaque changes in clinical studies. The flattened VWT maps can be averaged over a sample population for disease and control groups of population studies to study the localized response of plaque due to treatment. In addition to the use in clinical studies, the proposed VWT maps can also be used to compare segmentation methods to manual segmentation on a point-by-point basis [25].

6.7.6 Multi-region segmentation of the carotid lumen, outer wall, and plaque

For 3D carotid US images, algorithms described in Chapter 2 and 3 segment only the carotid lumen and the outer wall. Despite the popularity of the TPV measurement, only few previous techniques have been reported for generating TPV [26], due to numerous challenges faced by algorithms to segment the plaque boundaries. The multi-region segmentation algorithms described in this dissertation may be extended for segmenting plaque regions along with the lumen and outer wall regions to generate both TPV and VWV.

Due to superior vessel wall image contrast of carotid multispectral MR images and the ability to integrate image information from multiple MR pulse sequences, it is possible to identify individual plaque components to assess plaque instability, which is a predictor of stroke [14, 27]. One of the challenges in quantifying measurements of plaque components is the labour intensive and time consuming segmentation process of carotid artery VW, and the inherent inter- observer variability of the operators [14]. The developed algorithms may be extended to co-segment multi-spectral MR images by utilizing information from multiple sources. Moreover, with the availability of multi-spectral MR images from the CAIN project [24] and carotid endarterectomy specimens as ground truth for validation, there is potential for developing novel measurements of carotid atherosclerosis, which can assess the vulnerability to rupture.

In addition to the segmentation algorithms described in this work, various ideas presented can be utilized in segmentation of other structures. For example, the anchor point-based energy has been used in the prostate segmentations [28, 29].

References

[1] E. Ukwatta, J. Awad, A. D. Ward, D. Buchanan, J. Samarabandu, G. Parraga, and A. Fenster, "Three-dimensional ultrasound of carotid atherosclerosis: Semiautomated segmentation using a level set-based method," *Medical Physics*, vol. 38, p. 2479, 2011. 194

[2] I. Adame, P. de Koning, B. Lelieveldt, B. Wasserman, J. Reiber, and R. van der Geest, "An integrated automated analysis method for quantifying vessel stenosis and plaque burden from carotid mri images," *Stroke*, vol. 37, no. 8, pp. 2162–2164, 2006. 194, 195

[3] I. M. Adame, R. J. van der Geest, B. A. Wasserman, and e. a. Mohamed, M. A., "Automatic segmentation and plaque characterization in atherosclerotic carotid artery MR images," *Magn. Reson. Mater. Phy.*, vol. 16, no. 5, pp. 227–234, 2004. 194, 195

[4] E. Ukwatta, J. Awad, A. D. Ward, J. Samarabandu, A. Krasinski, G. Parraga, and A. Fenster, "Segmentation of the lumen and media-adventitia boundaries of the common carotid artery from 3D ultrasound images," in *Proceedings of SPIE*, vol. 7963, 2011, p. 79630G. 196

[5] E. Ukwatta, J. Yuan, D. Buchanan, B. Chiu, J. Awad, W. Qiu, G. Parraga, and A. Fenster, "Three-dimensional segmentation of three-dimensional ultrasound carotid atherosclerosis using sparse field level sets," *Medical physics*, vol. 40, p. 052903, 2013. 196

[6] E. Ukwatta, J. Yuan, M. Rajchl, D. Tessier, and A. Fenster, "3D carotid multi-region MRI segmentation by globally optimal evolution of coupled surfaces," *IEEE Transactions of medical imaging*, vol. 32, no. 4, pp. 770–85, 2013. 196

[7] J. Egger, R. Colen, B. Freisleben, and C. Nimsky, "Manual refinement system for graph-based segmentation results in the medical domain," *Journal of Medical Systems*, pp. 1–11, 2011. 197

[8] M. Rajchl, J. Yuan, J. A. White, C. M. S. Nambakhsh, E. Ukwatta, F. Li, J. Stirrat, and T. M. Peters, "A fast convex optimization approach to segmenting 3D scar tissue from delayed-enhancement cardiac MR images," in *MICCAI*, ser.

LNCS, N. Ayache, H. Delingette, P. Golland, and K. Mori, Eds., vol. 7510, 2012, pp. 659–666. 197

[9] N. D. Nanayakkara, B. Chiu, A. Samani, J. D. Spence, J. Samarabandu, and A. Fenster, "A twisting and bending model-based nonrigid image registration technique for 3-d ultrasound carotid images," *Medical Imaging, IEEE Transactions on*, vol. 27, no. 10, pp. 1378–1388, 2008. 197

[10] G. Yang, P. Kitslaar, M. Frenay, A. Broersen, M. J. Boogers, J. J. Bax, J. H. Reiber, and J. Dijkstra, "Automatic centerline extraction of coronary arteries in coronary computed tomographic angiography," *The International Journal of Cardiovascular Imaging*, vol. 28, no. 4, pp. 921–933, 2012. 198

[11] M. J. Powell, "An efficient method for finding the minimum of a function of several variables without calculating derivatives," *The computer journal*, vol. 7, no. 2, pp. 155–162, 1964. 198

[12] C. McIntosh and G. Hamarneh, "Is a single energy functional sufficient? adaptive energy functionals and automatic initialization," in *Medical Image Computing and Computer-Assisted Intervention–MICCAI 2007*. Springer, 2007, pp. 503–510. 198

[13] ——, "Optimal weights for convex functionals in medical image segmentation," in *Advances in Visual Computing*. Springer, 2009, pp. 1079–1088. 198

[14] C. Yuan, W. S. Kerwin, V. L. Yarnykh, J. Cai, T. Saam, B. Chu, N. Takaya, M. S. Ferguson, H. Underhill, D. Xu, F. Liu, and T. S. Hatsukami, "MRI of atherosclerosis in clinical trials," *NMR in Biomedicine*, vol. 19, no. 6, pp. 636–654, 2006. 199, 200

[15] V. Fuster, "The vulnerable atherosclerotic plaque: understanding, identification, and modification," *Cardiovascular Drugs and Therapy*, vol. 13, no. 4, pp. 363–363, 1999. 199

[16] C. Yuan, M. Oikawa, Z. Miller, and T. Hatsukami, "MRI of carotid atherosclerosis," *J Nucl. Cardiol.*, vol. 15, no. 2, pp. 266–275, 2008. 199

[17] C. Christodoulou, C. Pattichis, M. Pantziaris, and A. Nicolaides, "Texture-based classification of atherosclerotic carotid plaques," *Medical Imaging, IEEE Transactions on*, vol. 22, no. 7, pp. 902–912, 2003. 199

[18] M. Wintermark, S. Jawadi, J. Rapp, T. Tihan, E. Tong, D. Glidden, S. Abedin, S. Schaeffer, G. Acevedo-Bolton, B. Boudignon *et al.*, "High-resolution ct imaging of carotid artery atherosclerotic plaques," *American Journal of Neuroradiology*, vol. 29, no. 5, pp. 875–882, 2008. 199

[19] S. Clarke, R. Hammond, J. Mitchell, and B. Rutt, “Quantitative assessment of carotid plaque composition using multicontrast MRI and registered histology,” *Magnetic resonance in medicine*, vol. 50, no. 6, pp. 1199–1208, 2003. 199

[20] T. Saam, T. Hatsukami, N. Takaya, B. Chu, H. Underhill, W. Kerwin, J. Cai, M. Ferguson, and C. Yuan, “The vulnerable, or High-Risk, atherosclerotic plaque: Noninvasive MR imaging for characterization and assessment1,” *Radiology*, vol. 244, no. 1, pp. 64–77, 2007. 199

[21] W. S. Kerwin, K. D. O’Brien, M. S. Ferguson, N. Polissar, T. S. Hatsukami, and C. Yuan, “Inflammation in carotid atherosclerotic plaque: A dynamic contrast-enhanced MR imaging study1,” *Radiology*, vol. 241, no. 2, p. 459, 2006. 199

[22] B. A. Wasserman, E. M. Haacke, and D. Li, “Carotid plaque formation and its evaluation with angiography, ultrasound, and mr angiography,” *Journal of Magnetic Resonance Imaging*, vol. 4, no. 4, pp. 515–527, 1994. 199

[23] J. E. Wilhjelm, M.-L. Gronholdt, B. Wiebe, S. K. Jespersen, L. K. Hansen, and H. Sillesen, “Quantitative analysis of ultrasound b-mode images of carotid atherosclerotic plaque: correlation with visual classification and histological examination,” *Medical Imaging, IEEE Transactions on*, vol. 17, no. 6, pp. 910–922, 1998. 199

[24] J.-C. Tardif, J. D. Spence, T. M. Heinonen, A. Moody, J. Pressacco, R. Frayne, P. L’Allier, B. J. Chow, M. Friedrich, S. E. Black *et al.*, “Atherosclerosis imaging and the canadian atherosclerosis imaging network,” *Canadian Journal of Cardiology*, 2012. 200

[25] B. Chiu, E. Ukwatta, S. Shavakh, and A. Fenster, “Quantification and visualization of carotid segmentation accuracy and precision using a 2d standardized carotid map,” *Physics in medicine and biology*, vol. 58, no. 11, p. 3671, 2013. 200

[26] D. Buchanan, I. Gyacskov, E. Ukwatta, T. Lindenmaier, A. Fenster, and G. Parraga, “Semi-automated segmentation of carotid artery total plaque volume from three dimensional ultrasound carotid imaging,” in *SPIE Medical Imaging.* International Society for Optics and Photonics, 2012, pp. 83 170I–83 170I. 200

[27] C. Yuan and W. S. Kerwin, “MRI of atherosclerosis,” *Journal of Magnetic Resonance Imaging*, vol. 19, no. 6, pp. 710–719, Jun. 2004. 200

[28] W. Qiu, J. Yuan, E. Ukwatta, D. Tessier, and A. Fenster, “Rotational-slice-based prostate segmentation using level set with shape constraint for 3d end-firing trus guided biopsy,” in *Medical Image Computing and Computer-Assisted Intervention–MICCAI 2012.* Springer, 2012, pp. 537–544. 201

[29] ——, “Three-dimensional prostate segmentation using level set with shape constraint based on rotational slices for 3d end-firing trus guided biopsy,” *Medical Physics*, vol. 40, no. 7, p. 072903, 2013. 201

للاستشارات المنارة

Appendix A

Continuous max-flow based algorithm

In this chapter, the update equations of the continuous max-flow algorithm proposed in Chapter 4 are provided. Using the multiplier augmented method [1], the Lagrangian function is defined as follows.

$$\begin{aligned} L(p,q,u) \; &= \int_\Omega p_b(x)\,dx + \langle u_1, \operatorname{div} q_1 - p_w + p_l \rangle \\ &+ \langle u_2, \operatorname{div} q_2 - p_b + p_w \rangle \end{aligned}$$

along with its associated augmented Lagrangian function

$$\begin{aligned} L_c(p,q,u) \; &= L(p,q,u) - \frac{c}{2} \| \operatorname{div} q_1 - p_w + p_l \|^2 \\ &- \frac{c}{2} \| \operatorname{div} q_2 - p_b + p_w \|^2 \end{aligned}$$

where $c > 0$ is constant.

The new continuous max-flow algorithm can therefore be summarized as follows: for the k-th iteration,

- Update the flow functions simultaneously (flow maximization) by

$$q_i^{k+1}(x) := \arg \max_{|q_i(x)| \le \alpha_i} \; L_c(p^k, q_i, q_{j \ne i}^k, u^k)\,, \tag{A.1}$$

  where $i = 1, 2$;

$$p_i^{k+1}(x) := \arg \max_{p_i(x) \le D_i(x)} \; L_c(p_i, p_{j \ne i}^k, q^k, u^k)\,, \tag{A.2}$$

  where $i = l, w, b$.

- Update the labeling functions $u_i(x)$, $i = 1, 2$, by

$$u_1^{k+1}(x) \; = \; u_1^k(x) - c\big(\operatorname{div} q_1 - p_w + p_l\big)(x)$$

and

$$u_2^{k+1}(x) \,=\, u_2^k(x) - c\big(\operatorname{div} q_2 - p_b + p_w\big)(x)\,.$$

The flow-maximization steps (A.1) and (A.2) of the proposed algorithm can be fully parallelized. In this paper, we implement the proposed continuous max-flow algorithm on a GPU and obtain a high computational performance. The proposed continuous max-flow algorithm converges at the two optimal labeling functions $u^*_{1,2}(x) \in [0,1]$, which satisfy $u^*_1(x) \leq u^*_2(x)$ for $\forall x \in \Omega$. Note that, in Prop. 3 of Chapter 4, a parameter $\gamma \in (0,1]$ is chosen to threshold $u^*_{1,2}(x)$ to be $u^\gamma_{1,2}(x) \in \{0,1\}$. The labeling functions $u^\gamma_{1,2}(x)$ indicate the new positions of the two surfaces $\mathcal{C}_{LIB}$ and $\mathcal{C}_{AB}$ at the next time $t+1$, which are globally optimal to the optimization problem (4.17), and in turn to (4.15).

References

[1] D. P. Bertsekas, *Nonlinear Programming.* Athena Scientific, September 1999. 205

Appendix B

Copyright reprint permissions

American Association of Physicists in Medicine
One Physics Ellipse
College Park, MD 20740-3846
(301) 209-3350
Fax (301) 209-0862
http://www.aapm.org

Office of the Executive Director
Angela R. Keyser
Phone: [redacted] Fax: [redacted]
E-mail: [redacted]

DATE OF REQUEST: May 12, 2013

FROM:

Eranga Ukwatta, Robarts Research Institute, 100 Perth Drive, University of Western Ontario, London, ON, Canada, N6A 5k8

EMAIL ADDRESS: [redacted]

1. **Permission is granted to:**

   Eranga Ukwatta, Robarts Research Institute, 100 Perth Drive, University of Western Ontario, London, ON, Canada, N6A 5k8

2. **Permission is requested to use the following material:**

   E. Ukwatta, J. Awad, A. D. Ward, D. Buchanan, J. Samarabandu, G. Parraga, A. Fenster, "Three-dimensional ultrasound of carotid atherosclerosis: Semi-automated segmentation using a level set-based method," Medical Physics 38(5), 2479-95 2011.

   E. Ukwatta, J. Yuan, D. Buchanan, B. Chiu, J. Awad, W. Qiu, G. Parraga, A. Fenster, " Three-dimensional segmentation of three-dimensional ultrasound carotid atherosclerosis using sparse field level sets," Medical Physics 40(5), 2903-20, 2013.

3. **For what purpose:**

   My PhD thesis

Authors seeking permission must also notify the first author of the article from which permission is being sought.

Permission is hereby granted: [redacted] May 21, 2013

Date

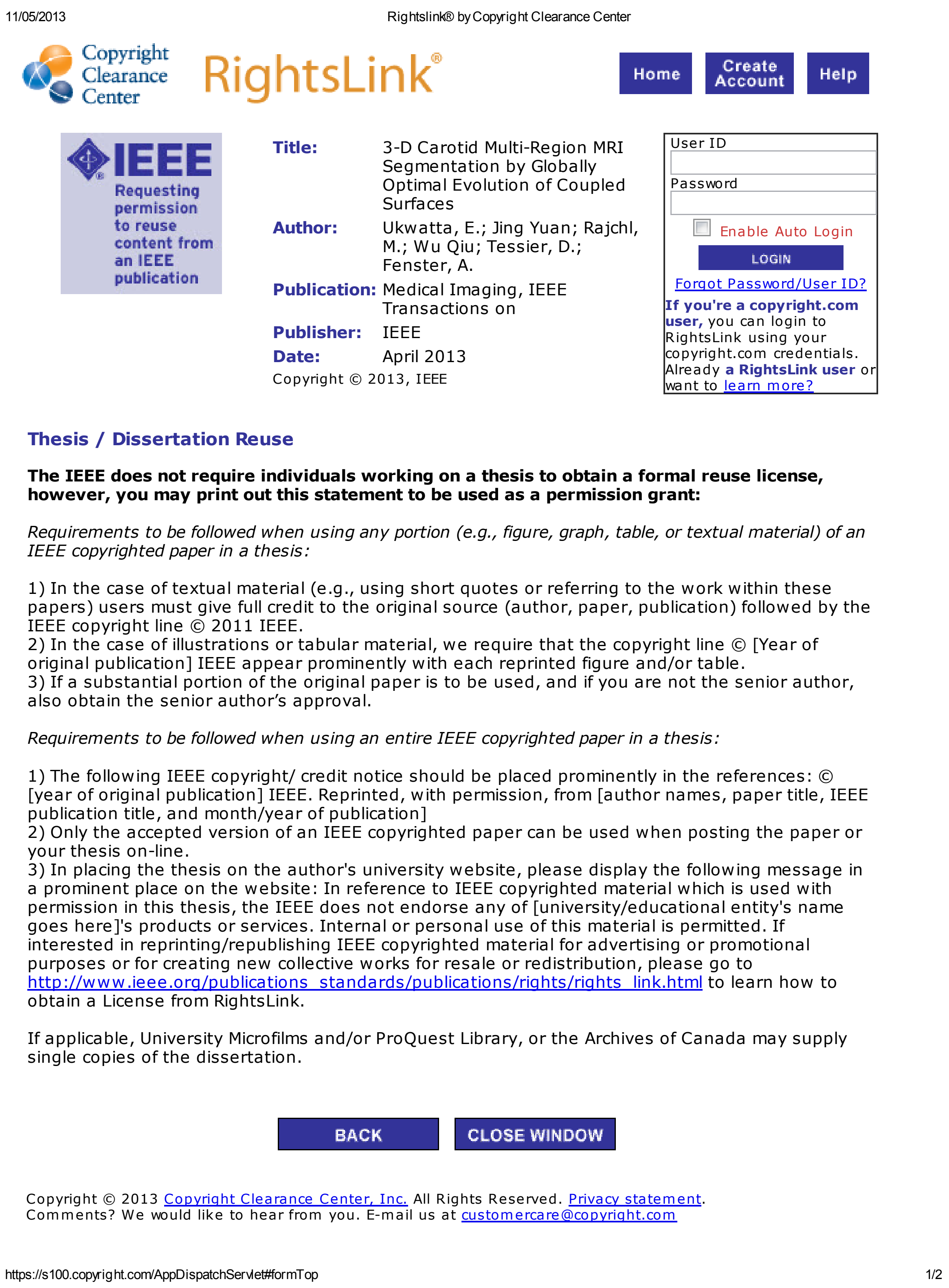

11/05/2013 Rightslink® by Copyright Clearance Center

Copyright Clearance Center RightsLink®

IEEE Requesting permission to reuse content from an IEEE publication

Title: 3-D Carotid Multi-Region MRI Segmentation by Globally Optimal Evolution of Coupled Surfaces
Author: Ukwatta, E.; Jing Yuan; Rajchl, M.; Wu Qiu; Tessier, D.; Fenster, A.
Publication: Medical Imaging, IEEE Transactions on
Publisher: IEEE
Date: April 2013

Copyright © 2013, IEEE

If you're a copyright.com user, you can login to RightsLink using your copyright.com credentials. Already **a RightsLink user** or want to learn more?

Thesis / Dissertation Reuse

The IEEE does not require individuals working on a thesis to obtain a formal reuse license, however, you may print out this statement to be used as a permission grant:

Requirements to be followed when using any portion (e.g., figure, graph, table, or textual material) of an IEEE copyrighted paper in a thesis:

1) In the case of textual material (e.g., using short quotes or referring to the work within these papers) users must give full credit to the original source (author, paper, publication) followed by the IEEE copyright line © 2011 IEEE.
2) In the case of illustrations or tabular material, we require that the copyright line © [Year of original publication] IEEE appear prominently with each reprinted figure and/or table.
3) If a substantial portion of the original paper is to be used, and if you are not the senior author, also obtain the senior author's approval.

Requirements to be followed when using an entire IEEE copyrighted paper in a thesis:

1) The following IEEE copyright/ credit notice should be placed prominently in the references: © [year of original publication] IEEE. Reprinted, with permission, from [author names, paper title, IEEE publication title, and month/year of publication]
2) Only the accepted version of an IEEE copyrighted paper can be used when posting the paper or your thesis on-line.
3) In placing the thesis on the author's university website, please display the following message in a prominent place on the website: In reference to IEEE copyrighted material which is used with permission in this thesis, the IEEE does not endorse any of [university/educational entity's name goes here]'s products or services. Internal or personal use of this material is permitted. If interested in reprinting/republishing IEEE copyrighted material for advertising or promotional purposes or for creating new collective works for resale or redistribution, please go to http://www.ieee.org/publications_standards/publications/rights/rights_link.html to learn how to obtain a License from RightsLink.

If applicable, University Microfilms and/or ProQuest Library, or the Archives of Canada may supply single copies of the dissertation.

Copyright © 2013 Copyright Clearance Center, Inc. All Rights Reserved. Privacy statement.
Comments? We would like to hear from you. E-mail us at customercare@copyright.com

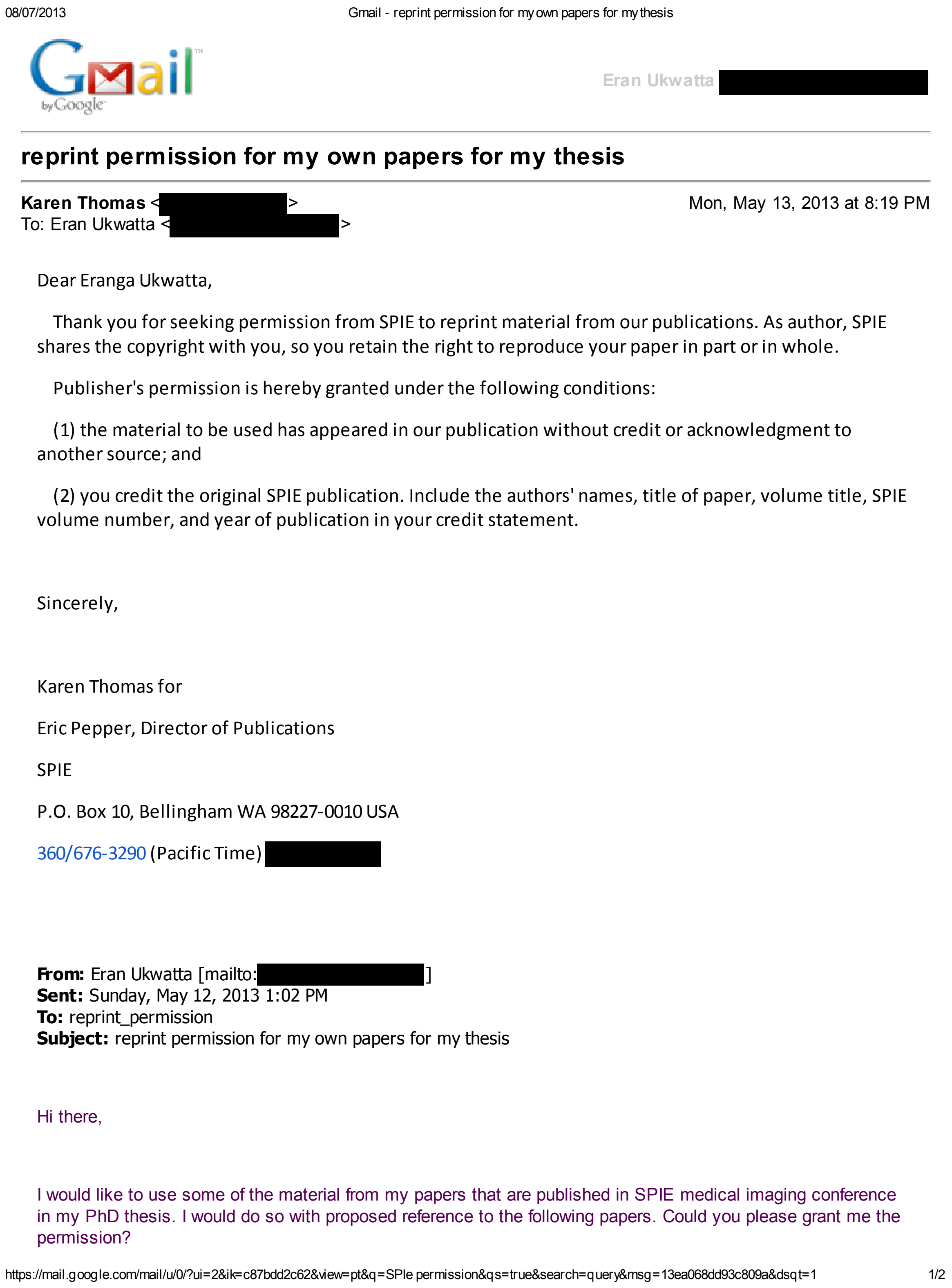

Eran Ukwatta [redacted]

reprint permission for my own papers for my thesis

Karen Thomas <[redacted]>
To: Eran Ukwatta <[redacted]>

Mon, May 13, 2013 at 8:19 PM

Dear Eranga Ukwatta,

Thank you for seeking permission from SPIE to reprint material from our publications. As author, SPIE shares the copyright with you, so you retain the right to reproduce your paper in part or in whole.

Publisher's permission is hereby granted under the following conditions:

(1) the material to be used has appeared in our publication without credit or acknowledgment to another source; and

(2) you credit the original SPIE publication. Include the authors' names, title of paper, volume title, SPIE volume number, and year of publication in your credit statement.

Sincerely,

Karen Thomas for

Eric Pepper, Director of Publications

SPIE

P.O. Box 10, Bellingham WA 98227-0010 USA

360/676-3290 (Pacific Time) [redacted]

From: Eran Ukwatta [mailto:[redacted]]
Sent: Sunday, May 12, 2013 1:02 PM
To: reprint_permission
Subject: reprint permission for my own papers for my thesis

Hi there,

I would like to use some of the material from my papers that are published in SPIE medical imaging conference in my PhD thesis. I would do so with proposed reference to the following papers. Could you please grant me the permission?

E. Ukwatta, J. Yuan, Wu Qiu, M. Rajchl, A. Fenster, "Efficient convex optimization-based curvature dependent contour evolution approach for medical image segmentation," *Proceedings of SPIE Medical Imaging: Image Processing*, Orlando, FL 2013.

E. Ukwatta, J. Awad, D. Buchanan, G. Parraga, A. Fenster, "Thee-dimensional semi-automated segmentation of carotid atherosclerosis from three-dimensional ultrasound images," *SPIE Medical Imaging*, San Diego, CA, 2012.

E. Ukwatta, J. Awad, A. D. Ward, A. Krasinski, J. Samarabandu, G. Parraga, A. Fenster, "Segmentation of the lumen and media-adventitia boundaries of the common carotid artery from 3D ultrasound images," *Proceedings of SPIE medical imaging*, Orlando, FL, 7963-15, 2011.

--

Thanks,

Eranga

Eranga Ukwatta
PhD Candidate
Robarts Research Institute

Western University

Phone: [redacted]

Curriculum Vitae

Name: Eranga Ukwatta

Post-secondary Education and Degrees:

2009–2013 **Ph.D.**
Biomedical Engineering Graduate Program
The University of Western Ontario
London, Ontario, Canada

2007–2009 **M.E.Sc.**
Electrical and Computer Engineering
The University of Western Ontario
London, Ontario, Canada

2001–2005 **B.Sc. Eng. Honours**
Electronic and Telecommunication Engineering
The University of Moratuwa
Moratuwa, Sri Lanka

Honors and Awards:

NSERC Alexander Graham Bell Canada Graduate Scholarship
2011–2013

SPIE Scholarship in Optics and Photonics
2011, 2012

Ontario Graduate Scholarship (Declined)
2011–2012

Ontario Graduate Scholarships in Science and Technology
2010–2011

CIHR Strategic Training Fellow in Vascular Research
2009–2011

Western Graduate Research Scholarship (WGRS)

للاستشارات المنارة

2009–2011

Western Engineering Scholarship
20007–2009

Research Assistantship
2007–2012

Mahapola Higher Education Scholarship
2001–2005

Third place award for poster presentation
Imaging Network Ontario 2013, Toronto, ON

First place poster award
Western Research Forum 2012, London, ON

First place poster award
Margaret Moffat Research Day 2011 Prize in Imaging
Schulich Medicine & Dentistry, The University of Western Ontario

Second best award for poster presentation
London Imaging Discovery 2011, London, ON

Second prize award for the poster presentation
Western Research Forum 2011, London, ON

Graduate thesis research award, 2011
Biomedical Engineering, The University of Western Ontario

Graduate thesis research award, 2009
Electrical and Computer Engineering,
The University of Western Ontario

Deans Honour list - First Class Honours
Dept. of Electronic and Telecommunication Engineering
University of Moratuwa
2001–2005

Prof. K.K.Y.W. Perera award for the highest overall GPA
in Fourth Year, University of Moratuwa
2005

Prof. Clevaland award for the highest GPA
GPA in Management Science, University of Moratuwa
2005

Related work experience:

2009–2012 **Teaching and Research Assistant**
Graduate Program in Biomedical Engineering
The University of western Ontario
London, ON, Canada

2007–2009 **Teaching and Research Assistant**
Department of Electrical and Computer Engineering
The University of western Ontario
London, ON, Canada

2009 **Research Intern**
Imaging Research Lab, Robarts Research Institute
London, ON, Canada

2005–2007 **Telecommunication Engineer**
Core Network Operations
Dialog Telekom Ltd, Colombo, Sri Lanka

2004 **Engineering Intern**
Dialog Broadband Ltd, Colombo, Sri Lanka

Publications:

Selected Peer Reviewed Journal Articles:

1. **E. Ukwatta**, J. Yuan, M. Rajchl, and A. Fenster, "3D Carotid multi-region MRI segmentation by globally optimal evolution of coupled surfaces," in *IEEE Transactions on Medical Imaging,* vol. 32(4), 2013, pp. 770–85.
2. **E. Ukwatta**, J. Yuan, D. Buchanan, B. Chiu, J. Awad, G. Parraga, and A. Fenster, "Three-dimensional Segmentation of Three-dimensional Ultrasound Carotid Atherosclerosis using Sparse Field Level Sets," in *Medical Physics,* 2013, vol. 40(5), pp. 2903–20.
3. B. Chiu, **E. Ukwatta**, S. Shavakh, A. Fenster, "Quantitative and visualization of carotid segmentation accuracy and precision using a 2D standardized carotid map," in *Physics in Medicine and Biology,* vol. 58(11), 2013, pp. 3671–703.

4. W. Qiu, J. Yuan, **E. Ukwatta**, D. Tessier, A. Fenster, "3D Prostate Segmentation Using Level Set with Shape Constraint Based on Rotational Slices for 3D End-firing TRUS Guided Biopsy," in *Medical Physics,* vol. 40(7), 2013, pp. 072903-1–12.
5. **E. Ukwatta**, J. Yuan, D. Buchanan, B. Chiu, J. Awad, W. Qiu, G. Parraga, and A. Fenster, "Three-dimensional ultrasound of carotid atherosclerosis: Semi-automated segmentation using a level set-based method," in *Medical Physics,* vol. 38(5), 2011, pp. 2479–2495.
6. **E. Ukwatta**, J. Samarabandu, and M. Hall, "Machine Vision System for Automated Spectroscopy," in *Machine Vision and Applications,* vol. 22(5), 2011, pp. 2479–2495.
7. **E. Ukwatta**, J. Yuan, M. Rajchl, Q. Wu, B. Chiu, A. Fenster, "Joint Segmentation of Lumen and Outer-Wall from 3D Femoral Artery MR Images: Towards Volumetric Phenotypes of Peripheral Arterial Disease," Submitted to IEEE Transactions on Medical Imaging, August 2013.
8. M. Rajchl, J. Yuan, J. A. White, **E. Ukwatta**, J. Stirrat, M. S. Nambakhsh, T. M. Peters, "Fast hierarchical convex relaxation approach to segmenting 3D scar tissue from delayed-enhancement cardiac MR images," Under review in IEEE Transactions of Medical Imaging, Dec 2012.
9. W. Qiu, J. Yuan, **E. Ukwatta**, Y. Sun, M. Rajchl, A. Fenster, "Dual optimization based prostate zonal segmentation in 3D MR images," Under review in Medical Image Analysis, May 2013.
10. W. Qiu, J. Yuan, **E. Ukwatta**, Y. Sun, M. Rajchl, A. Fenster, "Prostate segmentation: An efficient convex optimization approach with axial symmetry using 3D TRUS and MR images," Under review in IEEE Transactions on Medical Imaging, August 2013.

Selected Refereed Conference Papers:

1. **E. Ukwatta**, J. Yuan, B. Chiu, Q. Wu, M. Rajchl, A. Fenster, "Joint segmentation of 3D femoral lumen outer wall surfaces from MR images," in *proceedings of Medical Image Computing and Computer Aided Intervention (MICCAI),* Nagoya, Japan, Sept 2013.
2. **E. Ukwatta**, J. Yuan, W. Qiu, M. Rajchl, and A. Fenster, "Efficient convex optimization-based curvature dependent contour evolution approach for medical imaging segmentation," in *proceedings of Medical Imaging 2008: Image Processing, SPIE,* Orlando, FL, pp. 866902–1–9, Feb 2013.

3. J. Yuan, **E. Ukwatta**, W. Qiu, M. Rajchl, Y. Sun, X-C Tai, A. Fenster, “Jointly Segmenting Prostate Zones in 3D MRIs by Globally Optimized Coupled Level-Sets,” in *Proceedings of Energy minimization methods in Computer Vision and Pattern Recognition (EMMCVPR),* Lund, Sweden, July 2013.
4. Q. Wu, J. Yuan, **E. Ukwatta**, Y. Sun, M. Rajchl, A. Fenster, “Fast globally optimal segmentation of 3D prostate MRI with axial symmetry prior,” in *Medical Image Computing and Computer Aided Intervention (MICCAI),* Nagoya, Japan, Sept 2013.
5. J. Yuan, W. Qiu, **E. Ukwatta**, M. Rajchl, , X.C. Tai, A. Fenster, “Efficient 3D endfiring TRUS prostate segmentation with globally optimized rotational symmetry,” in *IEEE conference on computer vision and pattern recognition (CVPR),* Portland, OR, June 2013.
6. W. Qiu, J. Yuan, **E. Ukwatta**, M. Rajchl, A. Fenster, “Efficient 3D multi-region prostate MRI segmentation using dual optimization,” in *Information Processing in Medical Imaging (IPMI),* Springer Berlin Heidelberg, Asolomar, CA, pp. 304–315 June 2013.
7. Q. Wu, J. Yuan, J. Kishimoto, **E. Ukwatta**, A. Fenster, “Lateral ventricle segmentation of 3D pre-term neonates US using convex optimization,” in *Proceedings of Medical Image Computing and Computer Aided Intervention (MICCAI),* Springer Berlin Heidelberg, Nagoya, Japan, Sept 2013.
8. Wu Qiu, J. Yuan, **E. Ukwatta**, D. Tessier, A. Fenster, “3D prostate segmentation in 3D TRUS using convex optimization,” in *Proceedings of SPIE Medical Imaging: Image Processing,* Springer Berlin Heidelberg, Orlando, FL, pp. 866943–1–7, Feb 2013.
9. **E. Ukwatta**, J. Yuan, M. Rajchl, and A. Fenster, “Efficient global optimization based 3D carotid AB-LIB MRI Segmentation by simultaneously evolving coupled surfaces,” in *proceedings of MICCAI,* Springer Berlin Heidelberg, Nice, France, pp. 377–384, Oct 2012.
10. **E. Ukwatta**, J. Awad, D. Buchanan, G. Parraga, and A. Fenster, “Three-dimensional semi-automated segmentation of carotid atherosclerosis from Three-dimensional ultrasound images,” in *proceedings of Image Processing: Computer Aided Diagnosis /SPIE,* San Diego, USA, pp. 83150O–2, Feb 2012.
11. Q. Wu, J. Yuan, **E. Ukwatta**, D. Tessier, A. Fenster, “Rotational-slice-based prostate segmentation using level set with shape constraint for 3D end-firing TRUS guided biopsy,” in *Proceedings of Medical Image Computing and Computer Aided Intervention (MICCAI),* Springer Berlin Heidelberg, Nice, France, pp. 537–544, Sept 2012.

12. J. Yuan, Qiu Wu, **E. Ukwatta**, M. Rajchl, A. Fenster, “An efficient convex optimization approach to 3D prostate MRI segmentation with generic start shape prior,” in *MICCAI Grand Challenge:Prostate MR Image Segmentation,* Nice, France, Sept 2012.

13. M. Rajchl, J. Yuan, J. A. White, C. M. S. Nambakhsh, **E. Ukwatta**, F. Li, J. Stirrat, T. M. Peters, “A fast convex optimization approach to segmenting 3D scar tissue from delayed-enhancement cardiac MR images,” in *Proceedings of Medical Image Computing and Computer Aided Intervention (MICCAI),* Springer Berlin Heidelberg, Nice, France, pp. 659–666, Sept 2012,

14. M. Rajchl, J. Yuan, **E. Ukwatta**, T. M. Peters, “Fast interactive multi-region cardiac segmentation with linearly ordered labels,” in *Proceedings of IEEE International Symposium on Biomedical Imaging,* Barcelona, Spain, pp. 1409–12, May 2012.

15. D. Buchanan, I. Gyacskov, **E. Ukwatta**, T.Lindenmaier, A. Fenster, G. Parraga, “Semi-automated segmentation of carotid artery plaque volume from three dimensional ultrasound carotid imaging,” in *SPIE Medical Imaging,* San Diego, CA, Feb 2012.

16. **E. Ukwatta**, B. Buchanan, G. Parraga, and A. Fenster, “Three-dimensional ultrasound imaging of carotid atherosclerosis,” in *proceedings of IEEE International conference on Intelligent computation and Bio-medical instrimentation (ICBME),* Wuhan, China, pp. 81–84, Dec 2011.

17. **E. Ukwatta**, J. Awad, A. D. Ward, D. Buchanan, G. Parraga, A. Fenster, “Coupled level set segmentation approach for carotid segmentation using 3D ultrasound images,” in *IEEE International Symposium on Biomedical Imaging,* Chicago, IL, pp. 37–40, March 2011.

18. **E. Ukwatta**, J. Awad, A. D. Ward, A. Krasinski, J. Samarabandu, G. Parraga, A. Fenster, “Segmentation of the lumen and media-adventitia boundaries of the common carotid artery from 3D ultrasound images,” in *Proceedings of SPIE medical imaging,* , Orlando, FL, pp. 7963–15 79630G, Feb 2011.

19. **E. Ukwatta**, J. Awad, A. D. Ward, D. Buchanan, G. Parraga, A. Fenster, “Semi-automated segmentation method to quantify carotid arthrosclerosis from 3DUS images,” in *AAPM meeting,* Vancouver, BC, pp. 83170I–83170I–7, Aug 2011.

20. **E. Ukwatta**, J. Samarabandu, “Vision based metal spectral analysis using multi-label classification,” in *Proceedings of Canadian Conference on Computer and Robot Vision,* Kelowna, BC, pp. 132–139, May 2009.

21. **E. Ukwatta**, R. Rodrigo, J. Samarabandu, M. Hall, "Vision based spectroscopy simulation," in *Proceedings of Canadian Conference on Computer and Robot Vision,* Windsor, ON, pp. 363–368, May 2008.